Design and testing of a concentrator wind turbine

Thesis

DESIGN AND TESTING OF A CONCENTRATOR WIND TURBINE.

This is a thesis for a the degree of Doctor of Philosophy
in the discipline of Wind Engineering.

David Olivieri BSc(Hons).

27 November 1991

BRITISH LIBRARY

IMAGING SERVICES NORTH

Boston Spa, Wetherby
West Yorkshire, LS23 7BQ
www.bl.uk

VOLUME CONTAINS CLEAR OVERLAYS

OVERLAYS HAVE BEEN SCANNED SEPERATELY AND THEN AGAIN OVER THE RELEVANT PAGE

Abstract

Wind energy, being an indirect form of solar energy would initially seem a very promising form of energy. Unfortunately, it suffers from the problem of dilution. Wind turbine designers naturally try to compensate for this by increasing the size of the rotor to capture more of the kinetic energy of the wind. A major constraint in conventional wind turbine design is the reduction in rotational speed as the size of the rotor is increased. This means expensive gear boxes are unavoidable. The rotor also becomes considerably more complicated in design and heavier as the size increases, to mitigate working stresses.

Flow concentrators have been investigated in an attempt to alleviate wind turbine design problems, but flow concentrators usually incur the expense of high structural weight and size. The Helical Vortex Wind Concentrator (HVWC) is a recent addition to the list of flow concentrator types and its economic potential is, as yet unknown.

The principle of the HVWC has been demonstrated in a series of wind tunnel tests. The wind tunnel tests involved a direct comparison between the performance of a wind turbine with and without an HVWC attached. During these tests a definite increase in power out was observed when the concentrator was attached to the wind turbine. Previous to these successful wind tunnel tests, other wind tunnel and field tests had been conducted on less successful designs. These other tests were important in the development of the current theory and design of the HVWC. Future research will need to investigate both physical and economic limitations of this type of wind concentrator.

Contents

List of Figures

List of Tables

Acknowledgements

This work was funded by Marlec Engineering Ltd and the Science and Engineering Research Council. Wind tunnel test facilities were provided by Queen Mary and Westfield College (QMW) in London, Goldstein Laboratory in Manchester and the Department of Bionics and Evolution Technology in Berlin.

I would like to thank the following people for their assistance during this period;

- David Sharpe, senior lecturer in the Department of Aeronautical Science of QMW, and Godfrey Boyle, Head of the Open University Energy and Environment Research Unit, for their time and supervision.
- Professor Ingo Rechenberg of the Technical University of Berlin, for the two theses he sent to the author and for allowing the author to use their wind tunnel test facilities. This was extremely helpful in validating the author's model.
- Michael Bromillow, lecturer in the Department of Applied Mathematics of the Open University, for his advice on numerical methods.
- Dr. David Smith, Manager of Goldstein Laboratory, for use of their wind tunnel and flow visualization equipment.
- Mr. Holt, Chief Aerodynamicist of British Aerospace, Brough, for his advice in flow visualization techniques.
- Peter Zimmermann, research student at the Technical University of Berlin, in helping the author build and test the wind tunnel model in

Berlin.

- John Fawkes, Managing Director of Marlec Engineering Ltd, for use of the field test site and test facilities at Gretton, Northamptonshire, and for sponsoring the SERC CASE award which helped finance the project.

- John Butler and Scott Forrest, technicians of the Open University Energy and Environment Research Unit, for their assistance in manufacturing and testing the CWT field test rig.

- Richard Hearne, design technician in the Design Discipline at the Open University, for his assistance in photographic and video recording work.

Glossary

$A =$ Cross sectional area of the control volume.

$Ae =$ Exit sectional area of ducted augmentor, or frontal cross sectional area of the CWT system.

$At =$ Sectional area of duct at rotor location.

$c =$ Local chord of concentrator blade.

$C/s =$ Ratio of local chord to cascade blade spacing.

$C_D =$ Local drag coefficient of concentrator blade for single blade 2D flow.

$CD_{con} =$ Axial force coefficient of the concentrator.

$CD_{rotor} =$ Axial force coefficient of the rotor.

$C_L =$ Local lift coefficient of the concentrator blade for single blade 2D flow.

$C_p =$ Coefficient of performance $= P/(\frac{1}{2}\rho\pi r_R^2 V^3)$

$(C_p)_{Gross} =$ Gross coefficient of performance $= P/(\frac{1}{2}\rho A_e V^3)$

$C_{pa} =$ Augmented C_p of the rotor $= P_a/(\frac{1}{2}\rho\pi r_R^2 V^3)$

$C_R =$ Power concentrator ratio based on rotor swept area.

$(C_R)_{Gross} =$ Power concentrator ratio based on a swept area whose radius is equal to the outside radius of the concentrator.

$E =$ Loss of energy of system.

e = Internal energy per unit mass.

$\vec{f}$ = Body forces (ie gravity, e.m.f, etc) acting on the fluid as it flows through the control volume per unit volume.

$\vec{F}$ = Total axial force vector on the CWT.

F = Blade element circulation reduction factor due to tip loss, (ie $F = \Gamma/\Gamma_\infty$).

g = Acceleration due to gravity.

H_1 = Total pressure downstream of the concentrator blades.

H_0 = Total pressure upstream of the concentrator blades.

h = Inner radius of concentrator.

$\acute{h}$ = Inner radius of concentrator wake at concentrator disc.

h'' = Inner radius of concentrator wake at far wake.

I = Polar Moment of Inertia of the rotor in Kgm^2.

$\vec{M}$ = Total torque vector on the CWT.

N = Number of blades of the concentrator.

$\hat{n}$ = Unit vector normal to the surface.

P = Output power of an unaugmented wind turbine.

P_a = Output power from an augmented wind turbine.

p = Free stream static pressure.

p_{c1} = Static pressure at concentrator orifice.

p_e = Static pressure in outer region surrounding the concentrator wake at the far wake.

$\acute{p_e}$ = Static pressure in the annulus at far wake.

p'_{e1} = Static pressure in the annulus at the concentrator disc.

p''_e = Static pressure in rotor wake or core flow at far wake.

p_1 = Static pressure just upstream of the rotor.

p_2 = Static pressure just downstream of rotor.

$\acute{p}$ = Pressure increment across concentrator.

$\vec{q}$ = Flow vector at x,y,z .

$\vec{q}_{P_2}$ = Induced velocity vector at point P_2 due to infinite vortex strips representing bound vortices.

Q = Heat transfer.

Q_{vis} = Heat transfer to the control volume due to viscous friction.

q = Volume flow from the 'Ejector Effect'.

$\vec{q}$ = Flow velocity vector at x,y,z coordinates.

r = Radial distance from axis of symmetry of concentrator.

r_e = Rotor wake radius at far wake.

r_R = Radius of rotor blade.

$\vec{r}_n$ = Position vector of a node in the vortex wake structure relative to the origin for the nth iteration.

r_p = Power augmentation ratio = C_{pa}/C_p

R = Outside radius of the concentrator.

$\acute{R}$ = Outside radius of the concentrator wake.

R'' = Outer radius of the concentrator wake at far wake.

S = Surface area of vortex sheets.

$S(\omega_p)$ = Spectral density function of ω_p.

TI = Turbulence intensity or power output variation, which is the ratio of standard deviation to the mean value of the signal.

t = Unit time.

T = Drag thrust on concentrator blades.

T_A = Aerodynamic torque of the rotor in Nm.

T_0 = Load torque from the generator in Nm.

T_Q = Torque on concentrator blades.

T_s = Tip speed ratio of the rotor = $\Omega r_R/V$.

u = Axial velocity across concentrator blades; also total internal energy of a control volume.

u_1 = Axial far wake velocity between outside and inboard trailing vortices.

v = Radial velocity in the wake field.

V = Free stream velocity.

V_a = Total induced velocity from semi-infinite sheets representing the cylindrical component of the trailing vortices.

V_1, V_2 = Respective upper and lower contributions of induced velocity about the XY plane constituting V_a.

V_c = Axial flow velocity through the core at far wake (concentrator only).

V_{c1} = Axial flow velocity through the core at the concentrator disc (concentrator only).

V_{cr1} = Flow velocity through the CWT at rotor disc.

V_{cr} = Axial flow velocity of the rotor at the far wake.

V_{crr} = Axial flow velocity at any general point in the core flow region of the CWT.

V_T = Tangential flow velocity downstream of the blades.

V_t = Tangential flow velocity due to bound vortices only.

V_x = X component of induced velocity.

V_y = Y component of induced velocity.

V_z = Z component of induced velocity.

$\vec{V}_{eff}$ = Local effective velocity over the concentrator blade element due to the vector sum of $\vec{V}$ and $\vec{W}$.

$\vec{W}$ = Local vector sum of all 2D induced velocities $\vec{w}$ in the y,z plane at y_p, z_p.

Wk = Work transfer.

W_{vis} = Work transfer to the system due to viscous friction.

x, y, z = Spatial coordinates of point of induced velocity relative to X, Y, Z axes.

x_n = X coordinate of a node in the vortex wake structure for the nth iteration.

y_p, z_p = 2D coordinates of the bound vortex.

y/h = Ratio of axial distance from the origin to internal radius.

ω = Angular velocity of wake flow at the concentrator disc and angular frequency. Both are in radian/sec.

σ = Standard deviation.

α = Local angle of incidence of concentrator blade element and angular acceleration in radians/sec.

β = Helical vortex angle.

β_1, β_2 = Inboard and outboard helical vortex angles.

$\gamma, \gamma'', \acute{\gamma}$ = Vortex distribution of circulation strength per unit length of the vortex sheet, for cylindrical component of trailing vortices, axial component of trailing vortices and bound vortices respectively.

$\gamma_{rotor}, \gamma''_{rotor}, \gamma_{r\acute{o}tor}$ = As above except it refers to rotor wake.

Γ = Local blade element bound vortex circulation strength.

Γ_o = Maximum vortex circulation strength for the circulation over blade span.

Γ_R = Maximum rotor blade circulation.

Γ_∞ = Local blade element bound vortex circulation strength for concentrator or rotor with infinite number of blades.

δv = Induced axial velocity from the concentrator vortex wake at rotor disc.

δv_e = Induced flow from turbulent mixing (Ejector Effect).

$\delta \acute{v}$ = Induced axial velocity from the concentrator vortex wake in the far wake.

$\vec{\Delta}_n$ = Adjustment vector for a node in the vortex wake structure for the $(n+1)$th iteration.

Θ = Local blade twist angle between the chord line and a plane through the Y axis.

ω_p = Angular frequency per Nyquist frequency of the pth harmonic defined by $2\pi p/n$ where $p = 1, ..., n/2$

ω_1 = Angular velocity of the wake flow in radians in the far stream.

ρ = Air density.

ψ = Angular displacement about axis of symmetry between two adjacent blade span axes.

ϕ = Local flow angle along the blade.

ϕ^* = Local angle of the blade element trailing vortex sheet.

Ω = Rotational speed of the wind turbine.

ν = Volume of the control volume.

Chapter 1

INTRODUCTION

1.1 Background

A wind concentrator is a device that causes wind flow to be focused into a certain region of space. In this region of concentrated wind flow, a wind turbine can operate at a higher power output. This allows the rotor to be more compact and adaptable for a wider range of applications. The result of this might lead to a possible reduction in cost per unit power installed.

Considerable interest has been shown in wind concentrators in recent years, even though they are not a new concept. (See Savasegarem(1986)). To categorize the recent development of modern wind concentrators the following headings will be used;

1. Ducted Augmentation.
2. Obstruction-Type and Wind Deflection Systems.
3. Tip-Vane Systems.
4. Vortex Augmentation.
5. Vortex Screw Augmentation.

The final heading is the most recent addition to the different types of wind concentrators. All systems are suitable for axial-flow wind rotors. Cross-flow wind turbines like Darrieus and Savonius rotors cannot be used with

Vortex Augmentation, Vortex Screw Augmentation and Tip-Vane Systems. Savonius rotors are ideally matched to Wind Deflection Systems.

In the following sections the terms r_p, C_p and $(C_p)_{Gross}$ will be used. r_p is the ratio of output power of a concentrator wind turbine system to that of a conventional wind turbine system based on rotor swept area. (In each case the rotor design and size are the same). C_p refers to the ratio of rotor power to available free stream kinetic energy per unit time flowing over the rotor swept area. The $(C_p)_{Gross}$ is similar to C_p except it is based on the total cross sectional area of the CWT involved in blocking the air flow.

1.2 Ducted Augmentation

One of the earliest wind concentrators was used on ancient Persian windmills (see Sivasegarem(1986)), (see figure 1.1). In figure 1.1 the purpose of the duct was not only to focus the air flow onto the upper region of the rotor causing it to rotate, but to concentrate the air flow in this region at the same time. This particular design proved to be very ineffective. In recent years improvement on the concept was investigated theoretically by Frost *et al*(1982), (see figure 1.2). This machine was known as the 'Wind Wheel Turbine', and gave a C_p of 0.62 based on the air mass flow entering the concentrator wind turbine system per second. This was achieved at a very low tip speed ratio making it unsuitable for electrical generation.

Other types of ducted concentrator have been investigated with the most effective being the Venturi-Type duct. Ducts with a short converging section and a much longer diffuser section have proved to be the most effective, (see figure 1.3). Further improvement by use of flaps is shown in figure 1.3. Igra(1981) has shown from his research work that maximum augmentation can be obtained when the exit pressure p_e'' is a minimum, pressure difference $(p_e'' - p_2)$ approaches that of the free stream dynamic pressure and the ratio of exit to throat cross sectional flow areas A_e/A_t is as large as possible. The values of r_p reported from experiments with small wind tunnel models indicate $r_p > 3$ with flaps used on the concentrator.

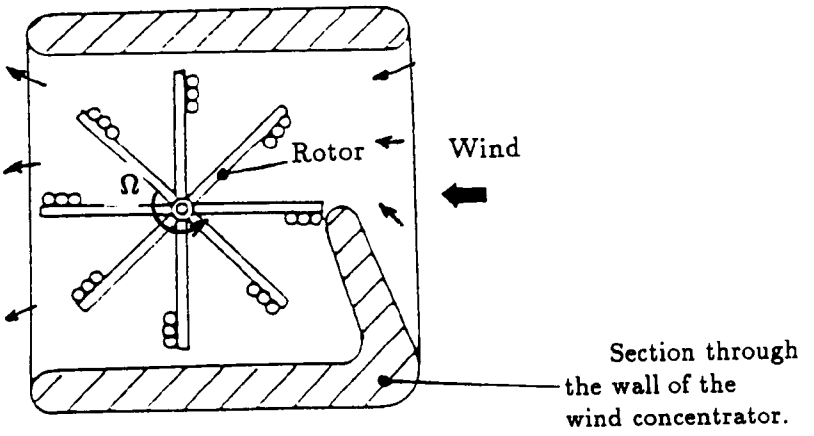

Figure 1.1 Sectional plan view of an ancient Persian Cross-Flow Turbine.

Source: Sivasegarem(1986)

The gross power coefficient possible for the ducted system based on A_e is of the order of 0.83. This was investigated by Dick(1986), which indicates a definite improvement over the conventional wind turbine. The construction weight can be reduced even more by using compact diffusers. This is achieved by using a diffuser with a segmented annulus as shown in figure 1.4. The flow through the slots can energize the boundary layer to allow greater diffusion in a shorter axial distance. Foreman *etal*(1979) reported $r_p > 4$ from experiments with wind tunnel models.

Foreman(1983) made a rough economic assessment of the concentrator by investigating the cost to weight ratio of different design of ducted systems. His results show that the cost to weight ratio varies inversely with the $\frac{5}{6}$ th power of the diameter.[1] A similar trend is noticed with cost to power ratio. This would indicate that large machines are very much more economical. The major objections to the size of the device would be in yaw and storm protection, which may explain why the idea has not been fully realized yet.

The application of ducted systems to Savonius-Type rotors has led to

[1]This was originally published to the 1/6 th power but had been corrected by the author as result of communication with Foreman.

an improvement in performance at the expense of direction-independent operation. In figure 1.5 different duct systems are shown. From the work done by various researchers (see Sivasegaram(1986)), the conclusion drawn from their experiments with different designs is that the greater the number of vanes, the greater the direction-independence of the duct and the lower the performance r_p. A compromise to this situation is to use a three or four vane system offering a r_p of 1.6 with better direction-independent operation.

As shown in figure 1.6 an $(r_p)_{max}$ of 1.8 can be achieved by using a thin walled diffuser system. With further improvements using carefully designed deflecting vanes, an $(r_p)_{max}$ of little over 2.0 can be achieved. (See Savasegarem(1986)).

The 'Mushroom Mill' is the last ducted wind turbine system to be covered in this section. Unlike the systems covered in figure 1.5, the augmentor shown in figure 1.7 is omni-directional in operation, with a Vertical Axis Wind Turbine working at the centre. An r_p of 2.5 has been reported by Bullen *et al*(1987) for the maximum performance of this machine.

The main problems associated with all ducted systems are bulkiness and poor yaw capability[2] , despite that fact that good r_p values have been reported. The economic potential is yet to be realized.

1.3 Obstruction-Type and Wind Deflection Systems.

In such devices the acceleration of wind flow past an obstacle provides the basis for an augmenting effect. Values of 2 to 3 for r_p are possible but are more suitable to slow running cross-wind machines.[3] (See Savasegarem(1986)). The result is a very large system and therefore low gross C_p, which makes this device uneconomical. (See figure 1.8).

[2]The Mushroom Mill has not the problem of poor yaw capability but is still very bulky with poor storm protection.

[3]Not all cross-wind machines are slow running. (e.g Darrieus, Musgrove H-VAWT and V-VAWT have working tip speed ratios between 6-8.)

Wind deflection devices have a special application to cross flow machines, in that they reduce the loss of torque owing to the wind resistance on the section of the rotor moving against the wind. (See figure 1.9). It also enables the savonius to generate electricity more effectively than before because of the increase in the rotational speed of the rotor, therefore avoiding the need for an expensive gear box. The main advantage of the wind deflection system is that its vanes are compact and easy to fabricate while the augmentation system is light enough to permit easy adjustment, (see Beurskens(1982)). The maximum value of r_p for this device was found to be 1.8. (See Savasegarem(1986).

1.4 Tip-Vane System.

In figure 1.10 shows the arrangement of the Tip Vane Wind Turbine which is simply a short auxiliary wing on the rotor blade tips of a conventional wind turbine. The tip-vanes effectively act like an aerodynamic venturi duct similar in effect to that described in section 1.2.

Dick(1986) investigates the performance of this device on the basis of the the experimental work done by van Holten(1981) and more advance work by Garside *et al*(1985). Initial test work was conducted on tip-vanes with a gauze screen. The screen was mounted at the position where the working wind turbine would be, with the tip-vanes mounted around the perimeter of the circular screen. When air was blown over the screen, the wake behind this would approximate the wake behind a working wind turbine. When the screen and tip-vanes were rotated about the polar axis of symmetry of the screen, the air flow interaction of the tip vanes and the screen wake would simulate the working situation of the tip-vane wind turbine. The results from these tests did reveal that a power augmentation effect was possible if a real turbine replaced the screens. It was only in later tests with real turbines that Garside and van Bussel reported no increase in power. The junction between the tip vane and the wind turbine rotor caused extensive flow separation preventing the tip vane from working properly. The flow

pattern over the tip vane is so complex that researchers may never be able to model this problem effectively.

1.5 Vortex Augmentation.

Vortex augmentation is unlike other methods of augmentation in that the concentration of wind energy takes the form of rotational kinetic energy. This rotational energy is provided by vortices shed off the leading edge of a Delta wing or from the tips of an ordinary wing, (see figure 1.11 (a)). Another method is to use the low pressure region generated inside the eye of a vortex created by a suitably designed tower, (see figure 1.11 (b)).

Results from Loth(1978), Sforza(1977) and Yen(1975) show that good concentration ratios can be achieved, but unfortunately large amounts of material are needed for these types of concentrator. This pessimistic conclusion is supported by the analysis covered by Dick(1986) which compares the performance of such concentrators with a conventional wind turbine, on the basis of total frontal area. Igra(1979), on the other hand, feels that there could be economic potential with Wing Tip Vortex Shedding Concentrators if improvements to the turbine were made. (Unfortunately vortex-shedding wing concentrators would still have to get over problems associated with yaw and storm protection.)

1.6 Conclusion.

Several types of concentrator have been surveyed, showing varying degrees of success in performance judged by both parameters r_p and gross C_p. Each have their merits but for electrical generation there is no wind concentrator to date which can rival the economic benefits of conventional wind turbine design, simply because high performance concentrators like the Ducted Augmentor have poor storm survival and yaw capability. Other augmentor types used with Cross-Flow turbines may have improved yaw capacity but at the expense of construction weight.

In chapter 2 an overview is given of a new type of wind concentrator which might be able to overcome the performance contraints of augmentors mentioned in this chapter.

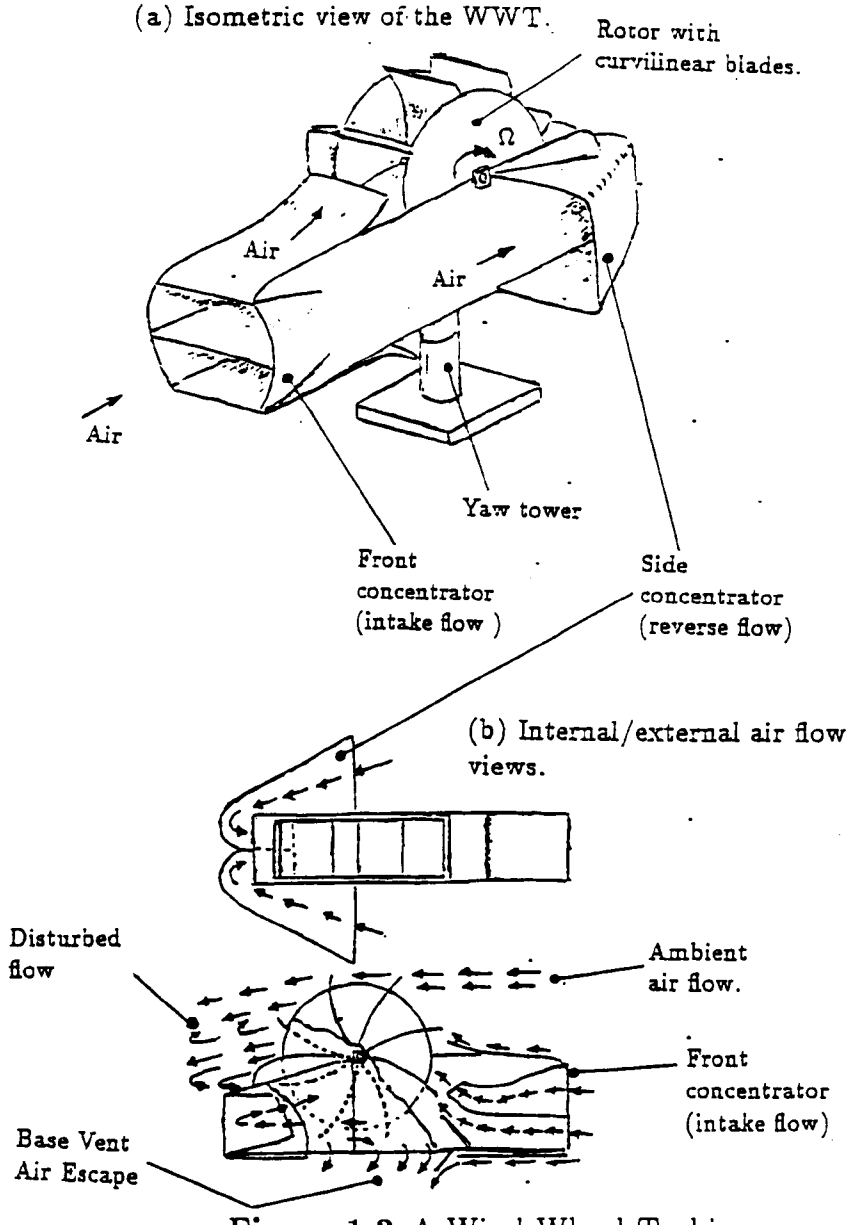

Figure 1.2 A Wind Wheel Turbine.

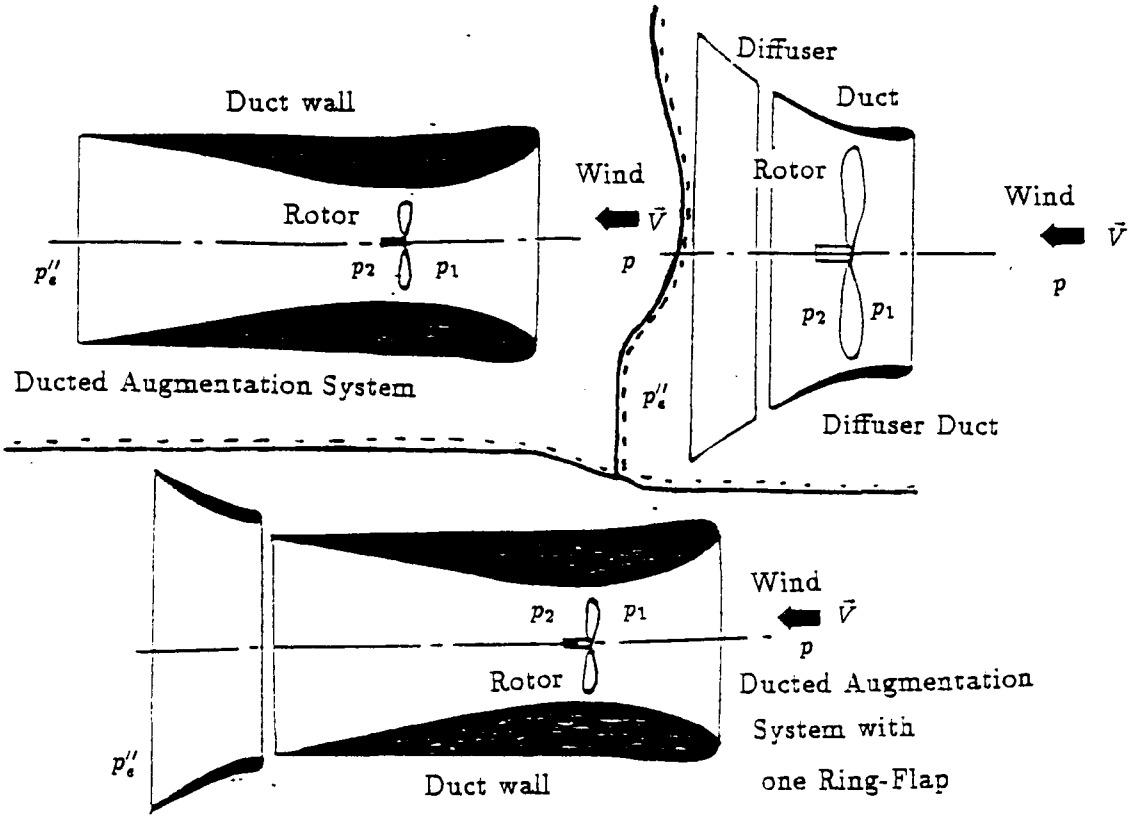

Figure 1.3 Ducted Diffuser Augmentation.

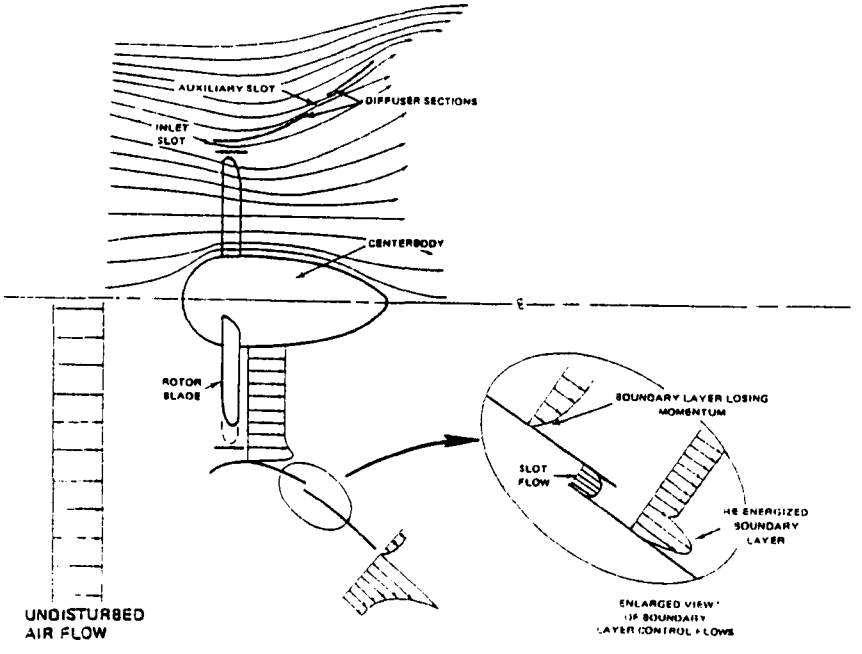

Figure 1.4 Ducted Diffuser with a segmented annulus.

Source: Foreman(1979)

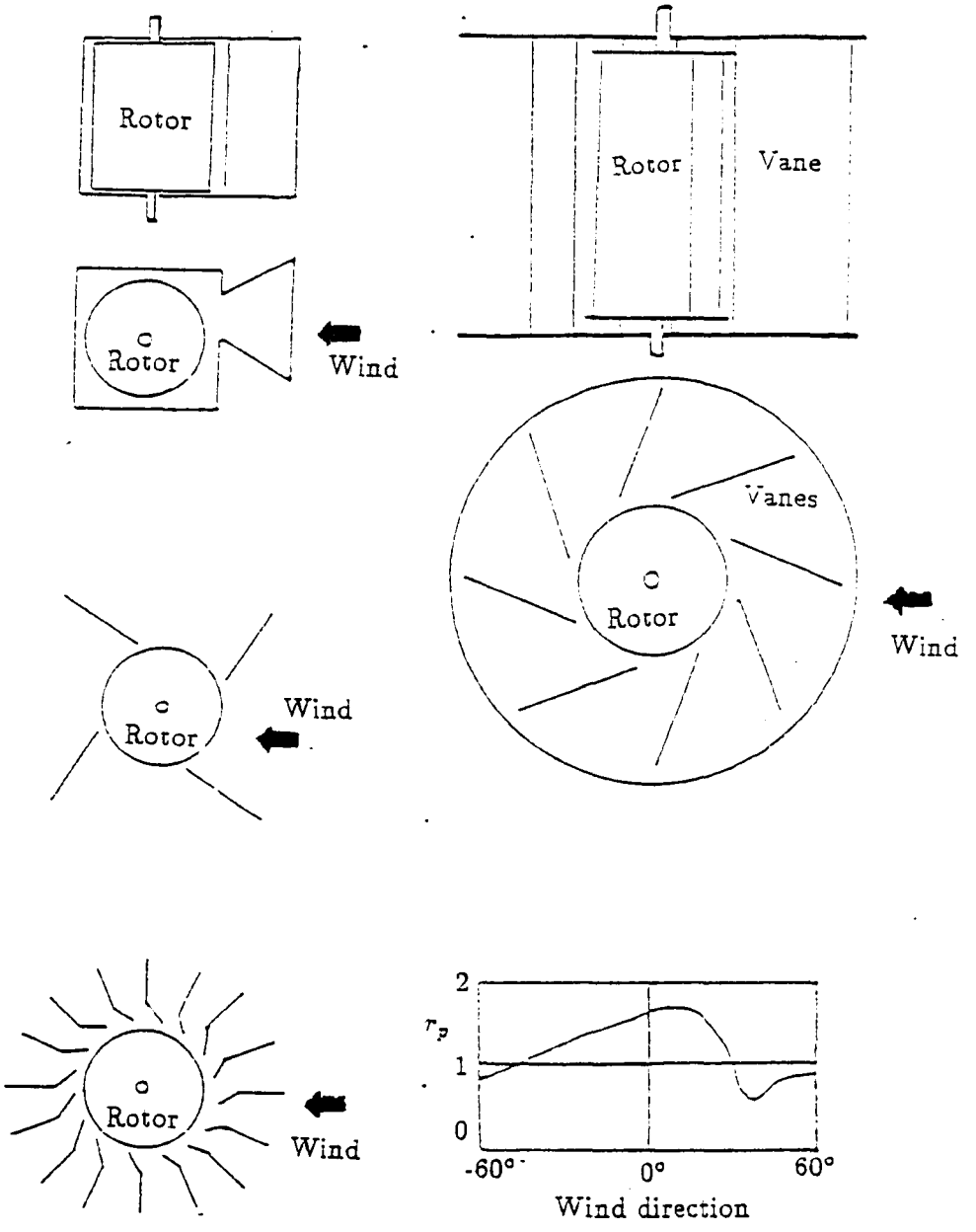

Figure 1.5 Ducted Concentration Augmentation Systems.
Source: Sivasegarem(1986)

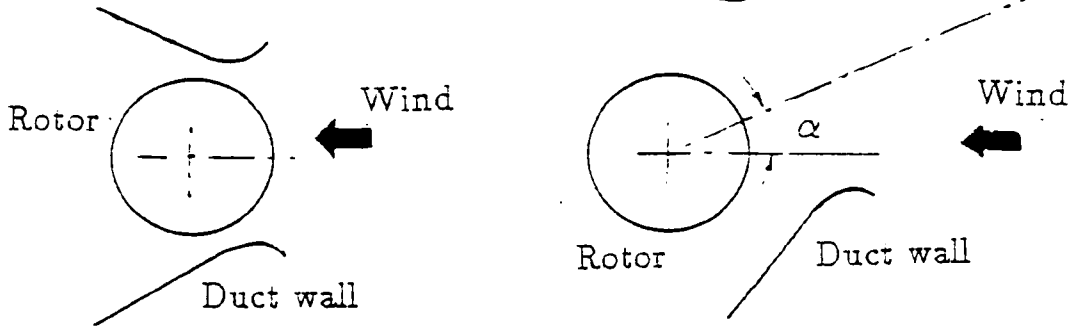

Duct parallel to the wind

Duct inclined to the wind

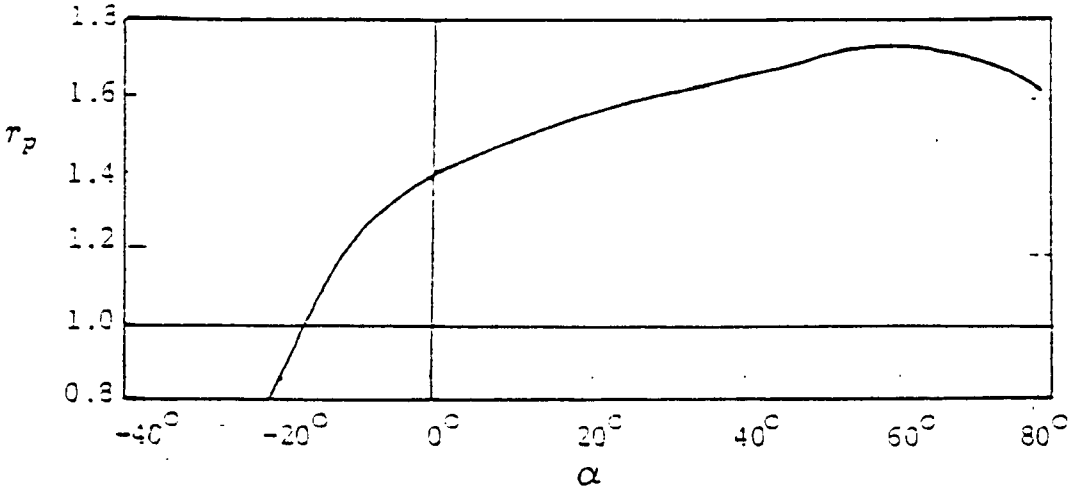

Influence of wind direction on performance.

Figure 1.6 Ducted Diffuser for Cross Flow Turbine.
Source: Sivasegarem(1986)

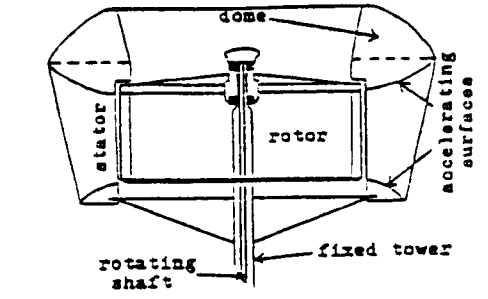

Elevation

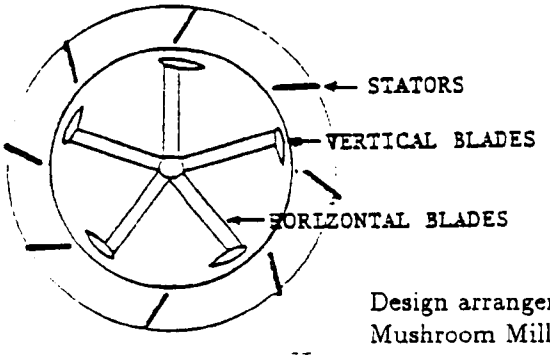

Design arrangement of the Mushroom Mill.

Plan

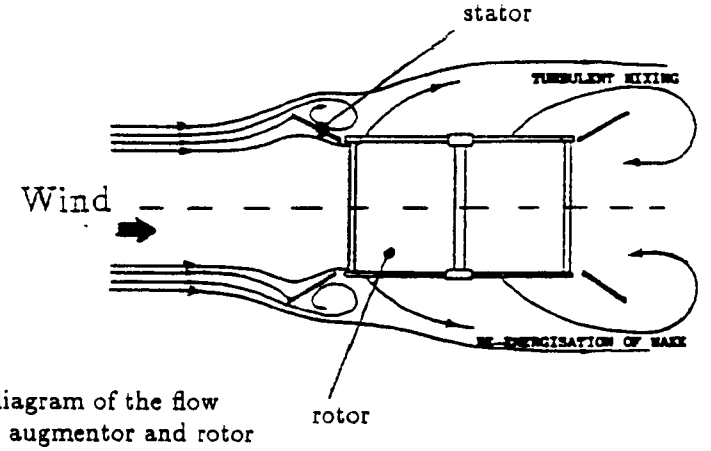

Schematic diagram of the flow through the augmentor and rotor wind.

Figure 1.7 Mushroom Mill wind turbine system.
Source: Bullen *et al*(1987).

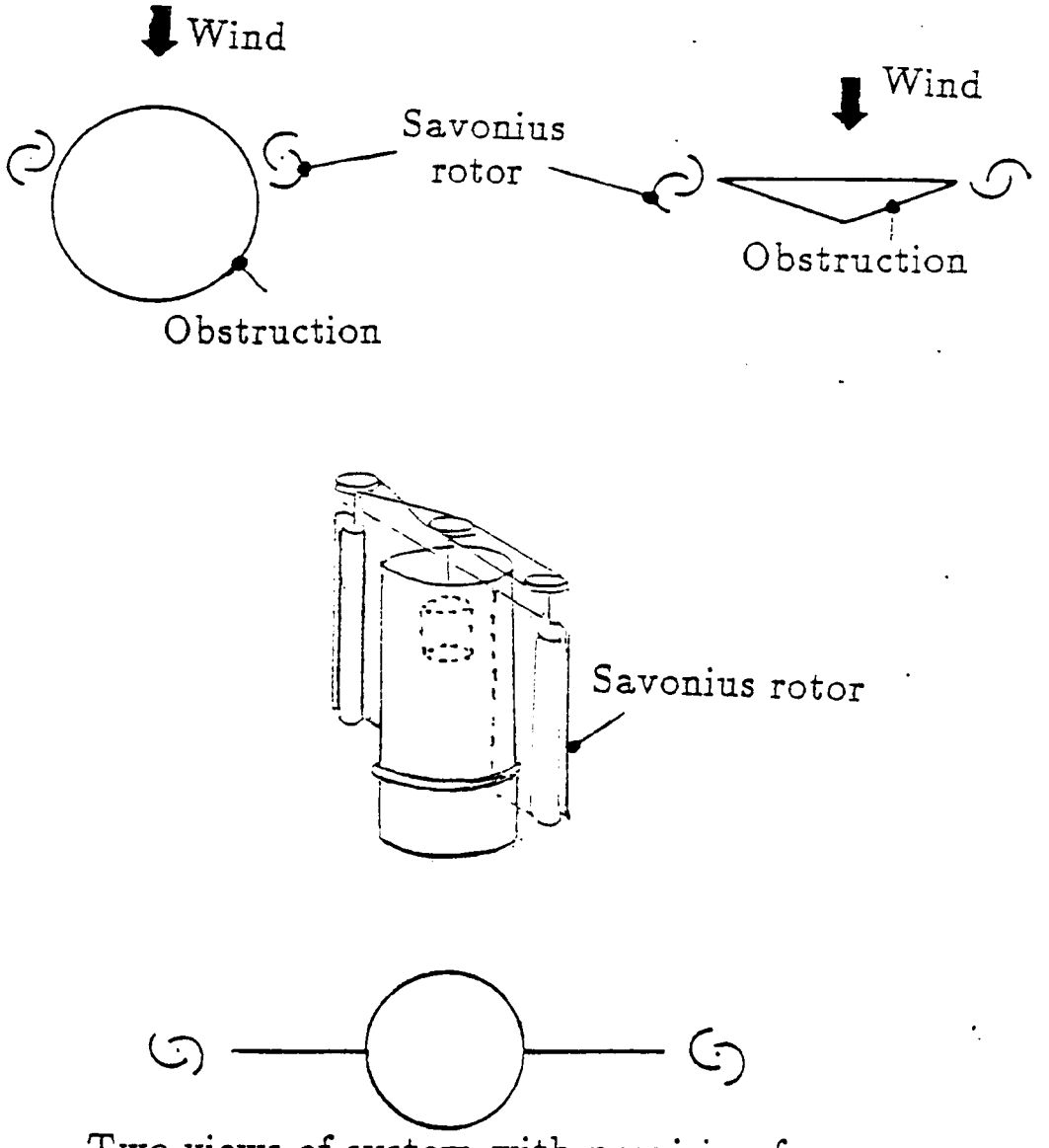

Figure 1.8 Obstruction Type Augmentation Systems.
Source: Sivasegarem(1986)

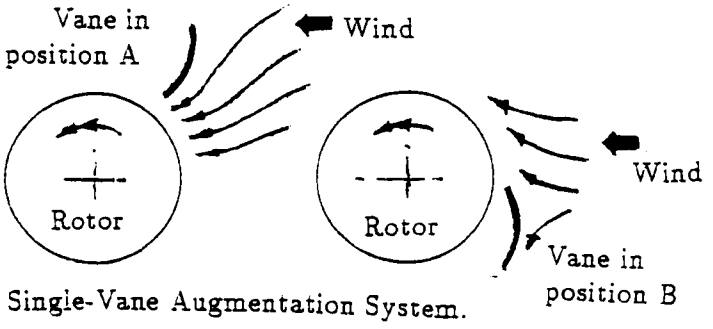

Single-Vane Augmentation System.

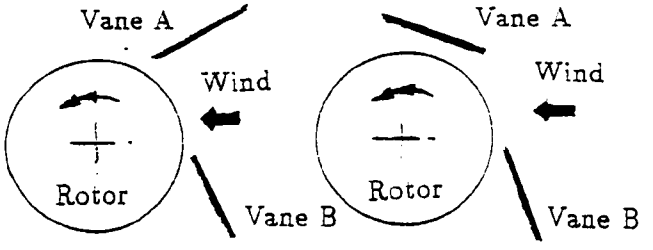

Two positions of effective power augmentation of the Two-Vane Augmentation System.

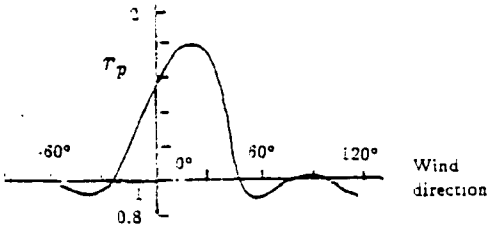

The effect of wind direction on performance.

Figure 1.9 Power Augmentation using Deflector Vanes.
Source: Sivasegarem(1986)

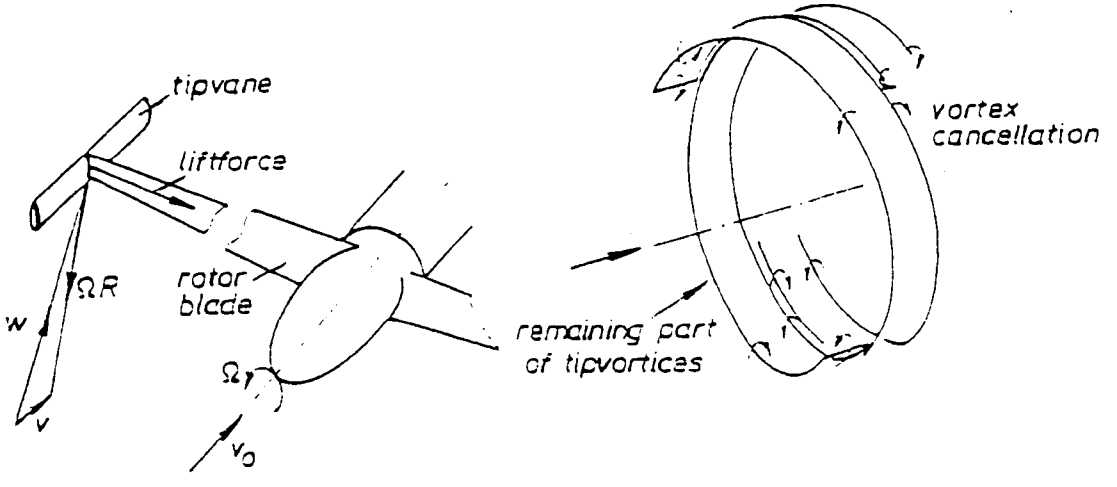

Figure 1.10 The Tip-Vane System of Van Holten.
Source: Sivasegarem(1986)

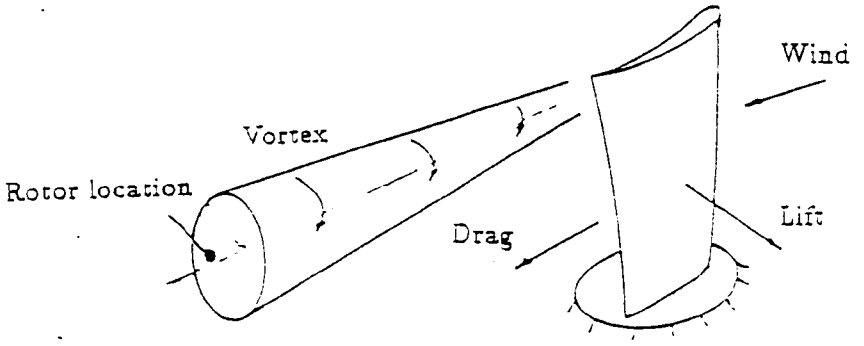

Vortex Augmentation using
Swept and Delta wings.

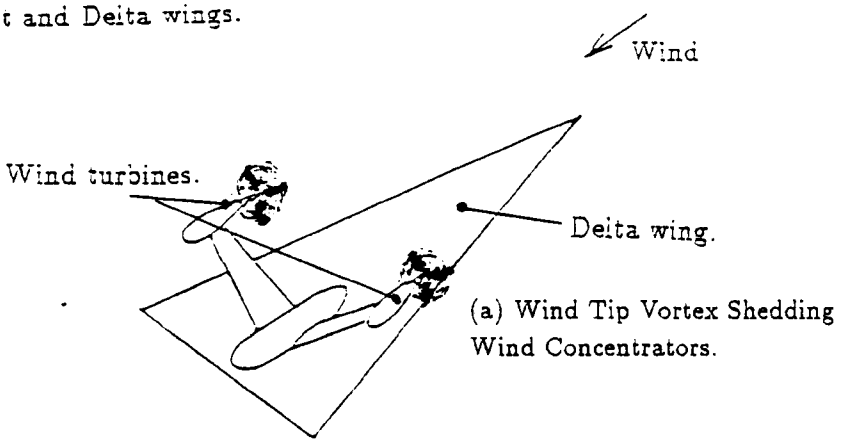

(a) Wind Tip Vortex Shedding
Wind Concentrators.

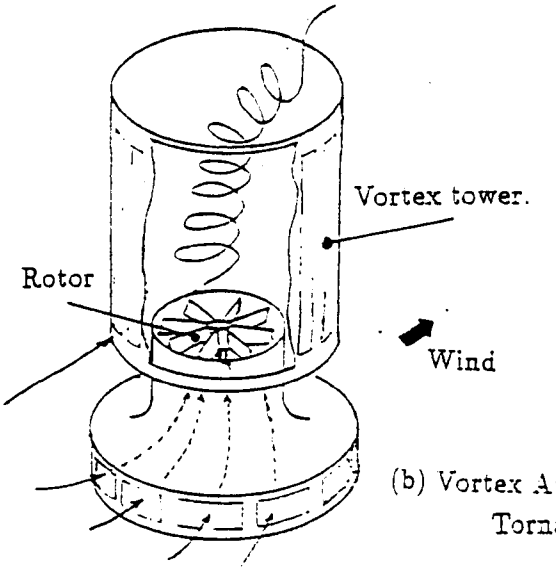

(b) Vortex Augmentation using a
Tornado Type System

Figure 1.11 Vortex Augmentation Systems.
Source: Sivasegarem(1986)

Chapter 2

OVERVIEW OF VORTEX SCREW AUGMENTATION.

Vortex Screw Augmentation is a method of concentrating the available kinetic energy of the air. It involves a Vortex Screw Wind Concentrator and Wind Turbine, or what the author refers to as a Concentrator Wind Turbine, (CWT). The Wind Concentrator is an annular disc of stationary, radially mounted aerofoil sectioned blades which entrain the wind, through the orifice formed by the surrounding blades, onto a wind turbine downstream, whose diameter is close to that of the orifice. The vortex shedding from the inboard tips of the stationary blades causes the entrainment effect to take place.

The next two sections will describe aspects of the CWT in more detail.

2.1 Vortex Screw Wind Concentrator.

In figure 2.1 only the concentrator is shown with one blade wake shown for the sake of clarity.

The balance of energy of a Helical Vortex Wind Concentrator is considered most conveniently by assuming the concentrator to be stationary in a stream of air of velocity V directed along its axis. Considering only the blade elements at a distance r from the axis, the power put into the concentrator is zero. The drag thrust dT operates on air moving with axial

velocity u and does $-u\frac{dT}{dr}$ units of work in unit time. Similarly the torque dT_Q operates on air moving with angular velocity $\frac{1}{2}\omega$ and does $\frac{1}{2}\omega\frac{dT_Q}{dr}$ units of work in unit time. Hence if $\frac{d\dot{E}}{dr}$ is the rate of loss of energy of the system, the energy equation becomes

$$\frac{d\dot{Q}}{dr} - \frac{d\dot{W}k}{dr} = -u\frac{dT}{dr} + \frac{1}{2}\omega\frac{dT_Q}{dr} + \frac{d\dot{E}}{dr} = 0 \tag{2.1}$$

since there has been no heat transfer Q or work transfer Wk. (For a more thorough investigation of the energy balance for a concentrator system see appendix B). Now the rate of energy loss, due to the profile drag of N blade elements, each experiencing the resultant velocity V_{eff} due to the induced velocity from the local blade circulation and free stream velocity V, given by

$$\frac{d\dot{E}}{dr} = \frac{1}{2}Nc\rho V_{eff}^3 C_D \tag{2.2}$$

where C_D and c are the local drag coefficient and chord length respectively. The energy of the air is represented by its total pressure which is constant across the concentrator if C_D is small. As the air passes through the concentrator disc it reduces in pressure by $\acute{p}$ by due to an increase in angular velocity ω without any change in axial and radial components of velocity. Bernoulli's equation applied in turn to the flow before and behind the concentrator gives

$$\begin{aligned}
H_0 &= p + \frac{1}{2}\rho V^2 \\
&= p'_{e1} + \frac{1}{2}\rho(u^2 + v^2) \\
\text{and } H_1 &= p'_{e1} - \acute{p} + \frac{1}{2}\rho(u^2 + v^2 + \omega^2 r^2) \\
&= p'_e + \frac{1}{2}\rho(u_1^2 + \omega_1^2 r_1^2) \\
\therefore\ H_1 - H_0 &= -\acute{p} + \frac{1}{2}\rho\omega^2 r^2 = 0 \qquad (2.3) \\
&\quad \text{since } H_1 = H_0 \\
\text{Hence } \acute{p} &= \frac{1}{2}\rho\omega^2 r^2 \qquad (2.4)
\end{aligned}$$

This effect on the air is due to an energy exchange process between the drag thrust and the torque $(-udT + \frac{1}{2}\omega dT_Q)$ on a volume $2\pi r u dr$ of air per

unit time. Hence

$$-u\frac{dT}{dr}+\frac{1}{2}\omega\frac{dT_Q}{dr}=2\pi ru(-\acute{p}+\frac{1}{2}\rho\omega^2r^2)=0 \tag{2.5}$$

But the element of drag thrust is clearly equal to the decrease of pressure over the annulus, or

$$\frac{dT}{dr}=2\pi r\acute{p} \tag{2.6}$$

and the element of torque is equal to the angular momentum imparted to the air in unit time, or

$$\frac{dT_Q}{dr}=2\pi\rho u\omega r^3 \tag{2.7}$$

These two expressions are consistent with the previous equation for energy, since the constant total pressure is due to the exchange between drag thrust and torque of blade elements respectively.

The effect the blades have on the air flow stream over the concentrator is not unlike that of an Obstruction-Type Augmentor, (see chapter 1, figure 1.8 and figure 2.1 of this chapter, and chapter 4, figures 4.15 and 4.27). The swirl is responsible for a leaky-obstruction effect, causing some of the flow stream in front of the concentrator to separate into two streams, one of the streams forms into a venturi shaped stream tube for the core flow region, the other creates a bell shaped flow pattern over the outer vortex sheet. The axial component of velocity in the annular helical flow region is determined by the strength of the outer vortex sheet, while the core flow is determined by the nett effect of the strength of inner and outer vortex sheets.

To prove the existence of the venturi shaped stream tube first consider the application of Bernoulli's equation along the axis of symmetry before and behind the plane of the concentrator to get

$$\begin{aligned} H_0 &= p+\frac{1}{2}\rho V^2 \\ &= p_{c1}+\frac{1}{2}\rho(V_{c1}^2+v^2) \\ H_1 &= p_{c1}+\frac{1}{2}\rho(V_{c1}^2+v^2) \end{aligned}$$

$$= p_e'' + \frac{1}{2}\rho V_c^2$$

Notice that the core has no rotational flow. This is because the core flow has not been subject to any torque reaction from the fixed blades.

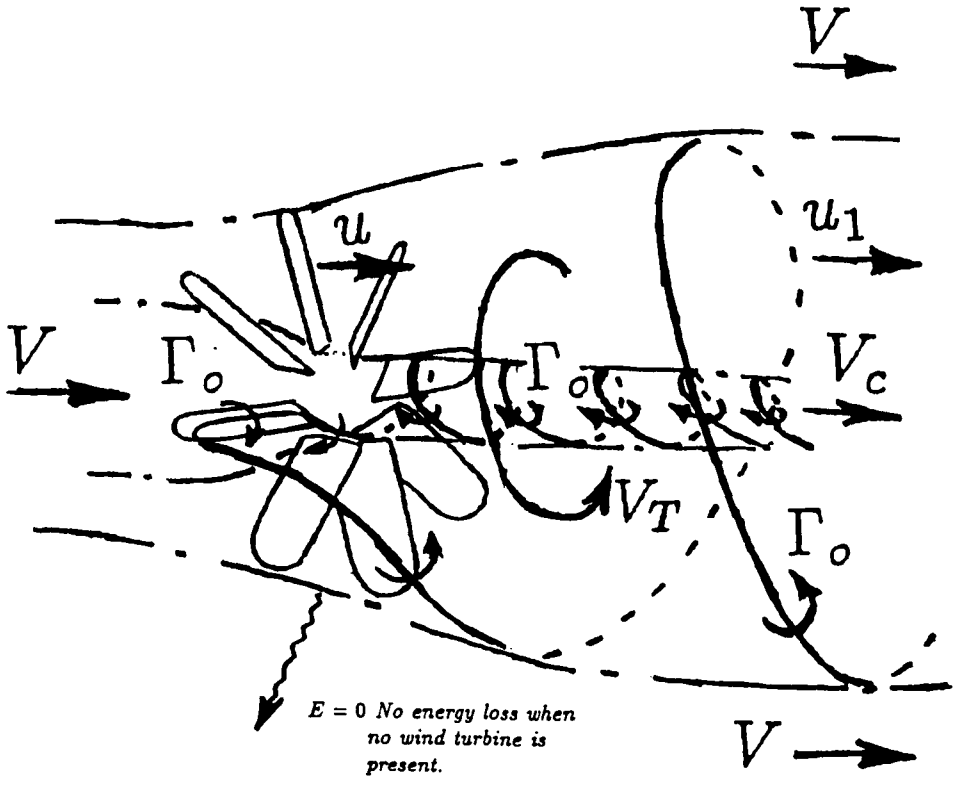

Figure 2.1 Idealized vortex wake structure of the Helical Vortex Wind Concentrator. (Only one blade wake is shown).

Downstream of the concentrator helical flow is set up in the annular region between the inner and outer vortex cylindrical vortex sheets. Now to maintain the circular flow about the axis of symmetry there must exist a pressure gradient across the annulus such that the pressure drops towards the inboard vortex cylindrical sheet. As a corollary to this, the swirl velocity increases towards the inboard vortex cylinder to maintain constant total pressure across the annulus. Next, applying Bernoulli's equation across the inner cylindrical vortex sheet just behind the concentrator disc, the static

pressure must be the same radially either side of the sheet. Therefore at $r = r_i$ and $\omega = \omega_i$ we get

$$\begin{aligned} H_1 &= p_{c1} + \frac{1}{2}\rho(V_{c1}^2 + v^2) \\ &= p'_{e1} - \acute{p} + \frac{1}{2}\rho(u^2 + v^2 + \omega_i^2 r_i^2) \\ &= H_0 \\ \text{and } p_{c1} &= p'_{e1} - \acute{p} \\ \therefore\ V_{c1}^2 &= u^2 + \omega_i^2 r_i^2 \end{aligned}$$

Finally, applying Bernoulli's equation across the outboard vortex sheet the static pressure again is the same either of the sheet for $r = r_0$ and $\omega = \omega_0$, so that

$$\begin{aligned} H_1 &= p'_{e1} - \acute{p} + \frac{1}{2}\rho(u^2 + v^2 + \omega_0^2 r_0^2) \\ &= p + \frac{1}{2}\rho V^2 \\ \text{Now } p'_{e1} - \acute{p} &= p \\ \therefore\ V^2 &= u^2 + v^2 + \omega_0^2 r_0^2 \end{aligned}$$

If $\omega_i r_i > \omega_0 r_0$ then $V_{c1} > V$ since the radial velocity v is small in comparison to V and the axial velocity u is virtually constant over the annular region. Now the axial velocity will continue to decrease downstream in the annulus so that $u > u_1$, causing the outboard vortex cylindrical sheet to increase in diameter downstream. The axial velocity in the core on the other hand will increase so that $V_c > V_{c1}$, causing the inboard vortex cylindrical sheet to decrease in diameter downstream. This is a consequence of the vortex coil structure shown in figure 2.1.

This increase in flow velocity in the core owes its existence to the swirl in the annular wake. The result is a stream tube through the core not unlike that of a venturi tube.

2.2 The advantages of turbulent mixing in turbine wakes.

Figure 2.2 shows a wind turbine which is very small in comparison to the large mountain. The flow over the ridge is increased by K times the freestream velocity V on its crest. Far behind the mountain the velocity returns to the undisturbed value. This type of flow can be considered as a diffuser flow. Turbulent mixing will occur over the crest in the wake of the turbine causing momentum transfer and a corresponding rise of dynamic pressure in the wake. If the mixing length downstream of the wind turbine is sufficiently long, the dynamic pressure will be sufficient to allow the wake to return to free stream static pressure p, and the wake velocity to return to the free stream velocity V on the downstream side of the mountain. What this infers is that the power augmentation for the wind turbine will be K^3. If the mountain is not large enough then the power augmentation will fall short of K^3. If no mixing with the surrounding air took place in the turbine wake beyond the point where the turbine decelerates the airflow to $\frac{1}{3}KV$, this velocity would be insufficient to overcome the drag rise on the back of the mountain as the static pressure recovers back to ambient pressure.

Proof of this can be seen from Bernoulli's equation applied to flow over the very large mountain

$$p_e'' + \frac{1}{2}\rho\left(\frac{1}{3}KV\right)^2 = p + \frac{1}{2}\rho V_{final}^2 \tag{2.8}$$

Where p_e'' is the static pressure on the crest of the mountain far upstream and downstream of the wind turbine, and p is the ambient pressure at ground level. If we apply Bernoulli's equation this time between the upstream point at ground level and the upstream point on the crest of the mountain we get

$$p_e'' + \frac{1}{2}\rho\left(KV\right)^2 = p + \frac{1}{2}\rho V^2 \tag{2.9}$$

If now consider the maximum augmentation situation whereby $V_{final} \rightarrow 0$

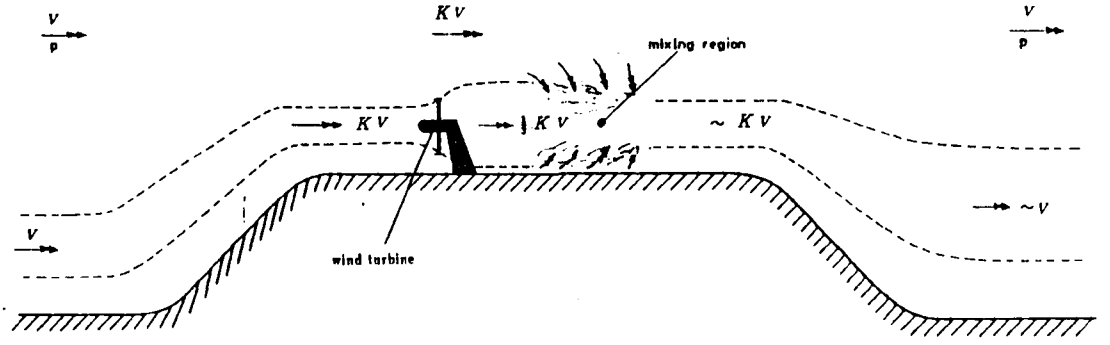

Figure 2.2 Viscous effects associated with a wind turbine on a large mountain

and substituting equation 2.9 into equation 2.8 we will find that $K = 1.06$. This would mean that no mass flow increase over the crest would be possible. Experience tells that this is in correct. Therefore turbulent mixing must take place in the downstream wake. The reader should appreciate that that the turbine can only extract energy from the air which flows through the turbine disc. What turbulent mixing does in the turbine wake is to allow re-energisation of the wake under loading conditions that would otherwise cause the wake to come to a complete stand still, which is not possible.

2.3 The Concentrator Wind Turbine.

In the last section the importance of turbulent mixing was emphasised. How this applies to the CWT is illustrated in figure 2.3, which shows both the Vortex Screw Wind Concentrator and the Wind Turbine. The effect that the turbine has on the concentrator aerodynamics described above, is to extract kinetic energy out of the stream tube of the axial core flow. Across the rotor disc the total pressure will be reduced as a result of the drop in static pressure. This is as a result of the low pressure forming on

the upper surface of the rotor blade aerofoil section along the span as it rotates. A rotational motion is also imparted to the rotor slipstream due to the reaction of the torque. The rotational motion is usually negligible for high tip speed ratio, low solidity rotors. Therefore it is easier to consider the rotor acting like an actuator disc with no rotational motion in the slipstream of the rotor.

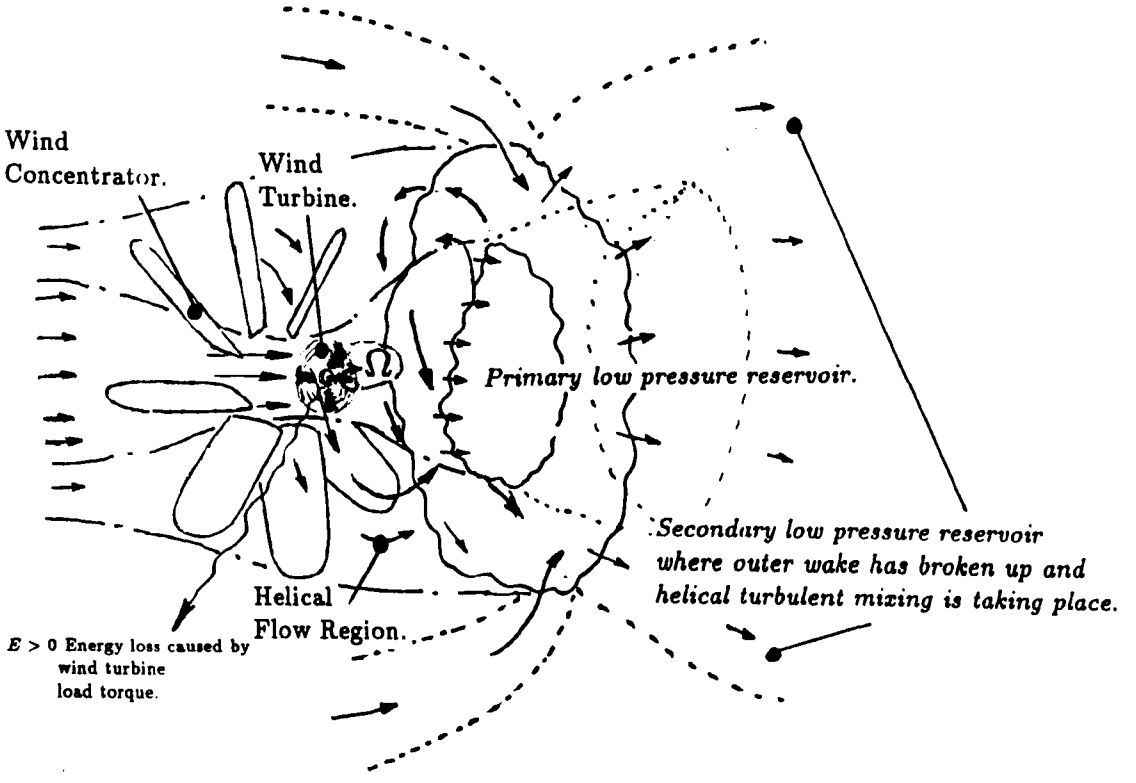

Figure 2.3 Concentrator Wind Turbine with hypothetical 'Ejector Mixing'.

To investigate the CWT closely we apply a Control Volume to the air flow over the device. The annular region between radii $\acute{R}$ and $\acute{h}$ experience a free vortex flow with progressively diminishing axial velocity component. Outside this region the flow has no rotational component. At some point downstream of the concentrator there is an actuator disc positioned in the core, representing the wind turbine. The sudden drop in static pressure

across the rotor disc instigates an exchange of kinetic energy to pressure energy until all available kinetic energy is exhausted in the core. At this point downstream of the rotor there will exist a 'Primary Low Pressure Reservoir'.

The interactive combination of the concentrator with the rotor changes the wake structure of the concentrator away from that shown in figure 2.1 to that shown in figure 2.3. The concentrator inner wake acts like a diffuser to the rotor wake in that it will increase the mass flow through the rotor disc. This in itself cannot increase the energy extracted per unit mass of air in the rotor wake. Every kg of air can give up its initial kinetic energy and no more as the pressure in the final pressure wake returns to ambient. Since both wake flows are not shielded from the external flow by a material wall, turbulent mixing will occur in the regions of reduced pressure. The external flow around a conventional wind turbine is at ambient pressure, and experience has shown that turbulent mixing between the rotor wake and the external flow is ineffective in preventing 'The Turbulent Wake State' from occurring with the rotor. Now the wind turbine of the CWT, compared with a conventional wind turbine could extract more energy per unit mass of flow before encountering The Turbulent Wake State, since the secondary flow of air leaching in from the sides of helical wake and into the rotor wake would ensure that a minimum value of velocity occurs at the entrance to the primary low pressure reservoir, thus postponing the Turbulent Wake State. The Theory of Ejectors by Bevilaqua(1978) indicates that better energy transfer between two flow streams is achieved when mixing is done at lower than ambient pressure because of lower energy dissipation. The existence of the annular and core flows act as the primary jet flow and the flow being drawn in from the sides acting as the secondary jet flow of the ejector. In van Holten(1982) an attempt to introduce a vortex ring to simulate the 'Ejector Effect' has been discussed. Its relevance to the CWT is considered in appendix A.

A Vortex Screw Concentrator, as previously mentioned in section 2.1, acts like a leaky obstruction augmentor in the shape of annular tube. This

is the result of the helical annular flow forming downstream. Now if the concentrator blades were so heavily loaded that no air were to flow through the annular disc, the fluid stream over the annular disc would divide about an imaginary cylindrical surface whose radius is that of the mean radius the concentrator so that $r = (R + h)/2$.[1] The result would be as seen in figure 2.4, with inviscid flow occuring upstream of the 'Dough Nut' shaped Obstruction Augmentor and ideal viscous mixing occuring down stream. The rotor would be placed at the throat of the inviscid stream tube in this situation.[2] If we consider continuity of flow between far upstream and the point where the rotor will operate, we get the maximum potential axial flow velocity through the core as

$$V_c = V\left(\frac{R+h}{2h}\right)^2 \tag{2.10}$$

This means at the rotor disc the potential power concentrator ratio would be

$$C_R = \left(\frac{R/h+1}{2}\right)^6 \tag{2.11}$$

if complete mixing occurs between the rotor wake and the surrounding flow at the far wake. Such a concentrator would not work in practice since the flow directly behind concentrator would be in a Turbulent Wake State and would not offer the advantages of turbulent mixing over sufficiently long enough mixing region. Therefore equation 2.11 gives us only an idea of what the ideal concentrator could achieve, and therefore serves only as a yard stick for performance.

This thesis covers a theoretical parametric study of the concentrator with very limited experimental verification. A parametric study of the complete CWT system has not been covered but this is discussed qualitatively in chapter 7. The author's method of blade design is currently at a

[1] This is only strictly true for a disc of R/h near unity.

[2] Note that the radius of the rotor, concentrator orifice and the throat of inviscid stream tube have all assumed to be equal.

rudimentary stage, and future improvements to method are also discussed qualitatively in chapter 7.

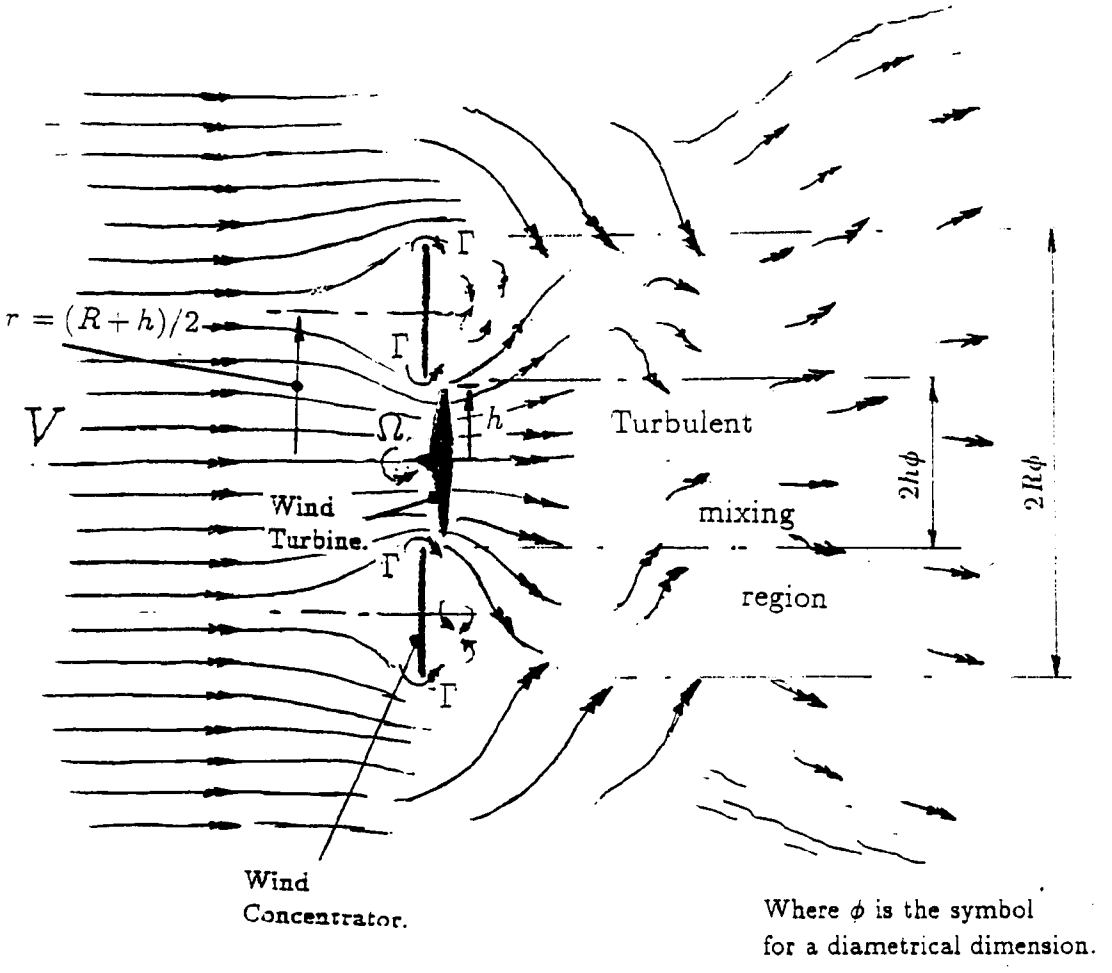

Figure 2.4 Side view of the ideal CWT with its wake flow.

Chapter 3

CONCENTRATOR THEORY.

3.1 Introduction.

Early attempts to assess Concentrator Theory have been made by Rosenbrock(1983), Rechenberg(1984) Hunter *et al*(1988). In each case none of them gave a full assessment. In this section a more complete examination is made of the concentrator performance, using firstly a purely analytical model and later a numerical model.

3.2 Blade Element Theory.

At first sight the application of blade element theory seems the obvious approach but in fact this proved to be an inadequate method for determining vortex wake geometry. Blade element theory was developed on the assumption that there would be an infinite number of blades, with the blade element wake flows confined to non-interactive helical motion with a small swirl velocity. Clearly this is not the case with the concentrator.

Appendix B gives details of the author's early attempts to design a wind tunnel model using blade element theory. It was soon evident from the results given in chapter 5, that the correct determination of the helical vortex angles and the position of the vortices in space were needed so that the increase in the flow velocity at the core could be calculated. (The helical vortex angles are shown as β_1 and β_2 in figure 2.1). The trailing vortices

coming off each blade element would roll up into two discrete vortices of equal and opposite strength. Blade element theory as a method cannot determine the angles of the rolled up vortices, since it considers only local blade element flow effects. The wake regions are clearly very interdependent under such heavily loaded conditions of circulation, and any attempt to use blade element theory has proven to be too inaccurate to be of any use. (See chapter 5 later).

3.3 Biot Savart Theory.

The problems described in section 3.2 indicated the need for a method which took into account the interdependent nature of the wake regions. Biot-Savart theory, if applied to a free wake scheme, solves this problem. In section 3.4 this approach is investigated numerically.

In this section, an analytical approach will be adopted involving a semi-prescribed cylindrical wake. The initial problem being the determination of angles β_1 and β_2. Figures 3.1 and 3.2 illustrate the method of analysis. The flow is assumed to be inviscid and incompressible throughout. Each blade with its wake is represented as a horseshoe vortex of rectangular blade circulation loading, which is equivalent to the prescribed elliptic loading, (the span of each blade is $(R - h)$ long).

Figure 3.1 represents the fixed concentrator blades as a annular bound vortex sheet, while the rolled up discrete trailing vortices are shown as cylindrical vortex sheets of radii $\acute{h}$ and $\acute{R}$ respectively. By considering points P_1 and P_2 at radial distance r just ahead of and just behind the disc, the symmetry of the bound vortex sheet will induce no axial velocity at these points. Therefore the axial velocity u through the disc remains the same. Now if the bound vortex sheet induces an angular velocity $-V_t$ at P_1, by symmetry it must induce an angular velocity V_t at P_2. Therefore the total induced angular velocity can be written as $\frac{1}{2}V_T - V_t$ at P_1 and $\frac{1}{2}V_T + V_t$ at P_2. But P_1 is in the irrotational flow field and therefore $\frac{1}{2}V_T - V_t = 0$. This means that the total angular velocity induced at P_2 by both bound

and trailing vortices is $V_T = 2V_t$. This value of V_T will remain constant downstream for a constant radial distance r.

Now from figure 3.2 it is assumed that $\beta_1 = \beta_2 = \beta$. The annular vortex sheet can be simplified into two parallel vortex strips of infinite length reflected about the XY plane. For trailing vortices, only the cylindrical component is considered. This is finally simplified into two semi-infinite sheets reflected about the XY plane. The strength of each of the vortex sheets is derived from the following relationships

$$\tan\beta = \frac{V_T}{u} \tag{3.1}$$

$$\gamma = d(\Gamma \sin\beta)/dl \simeq \Gamma \sin\beta/(2\pi \acute{h} \cos\beta/N)$$

$$\text{so that} \quad \gamma = N\Gamma \tan\beta/(2\pi \acute{h}), \tag{3.2}$$

$$\acute{\gamma} = d\Gamma/d\acute{l} \simeq N\Gamma/(2\pi((\acute{R} + \acute{h})/2))$$

$$\text{so that} \quad \acute{\gamma} = N\Gamma/(\pi(\acute{R} + \acute{h})), \tag{3.3}$$

$$\text{and} \quad \gamma'' = N\Gamma \cos\beta/(2\pi \acute{h}). \tag{3.4}$$

The outer vortex sheet strength is $\gamma \acute{h}/\acute{R}$ since a constant helical vortex angle β is assumed for both cylindrical vortex sheets down the wake.

From previous reasoning, the tangential velocity distribution across the annular area of the wake is the same at any axial position downstream of the blades. For far wake conditions at P_3 (see figure 3.1), we get the tangential induced velocity from Biot Savart theory as

$$V_T = \int_0^{2\pi} \Big\{ \frac{\gamma'' \acute{h} \cos(\theta + \alpha_1)}{2\pi r_1} - \frac{(\gamma'' \acute{h}/\acute{R})\acute{R} \cos(\theta + \alpha_2)}{2\pi r_2} \Big\} d\theta \tag{3.5}$$

Now from figure 3.1 we see that

$$r_1 = \sqrt{\acute{h}^2 + r^2 - 2\acute{h} r \cos\theta}$$

$$r_2 = \sqrt{\acute{R}^2 + r^2 - 2\acute{R} r \cos\theta}$$

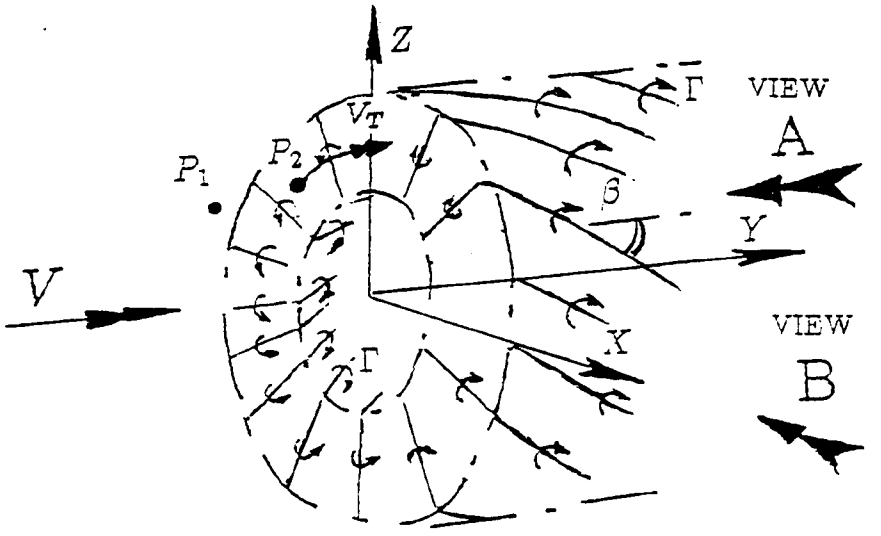

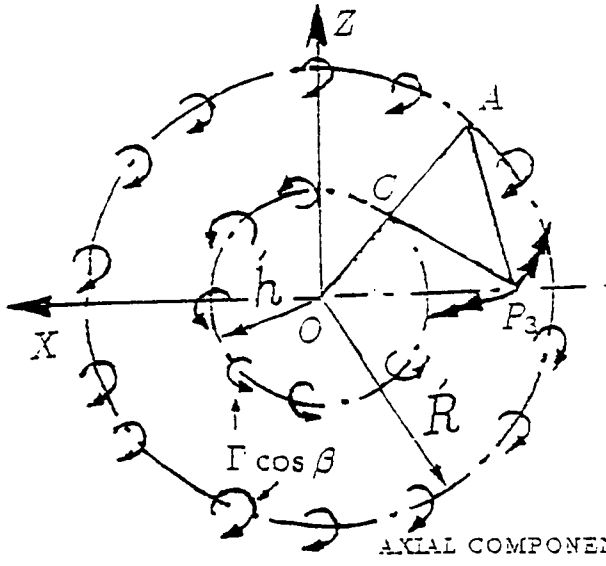

Note:

$\angle AOP_3 = \theta$

$\angle OCP_3 = \alpha_1$

$\angle OAP_3 = \alpha_2$

$OC = h$

$OA = R$

$OP_3 = r$

$P_3C = r_1$

$AP_3 = r_2$

AXIAL COMPONENT OF VORTEX CYLINDERS AT POINT P_3

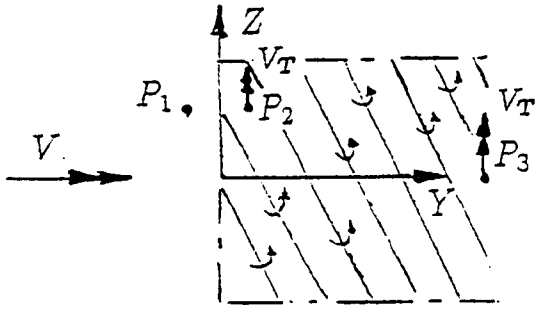

Figure 3.1 Concentrator with semi-prescribed cylindrical wake.

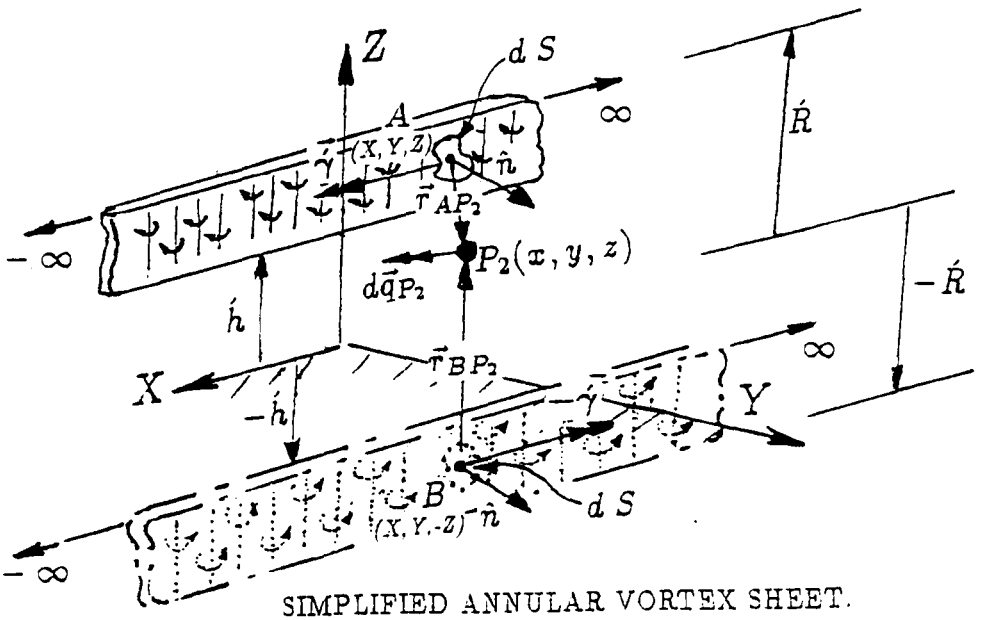

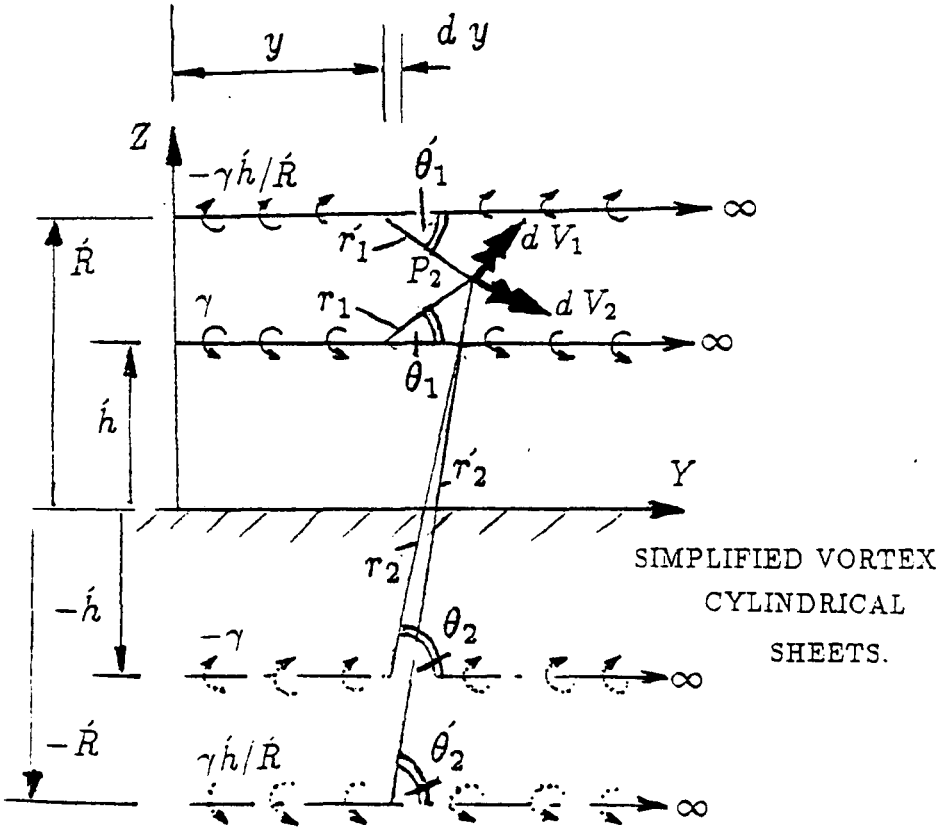

Figure 3.2 Simplified concentrator wake.

Using the above equations to solve equation 3.5 we get the following results (see appendix C for derivations)

$$\begin{aligned} V_T &= \frac{\gamma'' \acute{h}}{r} \quad \text{for} \quad \acute{h} < r < \acute{R} \\ V_T &= \frac{\gamma'' \acute{h}}{2r} \quad \text{for} \quad r = \acute{h} \text{ and } r = \acute{R} \\ V_T &= 0 \quad \text{for} \quad 0 < r < \acute{h} \\ &\quad \text{and} \quad r > \acute{R} \end{aligned} \tag{3.6}$$

(It can also be shown from Biot Savart theory that the radial induced velocity is zero.)

Equation 3.6 is the equation for free vortex flow between $\acute{h} < r < \acute{R}$ if γ'' is constant downstream for both vortex cylindrical sheets. We also notice that the core flow is irrotational. This would seem a reasonable result, since the flow through the core does not experience any angular momentum from blades or any other device. (The experimental results in chapter 5, based on the test work done at Queen Mary College by the author, confirm this conclusion).

Now figure 3.2 is a simplification of figure 3.1. If we first consider the induced velocity at P_2 from both infinitely long strips, which are of equal and opposite strength $\acute{\gamma}$, the total induced velocity will be $\vec{q}_{P_2}$. Points A and B are at separate points on each strip. The position vector connecting points A to P_2 is expressed as $\vec{r}_{AP_2}$. Similarly for points B to P_2 we have $\vec{r}_{BP_2}$. Also at each point A and B, the unit normals are the same and equal to $\hat{n}$ over an elemental surface area of dS. Considering the situation at P_2 in figure 3.2 and applying Biot Savart theory we get the following

$$\begin{aligned} \vec{q}_{P_2} &= \frac{1}{4\pi} \int \frac{(\hat{n} \wedge \vec{\acute{\gamma}}) \wedge \vec{r}_{AP_2}}{|\vec{r}_{AP_2}|^3} dS + \frac{1}{4\pi} \int \frac{(\hat{n} \wedge (-\vec{\acute{\gamma}})) \wedge \vec{r}_{BP_2}}{|\vec{r}_{BP_2}|^3} dS \\ &= \frac{\acute{\gamma}}{4\pi} \int_{-\infty}^{\infty} \int_{\acute{h}}^{\acute{R}} \frac{[\hat{\imath} y - \hat{\jmath}(x - X)] dX dZ}{[(z - Z)^2 + (x - X)^2 + y^2]^{\frac{3}{2}}} \\ &\quad - \frac{\acute{\gamma}}{4\pi} \int_{-\infty}^{\infty} \int_{-\acute{h}}^{-\acute{R}} \frac{[\hat{\imath} y - \hat{\jmath}(x - X)] dX dZ}{[(z - Z)^2 + (x - X)^2 + y^2]^{\frac{3}{2}}} \end{aligned}$$

If we solve the above integral we find that the Y component is zero, while the X component, V_x, is given by

$$V_x = \frac{\acute{\gamma}}{2\pi}\Big\{-\tan^{-1}\Big(\frac{z-\acute{R}}{y}\Big)+\tan^{-1}\Big(\frac{z-\acute{h}}{y}\Big)\Big\}$$
$$-\frac{\acute{\gamma}}{2\pi}\Big\{-\tan^{-1}\Big(\frac{z+\acute{R}}{y}\Big)+\tan^{-1}\Big(\frac{z+\acute{h}}{y}\Big)\Big\} \qquad (3.7)$$

(For derivations see appendix D). Now the induced velocity also at $P_2\,(xyz)$ from the semi-infinite sheets shown in figure 3.2 is again derived from Biot Savart theory. The total elemental induced velocity at P_2 shown in figure 3.2 will be $d\vec{V}_a = \sum d\vec{V}_1 + \sum d\vec{V}_2$. Where $|d\vec{V}_1|$ equals $\frac{\gamma dy}{2\pi r_1}$ from the inner vortex sheet and $-\frac{(\gamma\acute{h}/\acute{R})dy}{2\pi\acute{r_1}}$ from the outer vortex sheet. Also $|d\vec{V}_2|$ equals $\frac{\gamma dy}{2\pi r_2}$ from the reflected inner vortex sheet and $-\frac{(\gamma\acute{h}/\acute{R})dy}{2\pi\acute{r_2}}$ from the reflected outer vortex sheet.

Now consider only the Y component of induced velocity $d\vec{V}_a$ and integrating we get

$$V_y = \int_0^\infty \Big(\frac{\gamma\sin\theta_1}{2\pi r_1} - \frac{\gamma\acute{h}/\acute{R}\sin\acute{\theta_1}}{2\pi\acute{r_1}}\Big)dy$$
$$-\int_0^\infty \Big(\frac{\gamma\sin\theta_2}{2\pi r_2} - \frac{\gamma\acute{h}/\acute{R}\sin\acute{\theta_2}}{2\pi\acute{r_2}}\Big)dy$$
$$= \frac{\gamma}{2\pi}\Big\{\pi-\tan^{-1}\Big(\frac{y}{z-\acute{h}}\Big)+\tan^{-1}\Big(\frac{y}{z+\acute{h}}\Big)\Big\}$$
$$-\frac{\gamma\acute{h}}{2\pi\acute{R}}\Big\{\pi-\tan^{-1}\Big(\frac{y}{z-\acute{R}}\Big)+\tan^{-1}\Big(\frac{y}{z+\acute{R}}\Big)\Big\}$$
$$\text{for } |z| < \acute{h} \qquad (3.8)$$

$$= \frac{\gamma}{2\pi}\Big\{-\tan^{-1}\Big(\frac{y}{z-\acute{h}}\Big)+\tan^{-1}\Big(\frac{y}{z+\acute{h}}\Big)\Big\}$$
$$-\frac{\gamma\acute{h}}{2\pi\acute{R}}\Big\{\pi-\tan^{-1}\Big(\frac{y}{z-\acute{R}}\Big)+\tan^{-1}\Big(\frac{y}{z+\acute{R}}\Big)\Big\}$$
$$\text{for } \acute{h} < |z| < \acute{R} \qquad (3.9)$$

(For derivations see appendix E). The reason for not including in the above the influence of the axial component of vorticity of the helical trailing

vortices is to simplify the analysis using the relationship between V_T and V_t. The induced velocity from the bound vortices will be equal to the contribution from the axial component of vorticity of the helical trailing vortices at the concentrator disc face. The contribution would steadily increase to twice this value at far wake conditions, hence maintaining the constancy of V_T downstream of the concentrator at a constant radial distance r for cylindrical wake conditions. Therefore, from previous reasoning, it is reasonable to assume for values of R/h near unity that

$$V_t \simeq V_x \tag{3.10}$$

$$\text{and} \quad u = V + V_y \tag{3.11}$$

Equations 3.10 and 3.11 now enable a relatively simple analysis to be conducted. By applying the results of equations 3.1 to 3.3, 3.7 and 3.9 for $y = \epsilon$ and $z = \acute{h}$, where ϵ is a very small positive value, we get the following

$$\tan\beta = \frac{N\Gamma/V}{2\pi(\acute{R}+\acute{h})(1-\frac{N\Gamma/V\tan\beta}{4\pi\acute{R}})} \tag{3.12}$$

which can be solved to give

$$\beta = \tan^{-1}\Big(\frac{1-\sqrt{1-(N\Gamma/V)^2/(2\pi^2\acute{R}(\acute{R}+\acute{h}))}}{(N\Gamma/V)/(2\pi\acute{R})}\Big) \tag{3.13}$$

(The positive root has been discarded because β must be zero at zero blade loading).

The angle has been calculated from the induced flow just behind the concentrator disc rather than at infinity because of the fact that the induced axial flow gradually increases to its far wake value along the wake. In reality it means that γ, $\acute{\gamma}$ and γ'' would be a function of y making the analysis considerably more complicated. Therefore the most pessimistic value of β has been taken. (It must be remembered that the analytical model is a very approximate representation of the principle of wind concentration). Now from equation 3.8 we have the expression for the increase in axial velocity through the core for $|z| < \acute{h}$ and $y \to \infty$ of the form

$$V_y = \gamma - \gamma \acute{h}/\acute{R} \tag{3.14}$$

Therefore the velocity through the core becomes

$$V_c = V + \gamma - \gamma \acute{h}/\acute{R} \tag{3.15}$$

By substituting equations 3.2 and 3.13 in to equation 3.15 and dividing by V we get

$$\frac{V_c}{V} = 1 + \left(\acute{R}/\acute{h} - 1\right)\left(1 - \sqrt{1 - \frac{(N\Gamma/V)^2}{2\pi^2 \acute{R}(\acute{R} + \acute{h})}}\right) \tag{3.16}$$

Now consider the axial flow far downstream of the concentrator blades. For $\acute{h} < |z| < \acute{R}$ and $y \to \infty$ we get from equation 3.9

$$V_y = -\gamma \acute{h}/\acute{R} \tag{3.17}$$

If $u_1 = V + V_y$ then applying equation 3.13 and 3.17 to this expression we get

$$\frac{u_1}{V} = \sqrt{1 - (N\Gamma/V)^2/(2\pi^2 \acute{R}(\acute{R} + \acute{h}))} \tag{3.18}$$

Equation 3.18 would imply that, for inviscid theory to be valid, the model with a semi-infinite wake requires

$$(N\Gamma/V)^2/(2\pi^2 \acute{R}(\acute{R} + \acute{h})) \leq 1.$$

Above this value the wake cannot be infinite in length, indicating wake truncation; otherwise u_1 will become complex/imaginary which is impossible. (Note same applies to β and V_c).

If we define the concentration ratio C_R as the kinetic energy of concentrated flow captured per unit time far inside the inner cylindrical vortex sheet of a radius $\acute{h}$ to the kinetic energy of unconcentrated free stream flow available per unit time, we get

$$C_R = \frac{\frac{1}{2}\rho\pi \acute{h}^2 V_c^3}{\frac{1}{2}\rho\pi \acute{h}^2 V^3} = \left(\frac{V_c}{V}\right)^3 \tag{3.19}$$

Therefore the potential power that could be extracted from the core can be interpreted as

$$P_a = C_R C_p \frac{1}{2} \rho \pi \acute{h}^2 V^3 \tag{3.20}$$

When a wind turbine is placed in the way of the flow, there will obviously be a wake interaction between the wind turbine wake and concentrator wakes. The effect of this on V_c will possibly lead to a reduction in power P_a. (It is because of this fact that the performance factor r_p will always be less than C_R). Now from Rosenbrock(1983) the upper limit of the Concentration Ratio $C_R = (R/h)^2$. This is in line with Betz Theory since a concentrator and wind turbine would ideally be equivalent to a larger wind turbine of radius R. In the previous chapter the author compared the concentrator to a leaky Obstruction Augmentor. To exceed the Betz Limit it has been shown from the analytical theory above that wake downstream of the concentrator will need to become truncated. In the limit there would be no vortex wake with no velocity through the blades due to very high loading. This impossible concentrator would have a theoretical C_R as previously stated in equation 2.11. Therefore if a limited truncated vortex wake is possible downstream of the concentrator with effective viscous mixing in the far wake, the maximum C_R possible for the CWT could be between

$$\left(\frac{R}{h}\right)^2 < C_R < \left(\frac{R/h+1}{2}\right)^6$$

Expressing this in terms of gross C_R based on the swept frontal area whose radius is equal to R we then get for the above inequality as follows

$$1 < (C_R)_{Gross} < (h/R)^2 \left(\frac{R/h+1}{2}\right)^6$$

3.4 Numerical Wake Modelling.

The method by which wake modelling can be achieved is called 'Wake Relaxation'.

Figure 3.3 highlights the approach involved. An elliptic loading is specified for each blade which is simplified into an equivalent rectangular loading.

(The core radius of each vortex filament is one percent of the concentrator span to avoid spurious induced velocity effects). The wake of one blade is considered with the effect of other blade wakes. The other blade wakes are represented by transferring the current blade wake geometry of one blade about the Y axis, by a particular angle equivalent to the angular position of each blade, relative to the one blade and wake considered. (This is indicated as ψ in figure 3.3). The procedure for wake relaxation is illustrated in figure 3.3 and is as follows;

1. Induced velocities are calculated at mid-points B1 and B2 from all the elements in the wake.

2. The wake is then adjusted at each node C1 and C2 with the adjustment vectors $\vec{\Delta}(1)$ and $\vec{\Delta}(2)$. (Note the number in brackets refers to column number and not the iteration number).

3. This is repeated across each row of nodes from E to I say, using the same adjustment vectors.

4. Now new induced velocities are calculated for the next row of mid points D1 and D2 and steps 2 to 3 are repeated except new wake adjustment vectors will ripple down from nodes E1 and E2 to I1 and I2.

5. Step 4 will be repeated for new starting mid points F1 and F2 up to H1 and H2 say.

6. Repeat steps 1 to 5 until convergence has occurred.

7. Increase the number of elements which can be relaxed beyond nodes I1 and I2 each by one element length with the semi-infinite filaments attached now at nodes K1 and K2, and repeat steps 1 to 6 until the required length of relaxed wake has been met.

The above procedure is based on that given by Hunt(1981) . Step 6 usually involves no special process for a convergence test if the wake

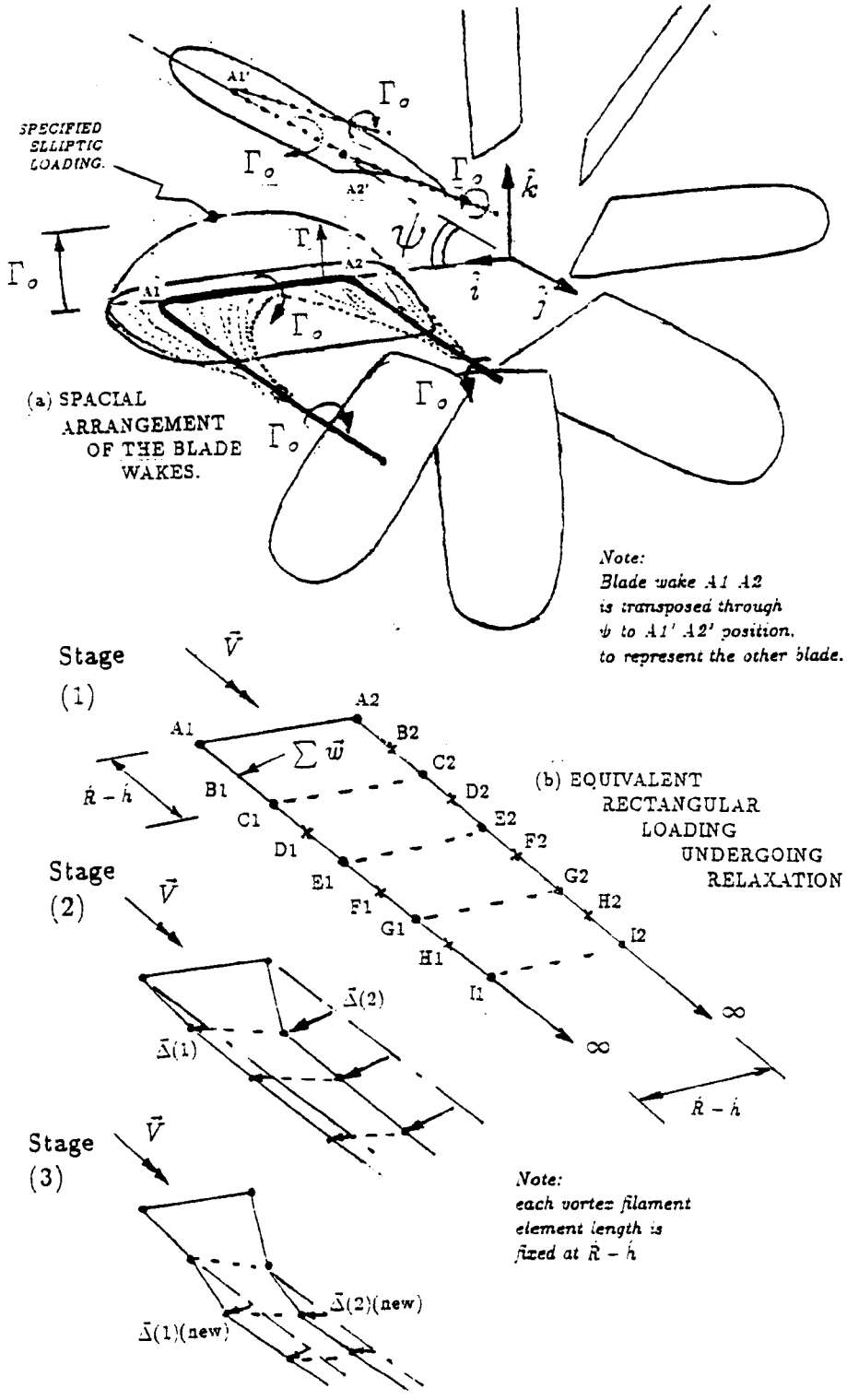

Figure 3.3 Wake Relaxation Method

converges quadratically. For the kind of wake relaxation work involved with a heavily loaded wake structure a much better method must be employed, since near the solution convergence is very slow. The OU Course Team no.M371(1988) describe a method called 'Aitken Acceleration' and offers a way of accelerating the iterative scheme since even if it does converge, the convergence is, in general, only linear. This means that close to a root say ε, we have for the $n+1$th iteration of the X component of a node in the vortex wake structure

$$|\delta x_{n+1}| \simeq |g'(\varepsilon)||\delta x_n|$$

therefore convergence will be very slow if $|g'(\varepsilon)|$ is only just less than one. To accelerate to the root the following method is used;

If x_o is the starting value of the iterative scheme for only one node then

(a) Calculate $x_1 = g(x_o)$, (ie do steps 1 to 5), and set n=2.

(b) Calculate $x_n = g(x_{n-1})$.

(c) Calculate the X component of the adjustment vector for the node and divide this by the previous value which will give you some value λ.

(d) Increase n by 1 and repeat steps (b) and (c) until successive values of λ seem to be settling down to some approximately constant value.

(e) Calculate the new X component for the node

$$x_{new} = x_n + \frac{\lambda}{1-\lambda}|\vec{\Delta}_{n-1}.\hat{i}|$$

where $\vec{\Delta}_{n-1} = \vec{r}_n - \vec{r}_{n-1}$

(f) Replace x_n by x_{new} and repeat from step(b) until the required accuracy is reached.

The above procedure is also applied to the other components Y and Z for the individual node. The process is then repeated for every X,Y,Z coordinates of all the nodes throughout the wake to ensure proper convergence is met. The final result of this method is a three dimensional

wake developed from the influence of the axial free stream velocity and the interdependence of all trailing vortex elements in the wake.

To design the concentrator blades involves previous knowledge of the characteristics of the chosen aerofoil for single blade 2D flow and what maximum value of C_L should be tolerated along the span to avoid stall. By using the approximate fluid model shown in figure 3.4 the following relationships are used to determine the value of the chord length c for the rectangular blade plan form and the local blade twist;

$$\begin{aligned} \vec{W} &= \sum \vec{w}(y_p, z_p) \\ &= \vec{V}_y + \vec{V}_z \qquad (3.21) \\ \phi &= \tan^{-1}\left(\frac{|\vec{V}_z|}{|(\vec{V} + \vec{V}_y)|}\right) \qquad (3.22) \\ C_L &= \frac{2\Gamma \cos\phi}{|(\vec{V} + \vec{V}_y)|c} \qquad (3.23) \\ \Theta &= \phi + \alpha \qquad (3.24) \end{aligned}$$

The procedure to find Θ and c is as follows

(A) Calculate $\vec{V}_y$, $\vec{V}_z$ and ϕ.

(B) Assume a value for c.

(C) Calculate C_L and if its value is too small return to (B) and consider a larger value of c. If not continue.

(D) Find the value of α from the aerofoil characteristic, (ie CL vs α graph.)

(E) Calculate Θ.

Note that equation 3.23 is an application of the Kutta-Joukowski theorem to the blade element

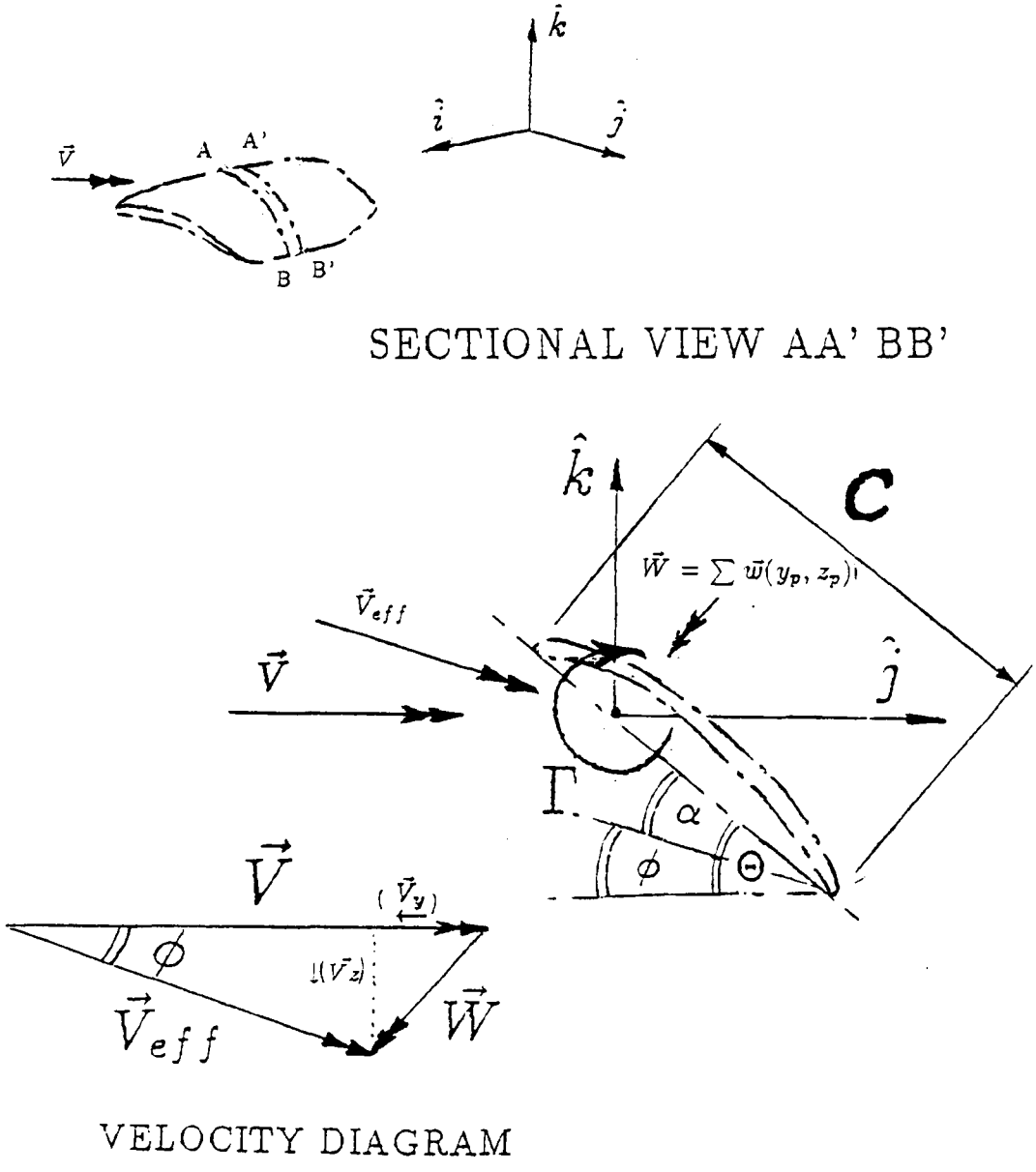

Figure 3.4 Concentrator blade design method on a blade element.

Chapter 4

DESIGN AND TEST WORK.

4.1 Introduction.

This section covers all the design and test work done by the author on the CWT. The results of these tests are given in chapter 5.

4.2 Wind tunnel test work at Queen Mary and Westfield College.

4.2.1 Design Work.

The research work on the CWT started in the summer of 1988. At that time the author was using blade element theory to design a wind tunnel model. The model had to fit into the exhaust airflow of the open jet wind tunnel at Queen Mary and Westfield College (QMW) in London. A wind tunnel wake scan had to be performed initially to check out flow abnormalities, and to decide where to put the model concentrator in relation to the wind tunnel. Figure 4.1 shows the distribution of tunnel air flow at different axial positions downstream of the wind tunnel exhaust jet tube y_t, with no model present.

Figure 4.2 gives the details of the optimum arrangement for the concentrator model in relation to the wind tunnel as a result of the wind tunnel wake scans. The model outer rim suffered a partial lack of air flow, which

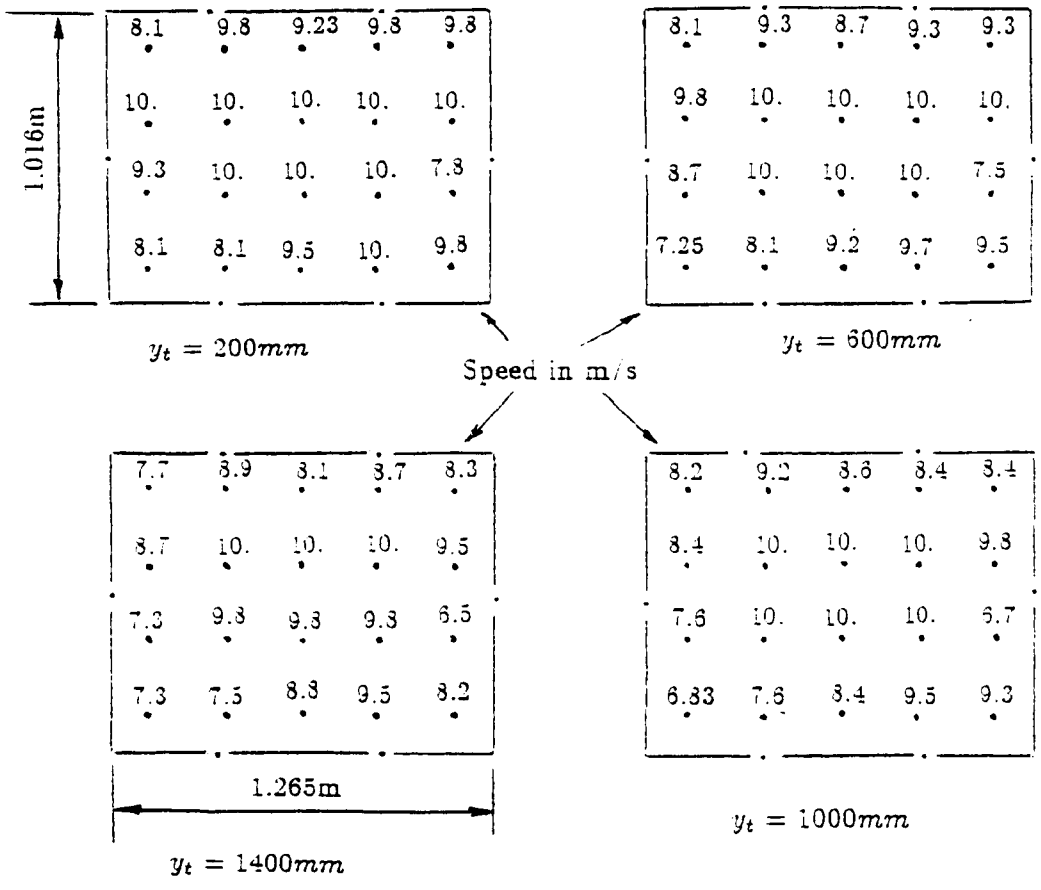

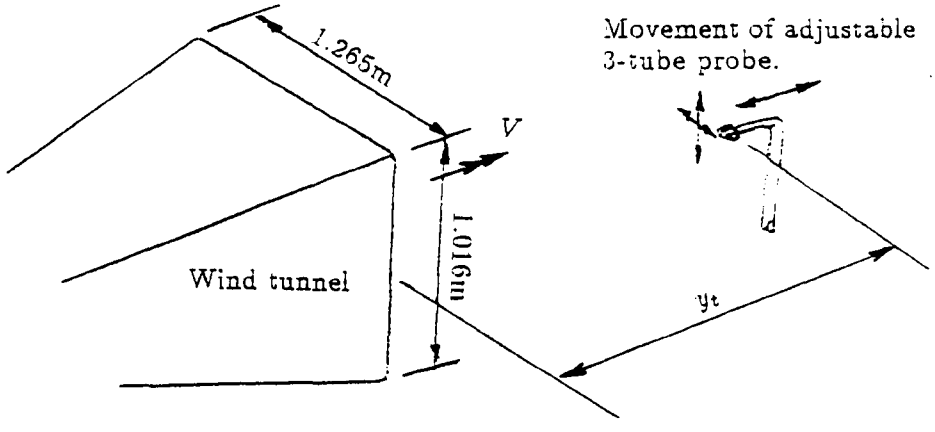

Figure 4.1 Initial wake scan of the tunnel used at the QMWC.

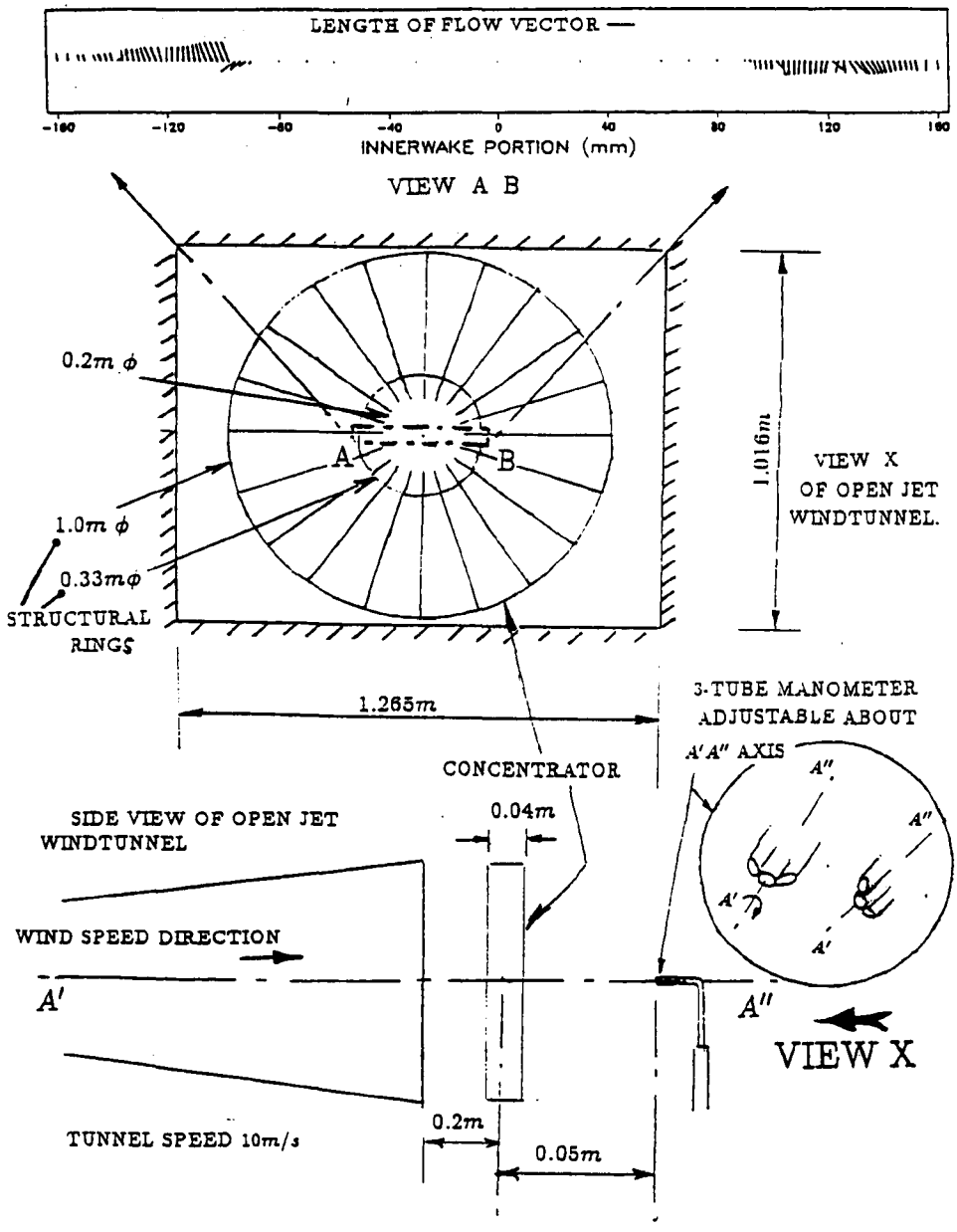

Figure 4.2 Wake Traverse experiment on early wind concentrator.

in turn affected the outer tip vortex development. Fortunately this did not affect the inboard flow air significantly if the concentrator was at the position of 0.2m downstream of the jet tube shown in figure 4.2. A three tube Total Pressure Probe was used to find air flow speed and direction by a diametrical traverse of the probe across the open jet flow. At different positions downstream of the concentrator, y/h, results were taken for each traverse. During the traverse the probe was rotated through 90° to measure airflow velocity in both Z and X directions. (The same instrument was used earlier to do the tunnel velocity plot). Appendix F covers details of calibration methodology for the Total Pressure Probe.

4.2.2 Manufacture of a Wind Concentrator for test work at QMW.

In figure 4.3 shows details of an early design of CWT which did not progress beyond the wind tunnel model stage, and was later tested at QMW with the wind tunnel arrangement indicated in figure 4.2. Figures 4.4, 4.5 and 4.6 show aspects of its manufacture. The mild steel blades were twisted at certain positions along the span relative to the mid-span section. Special vice jaws were made to hold the blade in a vice without destroying the blade section. The manufacturing tolerances were found to be within ±2°. Any kinks on the blades were removed with a soft hammer and an anvil.

Figures 4.5 and 4.6 also show how the blades were attached to the outer and inner structural rings. (All of the material used throughout was mild steel). The finished concentrator was finally was mounted on a 'Dexion' frame in the Open Jet exhaust flow as shown in figure 4.5

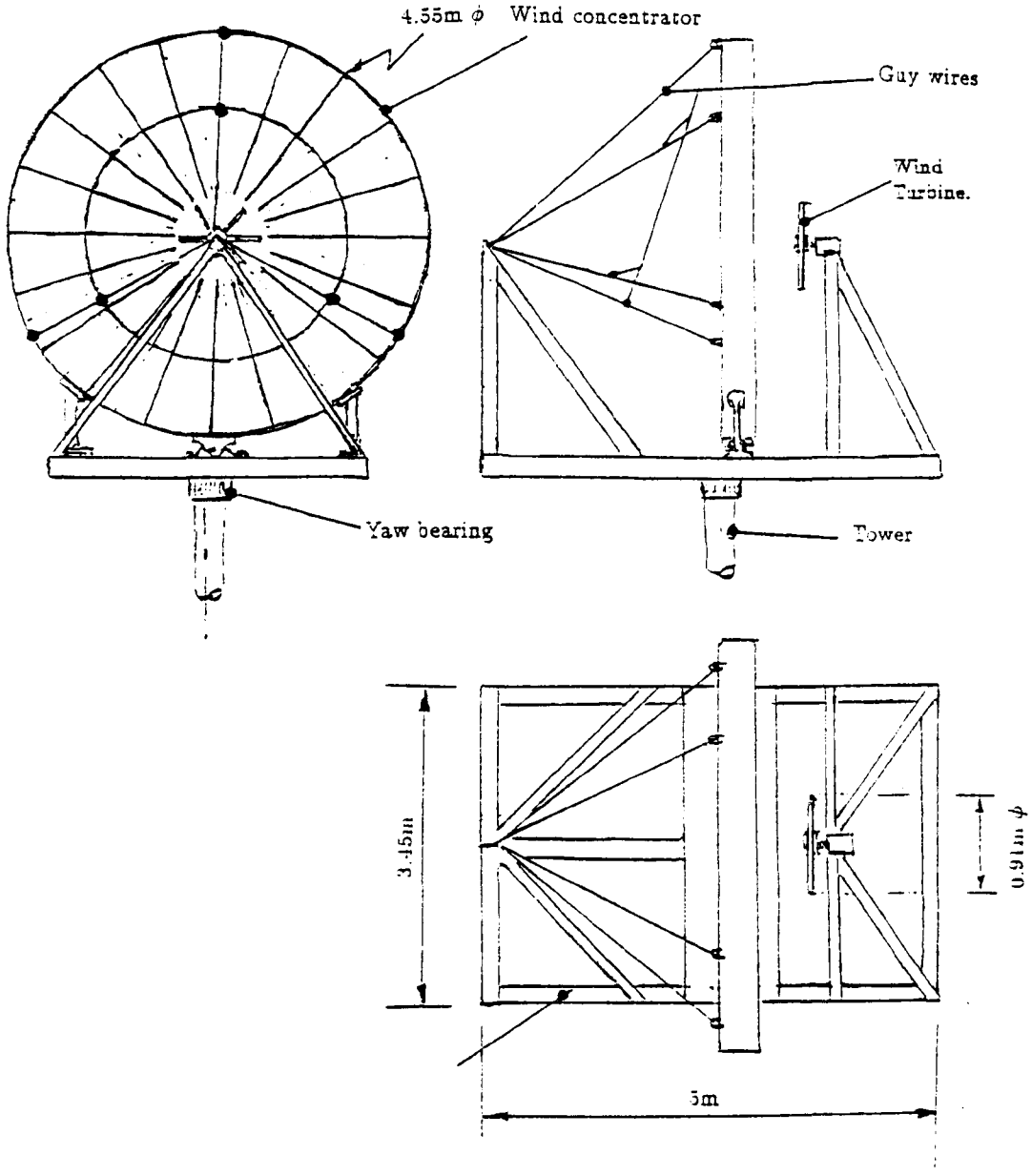

Figure 4.3 Early design of field test CWT .
All dimensions in metres.
Not drawn to scale.
DESIGN PARAMETERS
$\Gamma/(V(R-h))$=0.0469
$N = 20$
$R/h = 5$.
Aerofoil section is Gö417A. Blades twisted with constant chord length.

Figure 4.4 Equipment to produce steel concentrator blades.

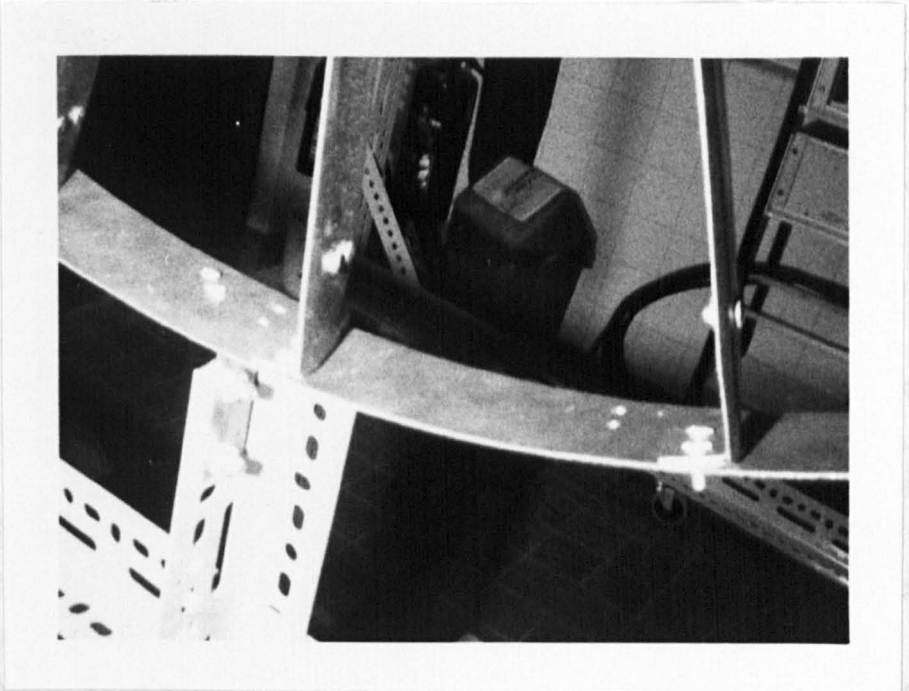

Figure 4.5 Mounting arrangement at outer concentrator structural ring.

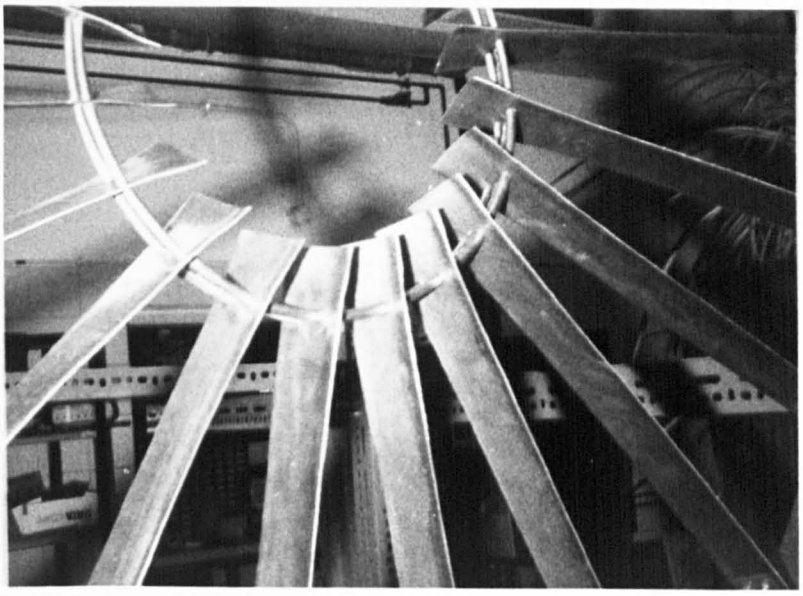

Figure 4.6 Mounting arrangement at inner concentrator structural ring.

4.3 Design and test work for CWT field test machine.

4.3.1 Design Work.

The results from test work done at QMW on the initial model were not very encouraging. It was initially thought that model scale effects were to blame for the poor agreement between theory and experiment. Therefore plans to build a larger machine were initially considered. From figure 4.3 it can be can be seen from the size of machine required that it would have been a major undertaking to build such a machine. It was because of this, the author decided to investigate a different approach to concentrator design, using Biot Savart Theory. (This is covered in chapter 3, sections 3.3 and 3.4). This new approach later proved much more successful at predicting concentrator performance, (see chapter 5, table 5.1).

A desire for a smaller more compact design of CWT for the field tests, made the author conduct a parametric study on different designs to find the optimum design of concentrator. The meaning of the word 'Optimum' is different from that for a wind turbine or propeller. The optimum de-

sign, for a given Concentrator Ratio C_R, is the design that minimizes the construction volume. Fabrication costs have not been considered in this project since it was not the aim of the research work to do a full economic study at this stage.

The results of the concentrator parametric design study using the numerical Biot Savart model are given in figures 4.9, 4.11 and 4.13. Figure 4.8 gives the results from the analytical Biot Savart model, and these compare well with the results shown in figure 4.9. This was done so that an initial check could be made on the numerical model. Designs above the 'Betz Limit line', as mentioned in chapter 3, indicate that only a truncated vortex wake is possible. Prediction of the viscous mixing processes that could be involved in the far wake is beyond the capability of the the inviscid model. Therefore it had to be assumed that any far wake affects would have little influence on near wake conditions. What was lacking from this study, was an idea of the construction volume required for a given aerofoil section for the concentrator blades. How thin the concentrator blades could be was a matter only settled by stress analysis. In figure 4.7 shows the kind of blade section used for the concentrator which was a Gö417A. The lift forces acting over the blade span would bend and possibly buckle a particular blade section at high loading. The aerodynamic design of the blades required that they would be highly twisted along the blade span. An investigation of the minimum bending stress to cause local blade section buckling, would have involved a study beyond the scope of the current research programme. Therefore, as an initial guide to the study of the least material concentrator, the blade thickness would be no greater than that specified aerodynamically. The construction volume of each particular concentrator design is calculated from the formula for total blade volume. The following relationships are typical for the section involved:

Cross sectional area of wing = Blade camber length $\times$ thickness

$$= 1.014 \times \text{chordlength} \times \text{thickness}$$

If thickness= t and chord length= c it is found empirically that t =

$0.0338c$. Now for a concentrator of ratio R/h, the blade span will be $(R-h)$. Therefore the construction volume ζ will be

$$\zeta = 0.03424c^2N(R-h) \tag{4.1}$$

Once ζ is known, the parametric study for different concentrator designs can be conducted again, except that now C_R will be divided by ζ. Figures 4.10, 4.12 and 4.14 show sample results. These figures show, for a particular R/h and C_R, that the volume ζ of construction material for the blades reduces as $N\Gamma/(V(R-h))$ involved in the design increases. This shows that for a fixed ratio R/h, as the strength of the annular vortex sheet representing the blades increases, the volume of construction material increases, but not as fast as C_R. From a structural stand-point, it is desirable to keep R/h as low as possible since a compact design has the advantage of reducing the possibility of fatigue when exposed to unsteady loads . Unfortunately, as the number of blades rises cascade flow problems become more complex due to the thickness of the blades, and manufacturing labour costs increase. Therefore the author conducted this design study more from the point of view of increasing experience in what can or cannot be built. (Later in chapter 5 the author highlights major lessons learnt from aerodynamic problems caused by poor blade design.)

A design based on a low ratio R/h and a high number of blades N was finally considered. What has been described above influenced the author in his decision to design a concentrator with 54 blades, with $R/h = 1.6$ and with $\Gamma/(V(R-h)) = 0.314$. The author wanted a machine which would give a significant V_{CF} of about 2 and have a low construction volume with reasonable blade spacing. An other reason for choosing this design is that the Betz Limit, based on a frontal swept area whose radius is that of the outside radius of the concentrator, could be exceeded if an 'Ejector Effect' exists in the far wake when a wind turbine is working in the core flow. This is discussed in more detail in chapter 2, section 2.3 and appendix A.

It will be noticed in figure 4.7 that the aerofoil section used only had a maximum C_L of approximately unity, but that the data on this aerofoil

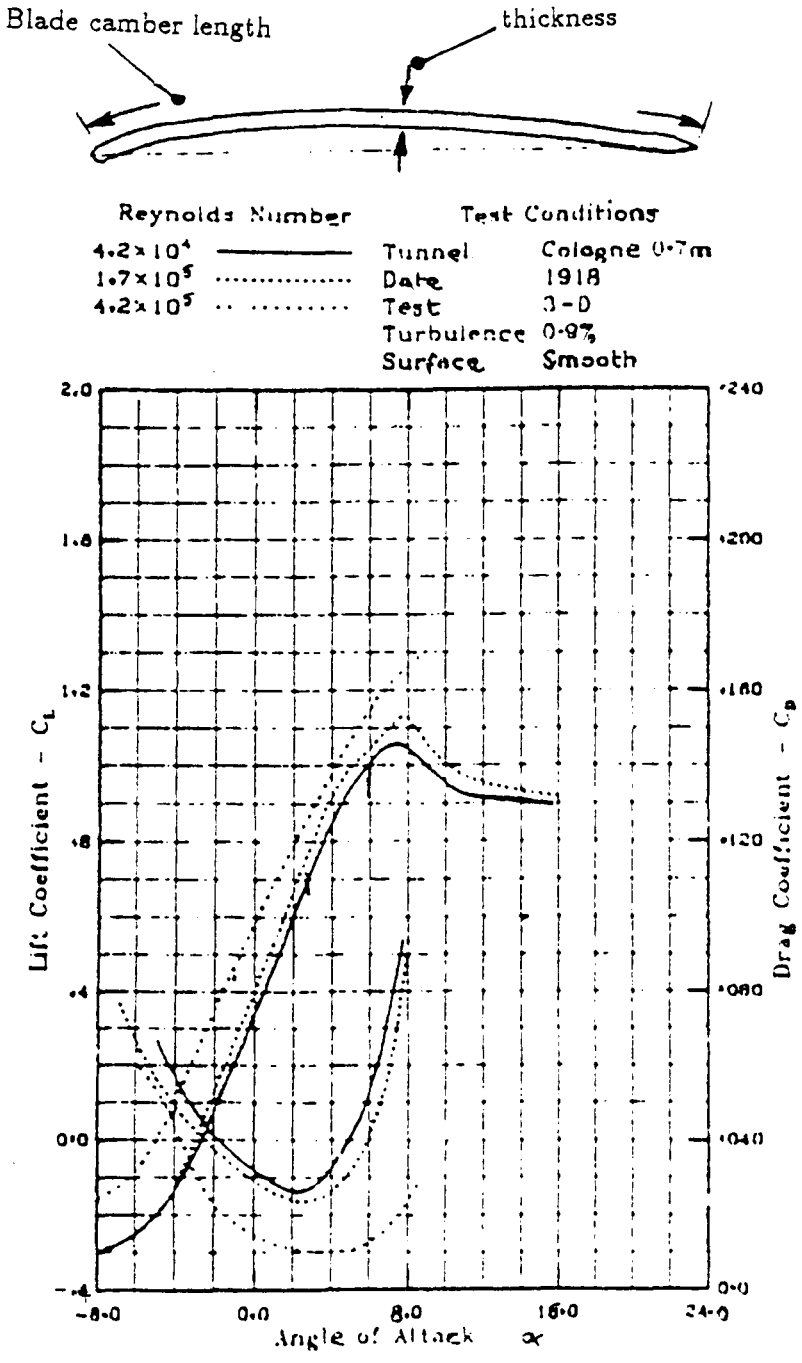

Figure 4.7 Gö417A aerofoil section for the concentrator blade.
Source: Miley(1982).

offered more reliable information at lower Reynolds Numbers compared to other aerofoils. This was calculated applying the blade design method given in section 3.4. From this design study, an aspect ratio of near unity was found. (Since a lifting line is used, it is not clear that the lifting line assumption is still valid in this situation.) On the strength of these results a new design for the full size CWT was conceived, and is shown in figure 4.16. The 'structural Ring' shown in figure 4.16 would effectively move the outer tip vortex to the ring itself, but this still would not improve the low aspect ratio. There was also a loss of effective aerofoil camber due to significant flow curvature across the concentrator. Lifting line modelling cannot determine this properly since the blade is represented as a discreet vortex. Lifting Surface modelling should be used, but lack of time prevented the author from making a complete theoretical investigation and the above assumptions had to be made.

Figure 4.16 shows a standard WG910 wind turbine. The most important design question during this early design stage was what power output would be possible from the CWT system? To be able to answer such a question sufficient knowledge of the generator and rotor characteristics is needed. Figures 4.17 and 4.18 show details of the generator performance characteristics and rotor design, supplied by Marlec Engineering Ltd. The rotor aerodynamic performance is shown in figure 4.19, calculated using Strip Theory with an assumed rotor blade element aerofoil section of Gö579. There are also curves for the generator power characteristics normalized with the kinetic energy of flow for the rotor swept area, calculated as follows:

Consider the definitions for Normalized Generator Powerout Coefficient $C_{P_{GOUT}}$, Normalized Generator Power Absorbed Coefficient $C_{P_{GIN}}$ and generator efficiency η_{GEN}

$$\eta_{GEN} = \frac{P_{GOUT}}{P_{GIN}} \tag{4.2}$$

$$P_{GOUT} = a\Omega + b \tag{4.3}$$

$$C_{P_{GOUT}} = \frac{P_{GOUT}}{\frac{1}{2}\rho\pi r_R^2 V^3} \tag{4.4}$$

$$C_{P_{GIN}} = \frac{P_{GIN}}{\frac{1}{2}\rho\pi r_R^2 V^3} \tag{4.5}$$

In equation 4.3 a and b are constants since most electrical generators have approximately a linear relationship between power generated and rotational speed. From the results shown in figure 4.17 the values of these constants are $a = 2.368$ and $b = -95.08$ for the WG910 generator. Now the tip speed ratio is $T_s = \Omega r_R / V$ so that we can rewrite equations 4.4 and 4.5 for a known rotor radius of $r_R = 0.455$m as

$$C_{P_{GOUT}} = 13.1\left(\frac{T_s}{V^2}\right) - \frac{239}{V^3}, \tag{4.6}$$

where V is the free stream velocity in m/s. Finally if we consider equations 4.2, 4.5 and 4.6 we get

$$C_{P_{GIN}} = 13.1\left(\frac{T_s}{V^2\eta_{GEN}}\right) - \frac{239}{V^3\eta_{GEN}} \tag{4.7}$$

We can see from equation 4.6 that the expression is linear in T_s for a particular wind speed. Therefore a change in wind speed causes a change in the slope and intercept as in figure 4.19 for different values of velocity concentration factor V_{CF}. The rotor characteristic on the other hand is only slight dependent on V due to Reynolds Number effects. As for $C_{P_{GIN}}$, it is non-linear for a particular wind speed owing to the variation in η_{GEN} with the rotational speed of the generator as shown in figure 4.17. It is this curve which determines the operating point on the rotor characteristic where the generator absorbs power equals the rotor input power for a particular wind speed. Vertically below the operating point the operating point is another point which is on the curve of $C_{P_{GOUT}}$. This is what the generator will provide in terms of electrical power output divided by the kinetic power of the far upstream flow over the rotor swept area.

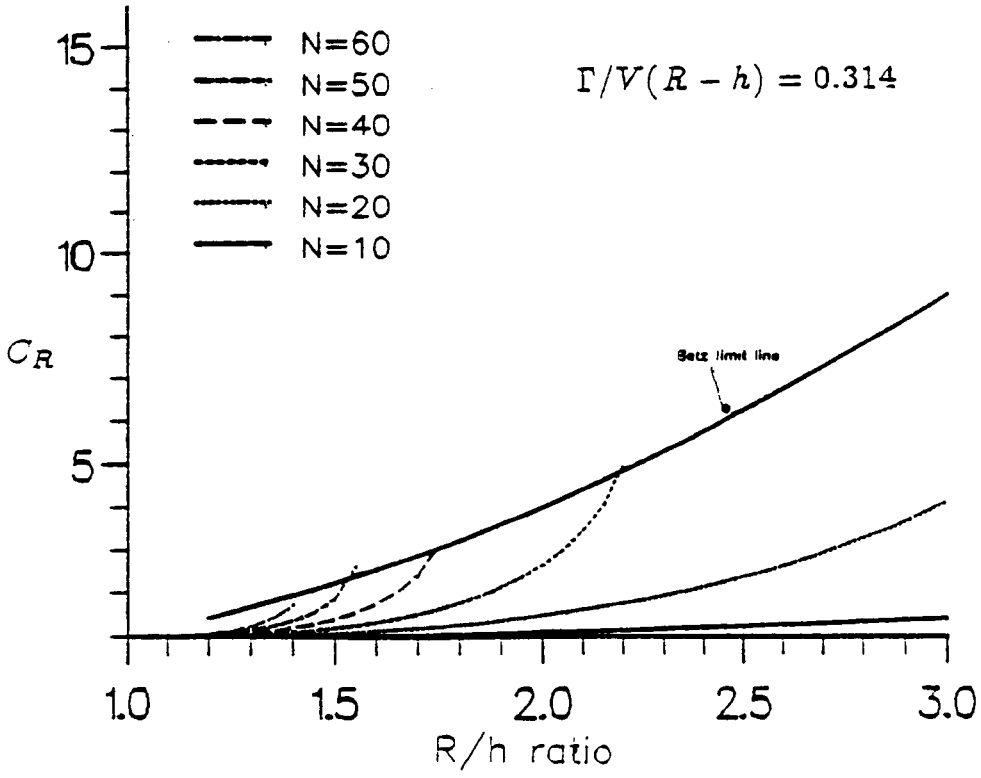

Figure 4.8 Parametric study of the wind concentrator.(Analytical model).

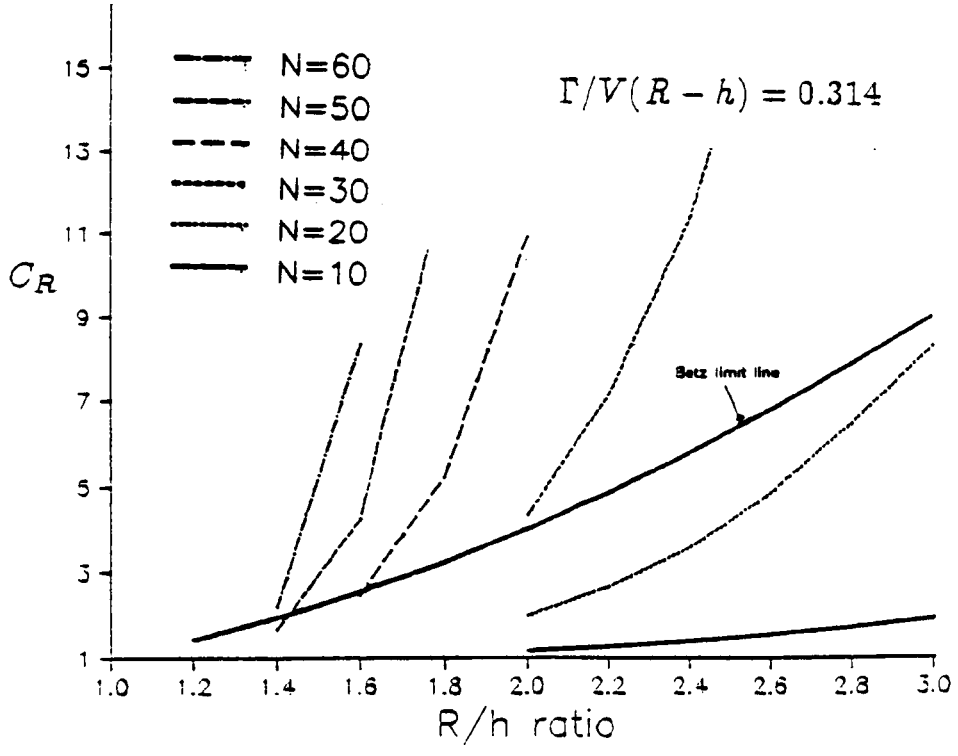

Figure 4.9 Parametric study of the wind concentrator.(Numerical model).

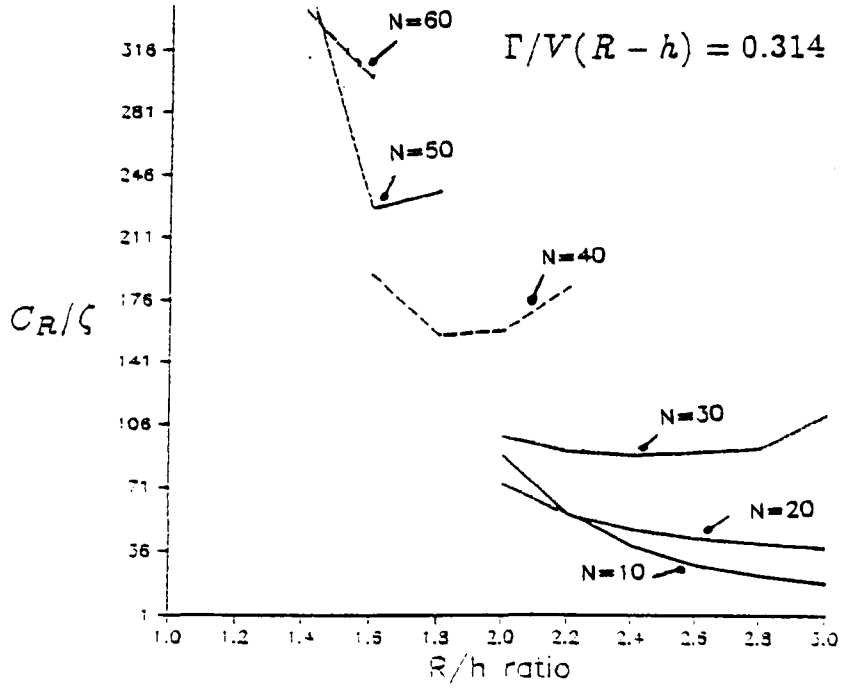

Figure 4.10 Construction volume study of the wind concentrator.(Numerical model).

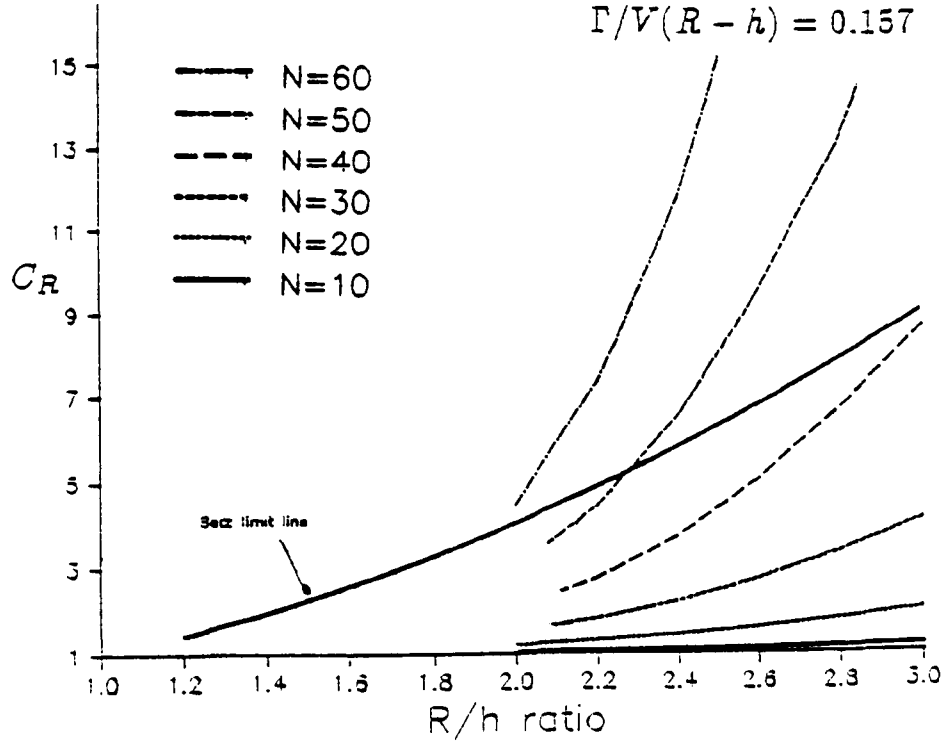

Figure 4.11 Parametric study of the wind concentrator.(Numerical model).

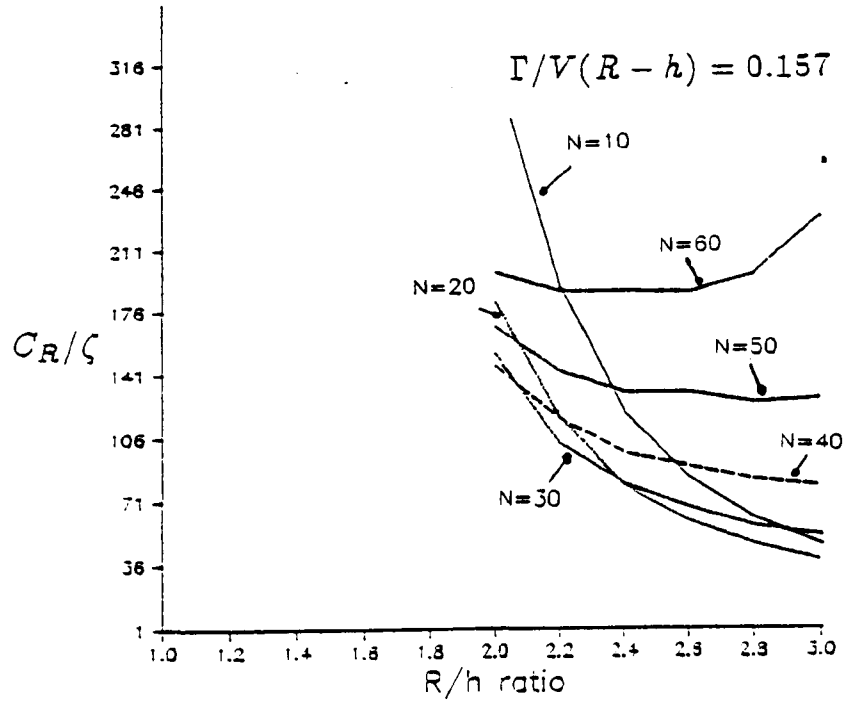

Figure 4.12 Construction volume study of the wind concentrator.(Numerical model).

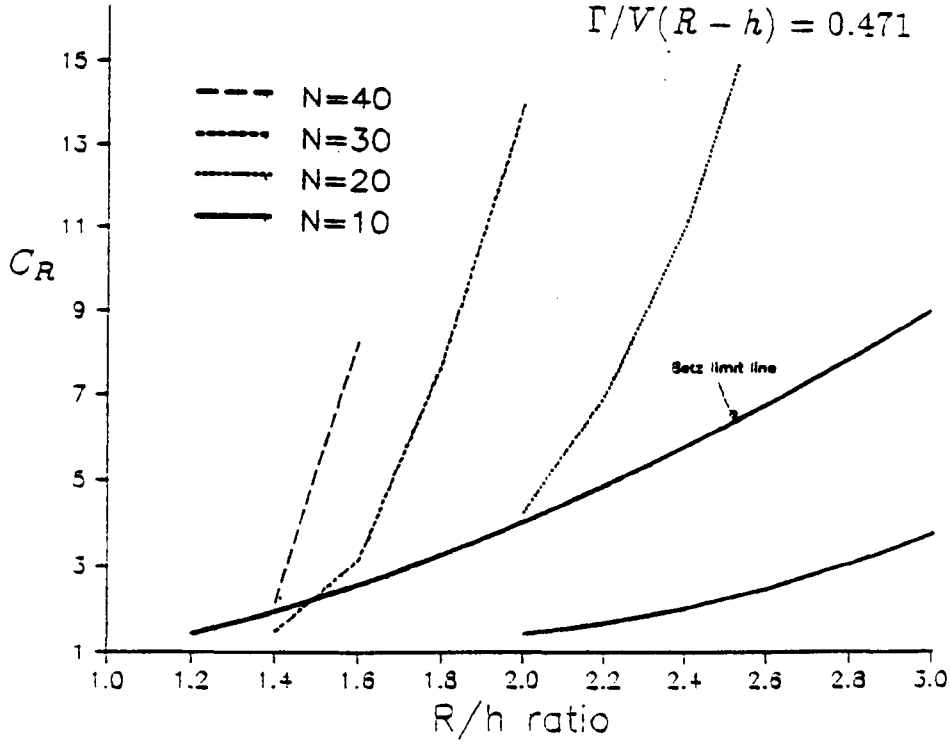

Figure 4.13 Parametric study of the wind concentrator.(Numerical model).

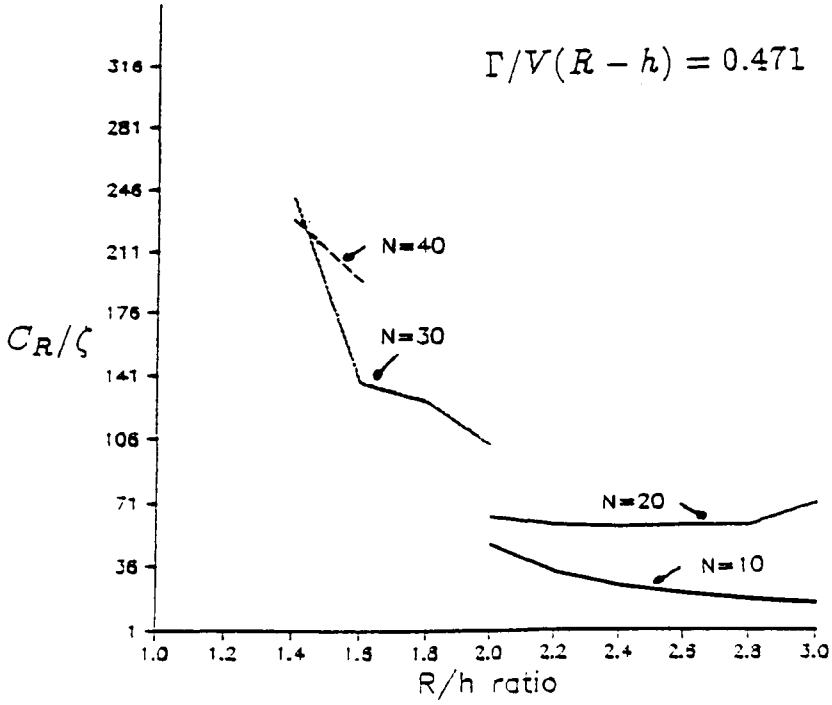

Figure 4.14 Construction volume study of the wind concentrator.(Numerical model).

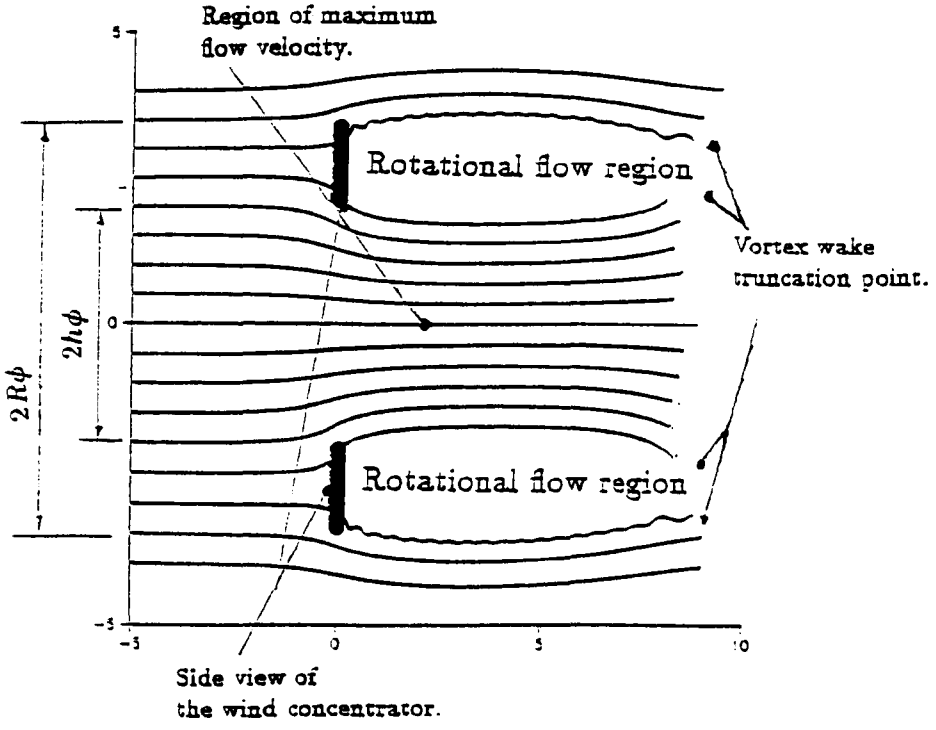

Figure 4.15 Theoretical Streamline plot across a wind concentrator.

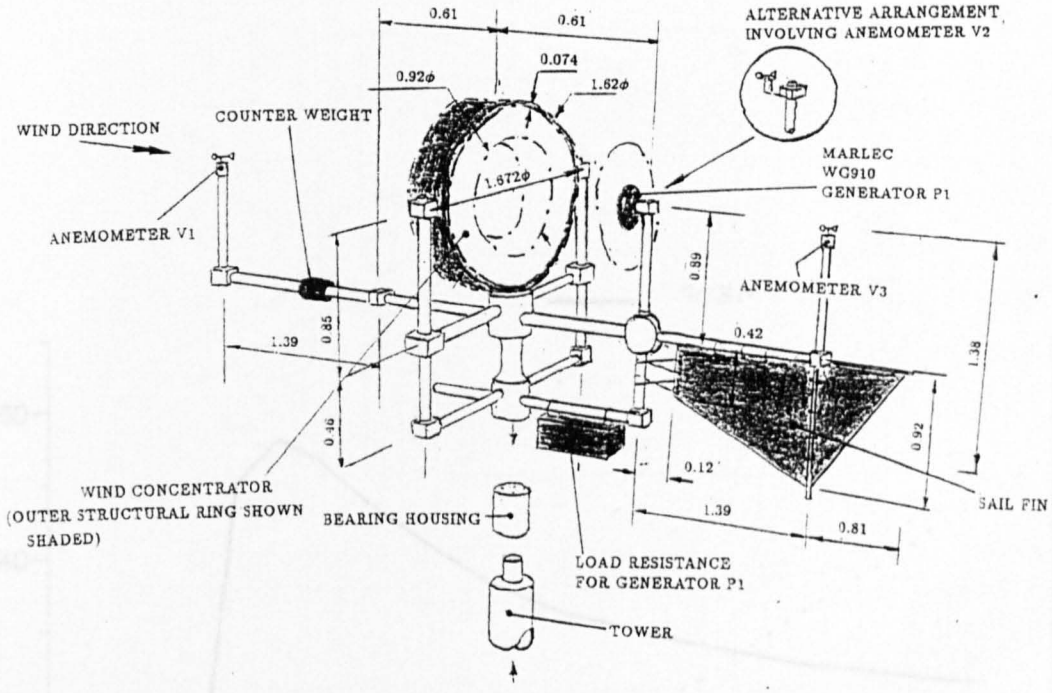

Figure 4.16 CWT structural and instrumentation arrangement.
All dimensions in metres.
Not drawn to scale.
All up weight excluding the tower: 100kg.
DESIGN PARAMETERS
$\Gamma/(V(R-h))$=0.314
$N = 54$
$R/h = 1.6$
Aerofoil section is Gö417A. Blades twisted with constant chord length.

Concentrator	Glass fibre and expanded polyurethane foam filling.
Structural bars	HE 30-TF duralumin (38mm ϕ O.D, 4.76mm thick).
Connecting blocks for structural bars	Machined aluminium blocks.
Counter weight	Mild steel.
Bearing housing	Mild steel.
Sail fin	Kevlar

Table 4.1 Materials list for the wind concentrator.

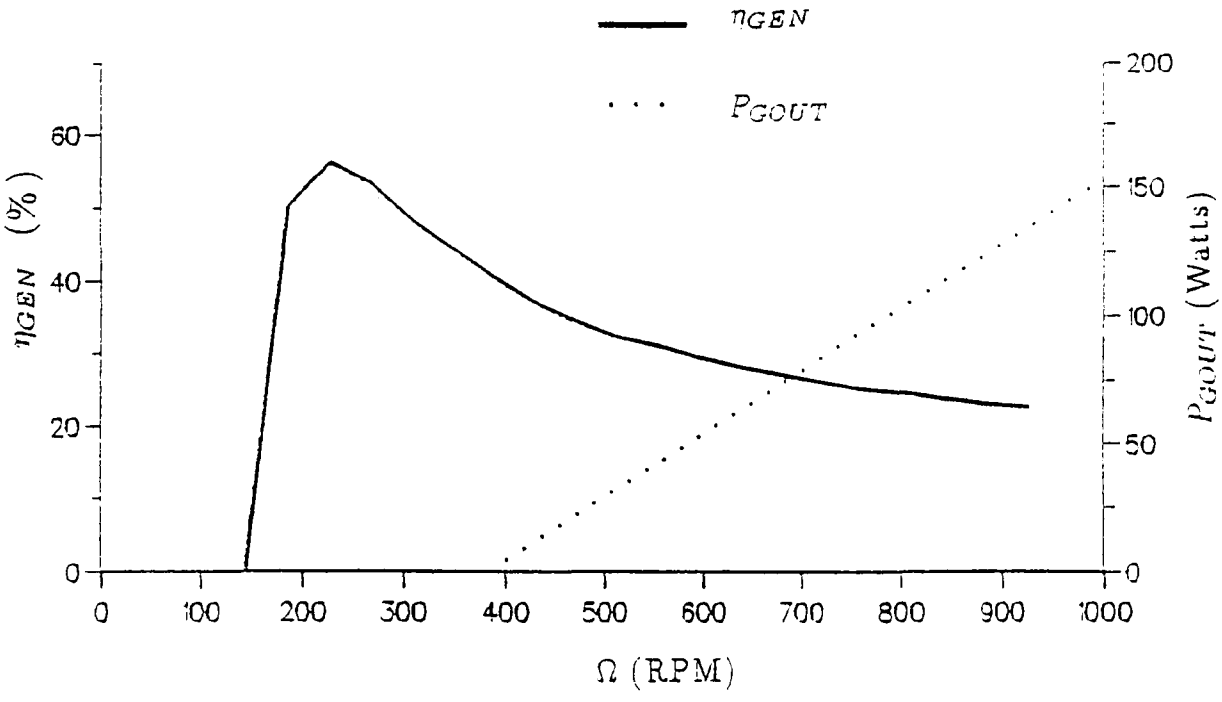

Figure 4.17 WG910 Generator performance characteristics.
Source: Marlec Engineering Ltd.

4.3.2 Manufacture of the CWT.

Manufacture of the wind concentrator shown in figure 4.16 involved fifty four blades which were made out of glass fibre with polyurethane foam filling. Figure 4.20 shows the glass fibre 'Female' moulds that had been previously made in order to produce the blades. (The Female mould itself had been produced from a plastic 'Male' mould which in turn had been previously produced from a clay Female mould.) The surfaces of the Female mould were first polished to allow easy mould release and later coated with resin. Glass fibre matt was finally pressed on to the wet resin and all

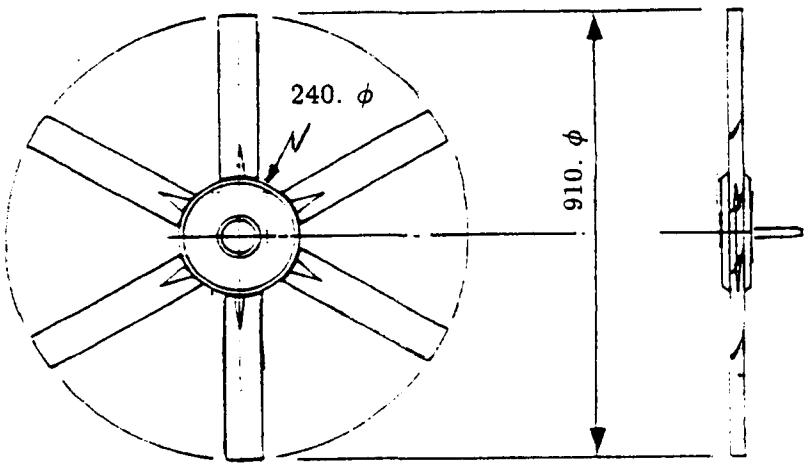

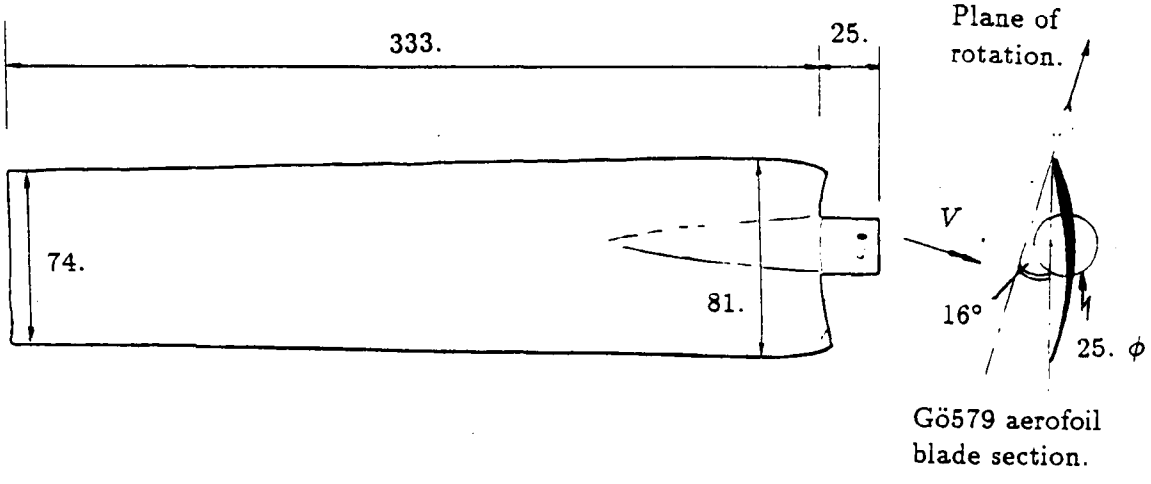

Dimensions in mm.

Figure 4.18 WG910 rotor design.
Source: Marlec Engineering Ltd.

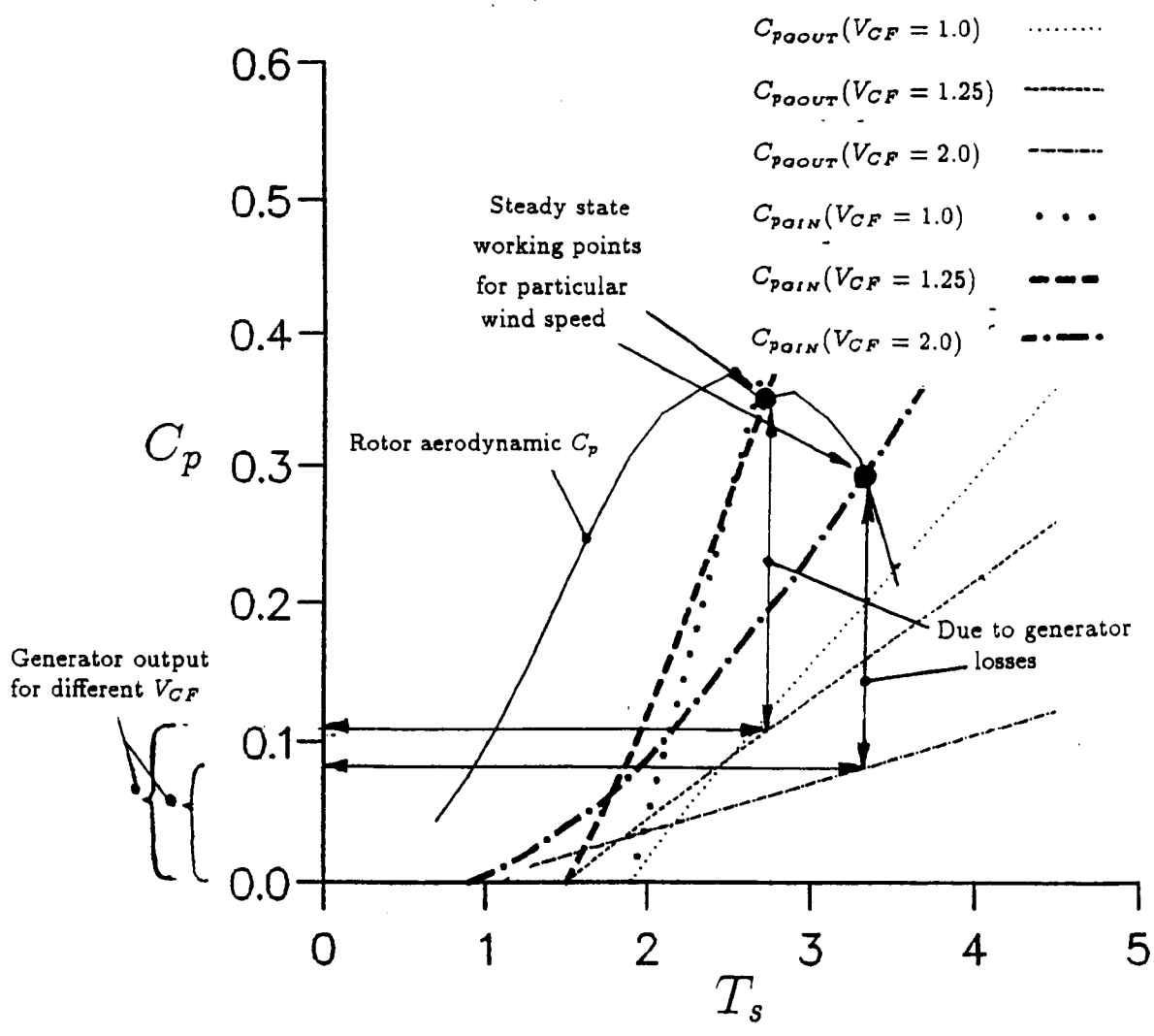

Figure 4.19 WG910 rotor performance characteristic for $V = 9.8$m/s.

three sides of the mould were then bolted together. At this point chemical constituents needed to produce the polyurethane foam were poured into the inner cavity of the Female mould. The foam quickly formed inside and created the necessary internal pressure to properly impregnate the glass fibre with resin to achieve full strength. Once the glass fibre and polyurethane foam had set, the Female mould was unbolted and carefully released from the finished blade so that it could be used again. In figure 4.21 shows the finished article. The surface quality was very good except a few holes which were filled with a plastic compound.

The final operation involved joining all the blades together. A wooden jig had to be built to hold each blade in place so that a glass fibre 'Lay Up'

of glass fibre cloth, rope and resin could be built onto the outboard part of the blade. This formed the outer structural ring of the concentrator. The blade pitch and spacing were very crucial to the concentrator design and were achieved to within a reasonable level of accuracy of $\pm 2°$ and difference of chord/spacing ratio of $\pm 4\%$. The blade elements radially beyond the mid-span were unfortunately not as specified because each blade had to blend into the outer structural ring. This was mainly for structural reasons. The weight of the concentrator at this point was 30kg. This was mainly due to the inefficient use of glass fibre, but since this was only a prototype testing out the principle of wind concentration, the author was not too worried about weaknesses in the design at this stage in CWT development.

The tubular space frame structure shown in figure 4.16 was made of duralumin with steel guy wires attached at several node points to support the structure. The tubes themselves were fixed together with aluminium connecting blocks. The blocks gripped tubes by a clamping action which prevent the tubes from being drilled and bolted. (A bolted joint would have been more susceptible to corrosion fatigue).

A counter weight was needed to balance the structure so that the yaw bearing could run smoothly and therefore allow the structure to yaw properly. The sail vane shown in figures 4.16, 4.24 and 4.25 was made of 'Kevlar' for lightness. The sail vane proved to be very responsive to yaw in the field which helped to provide the necessary test conditions for the CWT. The sail vane was placed below the wake of the wind concentrator to avoid interference with its wake swirl. The positioning of the turbine in relation to concentrator had been previously considered theoretically from numerical wake modelling of the wind concentrator. Figure 4.15 indicates that one internal diameter downstream would be sufficient to realize the maximum kinetic energy available in the core. The mounting of the turbine downstream in the concentrator wake was achieved with a duralumin tubular structure of smaller diameter to avoid wake disturbance in the swirl flow of the concentrator. To fair this structure properly would have involved the use of plasticine applied to the structure, and a wind tunnel to blow air over

Figure 4.20 Glass fibre mould arrangement to produce concentrator blades.

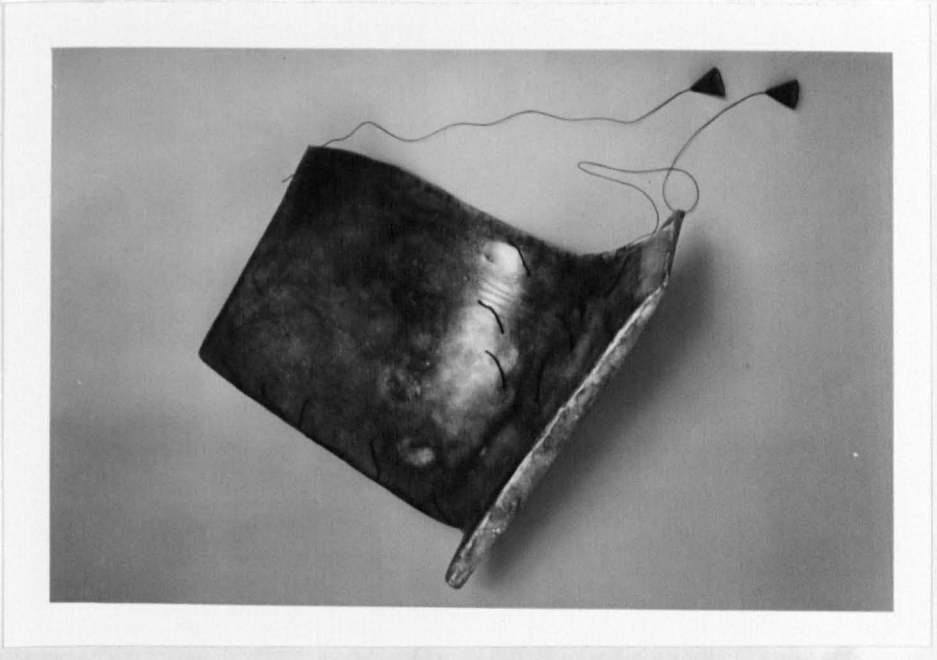

Figure 4.21 Paper cones with cotton line and cotton tufts attached to a specimen concentrator blade.

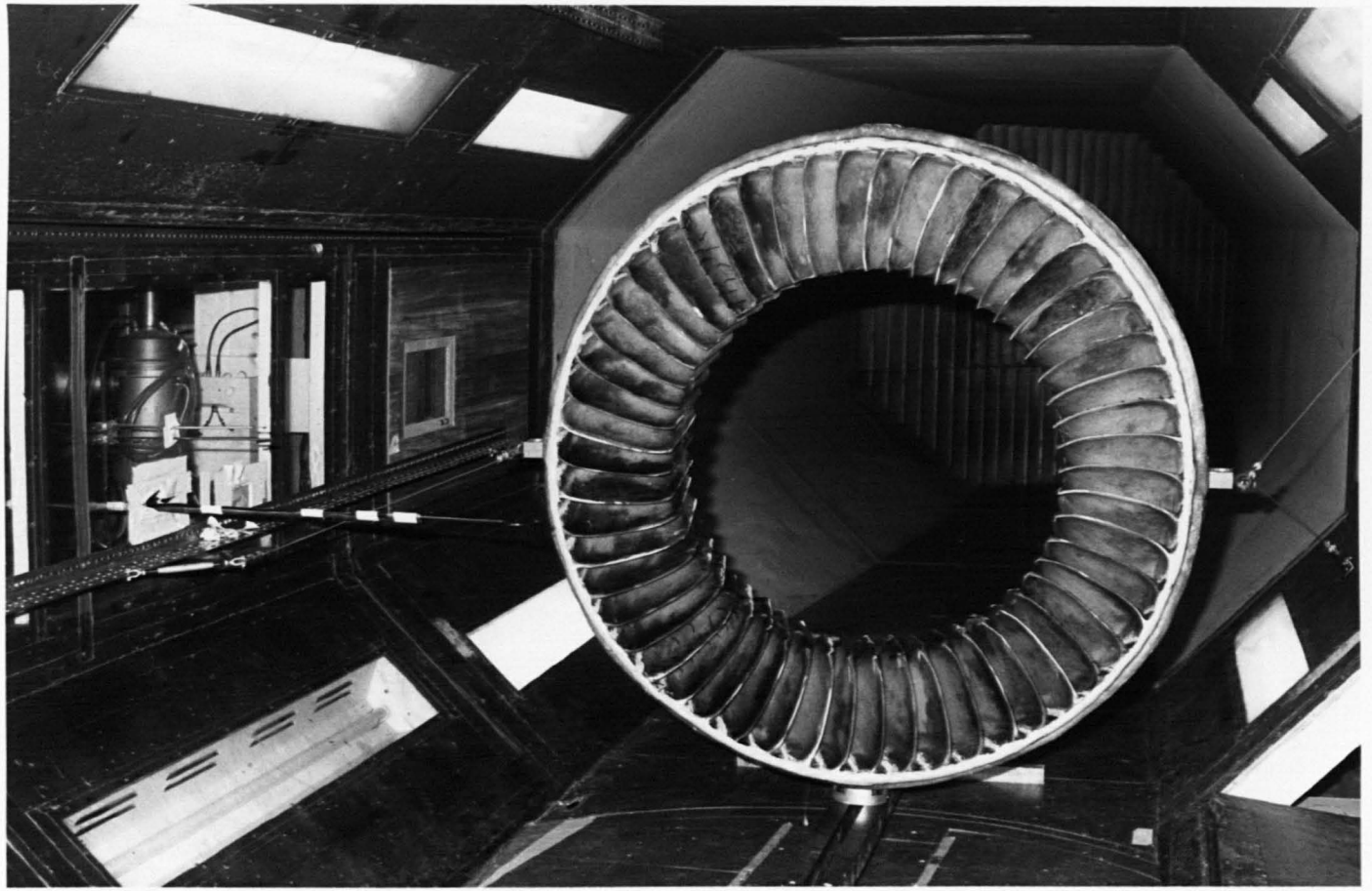

Figure 4.22 Test arrangements at Goldstein Aeronautical Engineering Research Laboratory

it to find the correct shape by trail and error. Chalk and water would have had to been painted over the surface before each test to help detect any boundary layer separation during the wind tunnel tests. Unfortunately this would have taken too long to achieve, therefore it had to be assumed that such a flow interference would not be too detrimental to the concentrator's performance.

Diametrical compressive loads on the concentrator structural ring were understood to exist due to the arrangement of the steel guys. After the manufacture of the concentrator the compressive loads were applied to the concentrator to see if the structure of the concentrator could sustain this loading. Fortunately the concentrator was well over designed and no problems were encountered.

The yaw bearing housing shown in figures 4.16 and 4.23 was made of steel and had a construction weight of 30kg. The construction weight could have been reduced considerably by using suitable aluminium alloy material for the housing, but since this was a prototype design the author was content to accept the weight. The size of the yaw shaft had to be large to sustain the large pitching moments. In future designs it is hoped that the yaw bearing can be mounted along the concentrator axis of symmetry. This would reduce the size and weight considerably. Future research work should investigate to what level of upstream frontal blockage can be tolerated before the performance of the concentrator significantly deteriorates.

4.3.3 CWT test work at Gretton.

Field test work started in early June 1990 and finished by the end of August 1990. The winds during this time fortunately gave a wide enough range to make the tests worth while. (0 to 15m/s).

Figures 4.16, 4.24 and figure 4.25 show the design of the test rig. It consisted of a concentrator and wind turbine with instrumentation. A separate control wind turbine was also used for comparative purposes. Two types of test were tried out one involving just the concentrator using three anemometers recording wind velocity, (shown in figure 4.24), and the other

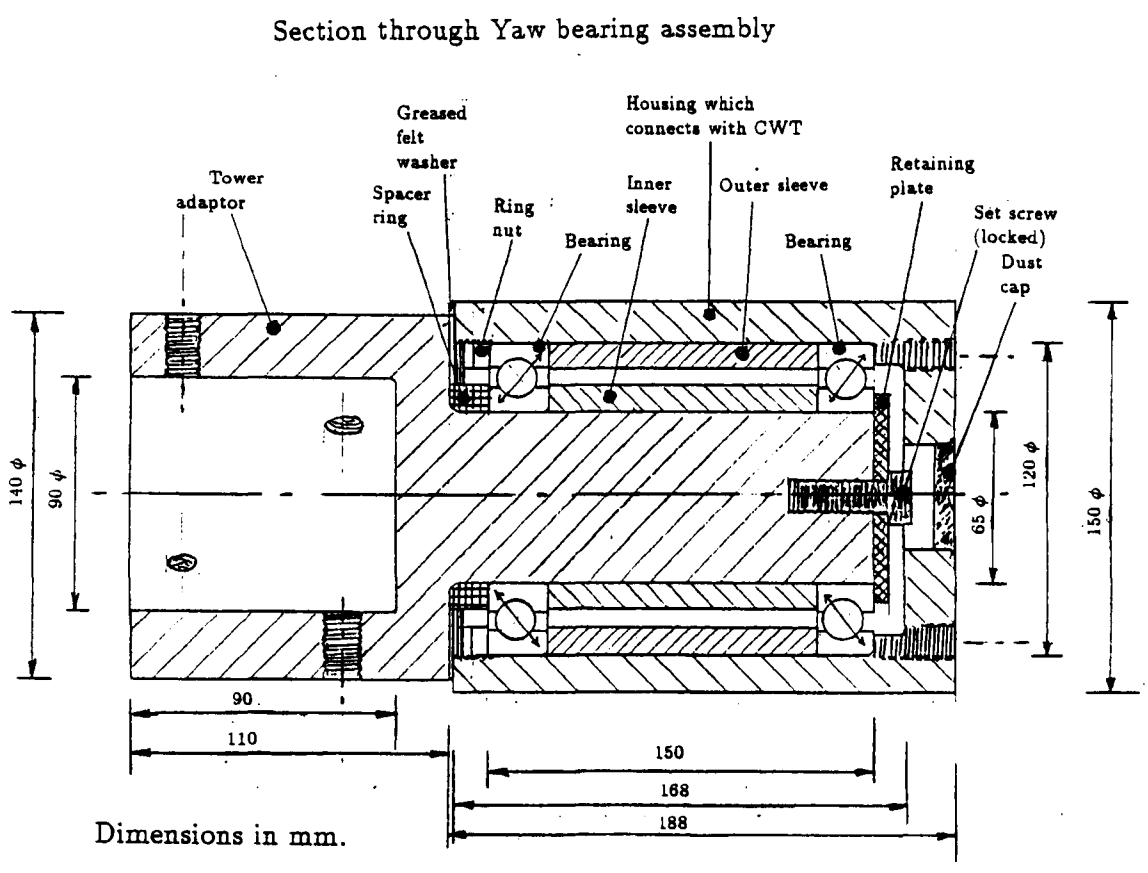

Figure 4.23 CWT Yaw Bearing Assembly.

involving the concentrator, wind turbine and the control wind turbine, (see figure 4.25). The second test only used the far up and downstream anemometers V1 and V3 and the power from the turbine P1 was compared with that from the control wind turbine P2 near to the CWT rig. The hub height of the CWT rotor above the ground was 8.58m while that of the control turbine was 6.58m above the ground. The reason for this difference in heights was that the CWT test rig continued to have major designs changes near to the time when tests were to be done. Therefore there was no time left in which to rectify the situation. Fortunately the tests were set up to detect very large differences in power generation, ie of the order of 700% for an expected 100% difference in air flow rate at the CWT rotor, compared to that at the hub height of the control wind turbine. Now the wind shear profile was unknown but if the most pessimistic profile of a 0.18 power law is assumed this would have only meant a 4.7% difference in flow rate producing a corresponding 13.4% difference in generated power

between the CWT and the control turbine. Therefore the mistake of not having the CWT and control turbine at the same height should not have had a serious effect on the validity of the experiment.

The two machines involved were both WG910 wind turbines, each with similar power characteristics with less than 1% difference between both generators. (These generators were tested comparatively in the laboratory). Power was calculated from the measured rotational speed of the generator by using the power characteristic shown in figure 4.17. (Rotational speed was easily found by counting electronically the generated voltage pulses per second, (ie four voltage pulses per revolution for the eight pole generator)).

The two main test areas involved first a series of fast monitoring runs each at a rate of ten readings a second over ten minutes, and the second test involving long term logging of one minute averages over several days.

The first method was designed to investigate the quality of the data. Measuring the velocity at three points with only the concentrator and later measuring the power output from the CWT and from the separate wind turbine, enabled time series analysis to be done on the data. The ratio of standard deviation and the mean of the signal gives an idea of how steady the output is. As a back up to this, a graph of spectral density function times frequency against the natural logarithm of frequency have been plotted, (see figures 5.2 to 5.11, chapter 5). The frequency range represents 0 to the Nyquist frequency which was 5 Hz and expressed in units of ω_p. All data has been mean and trend corrected. (Greater details of data logging for the field test are given in appendix G).

The area under these graphs equals the variance of the signal which is expressed mathematically in the equations below

$$\sigma^2 = \int_0^\infty S(\omega_p) d\omega_p \tag{4.8}$$

$$\text{Or} \quad \sigma^2 = \int_0^\infty \omega_p S(\omega_p) d(ln(\omega_p)) \tag{4.9}$$

This enables the reader to see at what frequency range the variance is generated. Different wind speed ranges were considered for the ten minute runs. ($<$ 7m/s for slow and between 7m/s and 15m/s high).

The second method of tests involved long term runs over several weeks. Each reading was logged at one minute average. The reason for the one minute average was to avoid time varying mean values and to obtain sufficient number of samples within the limited period of two weeks that was available. On the recommendation of Stacey *et al*(1984), logging data at one minute average will reliable mean values. After collecting this data, Linear Regression Analysis was performed to assess the velocity and power gains due to the influence of the wind concentrator, (see chapter 5, figures 5.12 to 5.14).

The final piece of work done on the data from the long term runs was a data process called 'Binning' (see Akins(1978)). By Binning the power out from both the CWT generator and the generator of the control wind turbine against the upstream anemometer wind readings, both characteristics can be compared to show at what wind speeds the power variation between the two machines is significant. (See figure 5.15).

The final tests were done on just the concentrator, and involved a smoke generator and video camera to record the flow visualization process across the machine. The smoke generator consisted of a smoke chamber (shown in two parts) with a pipe attached to the top part to convey the smoke to the required area of the machine without too much air disturbance, a smoke pellet, metal gauze to support the pellet and a hoisting pole attached to lower part of smoke chamber (See figure 4.26).

Further flow visualization work was briefly done on the 54 bladed wind concentrator at the Goldstein Aeronautical Engineering Research Laboratory, of University of Manchester during early October, 1990. Figure 4.21

indicates the method of flow visualization using cotton line, paper cones and tuffs attached to different parts of the concentrator. The use of smoke in the tunnel shown in figure 4.22 was not effective in showing off tip vortex flow features, due to low smoke density of the smoke producers available at Goldstein Laboratory. It was also noticed that the vortices themselves were too diffuse to be picked up successfully.

4.4 Wind tunnel test work at the Technical University of Berlin.

4.4.1 Design Work.

These tests were carried out in February 1991 at the Technical University of Berlin over one week and proved to be the most important and conclusive tests over the entire period of the project. The reason for this is that the test facilities at Berlin were designed for wind concentrator research, making wind tunnel model construction simple. The other reason for the success in that week is the design of the model was more closely in line with the stringent assumptions of the theory involved in the computer model. (This is discussed in more detail in the next chapter).

The wind tunnel model was generated from the numerical Biot Savart computer model and had the following design specification.

DESIGN SPECIFICATION FOR TEST MODEL.

$\Gamma/(V(R-h)) = 0.346$

$N = 16$

$R/h = 2.92$

$y/h = 1.2$

$\Theta = 32°$ (Constant along the blade span).

Aerofoil Section = Aerofoil section specified for each blade element along the axis of the bound vortex or prospective 1/4 chord blade axis of the concentrator blade = Gö576

Chapter 3 covers the concentrator blade design method for optimum blade twist with constant chord. To simplify manufacturing the author chose to vary the chord instead. This meant changing the blade design procedure in section 3.4 of chapter 3 to the following

$$
\begin{aligned}
\vec{W} &= \sum \vec{w}(y_p, z_p) \\
&= \vec{V}_y + \vec{V}_z \\
\phi &= \tan^{-1}\left(\frac{|\vec{V}_z|}{|(\vec{V} + \vec{V}_y)|}\right) \qquad (4.10) \\
\alpha &= \Theta - \phi \qquad (4.11) \\
c &= \frac{2\Gamma \cos\phi}{|(\vec{V} + \vec{V}_y)| C_L} \qquad (4.12)
\end{aligned}
$$

The above relationships were used to find the local chord c by the following procedure

(A) Calculate $\vec{V}_y$, $\vec{V}_z$ and ϕ from the relaxed wake.

(B) Find α from the specified blade pitch angle Θ.

(C) Use figure 4.28 to find local C_L from α. (Where α is outside this range, use linear interpolation to find C_L).

(D) Calculate the local chord from equation 4.12

Table 4.2 gives the results from this design process and the resultant chord distribution can be seen in figure 4.29. In figure 4.27 is shown the resultant streamline distribution of the concentrator, indicating that at one radius downstream would appear to be the best place for the wind turbine. This explains why the author chose to perform axial and swirl velocity measurements at $y/h = 1.2$ downstream of the quarter chord position of the concentrator blades. A special Pitot-Static adaptor was used for measuring swirl velocity. Obviously measuring flow velocities like this should have been done with a Five Tube Pitot Pressure Probe, (see appendix F on methodology). The instrument would have taken a very long time to calibrate, therefore some sacrifice of accuracy was needed in order to do the experiment in the very limited time available. A separate Pitot-Static tube was also mounted in the wind tunnel, (not shown in figure 4.29), and used to measure wind tunnel air flow speed.

Experiments involving a wind turbine with the concentrator were conducted in the way indicated in figures 4.29 and 4.32. The turbine was placed at same point downstream of the concentrator as the Pitot-Static probe was during the diametrical wake scan, (ie $y/h = 1.2$). The axis of rotation of the rotor was on the same axis of symmetry as that of the concentrator. Different sizes of rotor were tested from 250mm to 320mm diameter. Measurement of torque was achieved by applying a rope brake to the shaft of the spinning rotor. Measuring shaft speed was achieved by flashing a stroboscope on the rotating turbine. With the measurement of torque, shaft speed and wind tunnel speed, the wind turbine characteristic of power coefficient C_p and tip speed ratio T_s could now be partly found. (Where the slope of torque over rotational speed becomes positive, no further readings could be taken using the rope break system.)

Photographs shown in figures 4.31 and 4.32 show the extent of the test facilities involved to test a wind tunnel CWT model under steady state flow conditions. These facilities had previously been built specifically for Ingo Rechenberg's Evolutionary Technique experiments. His modelling methods involved a 'Trial and Error' approach to designing the optimum CWT system. (The general principle of his Evolutionary Technique is covered in Rechenberg(1989)). What can be seen in front in the Open Jet Wind Tunnel is the equipment to allow different blade pitch settings and different outside to inside diameter settings for the concentrator arrangement.

4.4.2 Manufacture of the CWT.

In figure 4.30 shows how the blades were manufactured for the wind tunnel test work at the Technical University of Berlin. A wooden former was made out of laminates of block board, each of which had previousiy been carved out to the required blade profile and then glued together. (Alignment of each laminate was about an axis through the quarter chord position.) Once the wooden former had been made, blades were cut out of a large sheet of lead shown on the left in figure 4.30, and then pressed formed by hand over the wooden former. It was extremely important that every blade element

along the span was formed to the correct profile as shown in figure 4.29 with the correct distribution of chord along the blades. Manufacturing tolerances proved to be within $\pm 1°$, (since there was no twist along the blade span), and the chord distribution was within $\pm \%1$ of the maximum chord. All kinks were removed from the lead blades to prevent any flow abnormalities occurring over the blade surface. After this holes were drilled into the blade to allow it to be mounted on the wind tunnel test rig as shown in figure 4.31.

The mounting arrangement was crucial so that the correct blade angle was achieved relative to the horizon. Surface quality of the lead blades was kept in a smooth and polished condition throughout the tests, since the information given in figure 4.28 was derived from two dimensional flow test conditions with an aerofoil section of smooth and polished surface quality used. During the tests no change to the blade element profile was noticed which highlights the effectiveness of the lead material.

In figure 4.32 shows the final arrangement under test with a model aeroplane propeller mounted 1.2 internal concentrator radii downstream of the quarter chord position of the concentrator blades. No manufacturing was involved with the propeller since this was bought locally in Berlin at a model aeroplane shop. The propeller was mounted on the rig in the reverse way to what it had been designed. This allowed it to operate like a very inefficient wind turbine, since the rotor blades had originally been optimally designed for propeller duty only, with the rotor operating the other way round. This explains why the maximum C_p of the rotor without concentrator was only 0.177.

Figure 4.24 Field test site with wind concentrator and control wind turbine.

Figure 4.25 CWT under test with a WG910 wind turbine involved.

Figure 4.26 Flow visualization smoke equipment used in the field.

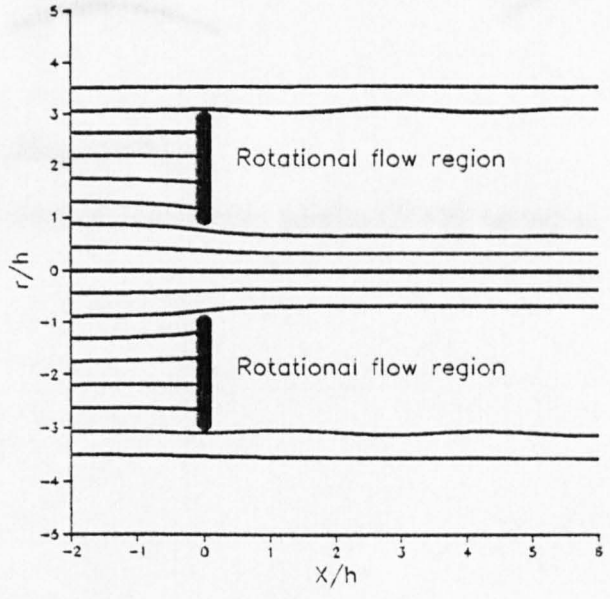

Figure 4.27 Theoretical streamline plot across a wind concentrator ($R/h = 2.92$).

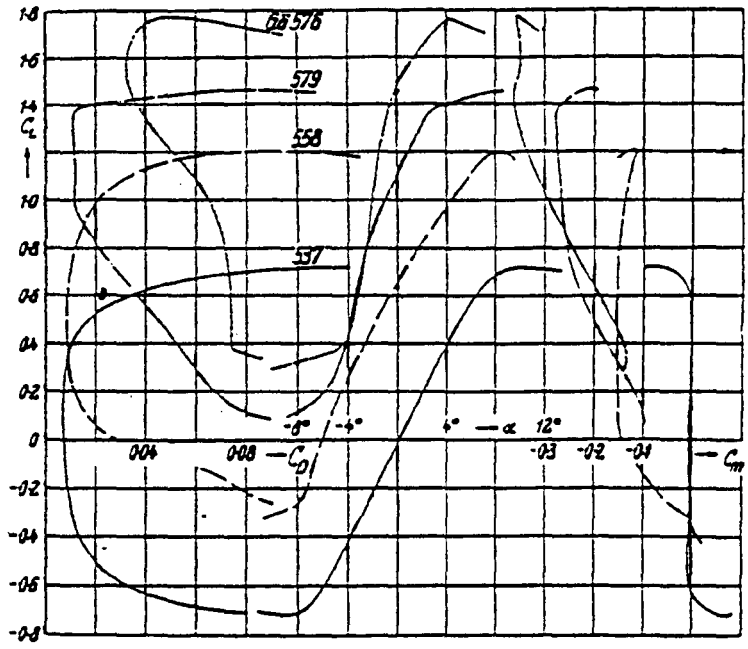

ASSUMED PROFILE

ACTUAL PROFILE

Source: reference Riegels(1961)

Figure 4.28 Polars of Joukowsky profile Gö576 tested at Reynolds Number $4.2.10^5$.

Blade Position	ϕ (degrees)	α (degrees)	CL
Inboard 0.0			
0.03	14.2	17.8	1.5*
0.08	22.3	9.7	1.65*
0.13	25.9	6.1	1.72
0.18	28	4	1.75
0.24	28.8	3.2	1.7
0.28	29	2.99	1.69
0.34	28.8	3.2	1.7
0.39	28.4	3.6	1.73
0.45	27.6	4.4	1.74
0.5	26.7	5.4	1.73
0.55	25.6	6.4	1.7
0.61	24.4	7.6	1.69*
0.66	23	8.9	1.67*
0.71	21.1	10.2	1.65*
0.76	20.5	11.5	1.63*
0.82	19.3	12.7	1.61*
0.87	18.3	13.7	1.59*
0.92	16	16	1.55*
0.97	7	25	1.4*
Outboard 1.0			

* = Estimated by linear interpolation.

Note: θ was constant along the span at 32°.

Table 4.2 Example results from the author's blade design model applied to the R/h=2.92 case.

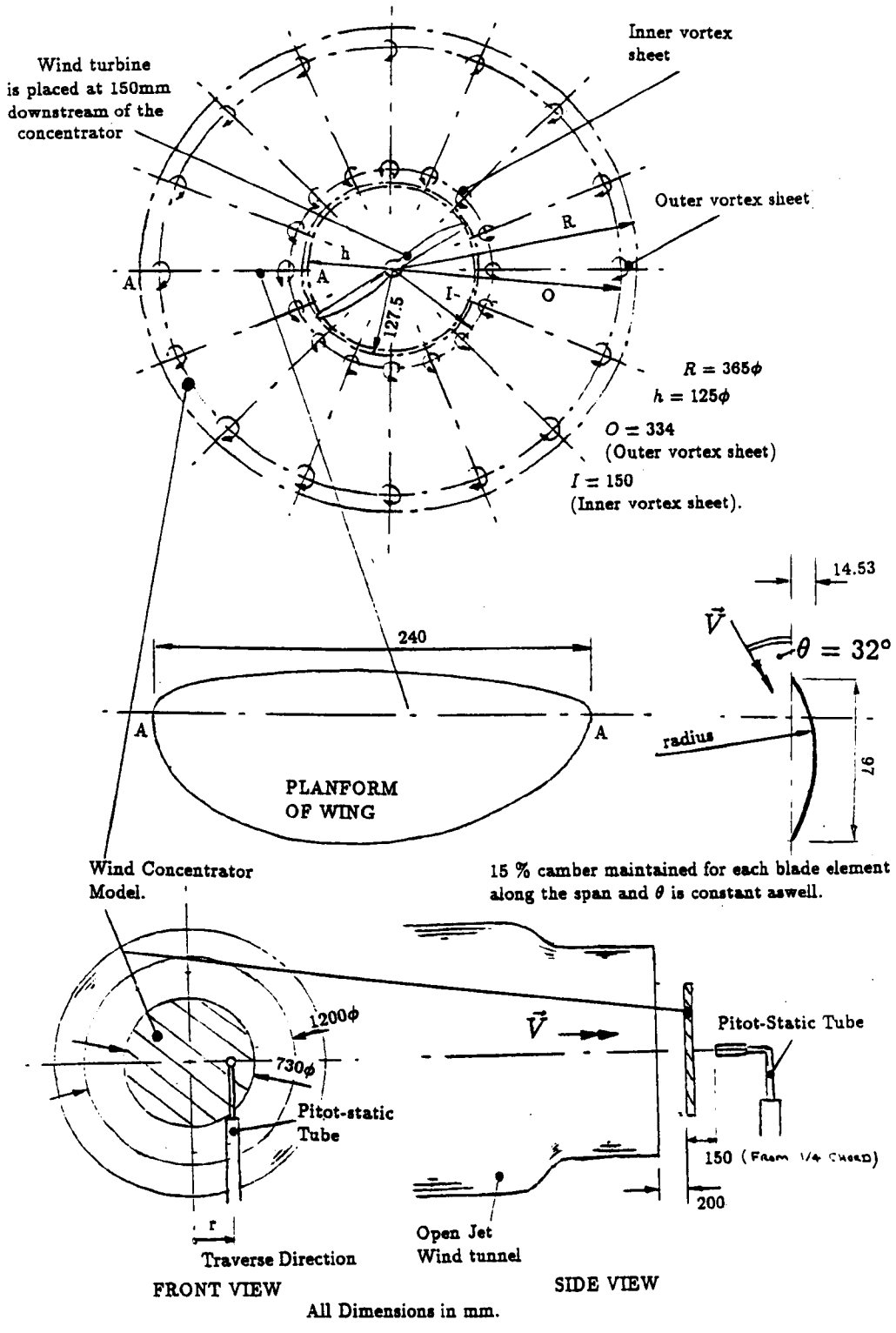

Figure 4.29 Experimental arrangement for testing author's CWT at Berlin.

Figure 4.30 Method of manufacture of the lead concentrator blades at the Technical University of Berlin.

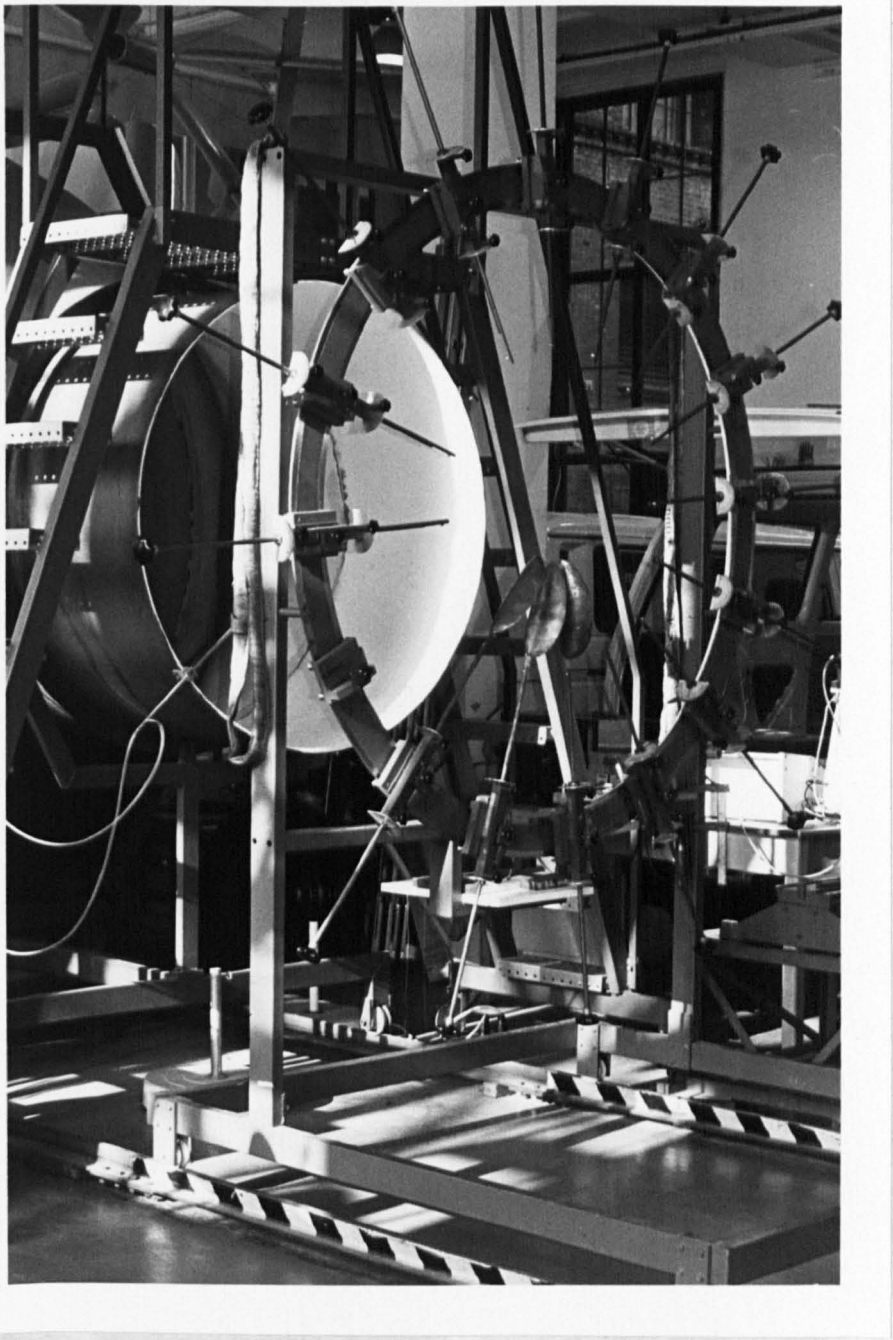

Figure 4.31 Equipment to test a CWT wind tunnel model at the Technical University of Berlin.

Figure 4.32 Author's design of CWT under test at Berlin.

Chapter 5

RESULTS.

5.1 Early wind tunnel tests.

The author's experimental wind tunnel results on the concentrator performance were initially sparse. The experimental data available was based on work done by the author at Queen Mary and Westfield College, London and the earlier work by Rechenberg(1984). (More compelling evidence of the effectiveness of the author's computer model is covered later, in section 5.4, based on further wind tunnel work conducted at the Technical University of Berlin). In all cases open jet wind tunnels were used. Figure 5.1 give results of the diametrical scans over the wake of the concentrator wind tunnel model tested at QMW. The turbulent wake effects of the inner structural ring show how it had some effect on the inner vortices, but the vortices persisted far enough down the wake to prove that inner structural ring had no significant effect on the V_{CF}. The initial reaction to the dissappointing results was to build instead a full size field test version to over come scale effects of the model. Ideally it would have been preferable to have improved the model and do more wind tunnel experiments. Fortunately time was found to improve the model while initial design studies were in progress. In table 5.1, the test data for V_{CF} from two different experiments are compared with various theoretical approaches at predicting V_{CF}. Each experiment involved a test model of different design, indicated by N, $\Gamma/(V(R-h))$ and R/h parameters. The position in the wake where the maximum V_{CF}

was found is indicated non-dimensionally by y/h and z/h.

It is noticed that blade element theory over-predicted the performance. This is due to the poor prediction of the helical vortex angle β in the wake, and the assumption that wake is cylindrical. The author's analytical model using Biot-Savart theory was more successful than Rechenberg's model. The assumptions of constant β angle along the wake, the wake being cylindrical and R/h being small, all contributed to poor accuracy. The Wake Relaxation model, being a purely numerical free wake model, offered the best agreement with experimental results for this simple parametric study.

The section 5.2 gives results from a field test machine designed with the Wake Relaxation model.

THEORETICAL MODELS	V_{CF}			
	1		2	
	Theory	Experiment	Theory	Experiment
Blade Element (Axial Momentum)	1.31	1.058	*	1.94
Biot-Savart (Analytical)	1.013		1.37	
Rechenberg (Analytical)	1.05		2.64	
Wake Relaxation (Numerical)	1.054		1.92	

Note different model tests :
Column 1; $y/h = 0.5$, $z/h = 0$, $R/h = 5.$, $N = 20$, $\Gamma/(V(R-h)) = 0.0469$ {Olivieri}
Column 2; $y/h = 2.0$, $z/h = 0$, $R/h = 5.545$, $N = 8$, $\Gamma/(V(R-h)) = 0.375$ {Rechenberg}

* Solution was not possible due to momentum theory breakdown.

Table 5.1 Comparison of performance predictions from different theories with experimental data.

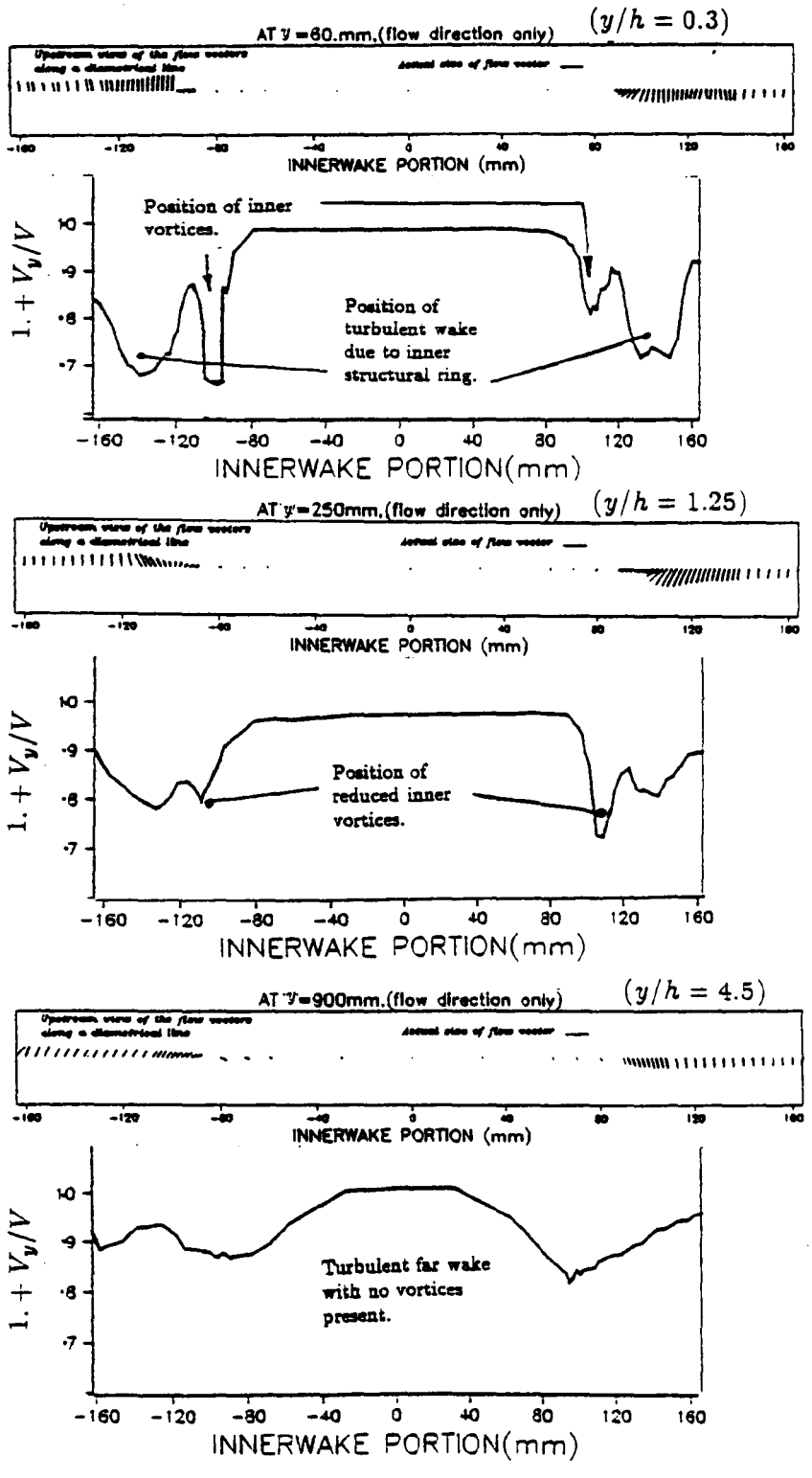

Figure 5.1 Results of diametrical wake scan of early Wind Concentrator.

5.2 Field test work at Gretton.

The results of the field tests for the fast monitoring at ten samples a second are given in figures 5.2 to 5.11. Figures 5.12 to 5.15 give the results for the long term runs taken over several weeks, with each reading taken at one minute average. (An explanation of these graphs was given in the previous chapter.)

Figure 5.16 shows the smoke generator working in the field, taken from a video run with just the wind concentrator working to provide flow visualization. The smoke generator seen in figure 5.16 was mounted on top of a long pole at the same height of the CWT. The smoke enabled flow visualization to reveal not only flow direction and vortices but also flow disturbances to a limited extent.

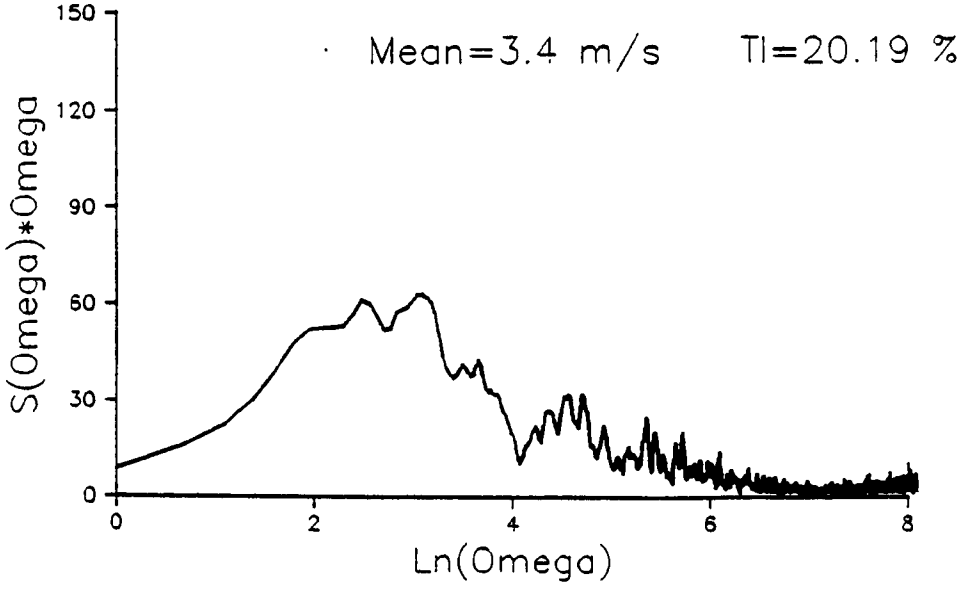

Figure 5.2 Spectral density function of V1 times ω_p against $\ln(\omega_p)$ for low wind speeds.

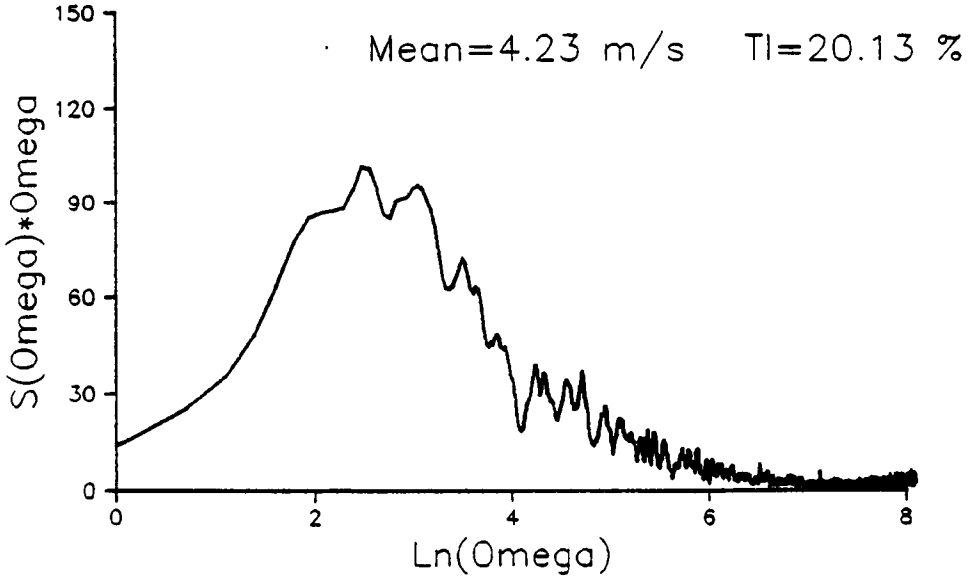

Figure 5.3 Spectral density function of V2 times ω_p against $\ln(\omega_p)$ for low wind speeds.

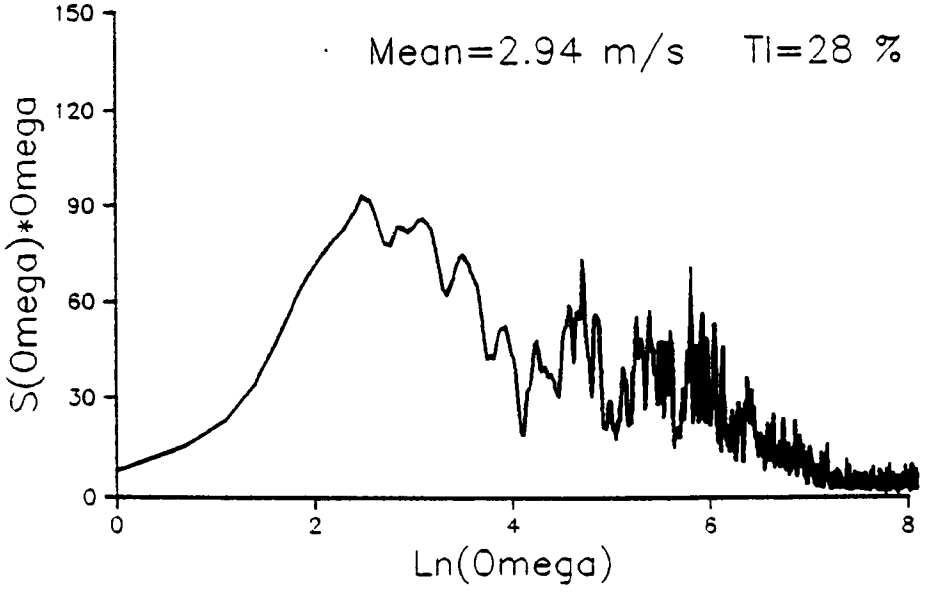

Figure 5.4 Spectral density function of V3 times ω_p against $\ln(\omega_p)$ for low wind speeds.

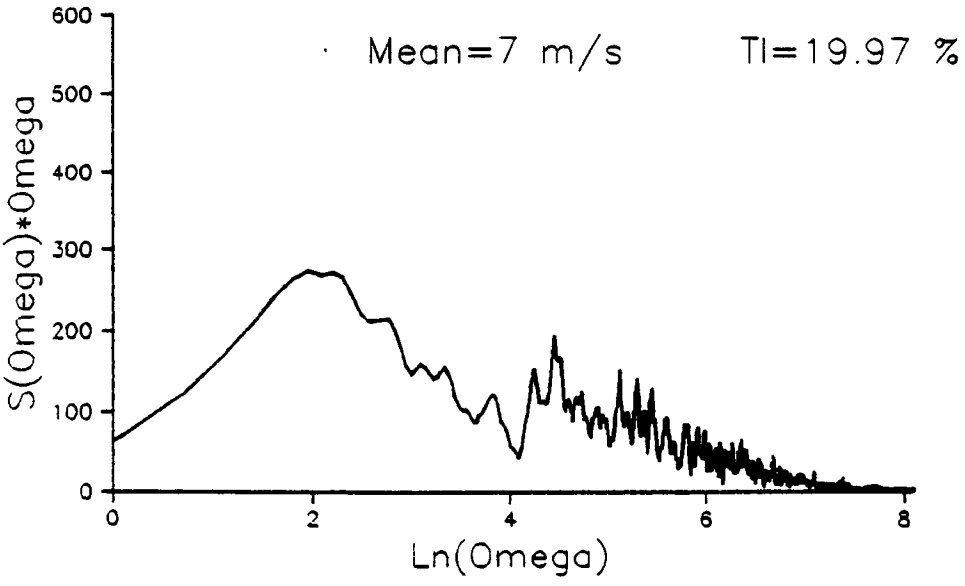

Figure 5.5 Spectral density function of V1 times ω_p against $\ln(\omega_p)$ for high wind speeds.

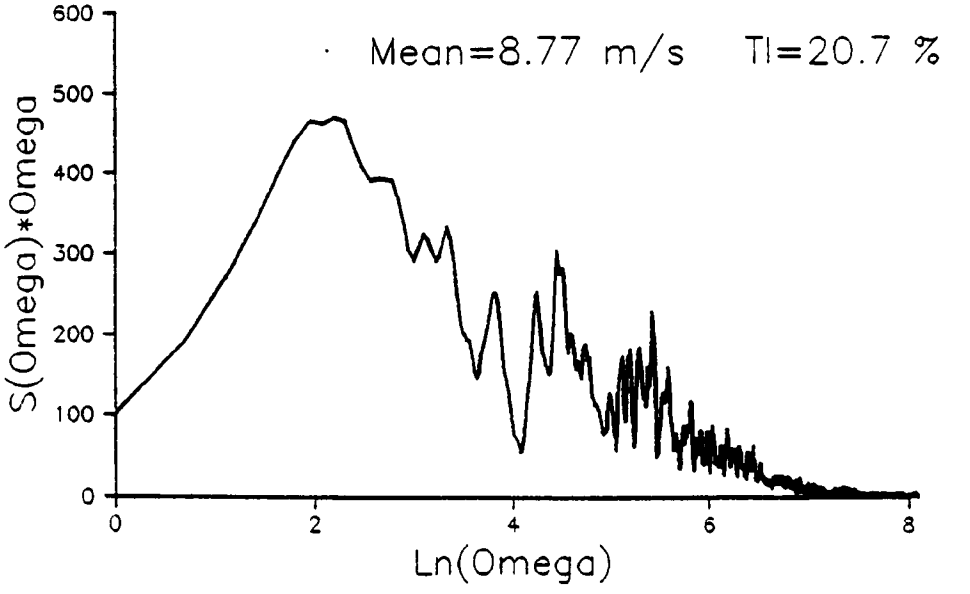

Figure 5.6 Spectral density function of V2 times ω_p against $\ln(\omega_p)$ for high wind speeds.

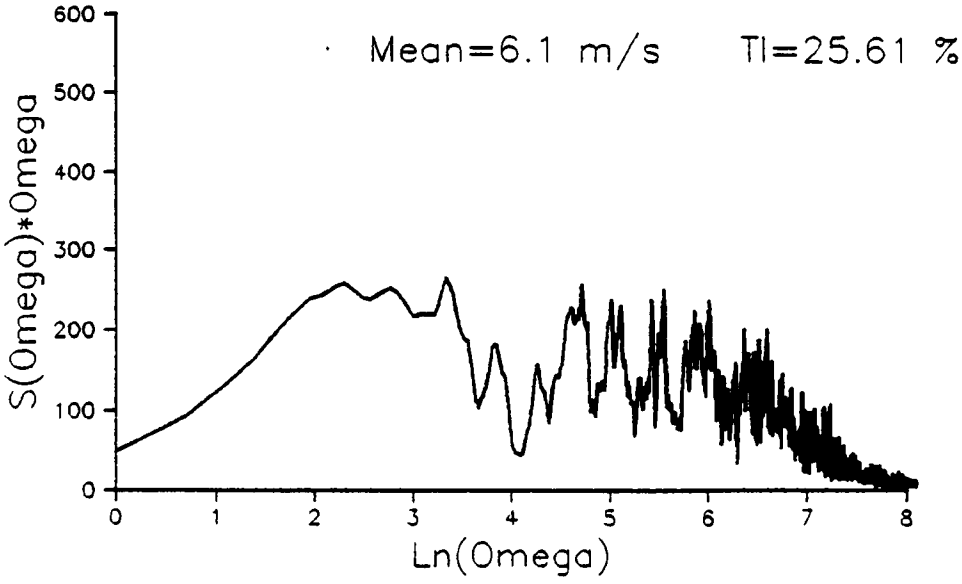

Figure 5.7 Spectral density function of V3 times ω_p against $\ln(\omega_p)$ for high wind speeds.

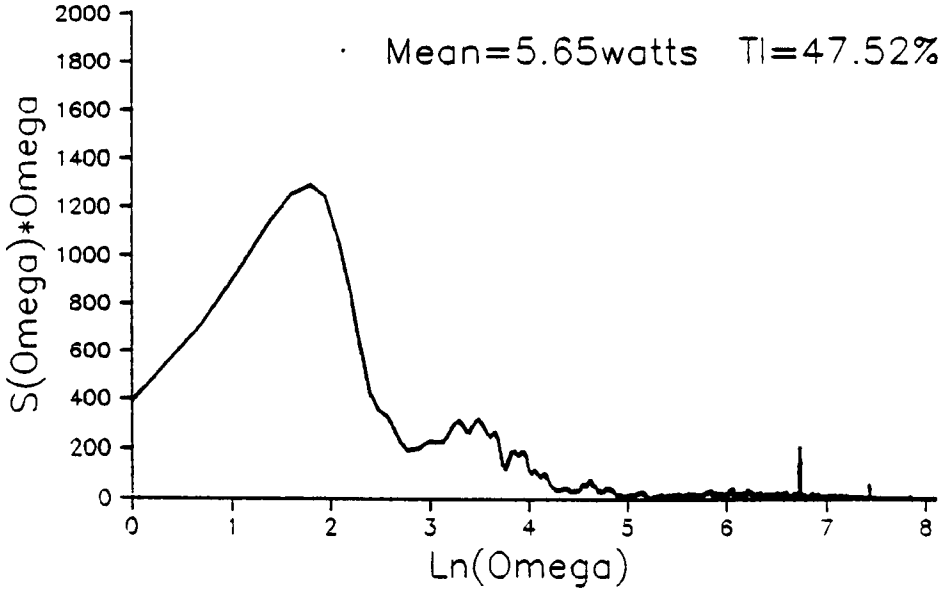

Figure 5.8 Spectral density function of P1 times ω_p against $\ln(\omega_p)$ for low wind speeds.

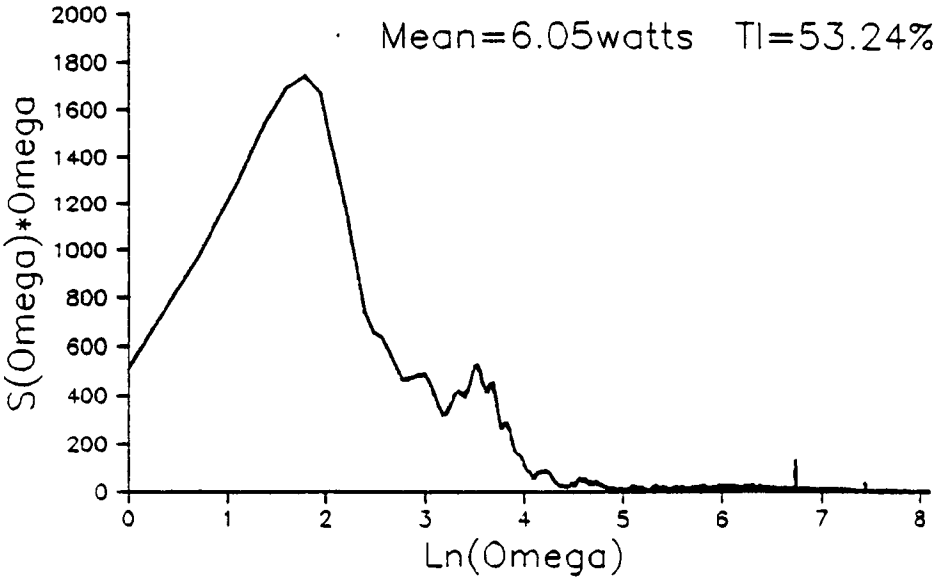

Figure 5.9 Spectral density function of P2 times ω_p against $\ln(\omega_p)$ for low wind speeds.

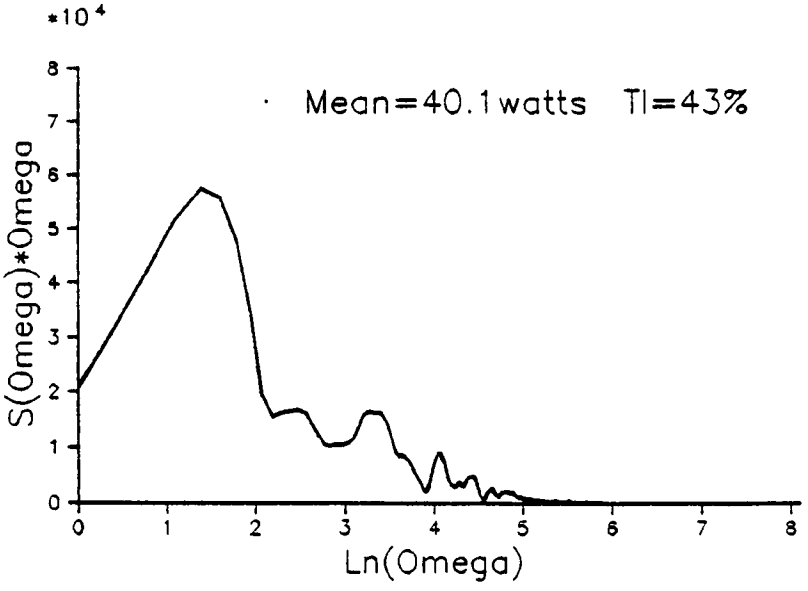

Figure 5.10 Spectral density function of P1 times ω_p against $\ln(\omega_p)$ for high wind speeds.

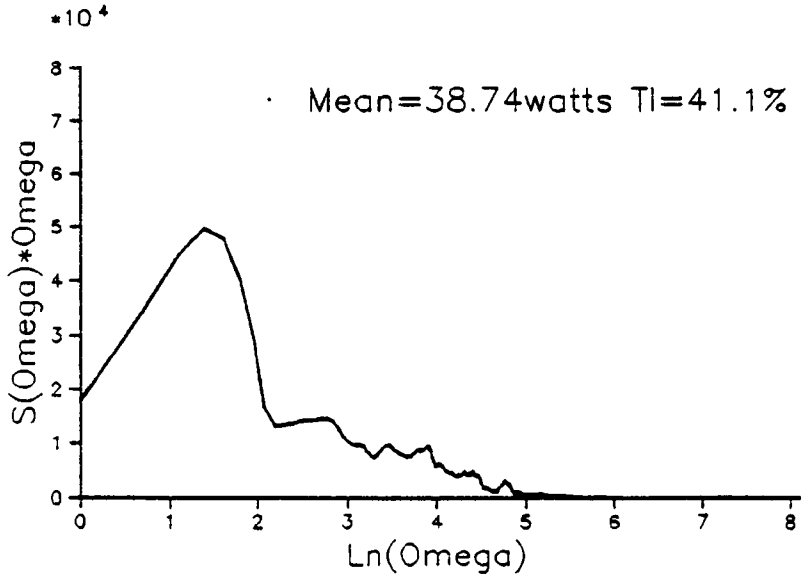

Figure 5.11 Spectral density function of P2 times ω_p against $\ln(\omega_p)$ for high wind speeds.

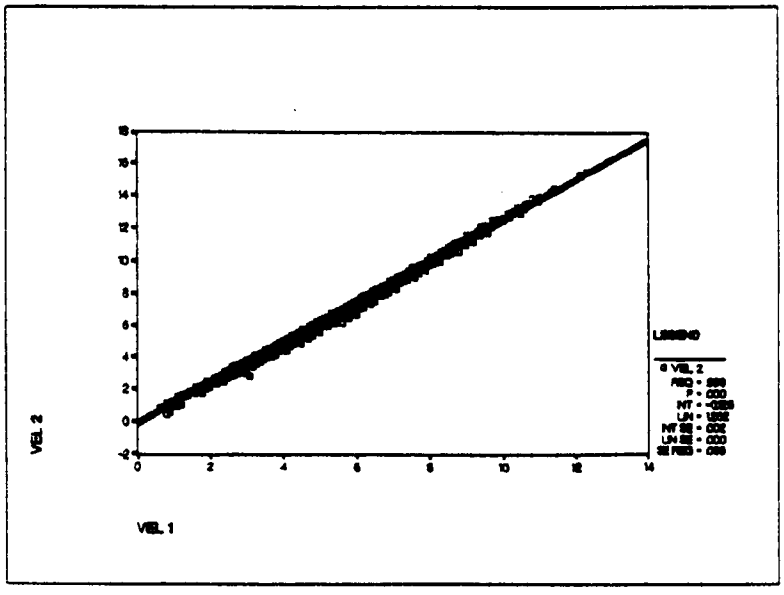

Figure 5.12 Correlation between wind velocity measuring points V2 and V1, both in m/s.

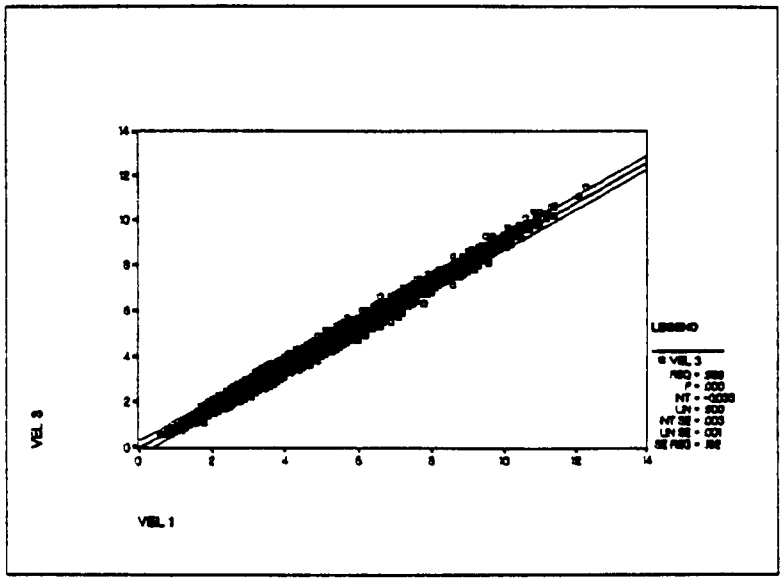

Figure 5.13 Correlation between wind velocity measuring points V3 and V1, both in m/s.

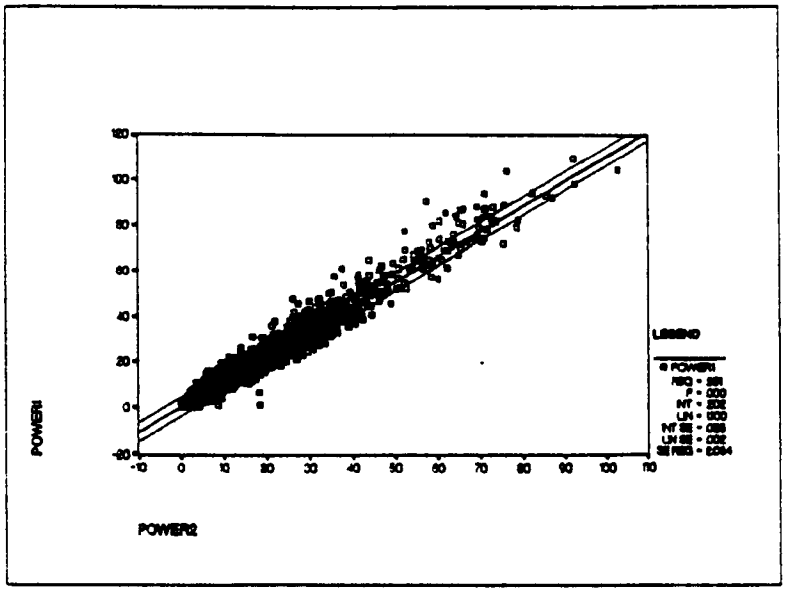

Figure 5.14 Correlation between power measuring points P1 and P2, both in watts.

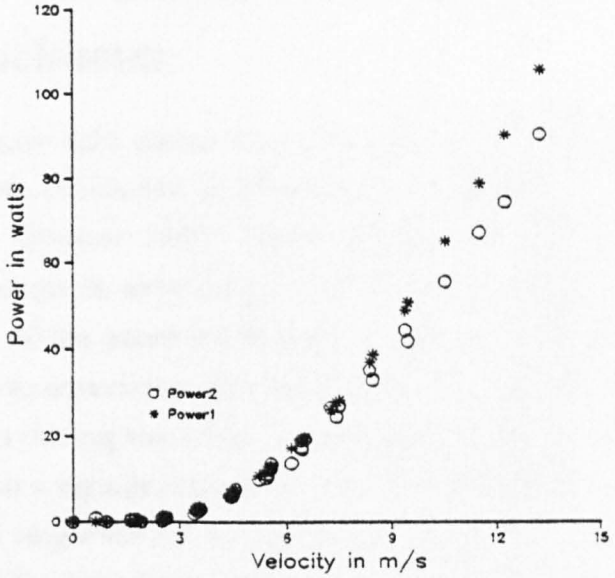

Figure 5.15 Binned results of power against wind velocity for the CWT (power1) and control turbine (power2).

Figure 5.16 Smoke equipment working at the field test site indicating inboard vortex tip development.

5.3 Flow visualization work at University of Manchester.

In chapter 4 figure 4.21 shows the tufts and paper cones used during the wind tunnel tests conducted at Goldstein Laboratory of the University of Manchester, in October 1990. Smoke equipment was provided but was not effective enough in showing up the vortex structure. Fortunately, the circular motion of the cones confirmed tip vortices, while the tufts showed no boundary layer separation over the blades. Tunnel air speed was between 5m/s and 10m/s during the tests. It was noticed that the inner tip vortices were conical with a significantly large semi-vertical angle. Vortices from the outer structural ring were not so noticeable since it was believed they would emerge as a vortex sheet from the trailing edge of the outer structural ring.

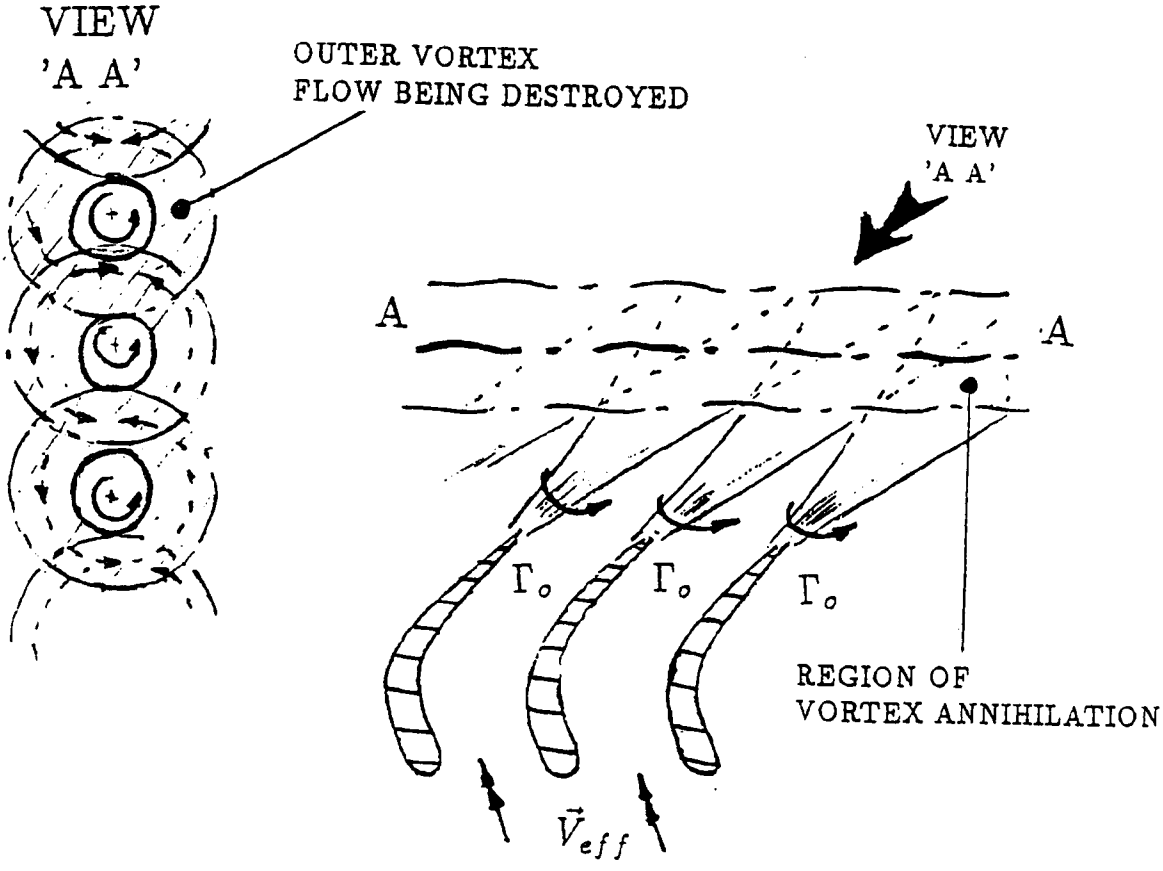

Figure 5.17 The effect of tip vortex interference on the wake.

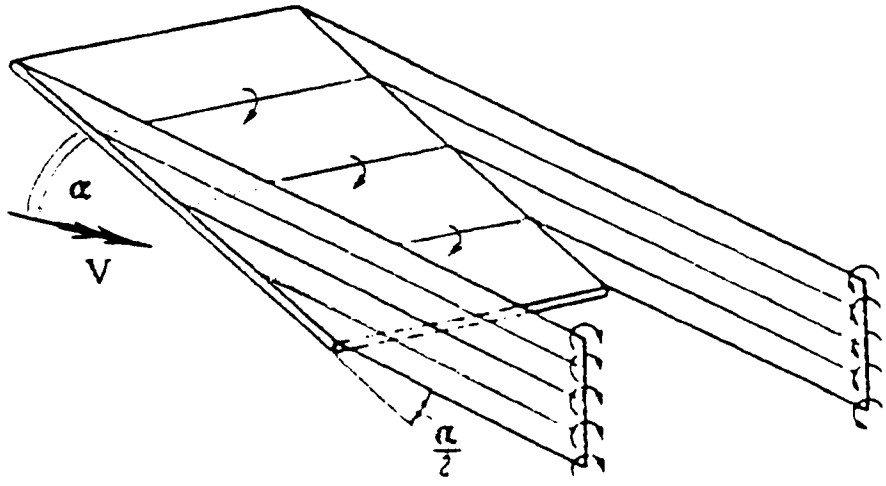

Figure 5.18 Vortex model of non-linear wing theory.

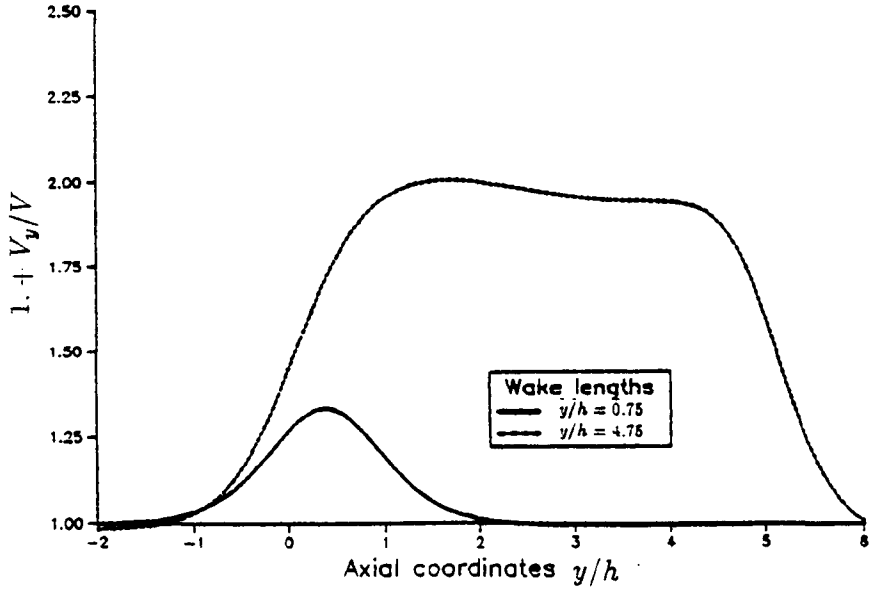

Figure 5.19 The effect of tip vortex interference on VCF.

5.4 Wind tunnel test work at the Technical University of Berlin

Figure 5.20 to 5.22 shows the results of the tests conducted at the Technical University of Berlin, using the test equipment and wind tunnel model whose design was covered in chapter 4. Figure 5.22 gives the results of the runs for the most effective rotor size of 255mm diameter. The wake of this rotor was smaller than the diameter of the inner concentrator vortex wake, (which had shown to be 300mm diameter from theory and test work, (see chapter 4, figure 4.29). This allowed the turbine to fully realize the increase in kinetic energy available at the core.

5.5 Discussion of results.

The very early design of wind concentrator proved to a have insufficient blade loading to offer any concentration effect. This is indicated in table 5.1 in column one and in figure 4.3 of chapter 4. It only served as a test for early theory development. Thanks to the results available at this early part of the project, shown in table 5.1, the correct course of action was taken in terms of improving the modelling. Unfortunately a lack of wind tunnel facilities and time prevented the author from fully verifying the Wake Relaxation method. One field test was not the best way of achieving this, and only at the very end of the project did the appropriate wind tunnel facilities become available.

Figures 5.2 to 5.7 indicate that no improvement was experienced in terms of wind turbulence filtering for the 54 bladed CWT design. The higher value of standard deviation caused by a higher mean wind speed at V2 (see figures 5.3 and 5.6) contributed to a larger area under the curve compared to V1. The turbulence intensity, however, was the same between V2 and V1. The frequency range at which most of the effect happened was around 0.09 Hz. Conditions at the rear of the concentrator were, as expected, more turbulent but at a lower mean wind speed. The information

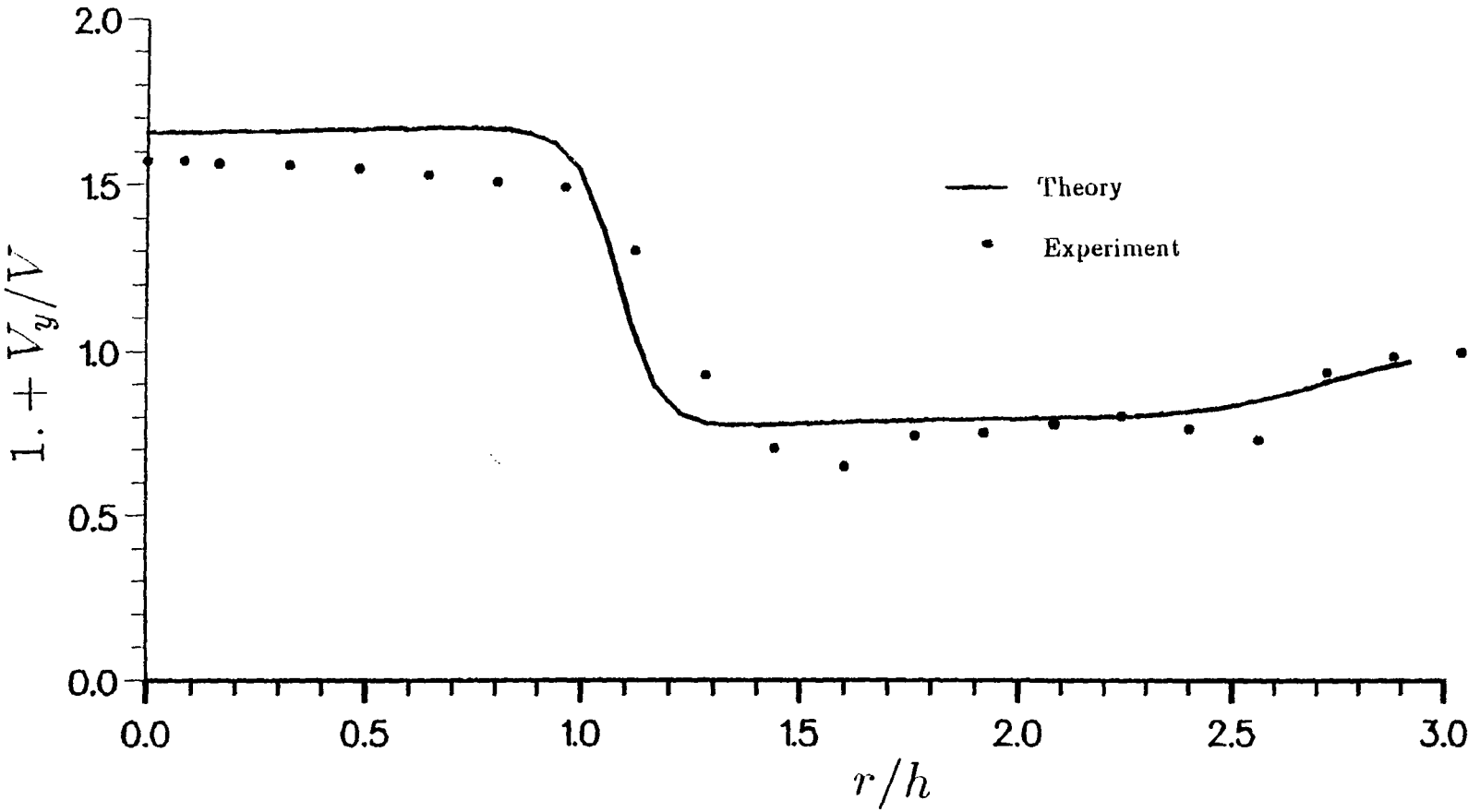

Figure 5.20 Distribution of axial induced velocity for $R/h = 2.92$.

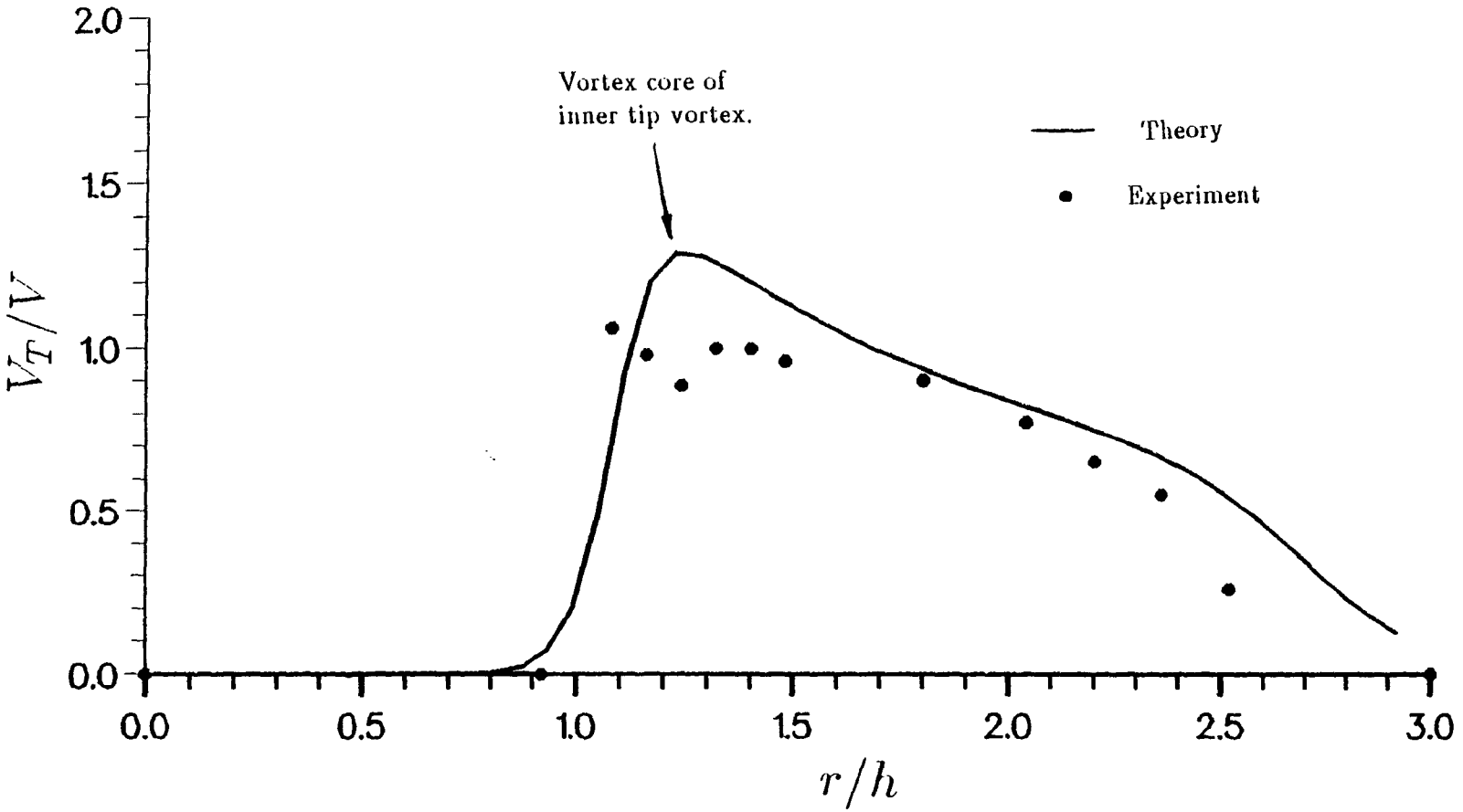

Figure 5.21 Distribution of induced swirl velocity for $R/h = 2.92$.

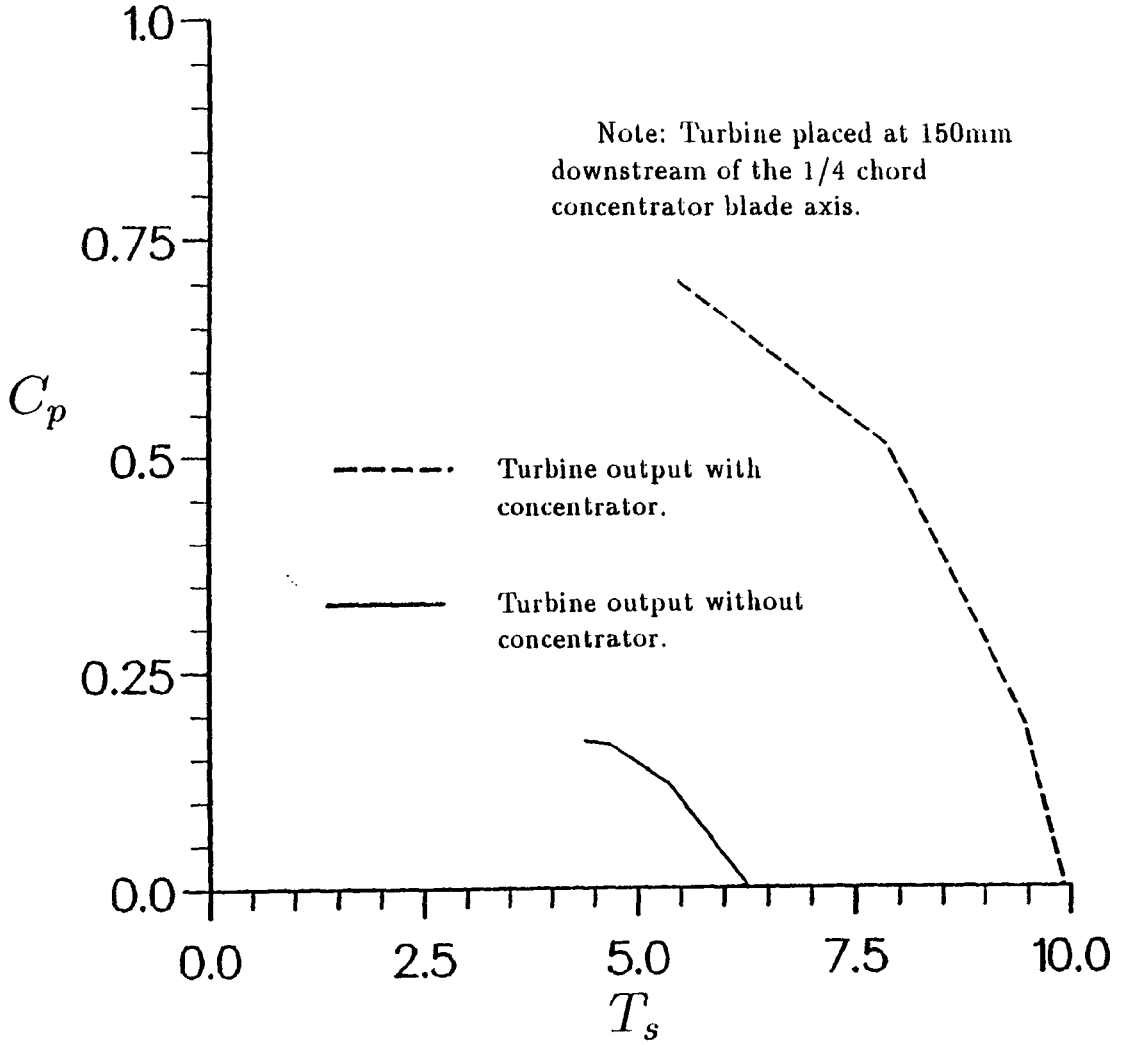

Figure 5.22 Comparitive power measurement of turbine with and without concentrator.

given here gives an idea of the life of the turbine, since it is a function of frequency response and standard deviation.

The effect this has on the generator output can be seen in figures 5.8 to 5.11. The spectral density function of power output from the CWT indicated as Power 1 or P1 is considerably more unsteady in its signal compared to the wind variation, but the frequency range at which most of the effect happened was around 0.01 Hz. The cause of this is due to the inertia of generator and the rotor combined with the large variation in tip speed ratio. The spectral density function of power output from the control wind turbine is shown in figures 5.9 and 5.11 as P2 for low and high wind cases. The TI for P1 and P2 indicate that the power variation from the CWT, (P1), and that from the control turbine, (P2), had little if any difference. This would indicate that the 54 bladed CWT shows no capability to filter power variations. The above results of TI for the wind concentrator alone indicates a similar results as well.

The long term logging at one minute averaging for the data is shown in figures 5.12, 5.13, 5.14 and 5.15. From figure 5.12 gives the velocity increase along the centre line between upstream V1 and concentrator core V2, and an increase of 26% was noticed. (The parameter 'LIN' under the legend gives the slope of the graph for the linear regression analysis). For V3 however the flow velocity was 10% less compared to V1. (See figure 5.13). Only a 10% improvement in power was noticed when the turbine P1 was placed at the position of the anemometer V2, which was one internal radius downstream of the concentrator, compared to the power output of the control turbine P2. Figures 5.12, 5.13 and 5.14 all show good linearity.

Figure 5.16 shows an attempt to assess the flow over the machine. The illustration was obtained from video recordings. The figure shows vortex tip development in the inboard region of the concentrator blade. It initially emerges as a sheet which appears to roll up downstream as the entire vortex helically moves away from the concentrator.

Section 5.3 covers the wind tunnel test work that was briefly done by

the author at Goldstein Aeronautical Engineering Research Laboratory. It would appear from the flow visualization work that the tip vortices do not last beyond one internal radius downstream of the concentrator. The main cause of this is that the tip vortices roll up in a conical fashion about the centre of vorticity initially, but later interfere with other neighbouring vortices. At this point the vortices effectively cancel out causing the wake vortices be truncated. (See figure 5.17). From Schlichting *et al*(1979) and figure 5.18 the reason why the vortices of low aspect wings are highly conical can be deduced. The low aspect ratio of the concentrator blades cause vortex shedding along the blade chord which are out of the plane of the blade chord, rather than in the plane of the blade chord which is the case for high aspect ratio blades. The author also designed the blades with elliptic loading rather than rectangular loading since it was felt that an elliptic loading was more realistic. The actual loading distribution would have been different from that intended, because the blade elements between the structural ring and the mid span were different from that previously designed. This serious compromise to the original design was necessary to give the blade structural support. The Aspect Ratio of the blade was near unity which made the use of Lifting Line Theory doubtful. Unfortunately this all contributed to poor performance, but it is still unknown how much the unsteady aerodynamics of the field contributed to the reduction the CWT performance, since no Open Jet Wind Tunnel tests were performed on the 54 bladed CWT due to a lack of resources.

Figure 5.19 shows the effect of wake truncation on V_{CF}. The wake was assumed to be 4.75 internal radii long for the concentrator design work. At one internal radius downstream, the V_{CF} should have been 2.0. With a wake of 75% of the internal radius long, this reduces the V_{CF} to about 1.2 which is near to the experimental value measured in the field. From the wind tunnel tests no serious turbulent activity was notice over the blades by observing the tufts. Therefore it can assumed that no serious blade stall had taken place during the tests.

The effect of the rotor on the concentrator flow field had not been

investigated with smoke in the field nor was it tested in the wind tunnel at Manchester. (Unfortunately there was insufficient time to any further tests). Premature truncation of the wake gave only a 26% improvement in the flow at the point where the turbine was to operate. This should have given the CWT turbine P1 double the output of the control P2 under perfect conditions, whereby the concentrator and rotor would have fine cylindrical vortices in their wake systems, and the far wake would have had little interaction with the concentrator wake near the concentrator disc and the rotor wake near the rotor disc.

Experiments conducted in February 1991 at the Technical University of Berlin on a 16 bladed CWT (see figures 5.20 to 5.22), show clear evidence of the principle of wind concentration under steady state conditions. The ease of model manufacture and the extent of the test facilities available allowed the author to design a wind tunnel model which could easily test the theory. To build full size such a machine using a WG910 for the wind turbine would have been a much greater structural design undertaking than that earlier tried with the 54 bladed CWT, (see chapter 4, figures 4.16, 4.24 and 4.25).

The 16 bladed CWT which was tested rigorously at Technical University of Berlin had concentrator blades with an Aspect Ratio of 3.2:1. The blades were not twisted but had variable chord instead which proved to be easier to manufacture accurately. The result was a CWT design more compliant with Lifting Line Theory. What was surprising was how close the distribution of induced velocity was compared to the theory (see figures 5.20 and 5.21). The effect of loss of camber due to flow curvature across the concentrator disc appears to have negligible significance in this instance, but as a safe guard for future design work the author recommends the use Vortice Lattice Methods to model lifting surface effects for very heavily loaded blades.

Other tests conducted at Berlin were with different sized wind turbines. These were tested with and without the concentrator to comparatively show up any increase in power. In chapter 4, figure 4.27 gives a theoretical streamline plot for the particular 16 bladed wind tunnel model. The slight

inner wake contraction of the inner wake downstream of the concentrator did not impose too great a problem for the turbines tested. Turbines of different sizes were used to explore the possibility having a turbine with a swept area larger than the cross sectional area of inner wake. It was finally noticed that the best turbine size was 85% of inner vortex wake diameter. If the rotor diameter is increased beyond this and approaches that of the inner wake the C_R starts to decrease significantly. This was a very important observation and explains why the field tests on the 54 bladed CWT had a C_R of near unity. As explained above the inner tip vortices were very conical on the 54 bladed concentrator with a significantly large semi-vertical angle, while the vortices from the 16 bladed machine properly rolled up into small vortex filaments and therefore were more stable and persistent downstream. This made the vortices from the 54 bladed concentrator large in diameter enough to effect the wind turbine. The turbine became effectively too close to the thick inner vortex sheet which meant that the Marlec WG910 rotor tips were working actually in the region of the inner vortex sheet. (See figure 5.23). Therefore it is strongly recommended that correct blade loading be used for the concentrator, and that the blade design be of high Aspect Ratio with variable chord distribution to ensure that the tip vortices form into small vortex filaments. The rotor size must also be sufficient less than the diameter of the inner vortex sheet for the rotor to realize the full power concentration effect at the core.

It was interesting to notice that the optimum size of rotor gave a Concentration Ratio (C_R) that was slightly more than that expected theoretically, based on the cube of the average axial air flow velocity through the inner cylindrical vortex sheet for a particular position downstream of the concentrator. The C_R from the concentrator was shown to be 3.954 from the results given in figure 5.22. Therefore the influence of the concentrator was to upgrade the rotor $(C_P)_{max}$ from 0.177 to 0.7. It may also be noticed that the tip speed ratio at runaway conditions, (ie maximum rotational at zero power), was increased by the same value of velocity increase through the concentrator core.

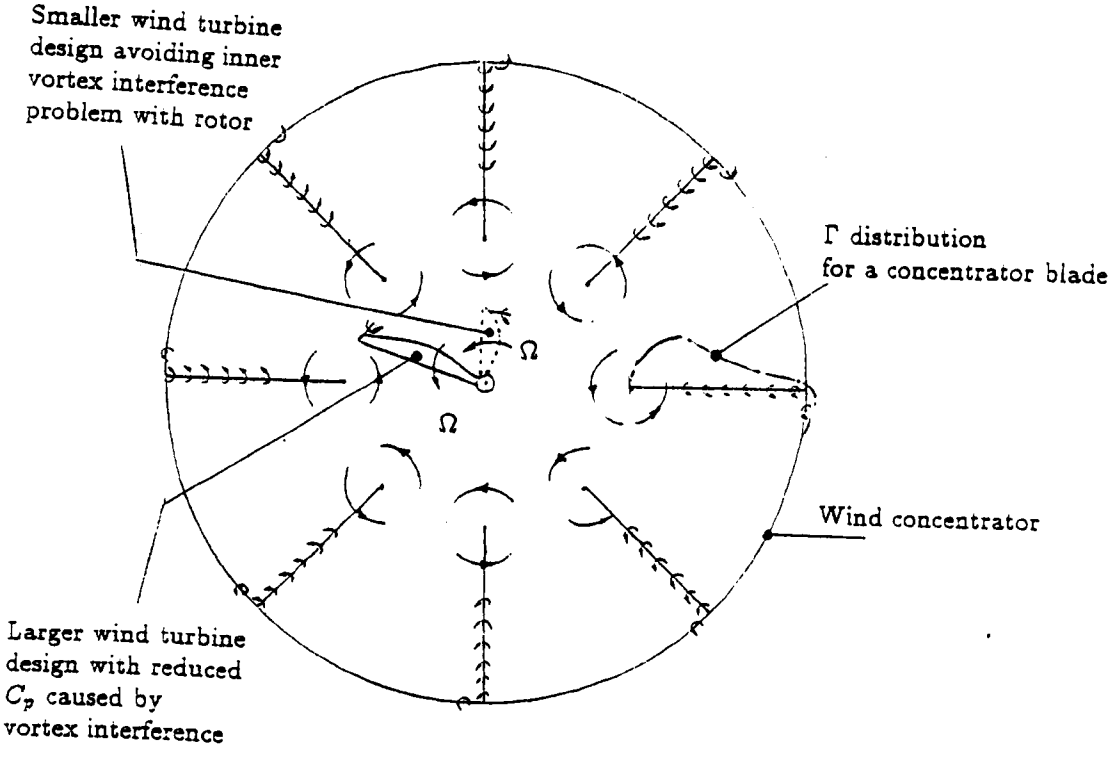

Figure 5.23 Effects of inner tip vortices on the performance of the wind turbine.

Chapter 6

CONCLUSIONS.

The following conclusions can be drawn from this thesis:

1. The principle of the Concentrator Wind Turbine (CWT) clearly works.

2. The Wake Relaxation model is capable of designing a concentrator with elliptical blade loading very accurately.

3. The size of the concentrator elliptic blade loading, the size of the rotor in relation to the size of the concentrator inner vortex cylindrical sheet, the number of concentrator blades and R/h ratio all have an enormous influence on the performance of the CWT.

4. It would appear from the computer modelling studies that the construction volume for the concentrator blades to achieve the desired concentration effect reduces as the blade loading increases, for a specified number of concentrator blades and R/h ratio.

5. The power concentration effect on a wind turbine working at the concentrator core equals the cube of the air flow increase at the core, as long the rotor diameter does not exceed 85 % of the inner concentrator vortex sheet diameter.

6. A CWT can be designed to yaw in the wind sucessfully as long as the tail fin is not in the way of concentrator slipstream.

At the moment there is no evidence to show that the CWT can exceed the Betz limit based on total frontal area, and that the concentrator can filter turbulence at the core flow of the CWT when working in free air conditions. Further research is needed to fully investigate these topics before a general conclusion can be made.

Chapter 7

FUTURE.

If further research is to be carried out on the CWT concept the following areas will need to be considered to continue what has been achieved so far;

1. CWT analytical modelling.
2. CWT numerical wake modelling.
3. Wind tunnel test work to develop CWT modelling and improve on the current method of CWT nacelle mounting on the tower.
4. Tip Winglets as a possible method of improving concentrator performance.

7.1 CWT Analytical Modelling.

So far attention has been given to the concentrator itself, but in order for the wind turbine to work effectively it must be properly matched with the concentrator. This means that a method of modelling the interactive nature of both the wind turbine and the concentrator wakes must be used.

In figures 7.1 and 7.2 the method of modelling is shown. It is noticed that the rotor wake is represented in the same way as the concentrator was with similar assumptions of constant β_{rotor} downstream from the rotor disc and evaluated at the disc from the contributions of induced swirl and axial velocities. Also the wakes are assumed cylindrical for both rotor and concentrator.

In figure 7.1 the swept annular area generated between the rotor tip and hub of the rotating wind turbine can be approximately represented by a strip of vorticity, reflected about the XY plane. (This was similarly done with the fixed array of concentrator blades in figure 3.2, chapter 3). At P_2 the total influence of both concentrator and wind turbine wake systems is considered. In figure 7.2 a similar situation is considered with the cylindrical component of trailing vortices of both concentrator and wind turbine wake systems.

Now to investigate the CWT parametrically the following parameters must be specified; $\Gamma/[(R-h)V]$, N, R/h, r_R/h, y_R/h, B and Γ_R. Now since the wake will be cylindrical the size of the rotor will be limited by the restraint $r_R/h \leq 1$.

The helical vortex angle for the rotor tip vortices will be β_{rotor}, and vortex sheets γ_{rotor} and $\gamma_{r\acute{o}tor}$ will be governed by the following relationships

$$\tan\beta_{rotor} = \frac{(V_T)_{rotor} + T_s V}{(V_y)_{rotor} + V_c} \tag{7.1}$$

$$\gamma_{rotor} = B\Gamma_R/(2\pi r_R)\tan\beta_{rotor} \tag{7.2}$$

$$\acute{\gamma}_{rotor} = B\Gamma_R/(\pi r_R) \tag{7.3}$$

$$\gamma''_{rotor} = B\Gamma_R \cos\beta_{rotor}/(2\pi r_{hub}) \tag{7.4}$$

$$\begin{aligned}(V_T)_{rotor} &= \frac{\gamma''_{rotor} r_{hub}}{r} \quad \text{for} \quad r_{hub} < r < r_R \\ &= \frac{\gamma''_{rotor} r_{hub}}{2r} \quad \text{for} \quad r = r_{hub} \quad \text{and} \quad r = r_R \\ &= 0 \quad \text{for} \quad 0 < r < r_{hub} \\ &\qquad\qquad \text{and} \quad r > r_R\end{aligned} \tag{7.5}$$

Now $(V_y)_{rotor}$ is the induced velocity due to the wind turbine vortex wake, with the induced velocities from the rotor hub vortex sheet neglected, and is expressed mathematically as

$$(V_y)_{rotor} = -\int_0^\infty \frac{\gamma_{rotor}\sin\acute{\theta}_{11}dy}{2\pi\acute{r}_{11}} - \int_0^\infty \frac{\gamma_{rotor}\sin\acute{\theta}_{22}dy}{2\pi\acute{r}_{22}} \tag{7.6}$$

and would have a solution similar to that given in appendix E. There

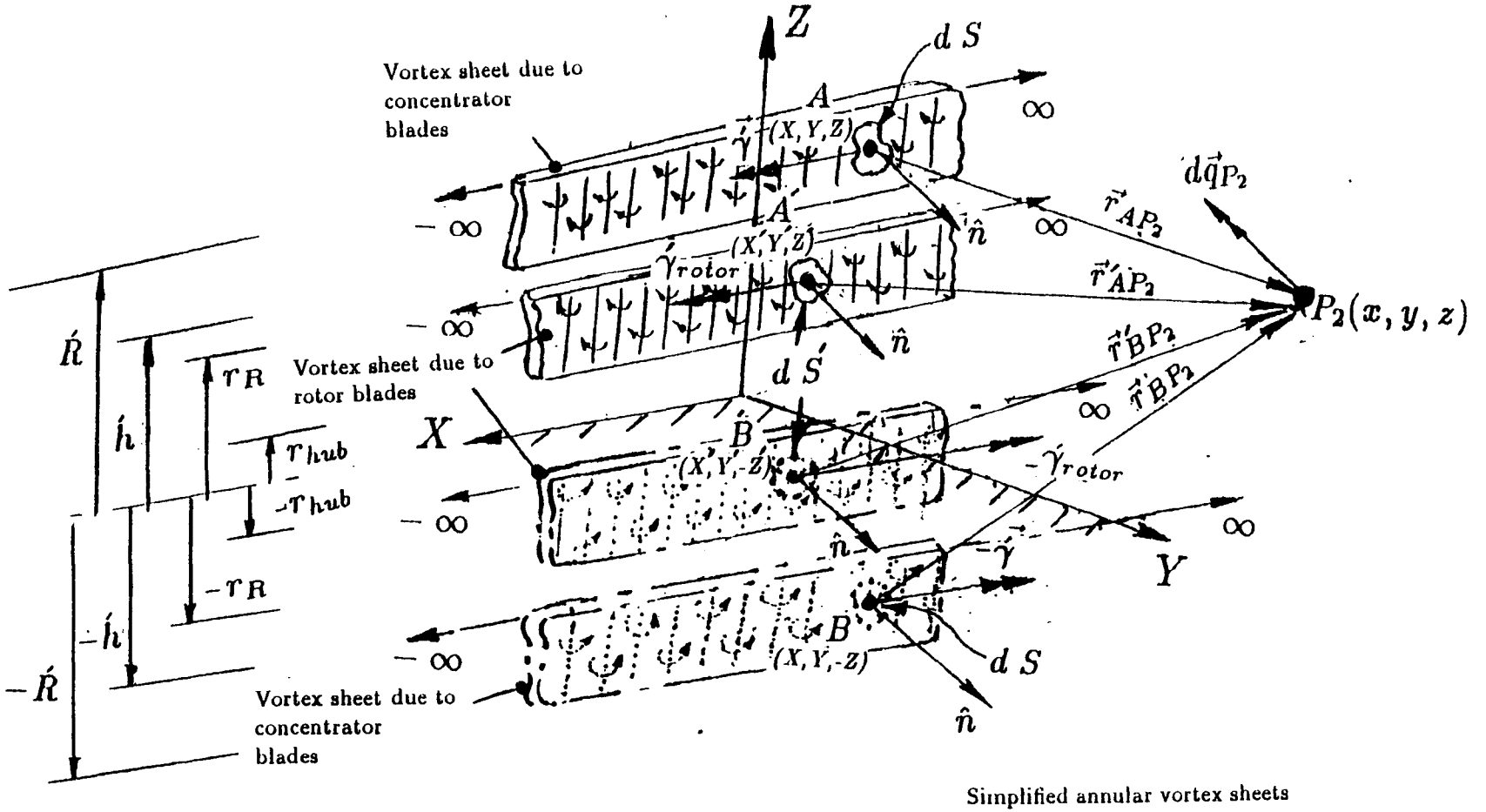

Figure 7.1 Analytical method for CWT model (part1)

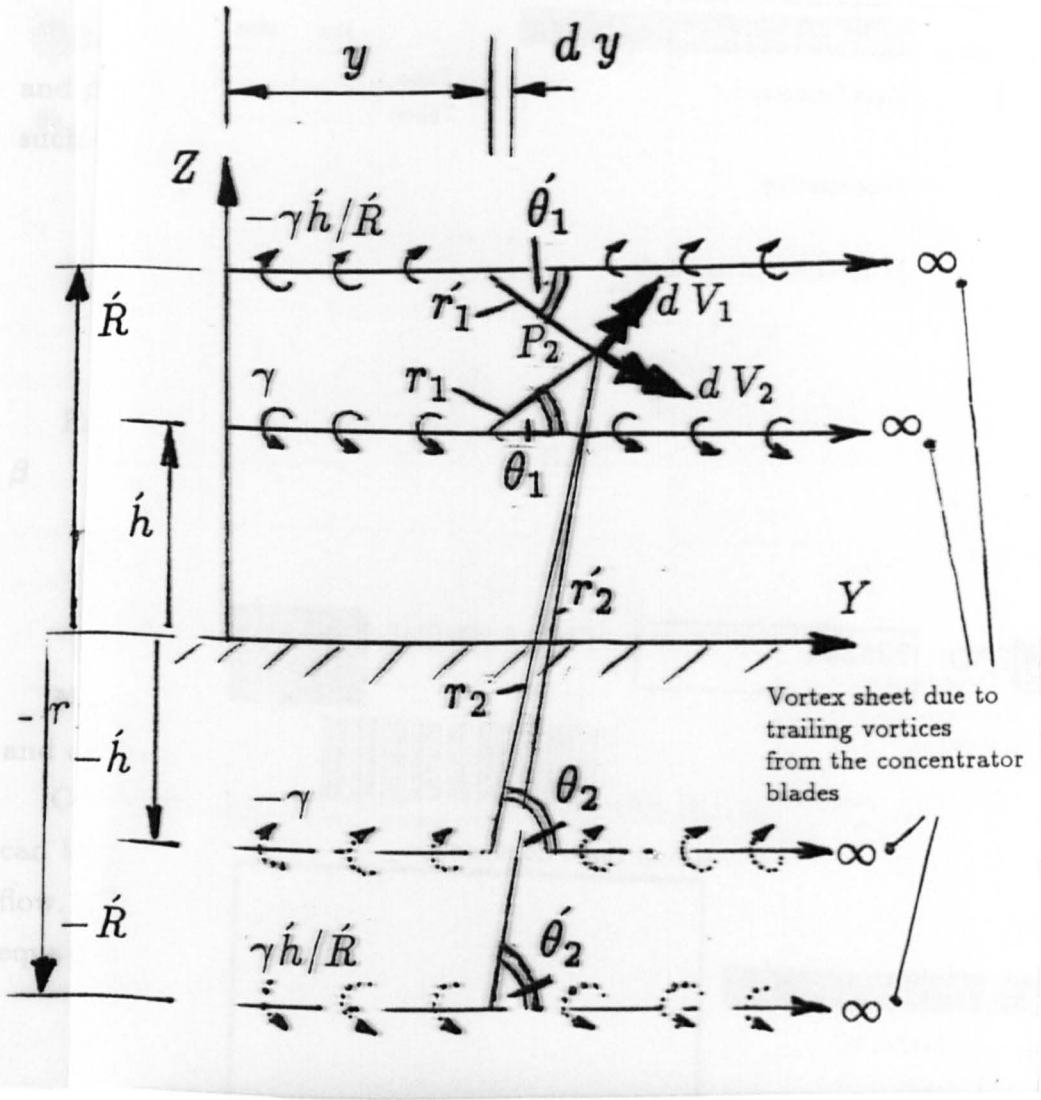
y
dy
Z
$-\gamma\acute{h}/\acute{R}$
$\acute{\theta}_1$
∞
$\acute{R}$
$\acute{r}_1$
P_2
dV_1
dV_2
γ
r_1
θ_1
$\acute{h}$
$\acute{r}_2$
Y
r_2
Vortex sheet due to trailing vortices from the concentrator blades
$-r$
$-\acute{h}$
θ_2
$-\gamma$
$-\acute{R}$
$\gamma\acute{h}/\acute{R}$
$\acute{\theta}_2$

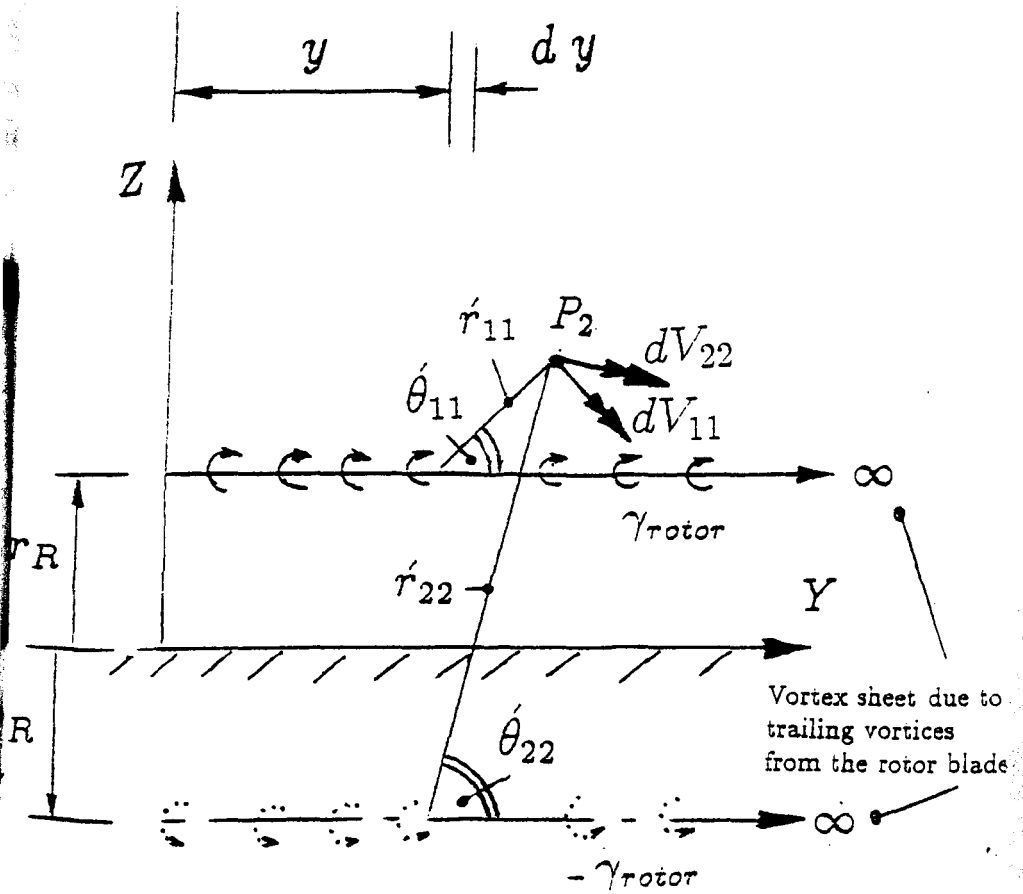

Figure 7.2 Analytical method for CWT model (part2)

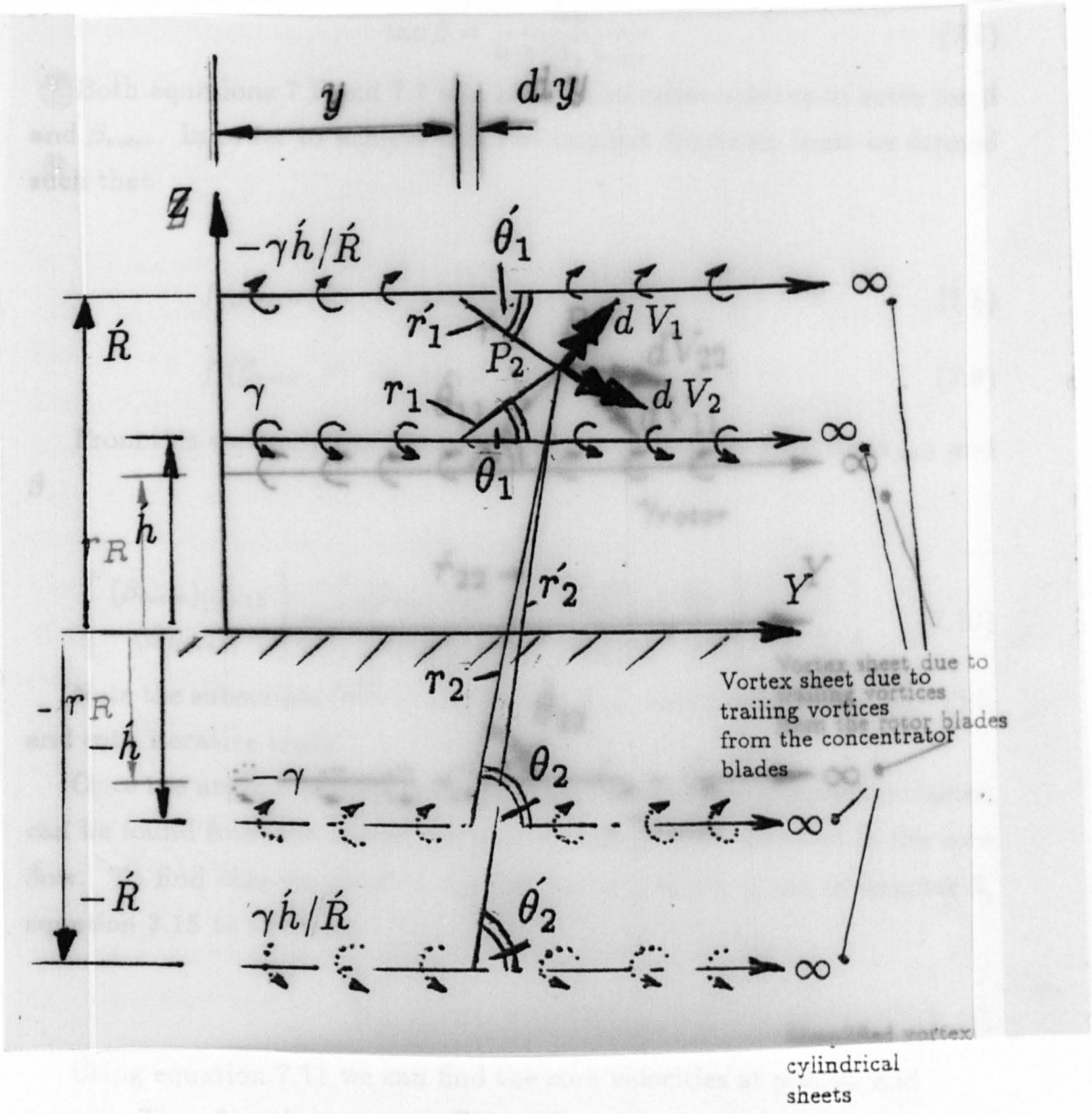

Figure 7.2 Analytical method for CWT model (part2)

will also be changes to the concentrator helical vortex angles as well which means that equation 3.1 will now become

$$\tan\beta = \frac{V_T}{u + (V_y)_{rotor}} \tag{7.7}$$

Both equations 7.1 and 7.7 will need an iterative scheme to solve for β and β_{rotor}. In order to achieve this two implicit functions must be formed such that

$$f_1(\beta_{rotor}, \beta) = \tan\beta_{rotor} - \frac{(V_T)_{rotor} + T_s V}{(V_y)_{rotor} + V_c} = 0 \tag{7.8}$$

$$f_2(\beta_{rotor}, \beta) = \tan\beta - \frac{V_T}{u + (V_y)_{rotor}} = 0 \tag{7.9}$$

From this we apply the Newton-Raphson method to solve for β_{rotor} and β

$$\begin{bmatrix} (\beta_{rotor})_{(m+1)} \\ (\beta)_{(m+1)} \end{bmatrix} = \begin{bmatrix} (\beta_{rotor})_{(m)} \\ (\beta)_{(m)} \end{bmatrix} - \begin{bmatrix} \frac{\partial f_1}{\partial \beta_{rotor}} & \frac{\partial f_1}{\partial \beta} \\ \frac{\partial f_2}{\partial \beta_{rotor}} & \frac{\partial f_2}{\partial \beta} \end{bmatrix}^{-1} \begin{bmatrix} f_1 \\ f_2 \end{bmatrix} \tag{7.10}$$

Note the subscripts $(m+1)$ and (m) on β_{rotor} and β refer to the $(m+1)$th and mth iterative trails.

Once the angle β and β_{rotor} are known an estimation of power extracted can be found from the loss of the rate of change of momentum in the core flow. To find this we need to modify the expression given in chapter 3, equation 3.15 to the form

$$V_{crr} = V + V_y + (V_y)_{rotor} \tag{7.11}$$

Using equation 7.11 we can find the core velocities at $y = y_R$ and $y \to \infty$. Therefore the power coefficient C_p can be found from the following expression

$$\begin{aligned} C_p &= CD_{rotor} V_{cr1}/V \\ &= \left((\frac{u_1}{V})^2 + (\frac{V_T}{V})^2 - (\frac{V_{cr}}{V})^2 \right) \frac{V_{cr1}}{V} \end{aligned} \tag{7.12}$$

where V_{cr1} and V_{cr} are V_{crr} at the rotor disc and the far stream positions respectively. Also u_1 and V_T are the far wake axial and swirl velocities just outside inner concentrator wake. (Equation 7.12 was derived from equation A.11 in appendix A[1]). Further effects with the CWT involving the Ejector Effect are discussed in appendix A.

7.2 CWT Numerical Wake Modelling.

In this section a numerical modelling approach is considered since this is closer to the complex interactive nature of the concentrator and wind turbine wakes. The method of wake relaxation is used except this time it is used on both wakes of the wind concentrator and wind turbine simultaneously, (see figure 7.3). The free stream velocity relative to the rotor would not be axial as with the wind concentrator, but helical since the rotor is working with a fixed specified tip speed ratio of T_s. The rotor wake for each blade would also have to be spread discretely over 2π radians about the axis of rotation, to assimilate the difference between the rotating rotor and the fixed concentrator. It must remembered that the rotor exacts energy while the concentrator does not. In each case Wake Relaxation can only be applied in a purely steady state situation. Spreading the rotor wake about the axis of rotation is an attempt to do this. How successful this method will be, can only be confirmed experimentally. Clearly the modelling will need to be checked under controlled conditions of steady wind speed and fixed rotational speed to enable tuning to be performed on the modelling. The 'Ejector Effect' can be theoretical simulated by a vortex ring situated at far down stream conditions to enable inviscid modelling to be performed more convincingly for designs which offer possible power output above Betz, (see chapter 2 and appendix A). The strength of the ring vortex will be found experimentally over an number of designs. This experimental knowledge would be implemented into Wake Relaxation process to aid the convergence process, and allow more 'Post-Betz' designs to be safely investigated

[1]The velocities are calculated with no Ejector Effect ie $\delta V_e = 0$

without getting spurious results.

Once both wake systems have been relaxed simultaneously, blade design can be performed on both concentrator and rotor systems using the design method given in section 4.4.1.

To design the rotor blades the rotor wake system would be represented not by a smeared wake system, but a wake system with the same number of tip, root and bound vortices as specified rotor blades. The relaxed wake of N concentrator blades however would be represented by spreading them discretely over 2π radians about the axis of symmetry. Once this was done the usual blade design process would be performed along the bound vortex of one of the rotor blades.

Designing the concentrator blades will involve leaving the relaxed rotor wake spread over 2π radians, and the usual blade design process performed at the bound vortex of a concentrator blade. This will give an initial idea of the chord or twist distribution for the concentrator blades. With this initial blade design knowledge, the Wake Relaxation process is repeated except the concentrator blades are now represented by a surface distribution of quadrilateral vortex rings to represent the concentrator blades, (see figure 7.4). This would take into account all of the three dimensional flow effects experienced by the blades to ensure an appropriate blade design is found to meet the specified distribution of circulation. The rotor on the other hand may not require Vortex Lattice modelling if the number of rotor blades is small, rotor solidity is low and the working T_s is high. This is because the effects of rotor swirl would be negligible. Further refinements to the method can still be made, by incorporating a 3D-Momentum Integral Boundary Layer model over the surface quadrilateral vortex rings of the concentrator blades and over the rotor blades surfaces if lifting surface modelling is used on the rotor aswell. The major disadvantage to this type of viscous modelling is large computing time and extra complexity. It could prove to be unnecessary if blade stall can be effectively investigated experimentally, and that pre-stall boundary layer effects prove to have little effect on the wake.

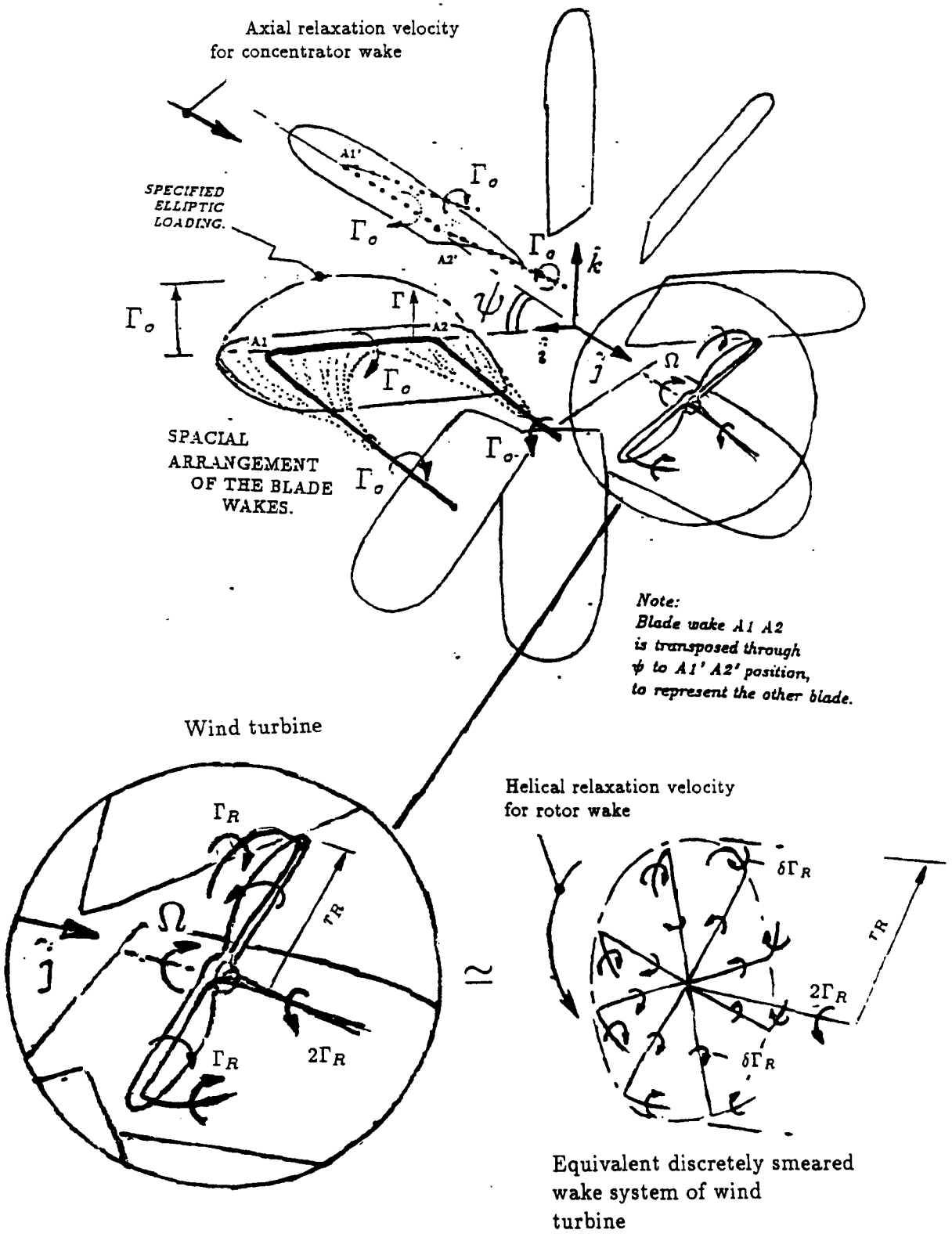

Figure 7.3 Numerical method for CWT model.

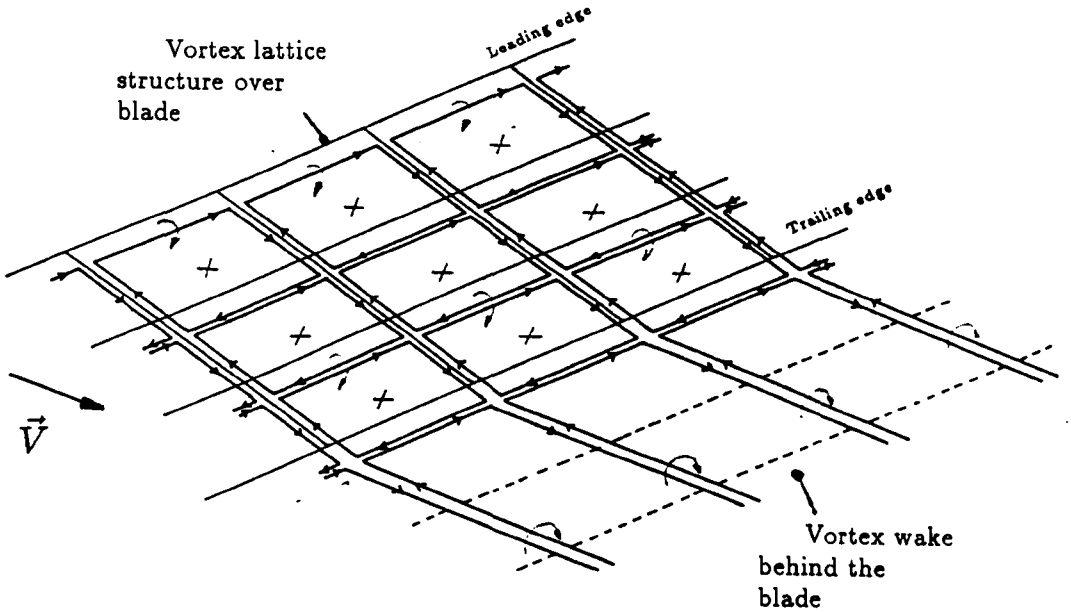

Figure 7.4 Higher order blade design method for CWT.

It can be realized from what has been described above that CWT modelling cannot be performed in isolation to experimental work, since experience is needed to model the viscous mixing and other wake effects properly. Chapter 5 examines concentrator modelling, and describes some limited test work to check this. CWT modelling needs the development stage involving wind tunnels, and because of this no modelling results have been given since insufficient time and resources were available. There were limited tests done in the field and wind tunnel on different CWT designs, but this was more to validate the principle of operation. Hence only qualitative analysis on CWT performance is given in this thesis.

7.3 Wind tunnel test work to develop CWT modelling and design.

The development of the CWT modelling would require a wind tunnel test rig to investigate several designs of CWT experimentally. In figure 7.5

shows the kind of arrangement required. In chapter 4, figure 4.29 shows the kind of arrangement basically required. In figure 7.5 shows the further tests that would need to be performed. Unsteady aerodynamics would need to be looked at to check for performance limitations. Turbulent air of different turbulence intensity TI would be blown over the CWT wind tunnel test models. This would be made possible by a wind turbulence generator which is shown in figure 7.5, positioned upstream of the wind tunnel model. These tests would be of great value since turbulence effects on concentrator performance would be difficult to verify in the field and very costly to correct. There would also be an opportunity to investigate the concentrator's ability to filter out turbulence in the core. This would add to the value of the concentrator concept, if this can be proved not only to work in the wind tunnel but in the field as well.

Initially gauze mesh would be used to simulate a working wind turbine to alleviate the amount of design and manufacturing involved for each new CWT set up. The gauze mesh would later be replaced by a wind turbine rotating at a fixed speed. The results from this would check the rotor blade design method. Different rotor and concentrator blade designs would be investigated under steady state constant T_s conditions. In both cases these tests would be designed to influence the progress of the CWT modelling. Once sufficient design confidence has been gained in CWT modelling, the next step would be to test a CWT under variable T_s conditions in the wind tunnel. Power and yaw control would have to be investigated as well. The wind tunnel model clearly would have to be of fixed design for this type of investigation. Hopefully by that time the most efficient and cost effective design would known.

The current method of mounting the concentrator is shown in chapter 4, figures 4.16 and 4.25. This arrangement unfortunately suffers the problem of high pitching moment at the yaw bearing. Ideally this would be solved by having the nacelle along the axis of symmetry upstream of the concentrator as shown in figure 7.5. Before such a design can be acceptable without adversely affecting concentrator performance, tests will need to be done

on aerodynamic 'Tower Shadow'. From these tests different methods of reducing the adverse effects of Tower Shadow might be found.

7.4 Tip Winglets as a method of improving CWT performance.

In chapter 3, equation 3.16 indicates that for a fixed number of blades and circulation, V_c/V is roughly proportional $\acute{R}/\acute{h}$. (This was developed from the analytical model based on a purely cylindrical wake with R/h near unity.) If the span could be increased artificially by way of Tip Winglets, as shown in figure 7.6, the improvement to power concentration could be dramatic without a large increase in construction material. The disadvantages of such a system would be very low Reynolds Number for each blade which could lead to boundary layer separation problems. This in turn would cause significant control problems. Only experimental tests would confirm if there is any potential in this idea. Modelling the flow would involve surface quadrilateral rings for the blades, the Concentrator Structural Ring and the Tip Winglets. Laminar flow separation over the Tip Winglets could be prevented by causing the boundary layer to become turbulent. Surface dimples like that on a golf ball could be used on the surface of Tip Winglets to achieve this. 3D-Momentum Integral Boundary Layer modelling could be used to improve the modelling on this but would be costly in computing time. How much material for the design and complexity of control, cost of manufacture and its ability to perform in unsteady conditions would all need to be considered before implementing it in future CWT designs.

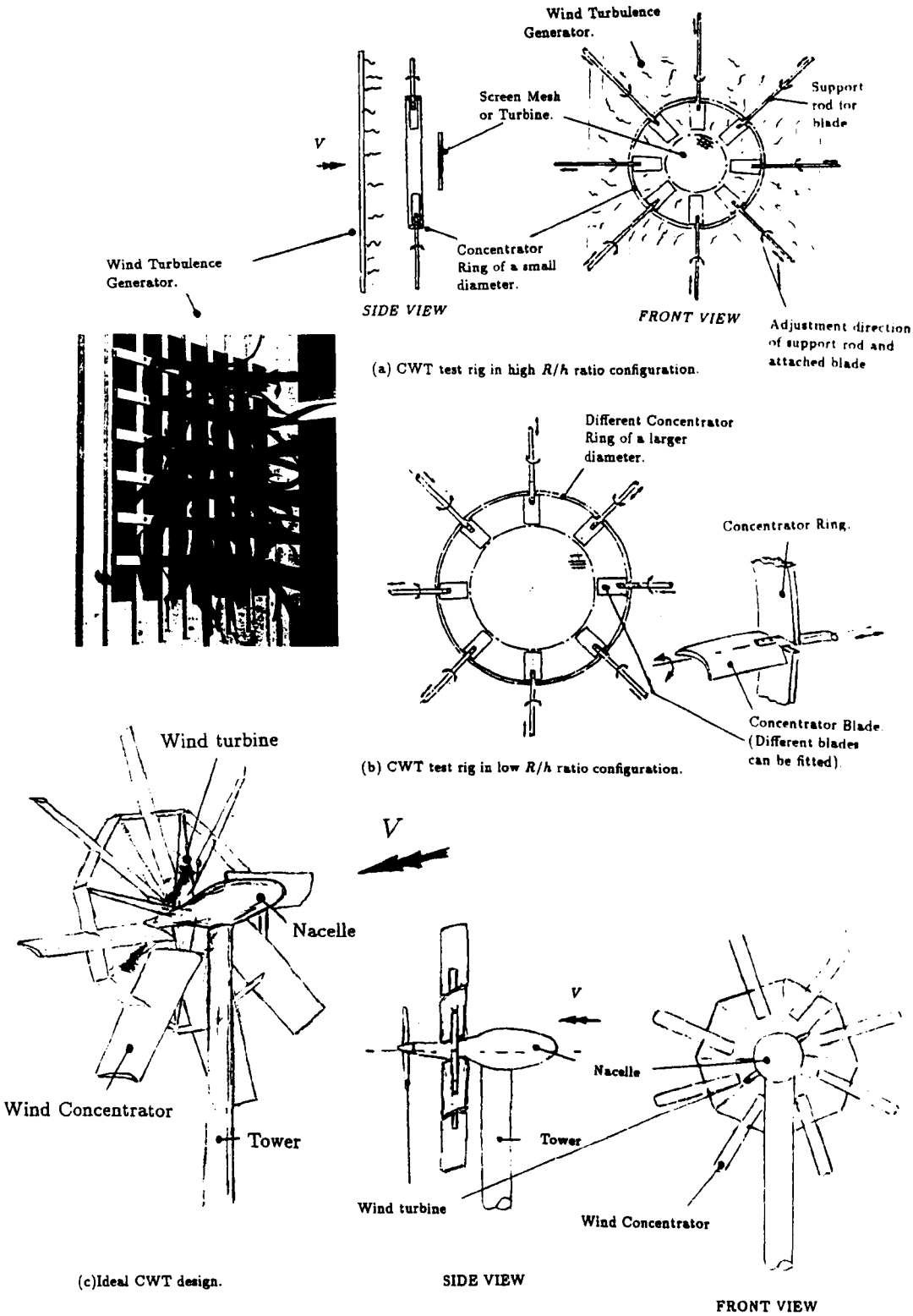

Figure 7.5 Wind Tunnel Test Rig for CWT

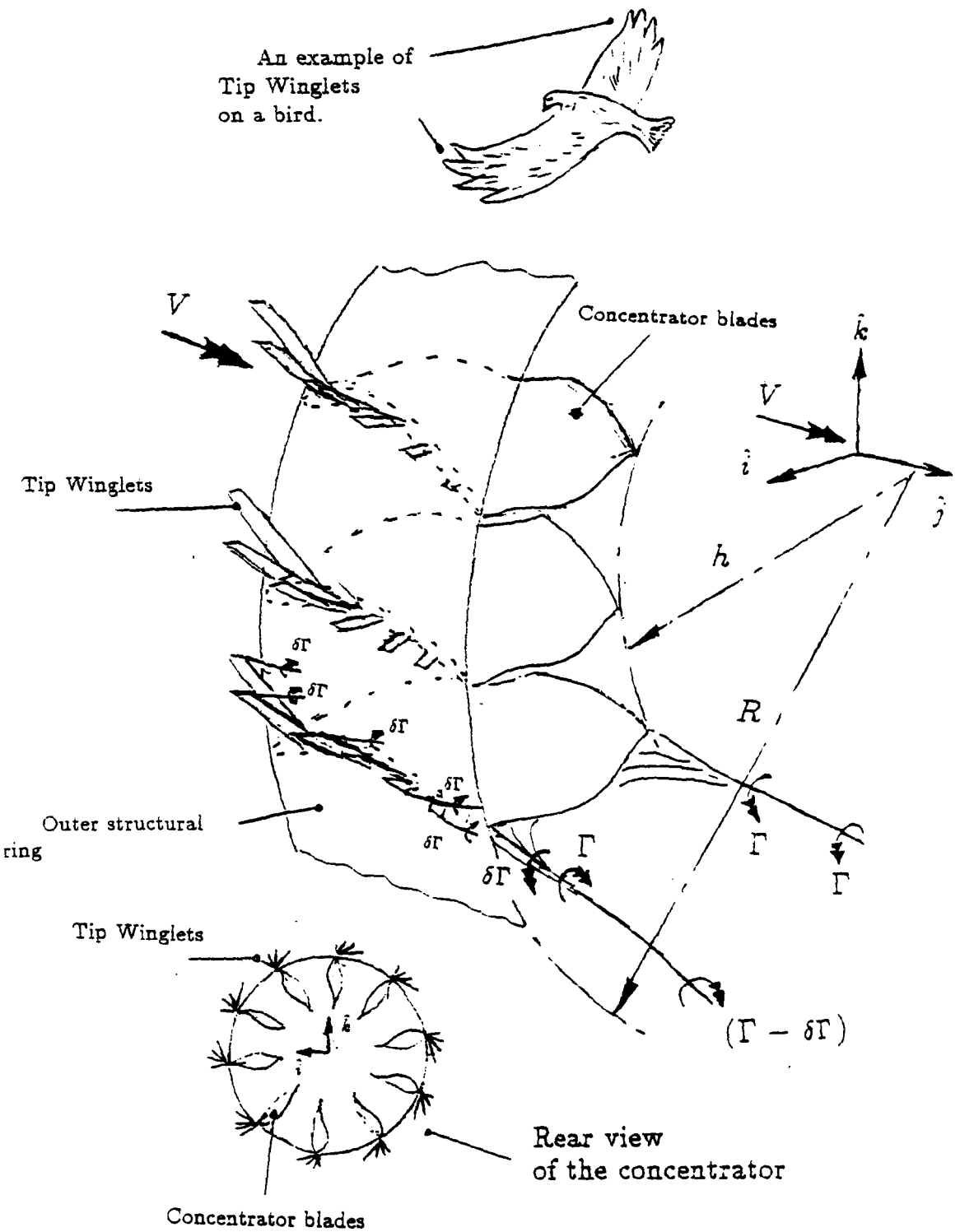

Figure 7.6 An improved CWT using Tip Winglets.

References

Bevilaqua, P.M. (1978)

'Lifting Surface Theory for Thrust-Augmenting Ejectors'. AIAA Journal vol. 16, no.5. pp 474-481.

Betz,A. (1919)

'Screw propellers with minimum loss of energy'. Nachr.der K.Gesellschaft der Wisenschaften zu Goettingen, 193.

Beurskens, H.J.M., (1982)

'The Dutch Wind Energy Programme'. 4th International Symposium on Wind Energy Systems, Stockholm.

Bullen, P.R., Mewburn-Crook, A., Read, S., (1987)

'The Performance of a novel Shrouded vertical axis wind turbine'. BWEA Annual Conference, Edinburgh, April 1987.

Dick, E. (1986)

'Power Limits for Wind Energy Concentrator Systems'. Wind Engineering Volume 10, no.2. pp 98-115.

Foreman, K.M., Gilbert, B.L., (1979)

'Further Investigations of Diffuser Augmented Wind Turbines, Part II-Technical Report'. U.S. Dept. of Energy Report C00-2616-2 (Part 2) (Rev 2), Grumann Aerospace Corp., Bethpage, N.Y., July 1979.

Foreman, K.M. (1983)

'Size Effect in DAWT Innovative Wind Energy System Design'. Journal of Solar Energy Engineering Trans. ASME, 105. pp 401-407.

Frost, W. and Kessel, P.A. (1982)

'Theoretical Design Study of the MSFC Wind Wheel Turbine'. NASA contractor Report 3532.

Garside, A.J van Bussel, G.J.W. (1985)

'Experimental Results Relating to Tip Vane Augmenters Fitted to a Horizontal Axis Turbine and Comparison with Predictions'. 7th BWEA Wind Energy Conference.

Hunter,R., Derrick,A. (1988)

'Progress in theoretical investigation of a stator flow concentrator'. Wind Energy Conversion. Proceedings of the 10th BWEA Wind Energy Conference.

Igra, O., (1979)

'Cost effectiveness of Vortex Augmented Wind Turbine'. Energy, Volume 4. pp 119-130.

Igra, O., (1981)

'Research and Development for Shrouded Wind Turbines'. Energy Conversion and Management, Volume 21 pp 13-48.

Infield, D. (1989)

'Wecs Field Testing-Instrumentation'. From 'Principles of Wind Energy Conversion' course notes. Imperial College, London. page 7.

Lerbs,H.W (1952)

'Moderately Loaded Propellers with a Finite Number of Blades and an Arbitrary Distribution of Circulation'. Transaction-Society Naval Architects and Marine Engineers. Vol 60 pp 73-117.

Loth, J.L. (1978)

'Wind Power Limitation Associated with Vortices'. Journal of Energy, Volume 2. pp 216-222.

Miley, S.J (1982)

'A Catalog of low Reynolds Number Airfoil Data for Wind Turbine

applications.' RFP-3387. Texas A and M Univ, College Station. pp A209-A209.

Newland, D.E (1971)

'An Introduction to Random Vibrations and Spectral Analysis'. Longmans. pp 118-120.

Stacey G., Musgove P.J, (1984)

'The Performance of Rutherford 6 metre diameter Vertical Axis Wind Turbine, including the effects of various Binning Techniques and Averaging Periods.' Wind Energy Conversion. Proceedings of 1984 6th BWEA Wind Energy Conference. Cambridge University Press. pp 110-129.

Schlichting, H. and Truckenbrodt, E. (1979)

'Aerodynamics of the Airplane'. McGrawhill, NY. pp 166-170.

Sforza, P.M. (1977)

'Vortex Augmentation for Wind Energy'. Wind Engineering, Volume 1. pp 186-197.

Sivasegarem,S. (1986)

'Power Augmentation in Wind Rotors: A Review'. Wind Engineering, Volume 10, no.3. pp 163-179.

Rechenberg,I. (1984)

'Berwian concentrates the wind: a report on a development at the Technical University of Berlin'. Sonnenergie, no 2, pp 6-10, (in German).

Rosenbrock, H.H. (1983)

'Proposal for a new Design of Wind Power Generator'. Wind Engineering, Volume 7, no.1.

Rechenberg,I. (1989)

'Artificial evolution and artificial intelligence'. Machine learning:

Principles and Techniques. Ed. Richard Forsyth. Chapman and Hall, London.

The OU Course Team no. M371. (1988)
'Introduction to Numerical Methods'. M371 Unit 1.1. The Open University Press. pp 39-41.

van Holten, Th. (1981)
'Concentrator Systems for Wind Energy with emphasis on Tip Vanes'. Wind Engineering, Volume 5. pp 29-45.

van Holten, Th. (1982)
'An Analytical Theory for Rotor-Tip Vanes Performance and Comparison with Experimental Results'. 8th European Rotorcraft Forum, Aix-en-Provence.

Vermeer, L.J. (1985)
'Windtunnel Experiments on the Diffuser Characteristics of a Tipvane Turbine.' Institute for Windenergy, Delft University of Technology. Report IW-R511.

Yen, J.T. (1975)
'Tornado Type Wind Energy System'. Proceedings 10th Intersociety Energy Conversion Conference. pp 987-994.

Appendix A

HYPOTHESIS OF AN EJECTOR EFFECT WITH A CWT.

Consider the Control Volume shown in figure A.1. To simulate the Ejector Effect we will adopt van Holten's approach of a vortex ring. This would have large dimensions compared with the wake, and placed sufficiently far downstream so that it does not introduce in any direct way additional velocities in the turbine disc. If δv_e is the additional velocity induced by the ring at "infinity", applying Bernoulli's Theory to the flow outside of the rotor wake yields the different static pressures p_e, p_e' and p_e'' in the far wake.

For region AA BB the static pressure is p_e so that

$$p + \frac{1}{2}\rho V^2 = p_e + \frac{1}{2}\rho(V + \delta v_e)^2$$

$$\therefore \quad p - p_e = \frac{1}{2}\rho\delta v_e(2V + \delta v_e) \tag{A.1}$$

Now at radius r in the annular region BB CC the static pressure is p_e' so that

$$p + \frac{1}{2}\rho V^2 = p_e' + \frac{1}{2}\rho(u_1 + \delta v_e)^2 + \frac{1}{2}\rho\omega_1^2 r^2$$

$$\therefore \quad p - p_e' = \frac{1}{2}\rho(u_1 + \delta v_e)^2 - \frac{1}{2}\rho V^2 + \frac{1}{2}\rho\omega_1^2 r^2 \tag{A.2}$$

Now at a point just outside of the inner concentrator wake CC the static pressure is $p_e' = p_e''$ and is assumed constant over the rotor wake at the far

wake

$$\therefore \quad p - p_e'' = \frac{1}{2}\rho(u_1 + \delta v_e)^2 - \frac{1}{2}\rho V^2 + \frac{1}{2}\rho\omega_1^2 h''^2 \qquad (A.3)$$

Applying Newton's 2nd Law to the cylindrical control volume of cross sectional area A we get

$$\frac{d}{dt}\int_\nu \rho\vec{V}d\nu = -\int_S [\rho\vec{V}(\vec{V}.\hat{n}) + p\hat{n}]dS$$

The amount of fluid entering the control volume from the sides would be

$$q = A\delta v_e - (2v_i - \delta\acute{v})\pi r_e^2 - (V - u_1)\pi(R''^2 - h''^2)$$

and for the final result to be independent of A this volume of air q must have an assumed average velocity of $V + \frac{1}{2}\delta v_e$. The axial momentum will be, for $r_e = h''$,

$$\begin{aligned}
\hat{j}.\vec{F} \;=\; & r_R^2\rho\pi(V - (V - 2v_i + \delta\acute{v} + \delta v_e))(V - v_i + \delta v) \\
& +(\acute{R}^2 - \acute{h}^2)\rho\pi u(V - (u_1 + \delta v_e)) \\
& +(\rho V A - r_R^2\rho\pi(V - v_i + \delta v) - (\acute{R}^2 - \acute{h}^2)\rho\pi u)(V - V - \delta v_e) \\
& +\rho(A\delta v_e - (2v_i - \delta\acute{v})\pi h''^2 - (V - u_1)\pi(R''^2 - h''^2))(V - (V + \frac{\delta v_e}{2})) \\
& +(p - p_e)(A - \pi R''^2) + \int_{h''}^{R''}(p - \acute{p_e})2\pi r dr + (p - p_e'')\pi h''^2 \qquad (A.4)
\end{aligned}$$

For the rate of change of angular momentum we get

$$\begin{aligned}
\hat{j}.\vec{M} \;&=\; \int_{h'}^{R'} 2\pi\rho u\omega r^3 dr \\
&=\; \int_{h''}^{R''} 2\pi\rho u_1\omega_1 r^3 dr \qquad (A.5)
\end{aligned}$$

The torque $\vec{M}$ and axial force $\vec{F}$ will be reacted by the tower and foundations. To investigate the forces on the rotor disc and concentrator we will evaluate equation A.4 by using equations A.1 to A.3, so that

$$\hat{j}.\vec{F} \;=\; (2v_i - \delta\acute{v})r_R^2\rho\pi(V - v_i + \delta v) + \delta v_e(v_i - \frac{\delta\acute{v}}{2})\rho\pi h''^2$$

$$+u(V-u_1)\rho\pi(\dot{R}^2-\dot{h}^2)+\frac{1}{2}\rho\delta v_e\pi(V-u_1)(R''^2-h''^2)$$
$$-\rho(\delta v_e V+\frac{1}{2}\delta v_e^2)\pi R''^2+\frac{1}{2}\rho(u_1+\delta v_e)^2\pi R''^2$$
$$-\frac{1}{2}\rho V^2\pi R''^2+\rho\pi\int_{h''}^{R''}\omega_1 r^3 dr+\frac{1}{2}\pi\rho\omega_1^2 h''^4 \qquad (A.6)$$

Let us consider the axial force acting on the rotor. If we apply Bernoulli's Theorem along a streamline from the far upstream to a point immediately upstream of the rotor disc, as well as applying it along a streamline running from immediately downstream of the rotor disc plane yields the following

$$D_{rotor}=(p_1-p_2)\pi r_R^2 \qquad (A.7)$$

Now $$p+\tfrac{1}{2}\rho V^2=p_1+\tfrac{1}{2}\rho(V-v_i+\delta v)^2$$
$$p_e''+\tfrac{1}{2}\rho(V-2v_i+\delta\dot{v}+\delta v_e)^2=p_2+\tfrac{1}{2}\rho(V-v_i+\delta v)^2$$
$$\therefore\quad p_1-p_2=(p-p_e'')+\tfrac{1}{2}\rho V^2-\tfrac{1}{2}(V-2v_i+\delta\dot{v}+\delta v_e)^2 \qquad (A.8)$$

If we applying equation A.3 to equation A.8 we get

$$p_1-p_2=\frac{1}{2}\rho(u_1+\delta v_e)^2+\frac{1}{2}\rho\omega_1^2 h''^2-\frac{1}{2}\rho(V-2v_i+\delta\dot{v}+\delta v_e)^2 \qquad (A.9)$$

If the axial force coefficient on the rotor is defined as

$$CD_{rotor}=\frac{D_{rotor}}{(\frac{1}{2}\rho V^2\pi r_R^2)} \qquad (A.10)$$

then

$$CD_{rotor}=(\frac{u_1}{V}+\frac{\delta v_e}{V})^2+(\frac{\omega_1 h''}{V})^2-(1-\frac{2v_i}{V}+\frac{\delta\dot{v}}{V}+\frac{\delta v_e}{V})^2 \qquad (A.11)$$

Solving for $\frac{v_i}{V}$ we get

$$\frac{v_i}{V}=\frac{1}{2}(\frac{\delta v_e}{V}+\frac{\delta\dot{v}}{V}+1)-\frac{1}{2}\sqrt{\frac{\omega_1^2 h''^2}{V^2}+(\frac{u_1}{V}+\frac{\delta v_e}{V})^2-CD_{rotor}} \qquad (A.12)$$

The maximum value of axial force which can be set up on the rotor occurs when the rotor flow, at entrance to the primary low pressure reservoir,

breaks down into a Turbulent Wake State. This is derived from equation A.12 to give

$$(CD_{rotor})_{max} = \frac{\omega_1^2 h''^2}{V^2} + (\frac{u_1}{V} + \frac{\delta v_e}{V})^2 \qquad (A.13)$$

Therefore the force on the rotor can exceed unity by virtue of an effective turbulent mixing process between the rotor and the annular wakes and the annular swirl velocity ω_1. To exceed the Betz Limit, based on total frontal area of the concentrator and the swept area of the rotor, it can only be achieved if $\delta v_e > 0$. (This is equivalent to the Tip Vane Wind Turbine). Now the axial force on the concentrator will be the difference between total and rotor forces. If we multiply equation A.11 by $\frac{1}{2}\rho V^2 \pi r_R^2$ and subtract it from equation A.6 we get

$$\begin{aligned} D_{con} &= \frac{1}{2}\pi r_R^2 \rho(V^2 - u_1^2) + \rho\pi r_R^2((V - u_1)\delta v_e + \delta\acute{v}V - 2v_i\delta\acute{v} + \frac{\delta\acute{v}^2}{2} + \delta\acute{v}\delta v_e) \\ &\quad + 2\pi r_R^2 v_i(\delta v - \delta v_e) + \delta v_e v_i \pi h''^2 + u(V - u_1)\rho\pi(R'^2 - h'^2) \\ &\quad + \frac{\pi}{2}\rho\delta v_e(V - u_1)(R''^2 - h''^2) - \rho(\delta v_e V + \frac{1}{2}\delta v_e^2)\pi R''^2 + \frac{1}{2}\rho(u_1 - \delta v_e)^2 \pi R''^2 \\ &\quad - \frac{1}{2}\rho V^2 \pi R''^2 + \rho\pi \int_{h''}^{R''} \omega_1^2 r^3 dr + \frac{1}{2}\pi\omega_1^2(h''^4 - h''^2 r_R^2) \end{aligned} \qquad (A.14)$$

When the turbine is not working $v_i = 0$, $r_R = h''$, $\delta\acute{v} = \delta v$, $\omega_1 h''/V > 1$ and $u_1 \geq 0$. Therefore D_{con} becomes

$$D_{con} \simeq \rho\pi \int_{h''}^{R''} \omega_1^2 r^3 dr$$

if the wake expansion is neglected. The reason for this has been explained earlier owing to the constant pressure head across the concentrator disc. This sets up an exchange between drag thrust and torque on the concentrator blade elements. Therefore D_{con} cannot not be zero without $|\vec{M}|$ and swirl being zero, otherwise the concentrator would be performing work which is impossible.

When the turbine is working the core flow structure will change considerably down stream of the turbine. This means that $v_i \neq 0$, $r_R < h''$, $V > u_1 > 0$, $\delta v_e \neq 0$, $\delta\acute{v} < \delta v$ and $D_{con} > 0$. The swirl $\omega_1 h''$ will be

less owing to the increase in the diameter of the rotor wake downstream, but the angular momentum of the annular flow will be same as before. The axial force on the concentrator would not only be due to the balance between work done by the drag thrust and torque on the air through the concentrator blade elements, but also due to the loss of axial momentum causing $v_i > 0$ in the core flow and the Ejector Effect caused by turbulent mixing between the different wakes of the CWT causing $\delta v_e > 0$.

The 'Helical Ejector Mixing Effect' has not been experimentally investigated yet, but from van Holten(1981), van Holten(1982) and Vermeer(1985) sufficient experimental evidence is available on an Ejector Effect with tip vanes and gauze screens. (See figure A.2, (the C_p values shown are only 8% more than the gross C_p values which would be based on total frontal swept area of the tipvanes and gauze screen tested.))

To finish off on the analysis on the CWT the possible C_p that could be achieved is considered as follows. In incompressible flow the drop of enthalpy equals the drop of total pressure $\Delta H/\rho$ across the turbine so that

$$P = \Delta H V_{cr1} \pi r_R^2$$

Since there is no discontinuity of velocity in the turbine disc plane ΔH is equal to the static pressure drop across the turbine. Now from the definition of C_P and equation A.10 we get

$$C_p = \frac{P}{1/2\rho V^3 \pi r_R^2} = CD_{rotor}(\frac{V_{cr1}}{V})$$

Now $V_{cr1}/V = 1 - v_i/V + \delta v/V$, but for $v_i = \frac{1}{2}(1 + \delta v/V + \delta v_e/V)$ CD_{rotor} is a maximum so that $(C_p)_{max}$ is

$$(C_p)_{max} = \frac{1}{2}(1 - \frac{\delta v_e}{V} - \frac{\delta v}{V} + 2\frac{\delta v}{V})(\frac{\omega_1^2 h''^2}{V^2} + (\frac{\delta v_e}{V} + \frac{u_1}{V})^2) \qquad \text{(A.15)}$$

Unfortunately the above expressions do not allow the reader to easily see the beneficial effects of the Ejector Effect on the rotor performance. In order to make this possible without delving into complex modelling a number of assumptions need to be applied to the above analysis. In equation A.12

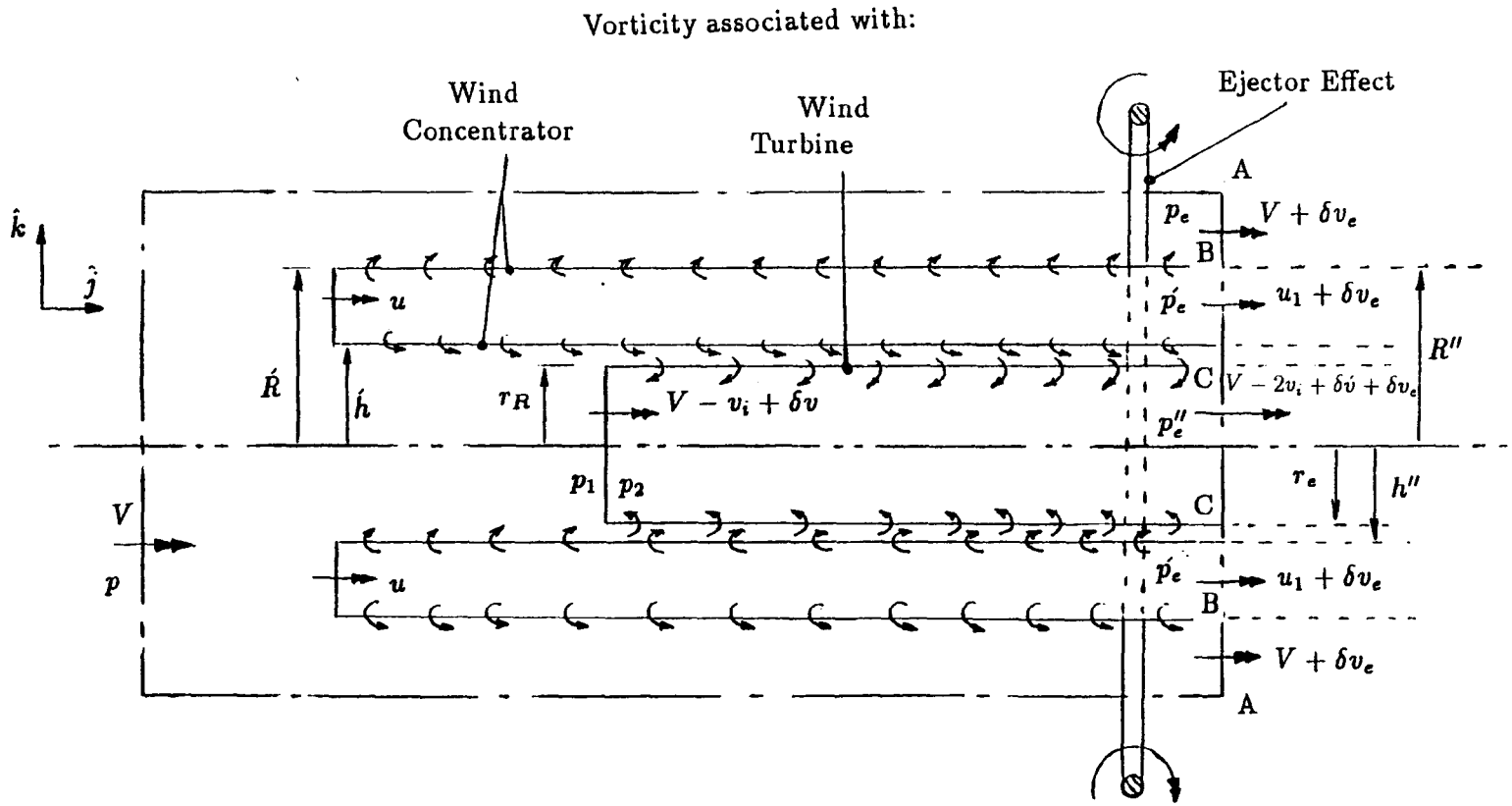

Figure A.1 Control Volume Analysis of a CWT with 'Ejector Effect'.

we have a complex expression. Now if we assume that the concentrator wake is truncated and the vortex wake is completely broken up by viscous diffusion, such that $\delta\dot{v} = 0$, $\omega_i^2 h''^2 = 0$ and $u_1 = V$ in the far wake, the expression would simplify to

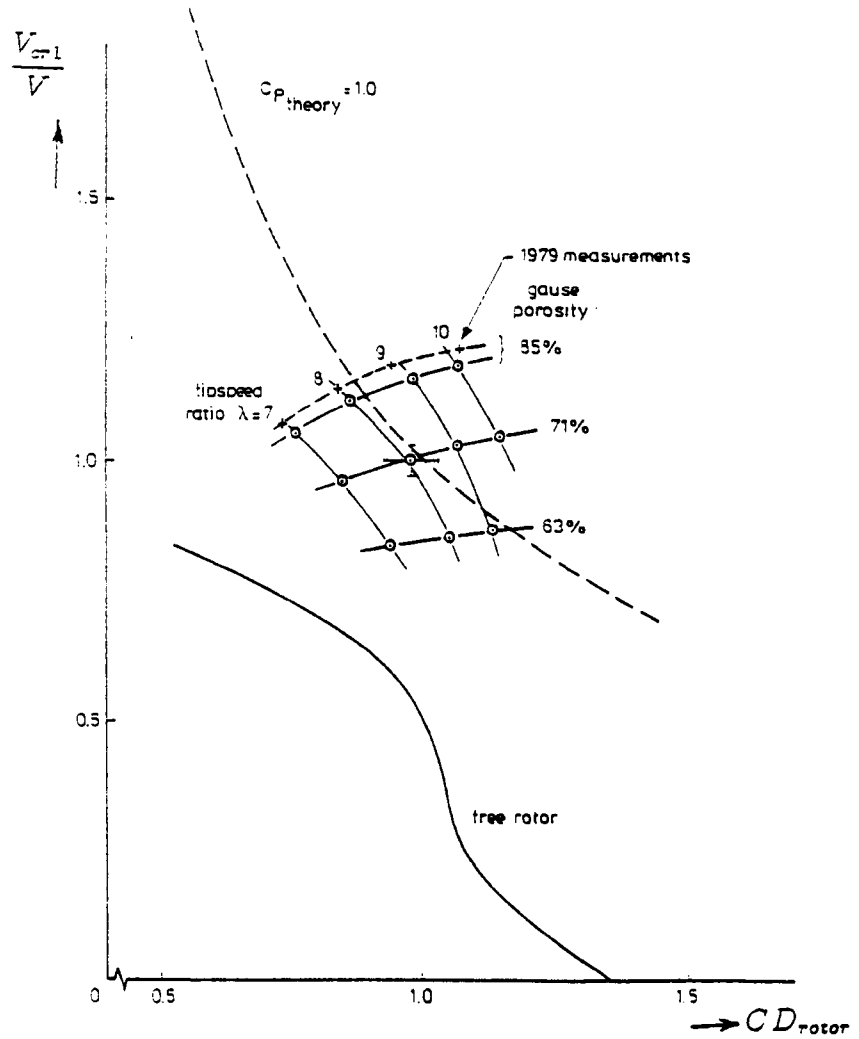

Figure A.2 Experimental results from tests with tip vanes and gauze screens.
Source: Vermeer(1985).

$$\frac{v_i}{V} = \frac{1}{2}\left(1 + \frac{\delta v_e}{V}\right) - \sqrt{\left(1 + \frac{\delta v_e}{V}\right)^2 - C D_{rotor}} \qquad \text{(A.16)}$$

From the information given in figure A.1, which is based on van Holten's Momentum Theory of Concentrator Systems (see van Holten(1981), we can

write for the velocity at the rotor disc as

$$\frac{V_{cr1}}{V} = 1 - \frac{v_i}{V} + \frac{\delta v}{V} \tag{A.17}$$

Substituting equation A.16 in A.17 we get

$$\frac{V_{cr1}}{V} = \frac{1}{2}\left(1 - \frac{\delta v_e}{V} + \sqrt{\left(1 + \frac{\delta v_e}{V}\right)^2 - CD_{rotor}}\right) + \frac{\delta v}{V} \tag{A.18}$$

The expression for C_p can be rewritten to give the equation for a hyperbola for curves of constant C_p of the form

$$\frac{V_{cr1}}{V} = \frac{C_p}{CD_{rotor}} \tag{A.19}$$

We can now plot equations A.18 and A.19 graphically as shown in figure A.3. The arrow indicating increasing diffuser effect is indicative of the effect of increasing δv, while the arrow showing increasing Ejector Effect is indicative of the effect of increasing δv_e. In figure A.3 shows that very high C_ps are possible for $CD_{rotor} > 1$ and $V_{c1}/V > 1$. These are based on rotor area only. The effectiveness of concentrator is dependant on the swirl imposed on the annular air mass and the ability of the swirl to aid viscous mixing in the far wake. Design parameters of the concentrator involve N, $\Gamma/[V(R-h)]$, and R/h. To avoid low C_p based on total frontal area of the CWT for a given R/h, $\Gamma/[V(R-h)]$ and N should be as high as possible. (Chapters 2 and 3 outline the limitations to this design philosophy if the designer wishes to exceed the Betz Limit.) This would inevitably lead to a cascade arrangement of concentrator blades of high camber and high aspect ratio to avoid large construction weight and poor yaw capability. Only simple and very rudimentary tests have been conducted on a particular design of concentrator (see section 5). Wind tunnel tests have shown that the principle is realizable, and given further development work may show even more success once the Ejector Effect can be proven to work with the CWT.

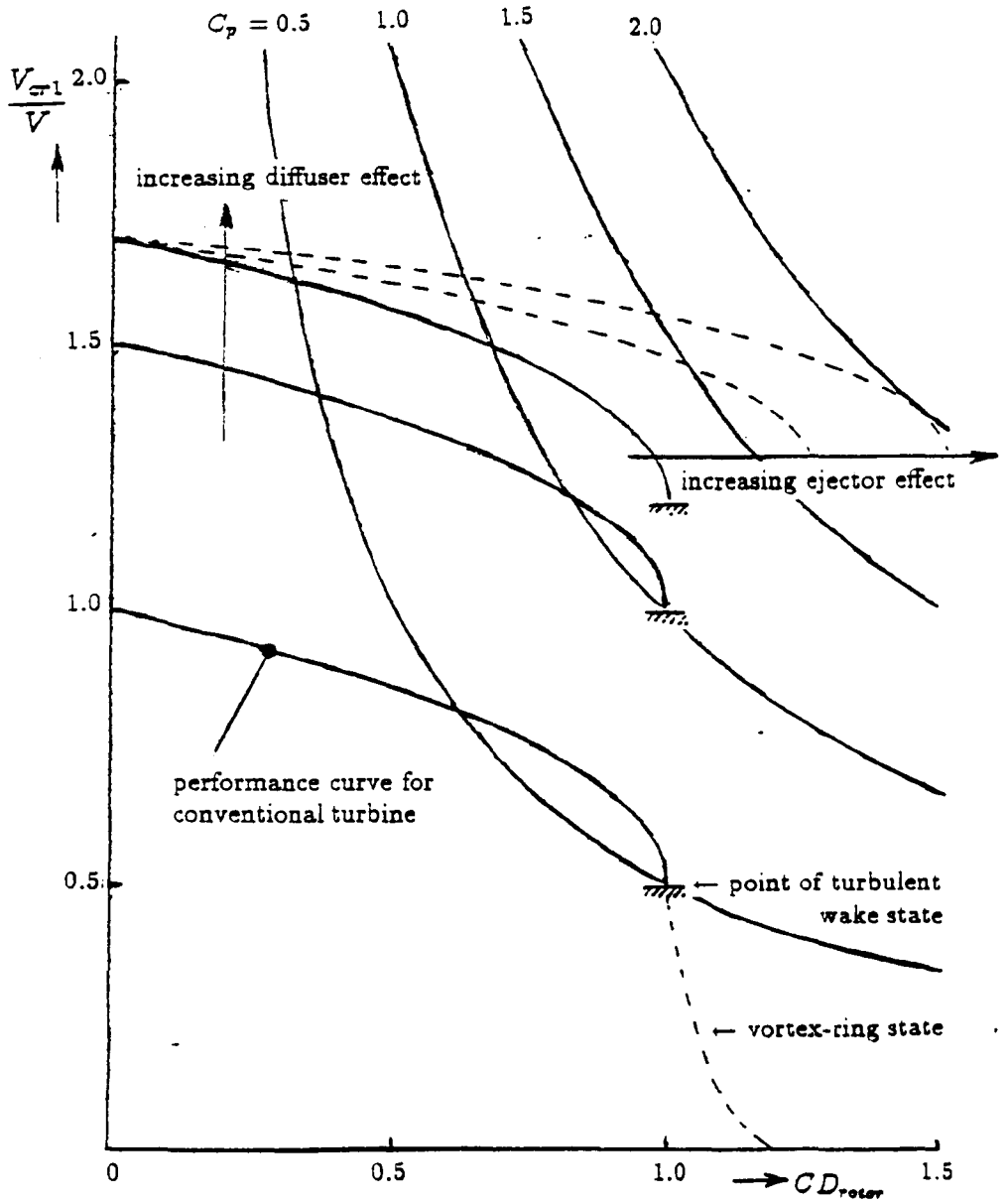

Figure A.2 Ejector Effect on wind turbine performance.
3

Appendix B

WIND CONCENTRATOR BLADE ELEMENT THEORY.

In chapter 2 the energy equation was considered. The energy equation in its most comprehensive form, for a control volume surrounding the concentrator, is

$$\delta\dot{Q} \quad - \quad \delta\dot{W}k = \delta\dot{u}$$

$$\left\{\int\int\int_{\nu}\rho\frac{d\dot{Q}}{d\nu}d\nu + \dot{Q}_{vis}\right\} \quad - \quad \left\{\int\int_{S}p\vec{q}.d\vec{S} - \int\int\int_{\nu}\rho(\vec{f}.\vec{q})d\nu - \dot{W}_{vis} - \dot{W}_{SHAFT}\right\}$$

$$= \frac{\partial}{\partial t}\int\int\int_{\nu}\rho(e + \frac{|\vec{q}|^2}{2} + gz)d\nu + \int\int_{S}\rho(e + \frac{|\vec{q}|^2}{2} + gz)\vec{q}.d\vec{S}. \qquad \text{(B.1)}$$

Since there is no shaft work the total pressure head is constant through out the flow field, no change in potential energy of the flow, incompressible and irrotational the following terms go to zero: $\dot{Q}$, e, $\dot{W}_{vis}$, $\dot{W}_{SHAFT}$, $\dot{Q}_{vis}$, z and $(\vec{f}.\vec{q})$. Equation B.1 now becomes as

$$-\int\int_{S}p\vec{q}.d\vec{S} = \frac{\partial}{\partial t}\int\int\int_{\nu}\rho\frac{|\vec{q}|^2}{2}d\nu + \int\int_{S}\rho\frac{|\vec{q}|^2}{2}\vec{q}.d\vec{S}. \qquad \text{(B.2)}$$

Since the total pressure head H is constant throughout the flow field we can write $H = p + \rho\frac{|\vec{q}|^2}{2}$ =Constant. This means that equation B.2 now can be written as

$$-H\int\int_{S}\vec{q}.d\vec{S} = \frac{\partial}{\partial t}\int\int\int_{\nu}\rho\frac{|\vec{q}|^2}{2}d\nu. \qquad \text{(B.3)}$$

The left-hand side of equation B.3 has the term $\int\int_S \vec{q}.d\vec{S}$ which represents the nett increase in volume flow rate across the control volume surfaces. Since we are considering a steady state situation, the mass flow across the control volume surfaces is constant therefore this term is zero. Therefore equation B.2 becomes

$$-\int\int_S p\vec{q}.d\vec{S} = \int\int_S \rho\frac{|\vec{q}|^2}{2}\vec{q}.d\vec{S}. \tag{B.4}$$

Equation B.4 can be interpreted as work done by the centrifugal pressure difference of the swirl on the control volume in unit time, equals the kinetic energy which passes across the surface of the control volume in unit time. The application of blade element theory has been based on the assumption of negligible wake swirl, regular helical vortices downstream of the disc and the number of blades involved being infinite. This is appropriate to lightly loaded propellers and wind turbine. This would mean that when there is a change in Total Pressure Head H across the rotor, becomes

$$\dot{W}_{SHAFT} - \int\int_S p\vec{q}.d\vec{S} = \frac{\partial}{\partial t}\int\int\int_\nu \rho\frac{|\vec{q}|^2}{2}d\nu + \int\int_S \rho\frac{|\vec{q}|^2}{2}\vec{q}.d\vec{S} \tag{B.5}$$

The Betz Law, (see Betz(1919)), is based on an optimum propeller where

$$\int\int_S p\vec{q}.d\vec{S} \to 0$$

because an optimum propeller has infinite rotational speed. Therefore there is no torque experienced on the rotor, and thus no swirl in the wake of the rotor. Hence there is no radial pressure gradient in the far wake either.

$$\frac{\partial}{\partial t}\int\int\int_\nu \rho\frac{|\vec{q}|^2}{2}d\nu \to 0$$

since the blade loading for an optimum rotor will be infinitesimal at infinitely large rotational speed. Therefore the vortex wake will not increase the kinetic energy within the control volume per unit time, because the induced vortex wake effects will be infinitesimal. Hence equation B.5 approaches the following condition for the most efficient rotor:

$$\dot{W}_{SHAFT} \rightarrow \int\int_S \rho \frac{|\vec{q}|^2}{2} \vec{q}.d\vec{S}$$

i.e. all the shaft work is converted to useful work and conveyed across the control volume surface per unit time with no increase in kinetic energy in the control volume per unit time. Near these conditions the assumption of regular helices for the vortex sheets in the wake can be made not only at the far wake but also at the rotor disc as well. Figures B.1 and B.2 show how the Betz Law can be approximately applied to lightly loaded propellers and wind turbines whereby the angle ϕ^* of the substituted vortex sheets and local flow angle ϕ can be equal. It is only this condition that allows us to find a solution for the flow angle by an iterative technique. (This is discussed in more detail by Lerbs(1952)). In figure B.3 the flow diagram of a wind concentrator blade element is considered. The concentrator is very much unlike a propeller with very high blade loading, high wake swirl and zero $\dot{W}_{SHAFT}$. Now equation B.4 can be rewritten in terms of the work done on the control volume by the axial forces acting on the blades due to pressure forces caused by swirl in unit time, and the induced kinetic energy flowing across the surface of the control volume causing the loss of pressure in unit time. This gives

$$\int_A u dT = \int_A \frac{1}{2} \omega dT_Q \qquad \text{(B.6)}$$

where the integrals are evaluated over the concentrator disc area A. (Note equation B.6 is the integral of equation 2.1 given in chapter 2).

The relevance of Blade Element Theory to the wind concentrator rests on the assumption of ϕ^* equalling ϕ in figure B.4. The Betz Law for an optimum propeller tells us that the influence of the vortices from a propeller blade wake, are of negligible consequence compared to the flow velocities

relative to the blade element caused by the free stream velocity V and rotation speed Ωr. Now the situation for the wind concentrator shown in figure B.3 makes such assumptions irrelevant since the device does not rotate and the blades are heavily loaded as well. Figure B.4 describes the

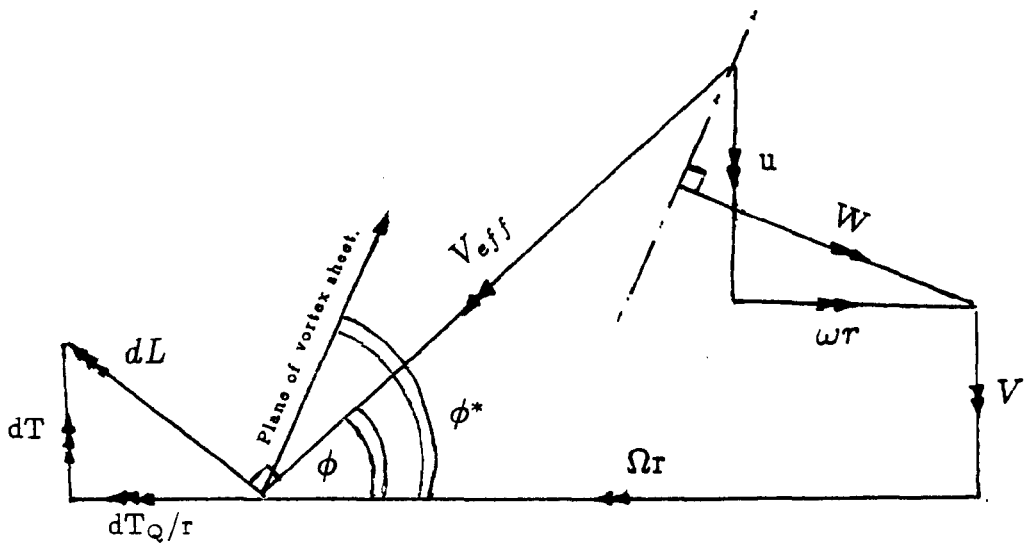

Figure B.1 Velocity diagram of a propeller blade element.

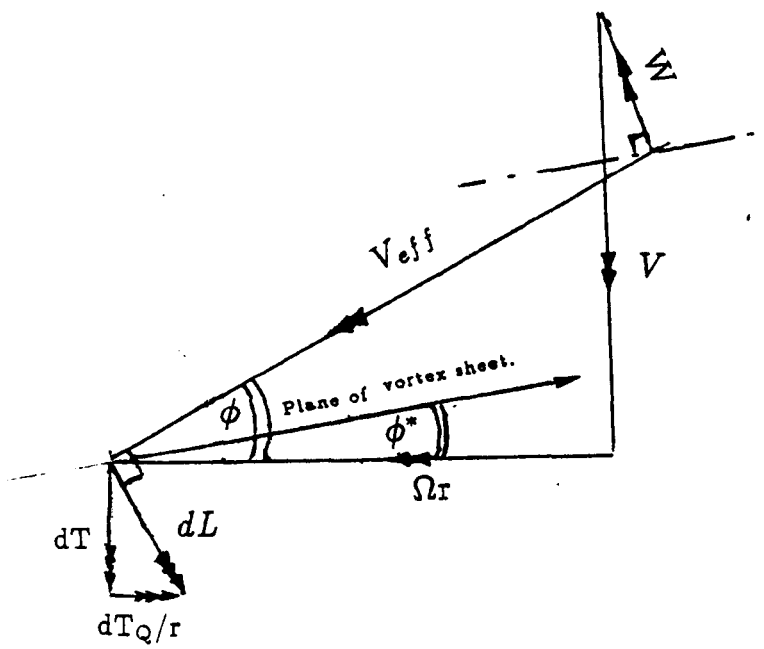

Figure B.2 Velocity diagram of a wind turbine blade element.

situation if we apply the Betz Law, allowing ϕ^* to equal ϕ. (Note that in the earlier figures dD was zero). How realistic figure B.4 was, was unknown to the author initially. The theory is given in this appendix and the results from different wind tunnel tests, to assess the accuracy of the model, are covered in chapter 5.

If we apply the Axial Momentum Theory for the annulus shown in figure B.4 we get

$$\begin{aligned} dT &= dL\cos\phi + dD\sin\phi \\ &= (\rho 2\pi r dr(V - F\cos\phi W))2W\cos\phi F \end{aligned} \tag{B.7}$$

where F is the local Prandtl factor for tip loss, given as

$$F = \frac{2}{\pi}\cos^{-1}[exp(-\acute{F})] \tag{B.8}$$

where

$$\acute{F} = \frac{N(R-r)}{2R\sin\phi}.$$

From Kutta-Joukowski we get for the blade element lift force

$$dL = NC_L(\frac{1}{2}\rho V_{eff}^2 c)dr \tag{B.9}$$

$$\text{where} \qquad C_L = 2\Gamma/(Vc\sin\phi). \tag{B.10}$$

Similarly, for the drag force similarly we get

$$dD = NC_D(\frac{1}{2}\rho V_{eff}^2 c)dr. \tag{B.11}$$

From figure B.4 we get

$$W = V\cos\phi \tag{B.12}$$

$$V_{eff} = W\tan\phi \tag{B.13}$$

Now applying equations B.9 to B.13 to equation B.7 we get

$$NC_L\frac{1}{2}\rho V_{eff}^2 c\cos\phi + NC_D\frac{1}{2}\rho V_{eff}^2 c\sin\phi = \rho 4\pi r\cos\phi VW(1 - F\cos^2\phi)F$$

If we assume zero blade drag then the above becomes

$$\cos\phi - \cos^3\phi F = \frac{C_L N c}{8\pi r F}(1 - \cos^2\phi). \qquad \text{(B.14)}$$

As $r \rightarrow R$, $F \rightarrow 0$ assume $\phi = \pi/2$. It can be seen that C_L and F are functions of ϕ so therefore an iterative process is needed to solve for ϕ.

If the local value of $\Gamma/(V(R-h))$ and chord c are known and the value of R/h and N are known as well then following iterative process applies

(1) Assume an initial flow angle for ϕ.

(2) Calculate the local Prandtl factor F.

(3) Calculate the local C_L from equation B.10.

(4) Solve equation B.14 to find the flow angle ϕ. If new ϕ is equal to old ϕ then stop; otherwise continue.

(5) Calculate new angle of attack α from the lift characteristics of the selected blade aerofoil section (ie C_L against α).

(6) Calculate new blade pitch angle Θ from the relationship $\Theta = \phi - \alpha$ and return to (2).

This iterative process is applied to each blade element until the necessary blade twist is achieved along the whole span. To predict the vortex angles at the inboard and outboard positions, the above process is applied at particular blade elements where it is believed the vortex sheet will roll up downstream according to the specified blade loading distribution. Once these angles are known the analysis covered in appendix D can be applied to find the axial velocity V_y. This would enable the reader to find the maximum V_{CR} for the particular design using this current method.

It should be appreciated that the above method is not accurate enough to find the induced velocities in the flow field around the concentrator, because the interdependent effects of the wake have been assumed negligible. (See chapters 3 and 5 for more details).

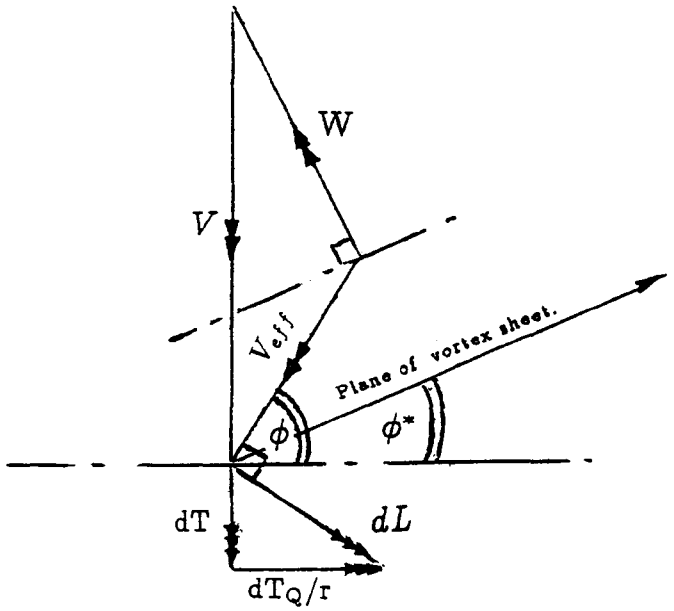

Figure B.3 Velocity diagram of a wind concentrator blade element.

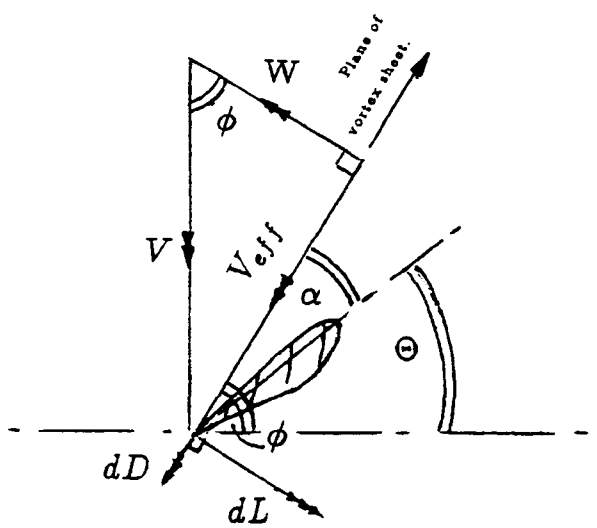

Figure B.4 Velocity diagram of a wind concentrator blade element with assumed wake of regular helical vortex sheets.

Appendix C

DERIVATION OF FAR WAKE SWIRL VELOCITY.

Let us consider the far wake position down stream of a wind concentrator. The inner wake is assumed to be a cylindrical vortex sheet, as shown in figure C.1, in isolation to the rest of the vortex wake.

The infinitesimal induced velocity at P is dV due to a small sheet of vorticity of strength γ and of length ds. The induced velocity would be as follows

$$dV = \frac{\gamma ds}{2\pi r_1} = \frac{\gamma R d\theta}{2\pi r_1} \tag{C.1}$$

Now from figure C.1 we apply the Sine and Cosine Rules so that

$$r_1 = \sqrt{R^2 + r^2 - 2Rr\cos\theta} \tag{C.2}$$

and

$$\frac{r_1}{\sin\theta} = \frac{r}{\sin\alpha} = \frac{R}{\sin(\pi - \theta - \alpha)} \tag{C.3}$$

From equation C.1 if we take the vertical and horizontal component of dV at P we get the tangential and radial components as well. Since the arrangement of vortices is symmetrical about the central axis, the tangential and radial components will not change for any angular position about the central axis for a particular radial distance from the origin. Therefore these components can be expressed mathematically as follows

$$dV_z = \frac{\gamma R \cos(\theta + \alpha) d\theta}{2\pi r_1} \tag{C.4}$$

$$dV_x = -\frac{\gamma R \sin(\theta + \alpha) d\theta}{2\pi r_1} \tag{C.5}$$

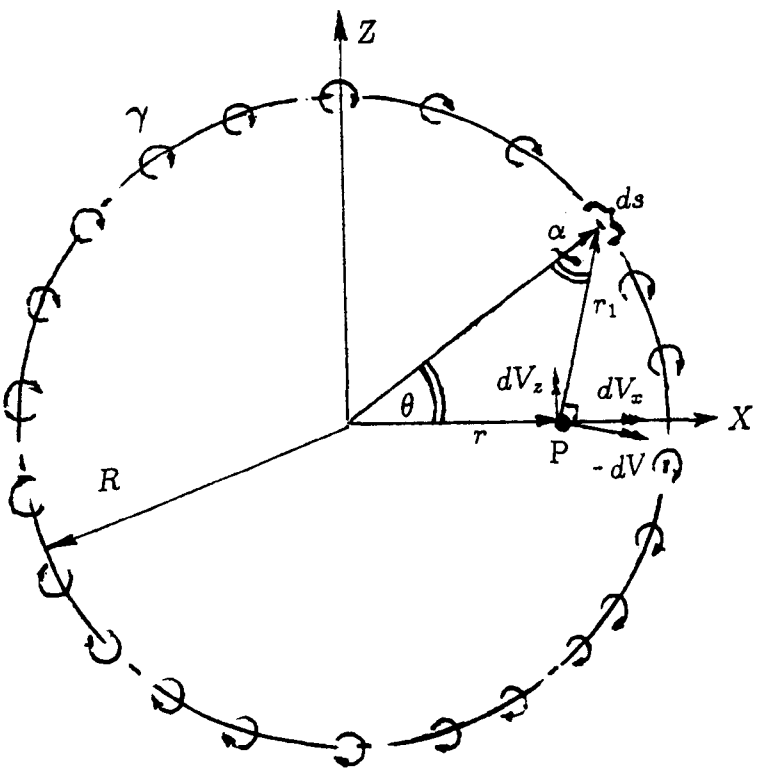

Figure C.1 Details of cylindrical vortex wake.

Let us consider equation C.4 only. We know that $\cos(\theta + \alpha)$ can be written as

$$\cos(\theta + \alpha) = \cos\theta \cos\alpha - \sin\alpha \sin\theta$$

Also from the Sine Rule we have

$$\sin\alpha = \frac{r}{r_1} \sin\theta$$

Therefore combining both of the above expressions we get

$$\begin{aligned}
\frac{\cos(\theta+\alpha)}{r_1} &= \{\cos\theta\sqrt{1-(\frac{r}{r_1})^2\sin^2\theta}-\frac{r}{r_1}\sin^2\theta\}/r_1 \\
&= \{\cos\theta\sqrt{R^2+r^2\cos^2\theta-2Rr\cos\theta}-r\sin^2\theta\}/r_1^2 \\
&= \{\cos\theta(R-r\cos\theta)-r\sin^2\theta\}/r_1^2 \\
&= \frac{R\cos\theta-r}{R^2+r^2-2Rr\cos\theta}
\end{aligned}$$

Note the positive value of $(R-r\cos\theta)$ is taken since this ensure that dV is of a correct sign for any value of θ. Now to find V_z we need to integrate equation C.4 over 0 to 2π radians. This involves integrals of the form

$$\int \frac{\cos\theta d\theta}{a+b\cos\theta}$$

and

$$\int \frac{d\theta}{a+b\cos\theta},$$

where $a=(R^2+r^2)$ and $b=-2Rr$

These integrals have solution

$$\int_0^{2\pi}\frac{\cos\theta d\theta}{a+b\cos\theta}=\frac{2\pi}{b}-\left[\frac{2a}{b\sqrt{a^2-b^2}}\tan^{-1}\left\{\frac{\sqrt{a^2-b^2}\tan\frac{\theta}{2}}{a+b}\right\}\right]_0^{2\pi} \qquad \text{(C.6)}$$

and

$$\int_0^{2\pi}\frac{d\theta}{a+b\cos\theta}=\left[\frac{2}{\sqrt{a^2-b^2}}\tan^{-1}\left\{\frac{\sqrt{a^2-b^2}\tan\frac{\theta}{2}}{a+b}\right\}\right]_0^{2\pi} \qquad \text{(C.7)}$$

These integrals involve the solution of $\theta=\tan^{-1}\{0\}$ which is many valued. Now by inspecting the above integrals over two different regions of the wake of $r<R$ and $r>R$ the following solutions are applicable

For $r<R$ we get

$$\int_0^{2\pi}\frac{\cos\theta d\theta}{a+b\cos\theta}=-\frac{\pi}{Rr}+\frac{\pi(R^2+r^2)}{Rr(R^2-r^2)} \qquad \text{(C.8)}$$

and

$$\int_0^{2\pi}\frac{d\theta}{a+b\cos\theta}=\frac{2\pi}{R^2-r^2} \qquad \text{(C.9)}$$

Therefore the total induced velocity V_z at point P for $r < R$ is

$$V_z = 0 \tag{C.10}$$

For $r > R$ we get

$$\int_0^{2\pi} \frac{\cos\theta d\theta}{a + b\cos\theta} = -\frac{\pi}{Rr} - \frac{\pi(R^2 + r^2)}{Rr(R^2 - r^2)} \tag{C.11}$$

and

$$\int_0^{2\pi} \frac{d\theta}{a + b\cos\theta} = -\frac{2\pi}{R^2 - r^2} \tag{C.12}$$

This makes the total induced velocity of V_z of point P for $r > R$ now

$$V_z = -\frac{\gamma R}{r} \tag{C.13}$$

Now let us consider the radial component at P, dV_x, for $r > 0$. First of all let us consider the expansion

$$\sin(\theta + \alpha) = \sin\theta\cos\alpha + \sin\alpha\cos\theta$$

and apply this and the Sine Rule to equation C.5 we get

$$\begin{aligned} dV_x &= \frac{\gamma R}{2\pi r_1}\left\{\sin\theta\sqrt{1 - (\frac{r}{r_1})^2\sin^2\theta} + \cos\theta\sin\theta(\frac{r}{r_1})\right\}d\theta \\ &= \frac{\gamma R}{2\pi r_1^2} R\sin\theta d\theta \end{aligned} \tag{C.14}$$

Therefore total radial component at P will be

$$\begin{aligned} V_x &= \int_0^{2\pi} \frac{\gamma R^2\sin\theta d\theta}{2\pi(R^2 + r^2 - 2Rr\cos\theta)} \\ &= \frac{\gamma R}{4\pi r}\left[\ln(R^2 + r^2 - 2Rr\cos\theta)\right]_0^{2\pi} \\ &= 0 \end{aligned} \tag{C.15}$$

Therefore there is no radial flow throughout the flow field due to the cylindrical vortex sheet. Tangential flow exists only in the region of $r > R$. Now the point where $r = R$ is the point of discontinuity for the function of

$V_z = f(r)$. From Fourier Series Analysis we may use Dirichlet condition to find V_z at $r = R$

$$\lim_{r \to R} V_z = \frac{f(R+0) + f(R-0)}{2} \tag{C.16}$$

where $f(R+0)$ and $f(R-0)$ are the right and left hand limits of $f(R)$ at $r = R$, and represent $\lim_{\epsilon \to 0_+} f(R+\epsilon)$ and $\lim_{\epsilon \to 0_+} f(R-\epsilon)$. Therefore from equation C.10 and C.13 we get

$$\lim_{r \to R} V_z = \frac{-\gamma + 0}{2} = -\frac{\gamma}{2} \tag{C.17}$$

Appendix D

DERIVATION OF AXIAL WAKE VELOCITY.

Now consider the situation shown in figure D.1. The infinitesimal induced velocity dV_a at P consists of the induced velocity dV_1 from the semi-infinite vortex sheet above the XY plane and dV_2 which is from the reflection of the semi-infinite vortex sheet.

Now the vortex sheet strength is defined as

$$\gamma = \frac{d\Gamma}{dl} = \text{Constant}$$

Total elemental velocity induced at P is

$$d\vec{V}_a = d\vec{V}_1 + d\vec{V}_2 \tag{D.1}$$

Where $|d\vec{V}_1| = \frac{\gamma dy}{2\pi r_1}$ which is the infinitesimal induced velocity from the upper vortex sheet, and $|d\vec{V}_2| = \frac{\gamma dy}{2\pi r_2}$ which is the infinitesimal induced velocity from the reflected vortex sheet which appears to exits below the XY surface plane. Also $r_1 = \sqrt{(h - z_0)^2 + (y_0 - y)^2}$ and $r_2 = \sqrt{(z_0 + h)^2 + (y_0 - y)^2}$.

The vertical and horizontal components of dV_a are respectively as follows

$$dV_z = \frac{\gamma \cos\theta_1 dy}{2\pi\sqrt{(h - z_0)^2 + (y_0 - y)^2}} - \frac{\gamma \cos\theta_2 dy}{2\pi\sqrt{(z_0 + h)^2 + (y_0 - y)^2}} \tag{D.2}$$

$$dV_y = \frac{\gamma \sin\theta_1 dy}{2\pi\sqrt{(h-z_0)^2+(y_0-y)^2}} + \frac{\gamma \sin\theta_2 dy}{2\pi\sqrt{(z_0+h)^2+(y_0-y)^2}} \tag{D.3}$$

Where $\cos\theta_1 = (y_0-y)/r_1, \quad \sin\theta_1 = (h-z_0)/r_1$

and $\cos\theta_2 = (y_0-y)/r_2, \quad \sin\theta_2 = (z_0+h)/r_2$

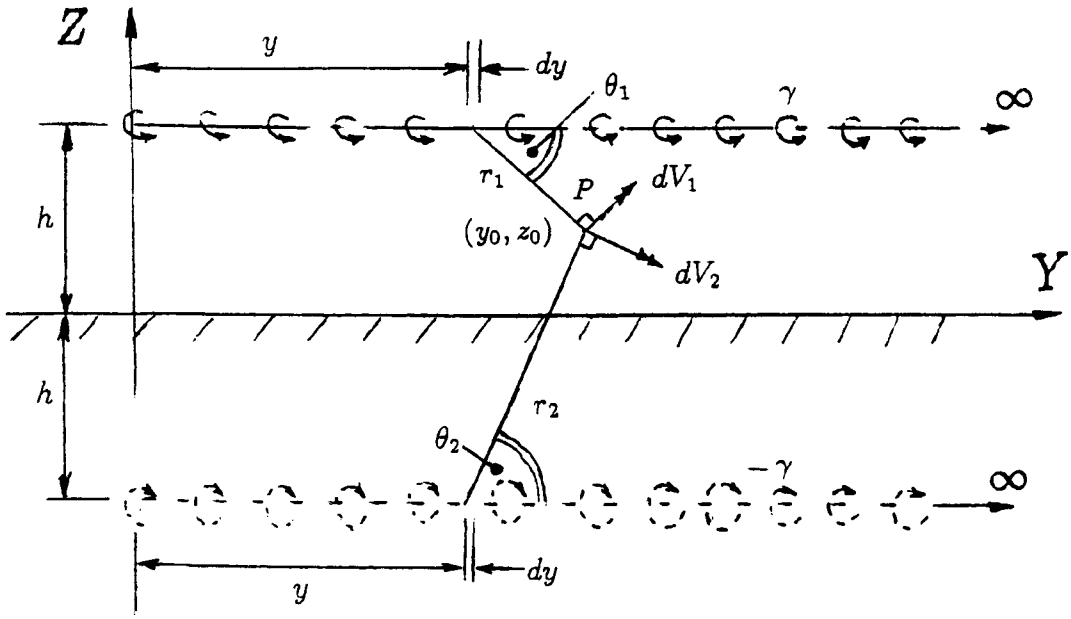

Figure D.1 Induced velocity due to a semi-infinite vortex sheet.

The total vertical induced velocity will now be for a sheet of length l

$$V_z = \frac{\gamma}{2\pi}\int_0^l \left\{ \frac{(y_0-y)}{(h-z_0)^2+(y_0-y)^2} - \frac{(y_0-y)}{(z_0+h)^2+(y_0-y)^2} \right\} dy \tag{D.4}$$

Let $u = y_0 - y \qquad du = -dy$

$$\begin{aligned} V_z &= -\frac{\gamma}{2\pi}\int_{y_0}^{y_0-l} \left\{ \frac{u}{(h-z_0)^2+u^2} - \frac{u}{(z_0+h)^2+u^2} \right\} du \\ &= \frac{\gamma}{2\pi} \ln \sqrt{\frac{((h-z_0)^2+y_0^2)((\frac{z_0+h}{y_0-l})^2+1)}{((\frac{h-z_0}{y_0-l})^2+1)((z_0+h)^2+y_0^2)}} \end{aligned} \tag{D.5}$$

Now if the vortex sheets are infinitely long l will become infinitely long

$$\therefore V_z = \frac{\gamma}{2\pi} \ln \sqrt{\frac{(h-z_0)^2 + y_0^2}{(z_0+h)^2 + y_0^2}} \tag{D.6}$$

since

$$\lim_{l \to \infty} \frac{1}{(y_0 - l)} = 0$$

Now $V_z \to 0$ as $|y_0| \to \infty$ and V_z will approach a maximum at $y_0 = 0$ as $z_0 \to h$, but $V_z = 0$ for $z_0 = 0$. You will notice a singularity at $(0, h)$ for situation shown in figure D.1.

For the total horizontal component of induced velocity the following applies

$$V_y = \frac{\gamma}{2\pi} \int_0^l \left\{ \frac{(h-z_0)}{(h-z_0)^2 + (y_0-y)^2} + \frac{(z_0+h)}{(z_0+h)^2 + (y_0-y)^2} \right\} dy \tag{D.7}$$

Let $u = y_0 - y \qquad du = -dy$

$$\begin{aligned} V_y &= -\frac{\gamma}{2\pi} \int_{y_0}^{y_0-l} \left\{ \frac{(h-z_0)}{(h-z_0)^2 + u^2} + \frac{(z_0+h)}{(z_0+h)^2 + u^2} \right\} du \\ &= \frac{\gamma}{2\pi} \left(\tan^{-1}\left(\frac{y_0 - l}{z_0 - h}\right) - \tan^{-1}\left(\frac{y_0}{z_0 - h}\right) - \tan^{-1}\left(\frac{y_0 - l}{z_0 + h}\right) + \tan^{-1}\left(\frac{y_0}{z_0 + h}\right) \right) \end{aligned} \tag{D.8}$$

Again since l is infinitely long V_y becomes

$$V_y = \frac{\gamma}{2\pi} \left(\pi + \tan^{-1}\left(\frac{y_0}{h - z_0}\right) + \tan^{-1}\left(\frac{y_0}{h + z_0}\right) \right) \tag{D.9}$$

for $z_0 < h$

when $y_0 \to -\infty \qquad V_y \to 0$

when $y_0 \to \infty \qquad V_y \to \gamma$

when $y_0 \to 0 \qquad V_y \to \frac{\gamma}{2}$

which confirms momentum theory for two dimensional flow.

If $z_0 > h$

$$V_y = \frac{\gamma}{2\pi}\left(\tan^{-1}\left(\frac{y_0}{h - z_0}\right) + \tan^{-1}\left(\frac{y_0}{h + z_0}\right)\right) \tag{D.10}$$

If $z_0 = h$ and $|y_0| > 0$

$$V_y = \frac{\gamma}{2\pi}\left(\frac{\pi}{2} + \tan^{-1}\left(\frac{y_0}{2h}\right)\right) \tag{D.11}$$

Appendix E

DERIVATION OF LATERAL WAKE VELOCITY.

Consider the induced velocity $dq\vec{_{P_2}}$ from the elemental vortex sheet of area dS. (See figure E.1). From Biot Savart we get

$$dq\vec{_{P_2}} = \frac{(\hat{n} \wedge \vec{\gamma}) \wedge \vec{r}_{AP_2} dS}{4\pi |\vec{r}_{AP_2}|^3} \tag{E.1}$$

If the sheet is of infinitesimal thickness and $|\vec{\gamma}|$ = Constant, so that $\vec{\gamma} = \hat{i}\acute{\gamma}$ and the position vector $\vec{r}_{AP_2} = (x - X)\hat{i} + y\hat{j} + (z - Z)\hat{k}$. Also the unit vector $\hat{n} = \hat{j}$. Applying this to equation E.1 we can now find the total induced velocity at P_2. Therefore we get

$$q\vec{_{P_2}} = \frac{\acute{\gamma}}{4\pi} \int_{-l/2}^{l/2} \int_{\acute{h}}^{\acute{R}} \frac{[\hat{i}y - \hat{j}(x - X)] dZ dX}{[(x - X)^2 + y^2 + (z - Z)^2]^{3/2}} \tag{E.2}$$

To solve this we need to look separately at each integration involved with equation E.2

$$\int_{\acute{h}}^{\acute{R}} \frac{y dZ}{[(x - X)^2 + y^2 + (z - Z)^2]^{3/2}}$$

Let $u = (z - Z)$, $du = -dZ$ and $k^2 = y^2 + (x - X)^2$. Applying the above substitutions to the above integral we can now consider the following integral and its solution

$$\therefore -\int \frac{du}{(u^2 + k^2)^{3/2}} = -\frac{u}{k^2\sqrt{u^2 + k^2}} + \text{Constant}$$

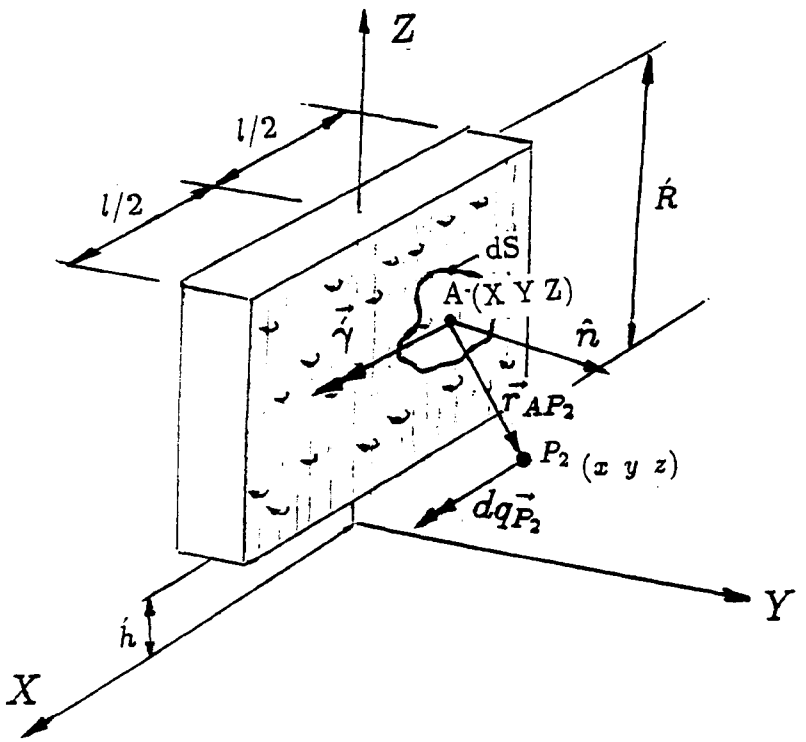

Figure E.1 Details of induced velocity from a small element dS.

$$\therefore \int_{\acute{h}}^{\acute{R}} \frac{y dZ}{[(x-X)^2+y^2+(z-Z)^2]^{3/2}}$$

$$= -\frac{(z-\acute{R})y}{(y^2+(x-X)^2)\sqrt{(z-\acute{R})^2+y^2+(x-X)^2}}$$

$$+\frac{(z-\acute{h})y}{(y^2+(x-X)^2)\sqrt{(z-\acute{h})^2+y^2+(x-X)^2}}$$

The integral in equation E.2 can now be considered w.r.t dX as follows

$$\int_{-l/2}^{l/2}\left\{-\frac{(z-\acute{R})y}{(y^2+(x-X)^2)\sqrt{(z-\acute{R})^2+y^2+(x-X)^2}}\right.$$

$$\left.+\frac{(z-\acute{h})y}{(y^2+(x-X)^2)\sqrt{(z-\acute{h})^2+y^2+(x-X)^2}}\right\}dX$$

$$\text{Let} \quad v = x - X \qquad dv = -dX$$

$$k_1^2 = (z - \acute{R})^2 + y^2 \;\text{ or }\; (z - \acute{h})^2 + y^2$$

By applying the above substitution we can now consider the following integral

$$\int \frac{dv}{(v^2 + y^2)\sqrt{k_1^2 + v^2}} \tag{E.3}$$

$$\text{Let} \quad q = \frac{v}{\sqrt{v^2 + k_1^2}}$$

$$\therefore dv = \frac{(k_1 + v^2)^{3/2} dq}{k_1^2} \tag{E.4}$$

If equation E.4 is substituted into equation E.3 we now get

$$\frac{1}{k_1^2} \int \frac{(k_1^2 + v^2)}{(v^2 + y^2)} dq = \int \frac{dq}{(y^2 + (k_1^2 - y^2)q^2)}$$

$$= \frac{1}{y\sqrt{(k_1^2 - y^2)}} \tan^{-1}\{q\sqrt{(k_1^2/y^2 - 1)}\} + \text{Constant}$$

$$= \frac{1}{y\sqrt{(k_1^2 - y^2)}} \tan^{-1}\left(\frac{v\sqrt{(k_1/y)^2 - 1}}{\sqrt{v^2 + k_1^2}}\right) + \text{Constant}$$

Returning to equation E.2 we have finally using the above results

$$\begin{aligned}
\hat{i}.\vec{q_{P_2}} \;=\; & \frac{\acute{\gamma}}{4\pi}\Bigg\{\tan^{-1}\left[\frac{(z - \acute{R})(x - l/2)}{y\sqrt{(z - \acute{R})^2 + (x - l/2)^2 + y^2}}\right] \\
& - \tan^{-1}\left[\frac{(z - \acute{R})(x + l/2)}{y\sqrt{(z - \acute{R})^2 + (x + l/2)^2 + y^2}}\right] \\
& - \tan^{-1}\left[\frac{(z - \acute{h})(x - l/2)}{y\sqrt{(z - \acute{h})^2 + (x - l/2)^2 + y^2}}\right] \\
& + \tan^{-1}\left[\frac{(z - \acute{h})(x + l/2)}{y\sqrt{(z - \acute{h})^2 + (x + l/2)^2 + y^2}}\right]\Bigg\}
\end{aligned} \tag{E.5}$$

As the length of sheet extends to infinity ie $l \to \infty$, equation E.5 becomes

$$\begin{aligned}\hat{i}.q_{\vec{P_2}} &= \frac{\acute{\gamma}}{2\pi}\left\{-\tan^{-1}\left(\frac{z-\acute{R}}{y}\right)+\tan^{-1}\left(\frac{z-\acute{h}}{y}\right)\right\} \\ &= V_x \end{aligned} \tag{E.6}$$

Let us consider the vertical component of $q_{\vec{P_2}}$.

$$\begin{aligned}\hat{j}.q_{\vec{P_2}} &= \frac{\acute{\gamma}}{4\pi}\int_{-l/2}^{l/2}\int_{\acute{h}}^{\acute{R}}\frac{(X-x)dZ\,dX}{[(X-x)^2+y^2+(Z-z)^2]^{3/2}} \\ &= V_y \end{aligned} \tag{E.7}$$

Consider the integration

$$\int_{-l/2}^{l/2}\frac{(X-x)dX}{[(X-x)^2+y^2+(Z-z)^2]^{3/2}}$$

Let $u = X - x$ $du = dX$ and $k_1^2 = y^2 + (Z-z)^2$.

The above integral becomes

$$\int \frac{u\,du}{(u^2+k_1^2)^{3/2}}.$$

If $u^2 + k_1^2 = v^2$

then $v\,dv = u\,du$

$$\int\frac{v\,dv}{v^3} = -\frac{1}{v} + \text{Constant}$$

$$\therefore \int_{-l/2}^{l/2}\frac{(X-x)dX}{((X-x)^2+y^2+(Z-z)^2)^{3/2}}$$

$$= -\{(x-l/2)^2+y^2+(Z-z)^2\}^{-1/2} + \{(x+l/2)^2+y^2+(Z-z)^2\}^{-1/2}$$

Finally we have for the integral in equation E.7

$$\int_{\acute{h}}^{\acute{R}}\left\{-\{(x-l/2)^2+y^2+(Z-z)^2\}^{-1/2}+\{(x+l/2)^2+y^2+(Z-z)^2\}^{-1/2}\right\}dZ$$

Let $u = z - Z$ $du = -dZ$

and $k_2^2 = y^2 + (x-l/2)^2$ or $y^2 + (x+l/2)^2$

With the above substitutions we can now consider the following integral with its solution

$$\int \frac{du}{\sqrt{u^2 + k_2^2}} = \ln|u + \sqrt{u^2 + k_2^2}|.$$

Therefore the Y component of induced velocity will finally be

$$\begin{aligned} V_y &= \frac{\acute{\gamma}}{4\pi}\left\{\ln\left|\frac{(z-\acute{R}) + \sqrt{(z-\acute{R})^2 + (x-l/2)^2 + y^2}}{(z-\acute{h}) + \sqrt{(z-\acute{h})^2 + (x-l/2)^2 + y^2}}\right|\right. \\ &\quad \left. - \ln\left|\frac{(z-\acute{R}) + \sqrt{(z-\acute{R})^2 + (x+l/2)^2 + y^2}}{(z-\acute{h}) + \sqrt{(z-\acute{h})^2 + (x+l/2)^2 + y^2}}\right|\right\} \end{aligned} \tag{E.8}$$

If the length $l \rightarrow \infty$ then $V_z \rightarrow 0$. Therefore there are no Y or Z components for the induced velocity $q\vec{_{P_2}}$ associated with a vortex strip of infinite length, only an X component.

Appendix F

AIR FLOW MEASUREMENT METHODOLOGY FOR WIND TUNNEL WORK.

This initial research work at Queen Mary and Westfield College (QMWC) involved wind tunnel test work on a model wind concentrator, details of which are given in chapters 4 and 5. In order to conduct these test properly air flow measuring equipment had to be calibrated and later a tunnel scan performed without any model present, (see chapter 4 on details of the tunnel scan).

In chapter 4, figure 4.2 shows details of the type of Total Pressure Probe used in the wake traverse tests at QMWC. Ideally a five tube probe is the most effective means of measuring three dimensional flow. The calibration methodology is covered by Bryer etal(1971) for this type of instrument. Unfortunately the time allowed to do the wind tunnel work was very limited and there would not have been sufficient time to do calibration and wind tunnel test work. Therefore a three tube probe was used which could be rotated about the Y axis as shown in figure F.1. From Bryer etal the methodology used to calibrate the five tube probe is modified slightly for the three tube arrangement.

$$K_p = \frac{p_0 - p_m}{1/2\rho|\vec{q}|^2} \tag{F.1}$$

$$f(\vartheta) = \frac{p_2 - p_1}{p_0 - p_m} = -f(\varphi) \qquad \text{(F.2)}$$

where $p_m = (p_1 + p_2)/2$

By yawing the instrument in unidirectional flow and measuring the Total Pressures p_0, p_1 and p_2 from the three tubes 0,1 and 2 respectively, calibration graphs as shown in figures F.2 and F.3 can be created. Once this is done the instrument will be used in such a way that it will not be yawed during any test work and only the three pressures p_0, p_1, p_2 will need to be measured in both the horizontal and vertical planes in order to find the $|\vec{q}|^2$, ϑ and φ. This is achieved by measuring the pressures and then rotating the instrument about the Y axis as shown in figure F.1 through 90°. The pressures are then measured a second time. This allows the three tube probe to operate approximately like a five tube probe.

The next step is to calculate $f(\vartheta)$ and $f(\varphi)$. This allows both ϑ and φ to be found. If the flow angles are known then the calibration constant K_p can be found from figure F.3 which finally enables us to obtain $|\vec{q}|$.

From Bryer etal the methodology for a 5 tube probe has shown good accuracy for measurements provided ϑ and φ are limited to ±40°. From figures F.2 and F.3 show a similar trend.

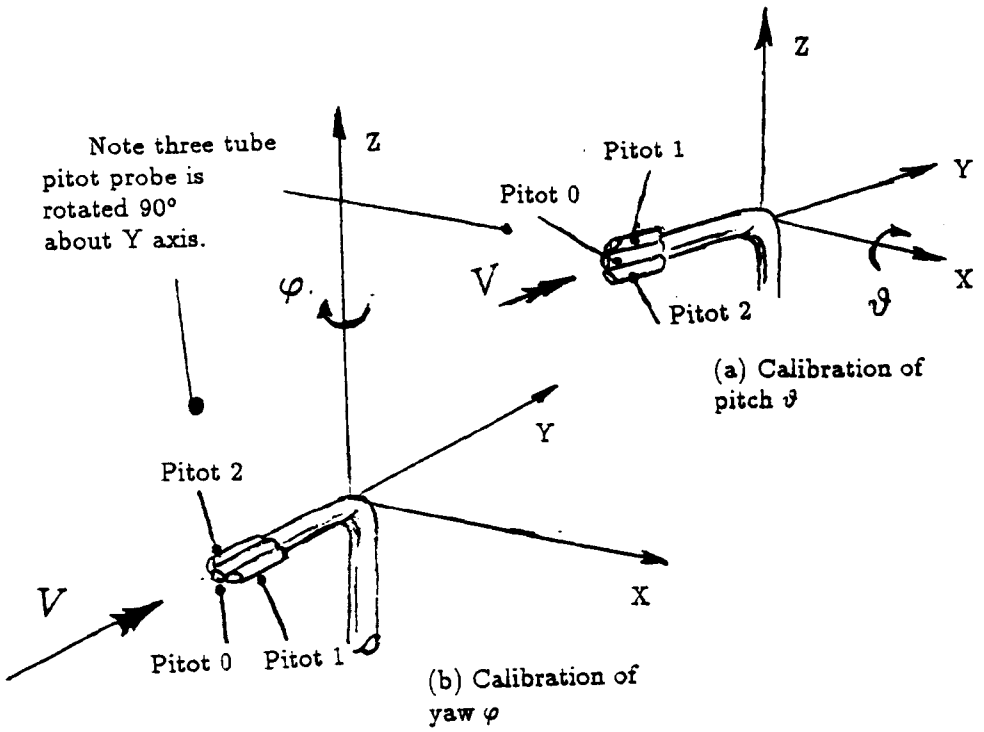

Figure F.1 Operation of the three tube probe used in the experiments at QMWC.

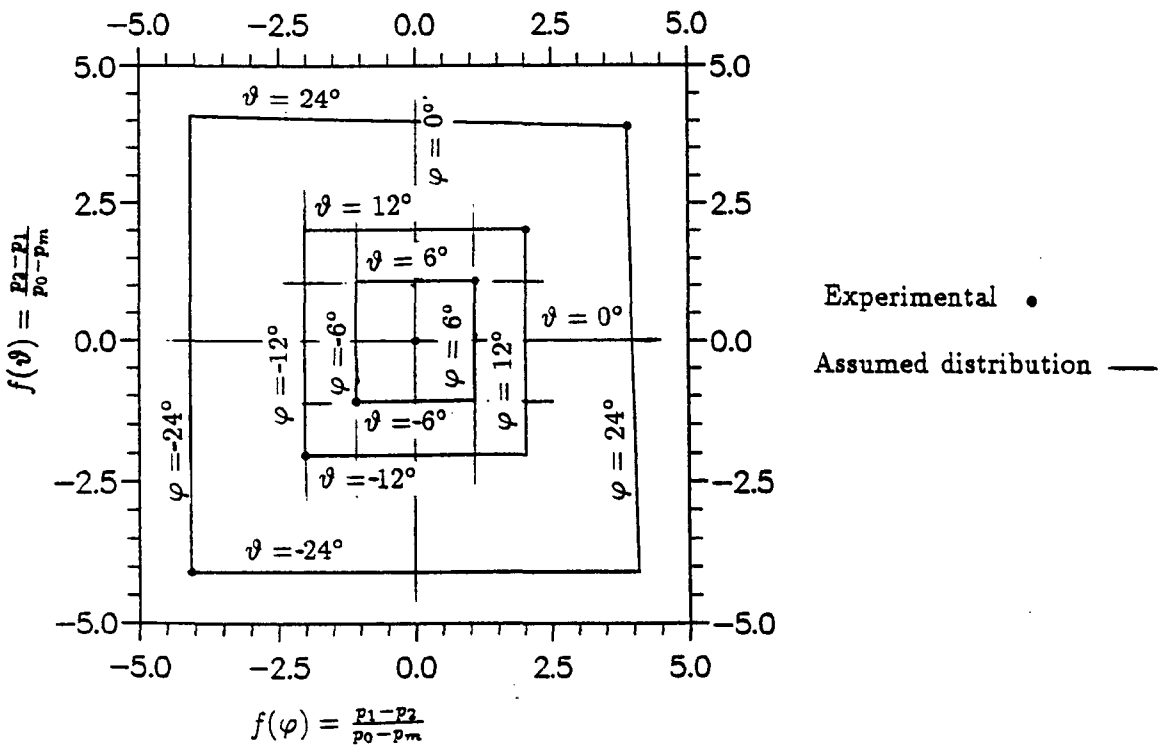

Figure F.2 Calibration graph for yaw angles ϑ and φ.

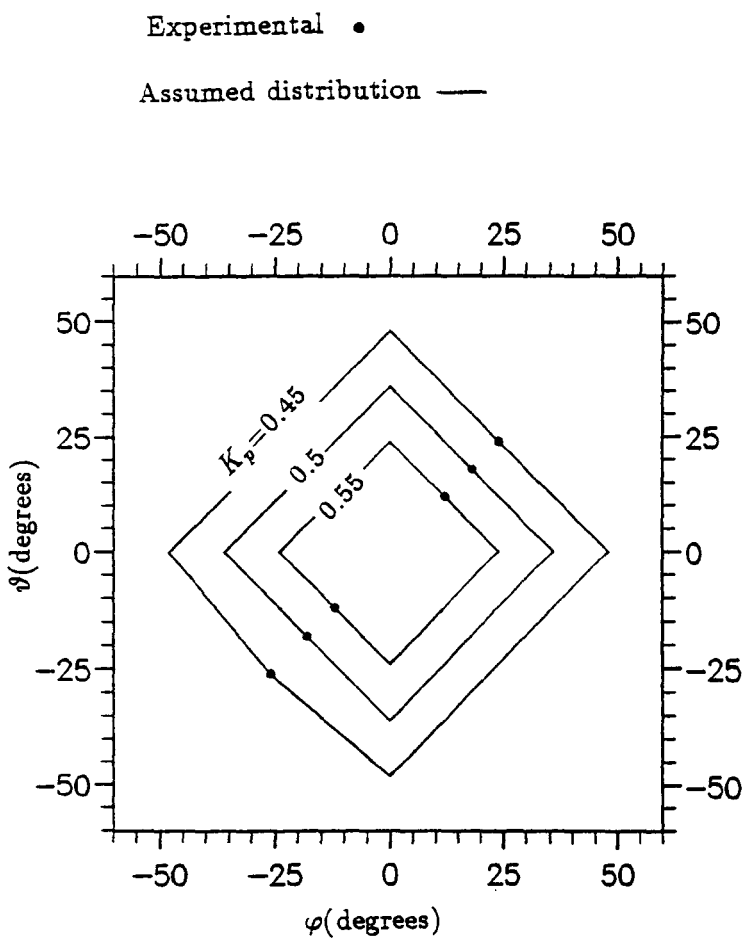

Figure F.3 Calibration graph to find K_p from known yaw and pitch angles.

Appendix G

DATA LOGGING FOR FIELD TEST WORK.

G.1 Introduction.

In order to test the Concentrator Wind Turbine in the field the right logging equipment was needed. This meant Dynamic Response Analysis was needed to find the Frequency Response of the system in order to determine the correct sampling frequency for logging data without the results being subject to an erroneous effect called 'Aliasing'. (See Newland(1971)). The logged data was then used to investigate the Wind Concentrator's ability to damp out wind turbulence at the core flow.

G.2 Theoretical response of a wind turbine.

Figure G.1 shows a horizontal axis wind turbine experiencing a change in wind speed of δV from the steady state value V_0. This will immediately cause an imbalance between the assumed constant torque load T_0 and the varying aerodynamic torque T_A. Since T_A is a function of the shaft speed Ω and wind speed V the following equation will apply

$$T_A = T_0 + (\frac{\partial T}{\partial \Omega})\delta\Omega + (\frac{\partial T}{\partial V})\delta V \qquad \text{(G.1)}$$

This means that the angular acceleration can be expressed as

$$T_A - T_0 = I\alpha \tag{G.2}$$

Combining equations G.1 and G.2, we get

$$(\frac{\partial T}{\partial \Omega})\delta\Omega + (\frac{\partial T}{\partial V})\delta V = I\alpha \tag{G.3}$$

The angular speed at any instant can be expressed as follows

$$\Omega = \Omega_0 + \delta\Omega \tag{G.4}$$

where Ω_0 is the steady state angular velocity. This means that equation G.3 can be expressed as a differential equation

$$\frac{d(\delta\Omega)}{dt} - (\frac{T_\Omega}{I})(\delta\Omega) = \frac{T_V}{I}(\delta V) \tag{G.5}$$

The turbulence in the air is of a complex nature but can be adequately represented as a cyclic forcing function. If we consider a disturbance of constant amplitude and of a particular frequency ω the free stream air velocity will now be written as follows

$$V = V_0 + \delta V_0 \sin\omega t \tag{G.6}$$

Equation G.5 can be solved by assuming a particular solution for $\delta\Omega$ of the form

$$\begin{aligned} \delta\Omega &= \delta\Omega_0 \sin(\omega t - \Phi) \\ &\quad Im\{\delta\Omega_0 e^{i(\omega t - \Phi)}\} \end{aligned} \tag{G.7}$$

If we substitute equation G.7 into equation G.5 and writing $\delta V = \delta V_0 \sin\omega t$ for equation G.6 we get

$$\delta\Omega_0 Im\{(i\omega - (\frac{T_\Omega}{I}))e^{i(\omega t - \Phi)}\} = Im\{(\frac{T_V}{I}\delta V_0)e^{i\omega t}\} \tag{G.8}$$

The particular solution to equation G.5 is derived from equations G.7 and G.8

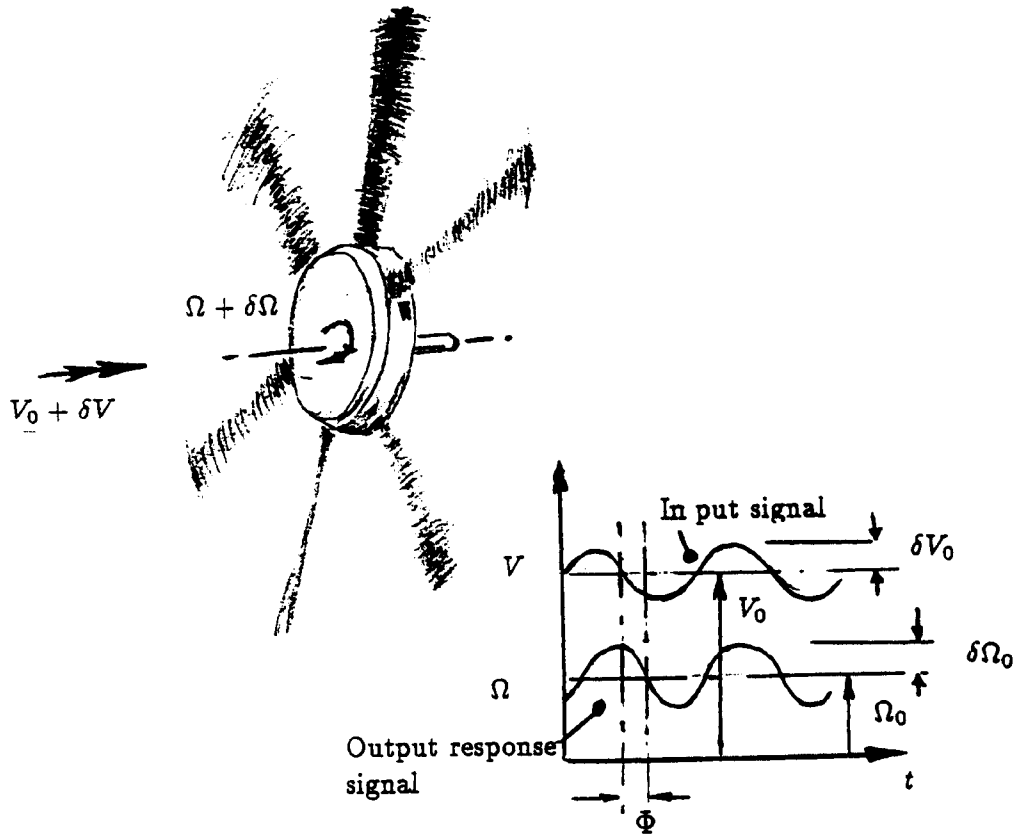

Figure G.1 Frequency Response of a Wind Turbine.

T_s	C_Q
1.9	0.1621
2.1	0.1615
2.3	0.1544
2.5	0.1475
2.7	0.1295
2.9	0.1224
3.1	0.1082
3.3	0.0924
3.5	0.0646
3.7	0.0642

Turbine Details
N_B=6, r_R=0.455m
Hub Radius=0.2m
Assumed Blade Section=Gö579
$\Theta = 16°$
Tip loss Model:Prandtl

Table G.1 Torque Characteristics of the WG910 Wind Turbine.

Lengths (mm)	
t_B	6
t_{HUB}	50
t_m	30
r_1	28
r_2	77.5
h_H	25
r_H	12.5
c	79
l_B	358
$\bar{r}$	250
r_{HUB}	120

Densities(kg/m^3)	
Hub ρ_H	1840
Blades ρ_B	1115
Magnets ρ_m	7840

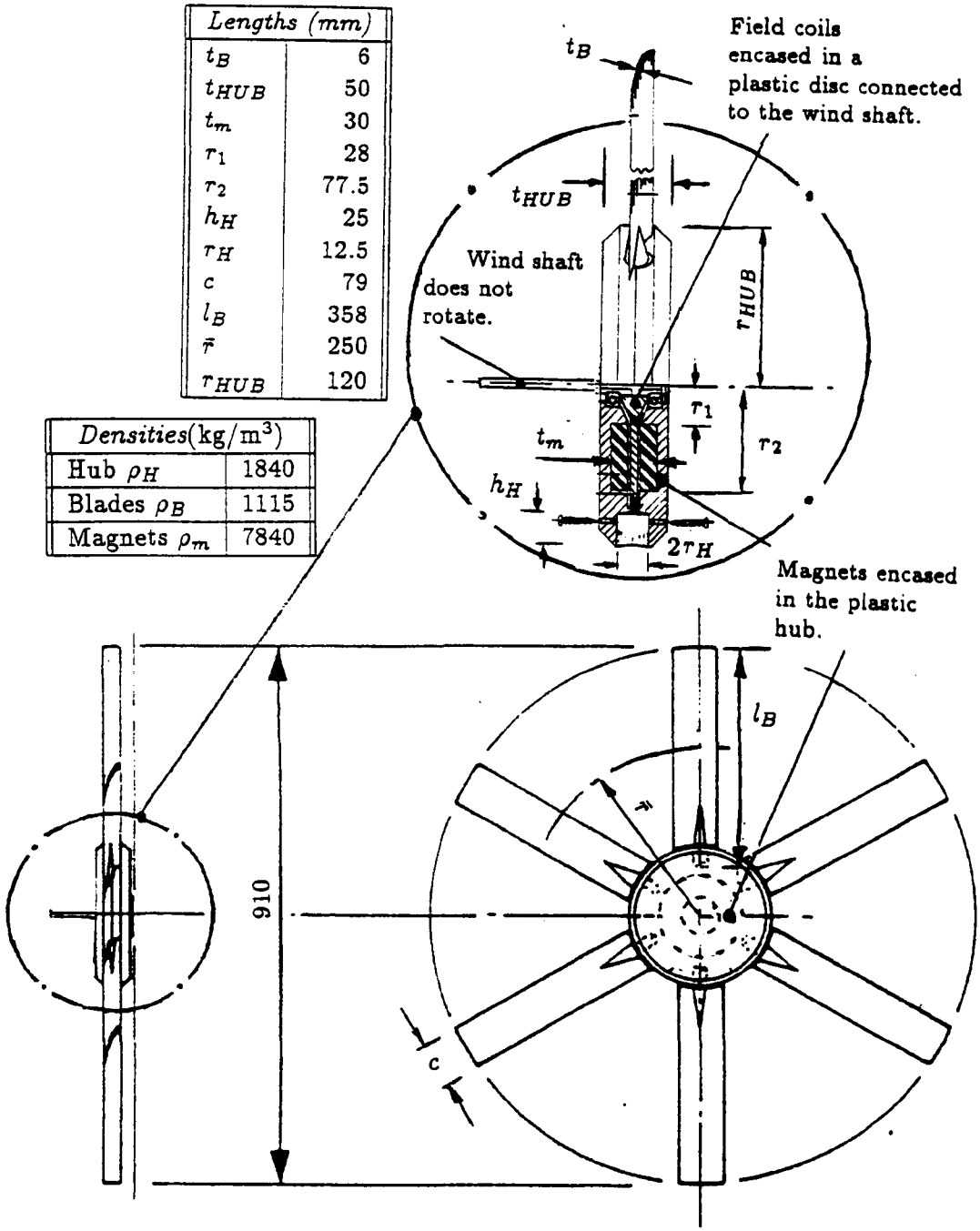

Polar Moment of Inertia (kgm^2)		
Hub	$\simeq \frac{1}{2}\rho_H(r_{HUB}^2 t_{HUB} - 6r_H^2 h_H - (r_2^2 - r_1^2)t_m)\pi r_{HUB}^2$	0.022
Blades	$\simeq 6((l_B^2 + c^2)/12 + \bar{r}^2)cl_B t_B \rho_B$	0.084
Magnets	$\simeq \frac{1}{2}\rho_m \pi t_m (r_2^4 - r_1^4)$	0.0131
	Total	0.1191

Figure G.2 Details of wind turbine rotor inertia.

$$\begin{aligned}\delta\Omega &= Im\left\{\frac{(T_V/I\delta V_0)e^{i\omega t}}{(i\omega-(T_\Omega/I))}\right\} \\ &= \frac{(T_V/I\delta V_0)\sin(\omega t-\Phi)}{\sqrt{\omega^2+(T_\Omega/I)^2}} \qquad \text{(G.9)}\end{aligned}$$

$$\Phi = -\tan^{-1}\left(\frac{\omega I}{T_\Omega}\right) \qquad \text{(G.10)}$$

From equation G.9 the gain of the system can be written, for a constant harmonic output frequency of ω, as follows

$$\frac{\delta\Omega_0}{\delta V_0} = \frac{T_V}{I\sqrt{\omega^2+(T_\Omega/I)^2}} \qquad \text{(G.11)}$$

If $\omega = 2\pi f$ equation G.11 can be written for the frequency of disturbance as

$$f = \frac{1}{2\pi}\sqrt{(T_V\delta V_0/(\delta\Omega_0 I))^2-(T_\Omega/I)^2} \qquad \text{(G.12)}$$

The operating point for the wind turbine is indicated in figure 4.10 of chapter 4. The figure shows that the operating point is approximately unchanged for different wind velocities, with $T_s = 3.2$ and $(C_p)_{ss} = 0.32$. Now table G.1 enables us to find the partial coefficients of T_V and T_Ω.

$$T_\Omega = \frac{\partial T}{\partial\Omega} = \frac{1}{2}\rho\pi r_R^2 V_0^2\frac{d(C_Q)}{d\Omega} \qquad \text{(G.13)}$$

To solve $\frac{d(C_Q)}{d\Omega}$ we must investigate the definition of Tip speed Ratio

$$\begin{aligned}\Omega_0 &= \frac{V_0 T_s}{r_R} \\ \therefore \delta\Omega_0 &= \frac{V_0\delta T_s}{r_R} \qquad \text{(G.14)}\end{aligned}$$

$$\text{Now} \qquad \frac{dC_Q}{d\Omega} \simeq \frac{\delta C_Q}{\delta\Omega_0} = \frac{r_R\delta C_Q}{V_0\delta T_s} \qquad \text{(G.15)}$$

If $r_R = 0.455$m and $\rho = 1.225$m/s then from table G.1

$$\frac{\delta C_Q}{\delta\Omega_0} = \frac{0.455(0.1082-0.0924)}{V_0(3.1-3.3)} = \frac{-0.035945}{V_0}$$

Substituting this in equation G.13 we get

$$T_\Omega = -0.0143193 V_0 \tag{G.16}$$

As for T_V the following applies

$$\begin{aligned} T_V &= \frac{\partial T}{\partial V} \\ &= (\rho V_0 (C_Q)_{ss} + \frac{d}{dV}(C_Q)\rho\frac{1}{2}V_0^2)\pi r_R^2 \end{aligned} \tag{G.17}$$

From table G.1 the steady state point for C_Q is $(C_Q)_{ss} = 0.1$ at $T_s = 3.2$. If we consider the definition of T_s again we can find δV_0 as follows

$$\frac{dV}{dT_s} = -\Omega_0 \frac{r_R}{T_s^2} \simeq \frac{\delta V_0}{\delta T_s} \tag{G.18}$$

$$\therefore \quad \frac{\delta C_Q}{\delta V_0} = -\frac{\delta C_Q T_s^2}{\Omega_0 r_R \delta T_s} \tag{G.19}$$

If $\Omega_0 = \frac{V_0 T_s}{r_R} = 7.03 V_0$ then equation G.19 becomes

$$\frac{\delta C_Q}{\delta V_0} = \frac{0.2529354}{V_0} \tag{G.20}$$

$$\therefore \quad T_V \simeq 0.1803786 V_0 \tag{G.21}$$

The Polar Moment of Inertia I for the wind turbine rotor has been calculated from the information given in figure G.2 to be $I = 0.118\text{kgm}^2$. In figure G.3 gives the frequency response for wind turbine systems for different wind speeds V_0. Note that the gain at zero frequency is the same for different wind speeds. The criterion for avoiding 'Aliasing' is that the sampling rate for measurements in field should be 2.5 times the cut off frequency which is shown in figure G.3 as f_c. (See Infield(1989) for further information). If we define f_c to be where the gain has dropped to 10% of the gain at zero output frequency, we can then write for $\delta\Omega_0$ using equation G.11 with $\omega = 0$ for $(\delta\Omega_0/\delta V_0)$

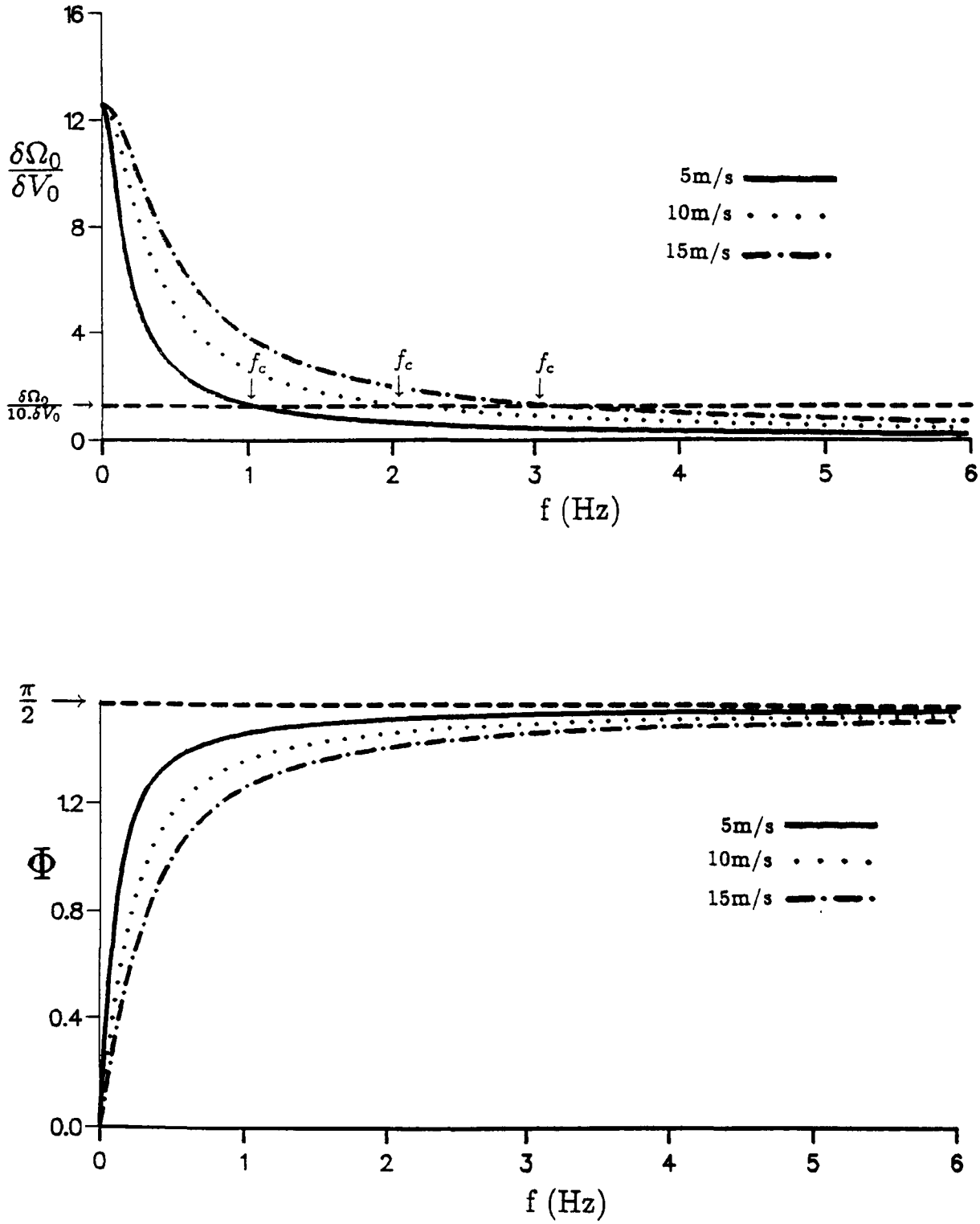

Figure G.3 Frequency Response curves for WG910 at different wind speeds.

$$\begin{aligned} \delta\Omega_0 &= (\frac{\delta\Omega_0}{\delta V_0})_{\omega=0}\frac{\delta V_0}{10} \\ &= \frac{T_V \delta V_0}{10 T_\Omega} \end{aligned} \tag{G.22}$$

Substituting this into equation G.12 we get for the cut off frequency f_c

$$\begin{aligned} f_c &= 1.5836\frac{T_\Omega}{I} \\ &= 0.2125 V_0 \end{aligned} \tag{G.23}$$

Equation G.23 is independent of turbulence intensity 'TI', since the criterion to avoid Aliasing was based on particular signal output amplitude reducing to a fraction of its value at zero output frequency. The highest value of velocity that was experienced in the field was $V_0 = 15\text{m/s}$. Therefore the minimum sampling rate to avoid Aliasing would be 8Hz. The selection of logging equipment was mainly dependent on the equipment being able to log information fast enough to avoid Aliasing effects. Fortunately the type of data logger used in the test work had a maximum sampling rate of 10Hz which proved adequate. (The data logger was a 'M1600 Microdata' Data Logger).

G.3 Response of a Anemometer.

Figure G.4 gives details of the type of anemometer used in the field tests. In the selection of such an instrument one of the factors which was involved in the selection process was its ability to respond fast enough. To investigate this, Frequency Response Analysis was conducted on the instrument.

Now for a particular anemometer the effectiveness of the instrument is judged by its 'Distance Constant'. It is defined as the length of wind run which must pass the anemometer for its output to reach within $1/e$ of its final value. Figure G.4 indicates this as a time constant τ. Now the six cup anemometer has a 1m distance constant which means τ would be

$$\tau = \text{Distance Constant}/(V_0 + \delta V_0)$$

Now for a particular anemometer of time constant τ and a gain of k the following system equation applies

$$\tau\dot{\Omega} + \Omega = kV \tag{G.24}$$

Let us consider the output of the system for a unit impulse. The rotational variation of the system $\Omega(t)$ will have a Fourier Transform of

$$\Omega(\omega) = \int_0^\infty \Omega(t)e^{-i\omega t}dt = H(\omega) \tag{G.25}$$

From this it will also follow that

$$\dot{\Omega}(\omega) = \int_0^\infty \dot{\Omega}(t)e^{-i\omega t}dt = i\omega H(\omega) \tag{G.26}$$

If we take the Fourier Transform of both sides in equation G.24 and apply the identities from equations G.25 and G.26 as well, observing the fact that the Fourier Transform for a unit impulse of wind $V(t) = \delta(t)$ is unity, we get

$$H(\omega) = \frac{k}{\sqrt{1 + (\tau\omega)^2}} \tag{G.27}$$

The definition of the cut off frequency f_c is such that $H(\omega) = k/10$. The maximum operating frequency of the instrument must be greater than that of the data logger sampling frequency for the instrument to be effective. Therefore the instrument f_c from equation G.27 will be

$$f_c = \frac{9.95}{\tau} = 9.95(V_0 + \delta V) \tag{G.28}$$

Comparing this with equation G.23 the instrument was clearly suitable for field test work.

G.4 Time Series Analysis on field data.

The two previous sections dealt with the necessary investigation on the wind turbine and the anemometer Frequency Response in order to record data

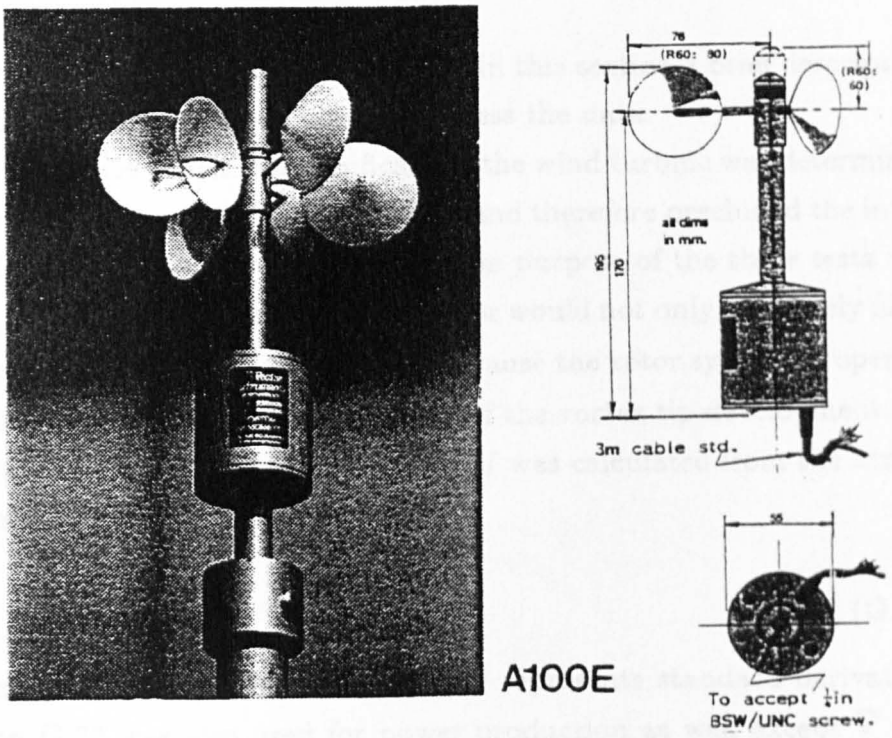

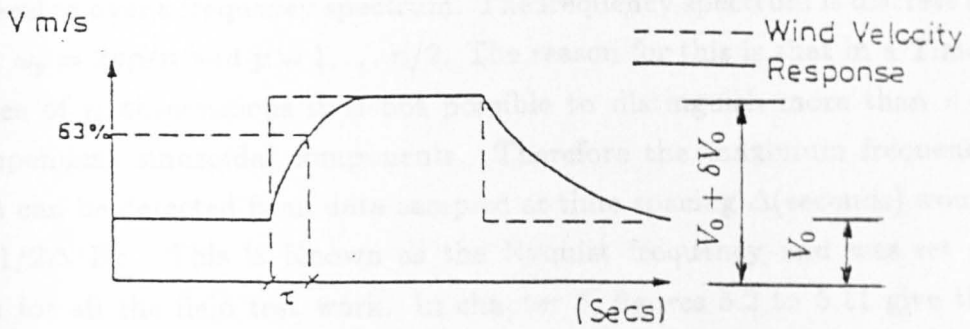

Figure G.4 Details of Anemometer used in field tests.

ANEMOMETER DETAILS.
Type:A100E (Vector Instruments).
Speed range: 0-26m/s
Distance Constant: 1m ± 15%
(fast response 6 cup rotor,R60)
Signal output: Pulse or analogue.

properly when sampling data in the field. In this section a brief description will be made of the methods used to process the data.

Air turbulence which was significant to the wind turbine was determined by the inertial characteristics of the rotor and therefore precluded the influence of higher turbulence effects. The main purpose of the these tests was to see if the vortex wake of the concentrator would not only effectively filter out higher frequency turbulence but also cause the rotor system to operate more smoothly due to the inertial effects of the vortex tip development. To investigate this the turbulence intensity TI was calculated from the simple relationship

$$TI = \frac{\sigma}{\overline{V}} \tag{G.29}$$

where $\overline{V}$ is mean wind speed while σ represents standard derivation. Equation G.29 was also used for power production as well except $\overline{V}$ was replaced by mean power. In equation 4.8 of chapter 4 the definition of Power Spectral Density is given. This allows us to see how the variance is generated over a frequency spectrum. The frequency spectrum is discrete in that $\omega_p = 2\pi p/n$ and $p = 1, \ldots n/2$. The reason for this is that in a Times Series of n observations it is not possible to distinguish more than $n/2$ independent sinusoidal components. Therefore the maximum frequency that can be detected from data sampled at time spacing Δ(seconds) would be $1/2\Delta$ Hz. This is Known as the Nyquist frequency and was set at 5Hz for all the field test work. In chapter 5, figures 5.2 to 5.11 give the results of Times Series Analysis conducted on the CWT. The area under these graphs represents the variance in each case. The data processing to produce these graphs was achieved by a NAG routine called G13CBF, which uses a trapezium frequency (Daniell) window to achieve Spectral Smoothing during the Univariate Time Series Analysis.

Appendix H

PUBLISHED PAPERS.

Papers reprinted from the following;

- *Design and Testing of a Concentrator Wind Turbine.*
  Wind Energy Conversion 1990.
  Proceedings of the 12th BWEA Wind Energy Conference.

- *Design and Testing of a Concentrator Wind Turbine.*
  Wind Engineering. Volume 14 No.5 1990.

Design and testing of a concentrator wind turbine

D A OLIVIERI, D SHARPE, G A BOYLE and D A TAYLOR
EERU, Open University, UK

SYNOPSIS Early attempts to assess the potential of the Concentrator Wind Turbine (CWT) were described in references 1 to 2, neither of which gave a full assessment. This paper re-examines the CWT using an analytical and numerical approach. This is later compared with experimental data from reference 3 and tests done at Queen Mary and Westfield College. (The project is currently at a interim stage.)

NOTATION.

c =Local chord of concentrator blade.
C_D =Local drag coefficient of concentrator blade.
C_p =Coefficient of performance.
C_R =Concentrator ratio.
E =Loss of energy of system.
H_1 =Total pressure head downstream of the concentrator blades.
H_0 =Total pressure head upstream of the concentrator blades.
h =Inner radius of concentrator.
$\acute{h}$ =Inner radius of concentrator wake.
N =Number of blades of the concentrator.
P =Power of the wind turbine.
p =Pressure increment across concentrator.
$\vec{q}_{P_2}$ =Induced velocity vector at point P_2 due to infinite vortex strips representing bound vortices.
Q =Heat transfer.
r =Radial distance from axis of symmetry of concentrator.
R =Outside radius of the concentrator.
$\acute{R}$ =Outside radius of the concentrator wake.
S =Surface area of vortex sheets.
t =Unit time.
T =Drag thrust on concentrator blades.
T_Q =Torque on concentrator blades.
u =Axial velocity across concentrator blades.
u_1 =Axial far wake velocity between outside and inboard trailing vortices.
V =Free stream velocity.
V_a =Total induced velocity from semi-infinite sheets representing the cylindrical component of the trailing vortices.
V_1, V_2 =Respective upper and lower contributions of induced velocity about the X Y plane constituting V_a.
V_c =Flow velocity through the core.
V_r =Resultant flow velocity through the blades.
V_T =Tangential flow velocity downstream of the blades. V_t =Tangential flow velocity due to bound vortices only.
V_x =X component of induced velocity $\vec{q}_{P_2}$.
V_y =Axial component of induced velocity V_a.
W =Work transfer.
x, y, z =Spacial coordinates of point of induced velocity relative to X, Y, Z axes.
X, Y, Z =Spacial coordinates of any point on infinite vortex strips representing the bound vortices relative to X, Y, Z axes.
ω =Angular velocity of wake flow in radians.
ρ =Air density.
Γ =Vortex circulation strength.
$\gamma, \gamma'', \acute{\gamma}$ =Vortex distribution of circulation strength per unit length of the vortex sheet, for cylindrical component of trailing vortices, axial component of trailing vortices and bound vortices respectively.
β_1, β_2 =Inboard and outboard helical vortex angles.
β =Helical vortex angle.
ϕ =Angular displacement about axis of symmetry between two adjacent blade span axes.

1 INTRODUCTION.

A major constraint in conventional wind turbine design is the reduction in rotational speed as the size of the rotor is increased . This means expensive gearboxes are unavoidable. The rotor also becomes considerably more complicated in design and heavy as the size increases to mitigate working stresses.

Flow concentrators have been pursued in an attempt to alleviate these problems, but these usually incur the expense of high structural weight and size. (Reference 4) .The Helical Vortex Wind Concentrator is a recent addition to the list of flow concentrator types. Its full potential is as yet unknown.

The CWT consists of a Helical Vortex Wind Concentrator and a wind turbine. The wind concentrator is an annular disc of stationary,radial,aerofoil sectioned blades which entrain the wind, through the orifice formed by the surrounding blades, onto the wind turbine downstream, whose diameter is no larger than that of the orifice. The vortex shedding

from the inboard tips of the stationary blades causes the entrainment effect to take place. (See figure 1). It is the main aim of this research project to predict the performance of the CWT by wake analysis only. With this method of analysis the CWT can be designed from a specified blade circulation distribution, number of blades, R/h ratio and blade.

2 CONCENTRATOR THEORY.

2.1 Energy and Momentum.

The balance of energy of a Helical Vortex Wind Concentrator is considered most conveniently by assuming the concentrator to be stationary in a stream of air of velocity V directed along its axis. Considering only the blade elements at distance r from the axis, the power put into the concentrator is zero. The drag thrust dT operates on air moving with the axial velocity u and does the work $-u\frac{dT}{dr}$ in unit time. Similarly the torque dT_Q operates on air moving with the angular velocity $\frac{1}{2}\omega$ and does the work $\frac{1}{2}\omega\frac{dT_Q}{dr}$ in unit time. Hence if $\frac{dE}{dr}$ is the rate of loss of energy of the system, the energy equation becomes

$$\frac{dQ}{dt} - \frac{dW}{dt} = -u\frac{dT}{dr} + \frac{1}{2}\omega\frac{dT_Q}{dr} + \frac{dE}{dr} = 0 \quad (1)$$

since there has been no heat transfer Q or work transfer W. Now the rate of energy loss is due to the profile drag of N blade elements, each experiencing the resultant velocity V_r due to the induced velocity from the local blade circulation and free stream velocity V, is as follows

$$\frac{dE}{dr} = \frac{1}{2}Nc\rho V_r^3 C_D \quad (2)$$

Where C_D and c are the local drag coefficient and chord respectively.

The energy of the air is represented by its total pressure head which is constant across the concentrator if C_D is small. As the air passes through the concentrator disc it reduces in pressure by $\dot{p}$ by virtue of an increase in angular velocity ω without any change in axial and radial components of velocity, and hence the increase of total pressure head is

$$H_1 - H_0 = -\dot{p} + \frac{1}{2}\rho\omega^2 r^2 = 0 \quad (3)$$

$$\therefore \qquad \dot{p} = \frac{1}{2}\rho\omega^2 r^2 \quad (4)$$

This effect on the air is due to an energy exchange process between the drag thrust and the torque $(-udT + \frac{1}{2}\omega dT_Q)$ on a volume of air $2\pi r u dr$. Hence

$$-u\frac{dT}{dr} + \frac{1}{2}\omega\frac{dT_Q}{dr} = 2\pi r u(-\dot{p} + \frac{1}{2}\rho\omega^2 r^2) = 0 \quad (5)$$

But the element of drag thrust is clearly equal to the decrease of pressure over the annulus, or

$$\frac{dT}{dr} = 2\pi r\dot{p} \quad (6)$$

and the element of torque is equal to the angular momentum imparted to the air in unit time, or

$$\frac{dT_Q}{dr} = 2\pi\rho u\omega r^3 \quad (7)$$

These two expressions are consistent with the previous equation for energy, since the constant total pressure head is due to the exchange between drag thrust and torque of blade elements respectively.

2.2 Blade Element Theory.

Applying Blade Element Theory at first sight seems the obvious approach but in fact this proved to be an inadequate method for determining vortex wake geometry. The Blade Element Theory was developed on the assumption of negligible wake swirl and trailing vortex effects, this is clearly not the case with the concentrator. (Note that $u < (V + u_1)/2$, see figure 1). The trailing vortices coming off each blade element would constitute a roll up into two discrete vortices of equal and opposite strength. The accuracy of the helical vortex angles of the two discrete vortices, (shown as β_1 and β_2), and their position in space is of great importance for determining the increase in flow velocity through the core. (See figure 1).

2.3 Biot Savart Theory.

The problems encountered in subsection 2.2 indicated a need for a method which took into account the interdependent nature of the wake. Biot Savart Theory if applied to a free wake scheme would solve this problem. This is covered numerically in section 3.

An analytical approach will be adopted involving a semi-prescribed cylindrical wake, the initial problem being the determination of angles β_1 and β_2. Figures 2 and 3 show the method of analysis. The flow is assumed to be inviscid and incompressible throughout. Each blade with its wake is represented as a horse shoe vortex of rectangular blade circulation loading, equivalent to the prescribed elliptic loading. (The span of each blade being $(R - h)$ long).

Figure 2 represents the fixed concentrator blades as a annular bound vortex sheet, while the rolled up discrete trailing vortices are shown as cylindrical vortex sheets of radii h and R respectively. By considering points P_2 and P_1 at radial distance r just ahead of and just behind the disc, the symmetry of the

bound vortex sheet will induce no axial velocity at these points. Therefore the axial velocity u through the disc remains the same. Now if the bound vortex sheet induces an angular velocity V_t at P_1, by symmetry it must induce an angular velocity $-V_t$ at P_2. Therefore the total induced angular velocity can be written as $\frac{1}{2}V_T + V_t$ at P_1 and $\frac{1}{2}V_T - V_t$ at P_2. But P_2 is in the irrotational flow field and therefore $\frac{1}{2}V_T - V_t = 0$. This means that the total angular velocity induced at P_1 by both bound and free vortices is $V_T = 2V_t$. This value of V_T will remain constant downstream for a constant radial distance r.

Now from figure 3 it is assumed that $\beta_1 = \beta_2$. The annular vortex sheet can be simplified into two parallel vortex strips of infinite length reflected about the z, y plane. For the trailing vortices, only the cylindrical component is considered. This is finally simplified into two semi-infinite sheets reflected about the z, y plane. The strength of each of the three vortex sheets are derived from the following

$$\tan\beta = \frac{V_T}{u} \tag{8}$$

$$\text{Now} \quad \gamma = \frac{d(\Gamma \sin\beta)}{dl} \simeq \Gamma \sin\beta/(2\pi\dot{h}\cos\beta/N)$$

$$\therefore \quad \gamma = \frac{N\Gamma}{2\pi\dot{h}}\tan\beta \tag{9}$$

$$\text{Also} \quad \dot{\gamma} = \frac{d\Gamma}{dl} \simeq N\Gamma/(2\pi(\frac{\dot{R}+\dot{h}}{2}))$$

$$\therefore \quad \dot{\gamma} = \frac{N\Gamma}{\pi(\dot{R}+\dot{h})} \tag{10}$$

$$\text{And} \quad \gamma'' = \frac{N\Gamma}{2\pi\dot{h}}\cos\beta \tag{11}$$

The outer vortex sheet strength is of $\gamma\dot{h}/\dot{R}$ since a constant helical vortex angle β is assumed for the both the cylindrical vortex sheets down the wake.

From previous reasoning, the tangential velocity distribution
across the annular area of the wake would be the same at any axial position downstream of the blades. For far wake conditions at P_3 (see figure 2), we get the following from Biot Savart Law for the tangential induced velocity (it can also be shown from Biot Savart Law that the radial induced velocity is zero)

$$V_T = \int_0^{2\pi}\Big\{\frac{\gamma''\dot{h}\cos(\theta+\alpha_1)}{2\pi r_1} - \frac{(\gamma''\dot{h}/\dot{R})\dot{R}\cos(\theta+\alpha_2)}{2\pi r_2}\Big\}d\theta \tag{12}$$

Now from figure 2 we see that

$$r_1 = \sqrt{\dot{h}^2 + r^2 - 2\dot{h}r\cos\theta}$$

$$r_2 = \sqrt{\dot{R}^2 + r^2 - 2\dot{R}r\cos\theta}$$

Using the above equations to solve equation 12 we get the following results

$$V_T = \frac{\gamma''\dot{h}}{r} \quad \text{for} \quad \dot{h} < r < \dot{R}$$

$$V_T = 0 \quad \text{for} \quad 0 < r < \dot{h} \quad \text{and} \quad r > \dot{R} \tag{13}$$

From equation 13 it can be seen that the equation is that for free vortex flow between $\dot{h} < r < \dot{R}$ if γ' is constant downstream for both vortex cylindrical sheets. We also notice that the core flow is irrotational. This would seem a reasonable result, since the flow through the core does not experience any angular momentum from blades or any other device. (The experimental results in section 4, based on the test work done at Queen Mary College by the author, confirms this conclusion).

Now figure 3 is a simplification of figure 2 . If we first consider the induced velocity at P_2 from both infinitely long strips, which are of equal and opposite strength $\dot{\gamma}$, the total induced velocity will be $\vec{q}_{P_2}$. Points A and B are at separate points on each strip. The position vector connecting points A to P_2 is expressed as $\vec{r}_{AP_2}$. Similarly for points B to P_2 we have $\vec{r}_{BP_2}$. Also at each point A and B, the unit normals are the same and equal to $\hat{n}$ over an elemental surface area of dS. Considering the situation at P_2 in figure 3 and applying Biot Savart Law we get the following

$$\vec{q}_{P_2} = \frac{1}{4\pi}\int\frac{(\hat{n}\wedge\vec{\dot{\gamma}})\wedge\vec{r}_{AP_2}}{|\vec{r}_{AP_2}|^3}dS + \frac{1}{4\pi}\int\frac{(\hat{n}\wedge(-\vec{\dot{\gamma}}))\wedge\vec{r}_{BP_2}}{|\vec{r}_{BP_2}|^3}dS$$

$$= \frac{\dot{\gamma}}{4\pi}\int_{-\infty}^{\infty}\int_{\dot{h}}^{\dot{R}}\frac{[\hat{i}y - \hat{j}(x-X)]dXdZ}{[(z-Z)^2+(x-X)^2+y^2]^{\frac{3}{2}}}$$

$$-\frac{\dot{\gamma}}{4\pi}\int_{-\infty}^{\infty}\int_{-\dot{h}}^{-\dot{R}}\frac{[\hat{i}y - \hat{j}(x-X)]dXdZ}{[(z-Z)^2+(x-X)^2+y^2]^{\frac{3}{2}}}$$

If we solve the above integral we find that the Y component is zero, while the X component will equal Vx so that

$$Vx = \frac{\dot{\gamma}}{2\pi}\Big\{-\tan^{-1}\Big(\frac{z-\dot{R}}{y}\Big) + \tan^{-1}\Big(\frac{z-\dot{h}}{y}\Big)\Big\} - \frac{\dot{\gamma}}{2\pi}\Big\{-\tan^{-1}\Big(\frac{z+\dot{R}}{y}\Big) + \tan^{-1}\Big(\frac{z+\dot{h}}{y}\Big)\Big\} \tag{14}$$

Now the induced velocity also at P_2 (x,y,z) from the semi-infinite sheets shown in figure 3 is again derived

from Biot Savart Law. The total elemental induced velocity at P_2 shown in figure 3 will be

$$dVa = dV_1 + dV_2$$
$$= \left(\frac{\gamma dy}{2\pi r_1} - \frac{(\gamma \acute{h}/\acute{R})dy}{2\pi \acute{r_1}}\right) - \left(\frac{\gamma dy}{2\pi r_2} - \frac{(\gamma \acute{h}/\acute{R})dy}{2\pi \acute{r_2}}\right)$$

Now consider only the Y component of induced velocity dVa and integrating we get

$$Vy = \int_0^\infty \left(\frac{\gamma \sin\theta_1}{2\pi r_1} - \frac{\gamma \acute{h}/\acute{R}\sin\acute{\theta_1}}{2\pi \acute{r_1}}\right)dy$$
$$- \int_0^\infty \left(\frac{\gamma \sin\theta_2}{2\pi r_2} - \frac{\gamma \acute{h}/\acute{R}\sin\acute{\theta_2}}{2\pi \acute{r_2}}\right)dy$$
$$= \frac{\gamma}{2\pi}\left\{\pi + -\tan^{-1}\left(\frac{y}{z-\acute{h}}\right) + \tan^{-1}\left(\frac{y}{z+\acute{h}}\right)\right\}$$
$$-\frac{\gamma \acute{h}}{2\pi \acute{R}}\left\{\pi - \tan^{-1}\left(\frac{y}{z-\acute{R}}\right) + \tan^{-1}\left(\frac{y}{z+\acute{R}}\right)\right\}$$
$$\text{for } |z| < \acute{h} \qquad (15)$$

$$= \frac{\gamma}{2\pi}\left\{-\tan^{-1}\left(\frac{y}{z-\acute{h}}\right) + \tan^{-1}\left(\frac{y}{z+\acute{h}}\right)\right\}$$
$$-\frac{\gamma \acute{h}}{2\pi \acute{R}}\left\{\pi - \tan^{-1}\left(\frac{y}{z-\acute{R}}\right) + \tan^{-1}\left(\frac{y}{z+\acute{R}}\right)\right\}$$
$$\text{for } \acute{h} < |z| < \acute{R} \qquad (16)$$

The reason for not including in the above the influence of the axial component of the helical trailing vortices is to simplify the analysis by use of the previous reasoning, involving the significant relationship between V_T and V_t. The induced velocity from the bound vortices will be equal to the contribution from the axial component of the helical trailing vortices at the concentrator disc face. (This contribution would steadily increase to twice this value at far wake conditions, hence maintaining the constancy of V_T downstream of the concentrator at a constant radial distance r for cylindrical wake conditions). Therefore from previous reasoning it would be reasonable to assume for values of R/h near unity that

$$V_t \simeq Vx \qquad (17)$$
$$\text{Also} \quad u = V - Vy \qquad (18)$$

Equations 17 and 18 now enable a relatively simple analysis to be conducted. By applying the results of equations 8 to 10, 14 and 16 for $y = \epsilon$ and $z = \acute{h}$, where ϵ is a very small positive value, we get the following

$$\tan\beta = \frac{N\Gamma/V}{2\pi(\acute{R}+\acute{h})(1 - \frac{N\Gamma/V\tan\beta}{2\pi\acute{R}})} \qquad (19)$$

which can be solved quadratically to give

$$\beta = \tan^{-1}\left(\frac{1 - \sqrt{1 - (N\Gamma/V)^2/(2\pi^2\acute{R}(\acute{R}+\acute{h}))}}{N(\Gamma/V)/(2\pi\acute{R})}\right) \qquad (20)$$

This is valid for inviscid theory with assumed infinite wake as as

$$(N\Gamma/V)^2/(2\pi^2\acute{R}(\acute{R}+\acute{h})) \leq 1$$

Now from equation 15 we have the expression for the axial increase in velocity through the core for $|z| < \acute{h}$ and $y \rightarrow \infty$ of the form

$$Vy = \gamma - \gamma\acute{h}/\acute{R} \qquad (21)$$

Therefore the velocity through the core becomes

$$V_c = V + \gamma - \gamma\acute{h}/\acute{R} \qquad (22)$$

If we define the concentration ratio C_R as the kinetic energy of flow at the core to the kinetic energy of flow at far upstream conditions through a stream tube of radius h we get

$$C_R = \frac{1/2\rho\pi\acute{h}^2V_c^3}{1/2\rho\pi h^2V^3} \qquad (23)$$

Therefore the potential power that could be extracted from the core can be interpreted as

$$P = C_R C_p 1/2\rho\pi h^2V^3 \qquad (24)$$

When a wind turbine is placed in the way of the flow, there will obviously be a wake interaction between the wind turbine wake and concentrator wakes. The effect of this on V_c will possibly lead to a reduction in power P. Unfortunately this cannot be assessed analytically because of the interactive nature of both concentrator and wind turbine wakes. Using a numerical model should solve this problem. (A numerical model is currently being considered for the future and is qualitatively discussed in Section 5). Now from reference 1 the upper limit of the Concentration Ratio $C_R = (R/h)^2$. This is in line with Betz Theory since a concentrator and wind turbine would ideally be equivalent to a larger wind turbine of radius R.

There is also another performance parameter that has been used in reference 2 called 'Velocity Concentration Factor' or V_{CF}. This is defined mathematically

$$V_{CF} = \frac{V_c}{V}$$

3 NUMERICAL WAKE MODELLING.

The method by which wake modelling can be achieved is by a method called 'Wake Relaxation'.

Figure 4 highlights the method involved. An elliptic loading is specified for each blade which is simplified into an equivalent rectangular loading. (The core radius of each vortex filament is of one percent of the concentrator span). The wake of one blade is considered with the effect of other blade wakes. The other blade wakes are represented by transferring the current blade wake geometry of one blade about the Y axis, by a particular angle equivalent to the angular position of each blade, relative to the one blade and wake considered. (This is indicated as ϕ in figure 4). Also the length of trailing vortex wake involved in each relaxation process grows at a rate of one vortex filament element length after each successful relaxation. (Each relaxation process involves the entire current length of wake). This allows for ease of convergence in the next stage of relaxation. (See figure 4). The procedure for wake relaxation is given in reference 5. The final result of this method is a three dimensional wake developed from the influence of the axial free stream velocity and the interdependent nature of each trailing vortex element in the wake.

To design the concentrator blades, the local resultant flow velocity V_r is found along the bound vortex line of one blade with the influence of the now entire relaxed wake. By adding on the two dimensional angle of incidence necessary to meet the specified local value of Γ, the blade twist can be finally be found.

4 RESULTS

Experimental results on the concentrator performance are unfortunately sparse at this point in time, since this is an interim report. The experimental data that is available is based on work done by the author at Queen Mary College, London and the earlier work by Rechenberg (reference 3). In both cases open jet windtunnels were used. In table 1, the test data for V_{CF} from two different experiments are compared with various theoretical approaches at predicting V_{CF}. Each experiment involved a test model of different design, indicated by N, $\Gamma/(V(R-h))$ parameters. $(\Gamma/(V(R-h))$ is a non-dimensional scaling factor which represents the required mid-blade circulation, divided by the free stream velocity and blade span). The position in the wake where the maximum V_{CF} was found is indicated non-dimensionally by y/h and z/h.

THEORIES & EXPERIMENT	V_{CF}	
	1	2
Blade Element (Axial Momentum)	1.31	*
Biot-Savart (Analytical)	1.013	1.83
Rechenberg (Analytical)	1.05	2.64
Wake Relaxation (Numerical)	1.054	1.92
Experimental	1.058	1.94

Note: $y/h = 0.5$, $z/h = 0$, $N = 20$, $\Gamma/(V(R-h)) = 0.0469$ (column 1) {Olivieri}
$y/h = 2.0$, $z/h = 0$, $N = 8$, $\Gamma/(V(R-h)) = 0.4775$ (column 2) {Rechenberg}

* Solution was not possible due to momentum theory breakdown.

Table 1: Comparison of different theories with experimental data.

Figure 5 gives a diametrical plot of swirl and radial flow vectors across the core flow area, calculated from the results derived from the tests done at Queen Mary College. The unusual swirl at the boundary of the orifice is due to the inboard tip vortices.

Figures 6 and 7 are derived from equations 20 to 23. The Betz limit line is derived from what was earlier stated in relation to the limit of C_R from reference 3 which is

$$C_R \leq (R/h)^2 \quad .$$

for an infinite wake. This coincides with the limiting condition of equation 20.

Figures 8 and 9 show the results from the inviscid numerical model for infinite and truncated wakes. Significant wake truncation is required above the Betz limit line. In this region solutions become progressively more difficult, causing less wake to be available. It should be remembered that these graphs show only potential concentration of kinetic energy at the core without a wind turbine in place.

5 CONCENTRATOR-WIND TURBINE MODELLING

The method of modelling the interactive nature of both the wind turbine and concentrator wakes will be similar to the method mentioned in section 3 and

is currently under development. The only difference will be in the wind turbine wake. Instead of having an axial free stream velocity involved in the relaxation process it will have a helical free stream velocity, due to the rotation of the rotor blades. Also each rotor wake system will need to be smeared over 2π radians about the axis of rotation. This should assimilate the difference between fixed and rotating wakes systems.

The optimum wind turbine will be represented by a scheme of horse shoe vortices for each blade. Trailing root vortices will be aligned with the axis of rotation while the tip vortices will be allowed to freely relax into the required geometry as the wake relaxation process proceeds. The core radius of each vortex filament of the rotor wake will be as specified in reference 6.

6 CONCLUSIONS.

The results given in table 1 show encouraging agreement between the experimental values and those obtained by use of the numerical model. The Biot Savart analytical model slightly underestimates the performance. This indicates the importance of free wake modelling. Rechenberg's model appears to have little agreement with the experimental results especially at higher blade loading conditions.

The streamlines shown in figure 10 show evidence of strong cross flow forces on the core flow stream tube. (This was derived from the numerical model for $N = 54$, $R/h = 1.66$ and $\Gamma/(V(R-h)) = 0.314$). The flow conditions near the core would be equivalent to that indicated in reference 7 as a 'Diffuser-Type Augmentation' process under no-load conditions. (The length of wake possible was limited to one and a half outside diameters for this particular design).

The high C_{RS} shown in figures 8 and 9 will definitely need experimental verification. To exceed the Betz Limit an 'Ejector-Type Augmentation' process would need to be evident down stream of the concentrator and wind turbine. (See reference 7). This effect has been noticed by van Holten using 'Tipvane' blades and a screen to represent a working turbine, under open jet windtunnel conditions. (See reference 8). From the theory of ejectors given in reference 9, shows that better energy transfer between two streams is achieved when mixing is done at lower than ambient pressure because of lower energy dissipation. The concentrator core flow is clearly below ambient pressure making conditions favourable. This effect has yet to be fully realized on the particular type of concentrator being investigated here. The current method of modelling used by the author is based on an inviscid assumption involving just the concentrator. The further modelling outlined in the previous section may give less optimistic results and will still involve an inviscid assumption. Further research into the augmentation process will require experimental investigation.

7 FUTURE WORK.

Future work will soon involve a field test on a fifty four bladed concentrator, ($R/h = 1.6$ and $\Gamma/(V(R-h)) = 0.314$ design), and a Marlec WG910 wind generator. It is hoped that this design will give a maximum $V_{CF} = 2$.

Further computer modelling, along the lines outlined in section 5, will be investigated soon after completion of the first phase of field tests.

ACKNOWLEDGEMENTS.

This work is currently funded by Marlec Engineering Ltd and the Science and Engineering Research Council. Windtunnel test facilities were provided by Queen and Westfield College.

REFERENCES

1 Rosenbrock, H.H.(1983):*Proposal for a New Design of Wind Power Generator.* Wind Engineering, Vol 7, No1.

2 Hunter, R. and Derrick, A.(1988):*Progress in theoretical investigation of a Stator Flow Concentrator.* Wind Energy Conversion. Proceedings of BWEA.

3 Rechenberg, I.(1984):*Berwian Konzertriert den Wind Zeitschrift für regenerative Energiequellen und Energie insparung.* Sonnenergie. pp 6-10.

4 Dick, E.(1981):*Power limits for Wind Energy Concentrator Systems.* Wind Engineering, Vol.5, No.1. pp 29-45.

5 Hunt, B.(1981):*The Role of computational Fluid Dynamics in High Angle-of-Attack Aerodynamics.* AGARD Conference Proceeding No 335. pp 6-1, 6-28.

6 Anderson, M.B.(1980):*A Vortex-Wake Analysis of a Horizontal-Axis Wind Turbine and a Comparison with a Modified Blade-Element Theory.* Proc.3rd Int.Symp. Wind Energy Systems, Copenhagen. BHRA, Cranfield, U.K.

Proc.3rd Int.Symp. Wind Energy Systems, Copenhagen. BHRA, Cranfield, U.K.

7 van Holten, Th.(1981):*Concentrator Systems for Wind Energy, with emphasis on Tip-vanes.* Wind Engineering, Vol.5,No.1. pp 29, 45.

8 van Holten, Th.(1982):*An Analytical Theory for Rotor-Tipvane Performance and Comparison with Experimental Results.* 8th European Rotorcraft Forum, Aix-en-Provence.

9 Bevilaqua, P.M.(1978):*Lifting Surface Theory for Thrust-Augmenting Ejectors.* AIAA Journal vol. 16, no.5. pp 475, 481.

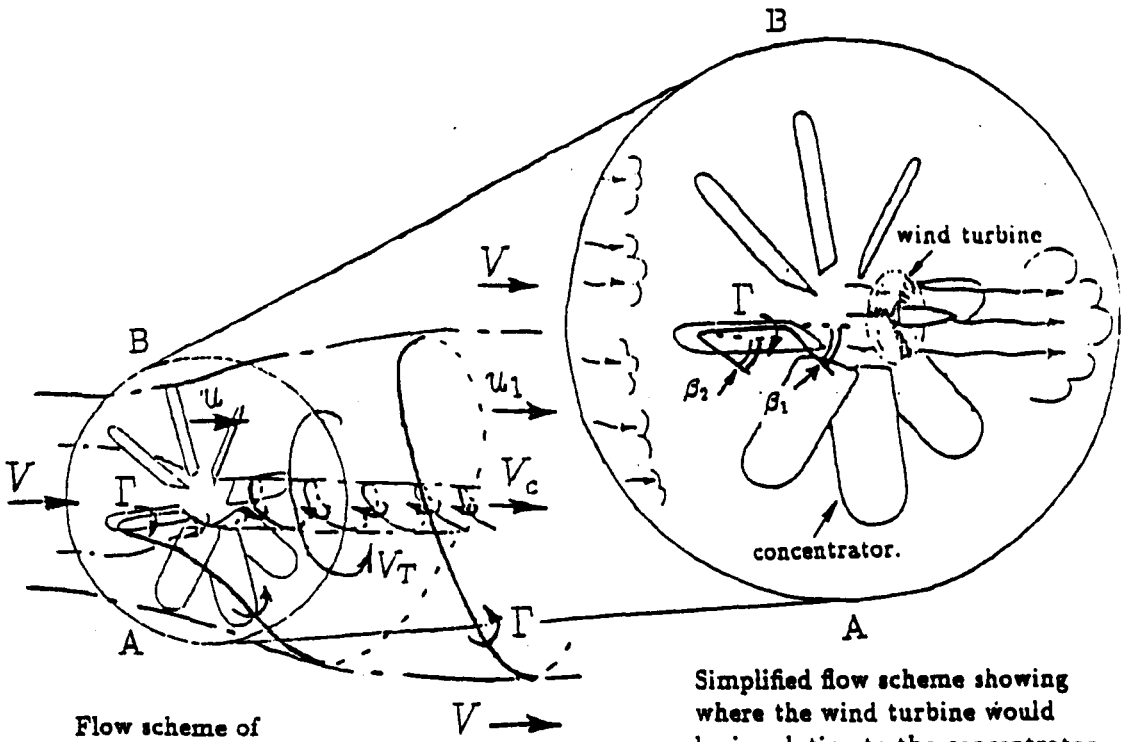

Flow scheme of concentrator only.

Simplified flow scheme showing where the wind turbine would be in relation to the concentrator.

Fig 1 Flow scheme of a wind concentrator

279

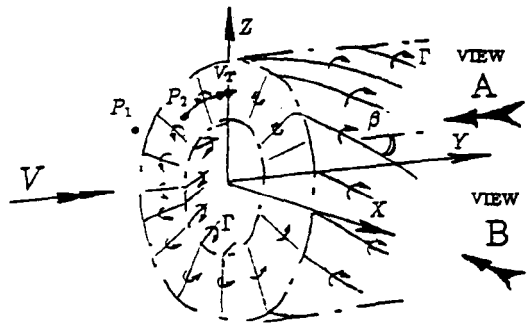

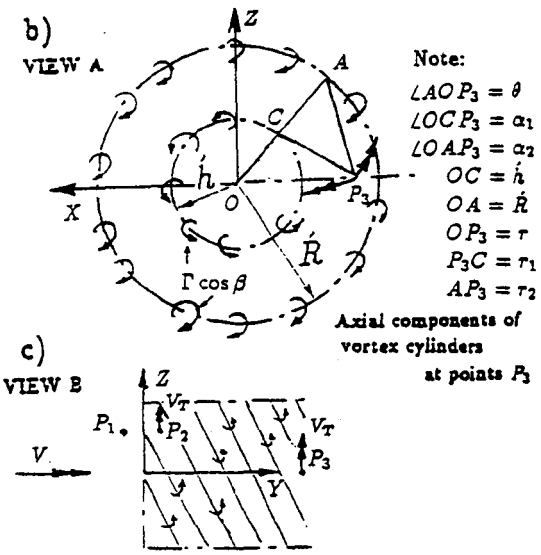

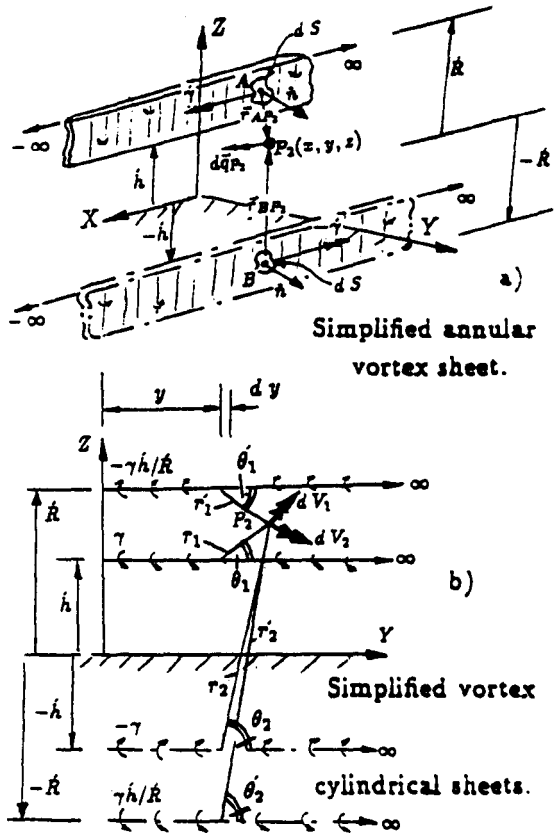

Fig 3 Simplified concentrator wake

Fig 2 Concentrator with semi-prescribed cylindrical wake

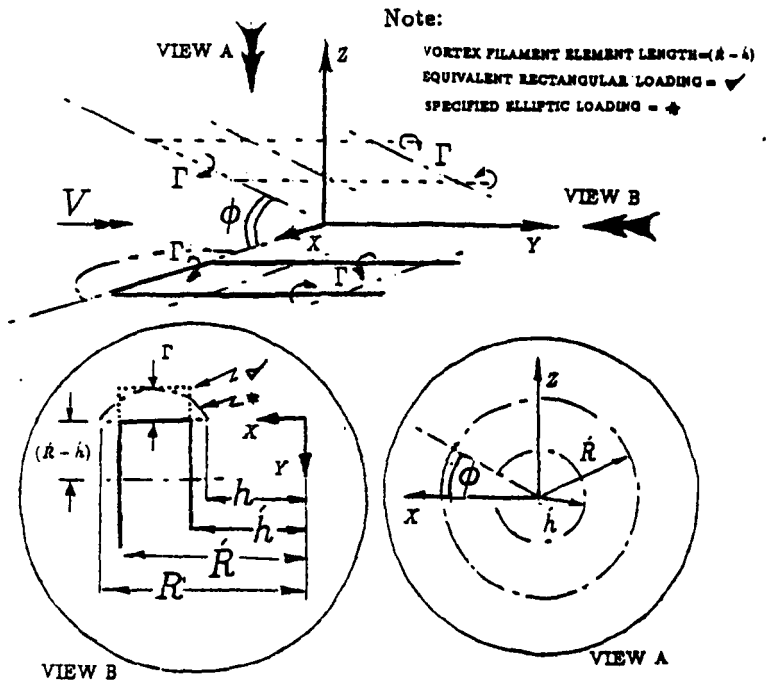

Fig 4 Wake relaxation method

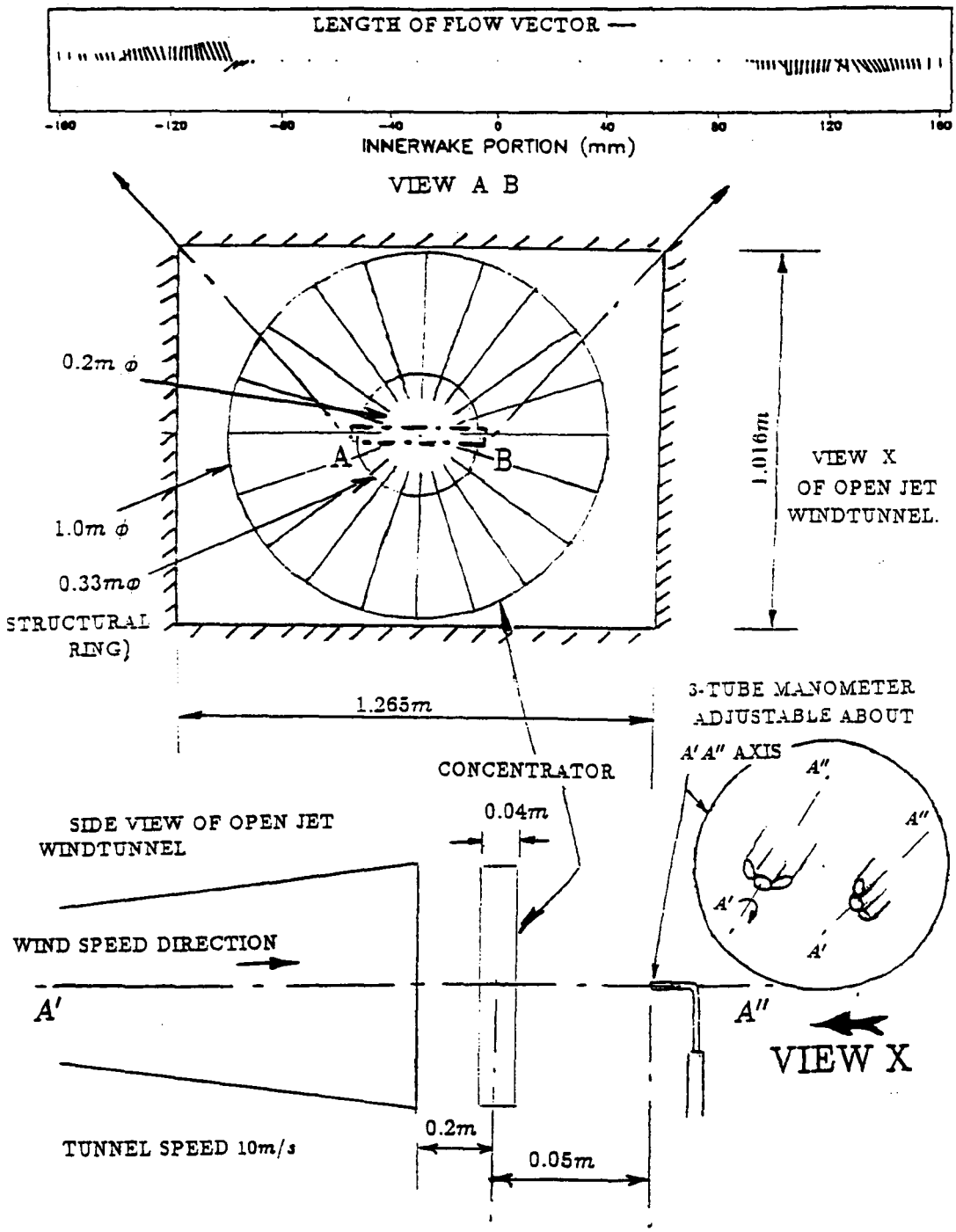

Fig 5 Wake traverse of concentrator (flow direction only)

281

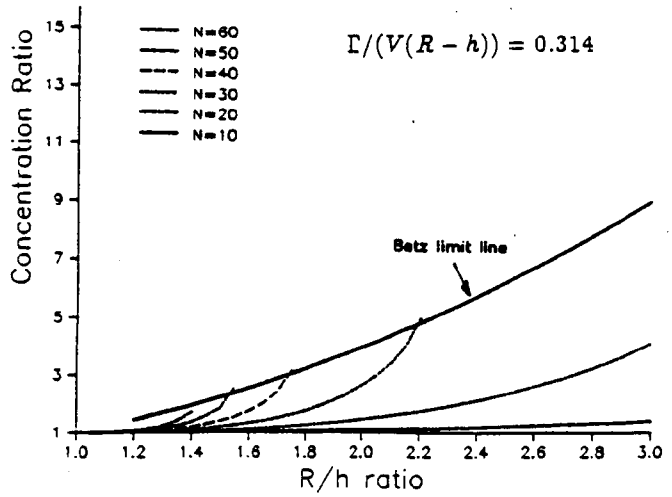

Fig 6 Parametric study of the wind concentrator (analytical model)

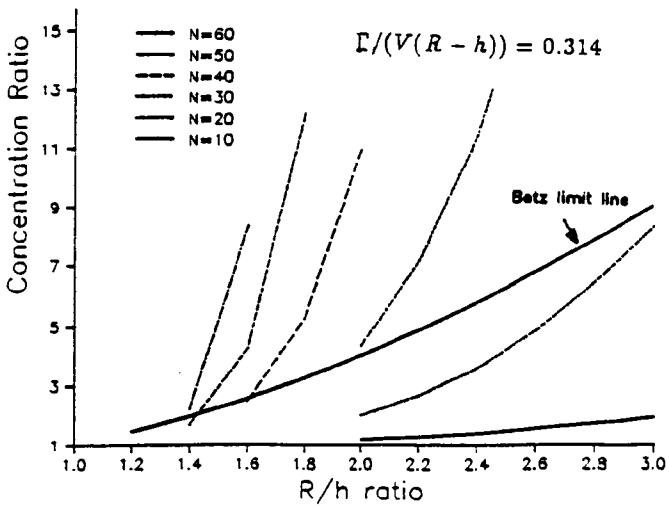

Fig 7 Parametric study of the wind concentrator (wake relaxation)

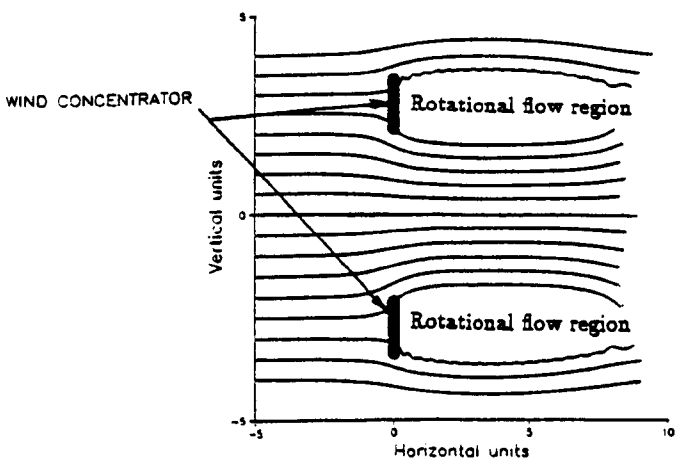

Fig 8 Theoretical streamline plot across a wind concentrator

Design and Testing of a Concentrator Wind Turbine

D.A. Olivieri
EERU. Open University, U.K.

ABSTRACT

Early attempts to assess the potential of the Concentrator Wind Turbine (CWT) were described by Rosenbrock (1983) and Hunter et al (1988), neither of which gave a full assessment. This paper re-examines the CWT using an analytical and numerical approach. Theoretical predictions are compared with experimental data from Rechenberg (1984) and with tests done at Queen Mary and Westfield College, Marlec Engineering Ltd and Goldstein Laboratory, University of Manchester.

Notation

c	Local chord of concentrator blade
C_D	Local drag coefficient of concentrator blade for single blade 2D flow
C_L	Local lift coefficient of the concentrator blade for single blade 2D flow
C_p	Coefficient of performance
C_R	Concentrator ratio
E	Loss of energy of system
H_1	Total pressure head downstream of the concentrator blades
H_0	Total pressure head upstream of the concentrator blades
h	Inner radius of concentrator
h'	Inner radius of concentrator wake
N	Number of blades of the concentrator
P	Power of the wind turbine
p'	Pressure increment across concentrator
q_{P_2}	Induced velocity vector at point P_2 due to infinite vortex strips representing bound vortices
Q	Heat transfer
r	radial distance from axis of symmetry of concentrator
r_n	Position vector of a node in the vortex wake structure relative to the origin for the nth iteration
R	Outside radius of the concentrator
R'	Outside radius of the concentrator wake
S	Surface area of vortex sheets
t	Unit time
T	Drag thrust on concentrator blades
T_Q	Torque on concentrator blades
u	Axial velocity across concentrator blades
u_1	Axial far wake velocity between outside and inboard trailing vortices
V	Free stream velocity
V_a	Total induced velocity from semi-infinite sheets representing the cylindrical component of the trailing vortices
V_1, V_2	Respective upper and lower contributions of induced velocity about the XY plane constituting V_a
V_c	Flow velocity through the core
V_r	Resultant flow velocity through the blades
V_T	Tangential flow velocity downstream of the blades
V_t	Tangential flow velocity due to bound vortices only

V_x	X component of induced velocity q_{p_2} for the analytical model and the total X component of induced velocity for the numerical model
V_y	Axial component of induced velocity V_a for the analytical model and the total Y component of induced velocity for the numerical model
V_z	Total Z component of induced velocity for the numerical model
V_{eff}	The effective 2D flow velocity over the local blade element
W	Local vector sum of all 2D induced velocities ω in the y,z plane at y_p, z_p
W	Work transfer
x,y,z	Spatial coordinates of point of induced velocity relative to X, Y, Z axes
y_p,z_p	2D coordinates of the bound vortex
X,Y,Z	Spatial coordinates of any point on infinite vortex strips representing the bound vortices relative to X, Y, Z axes
y/h	Ratio of axial distance from the origin to internal radius
ω	Angular velocity of wake flow in radians/s
ρ	Air density
Γ	Vortex circulation strength
Γ_0	Maximum vortex circulation strength for the circulation over blade span
γ,γ'',γ'	Vortex distribution of circulation strength per unit length of the vortex sheet, for cylindrical component of trailing vortices, axial component of trailing vortices and bound vortices respectively
β_1,β_2	Inboard and outboard helical vortex angles
β	Helical vortex angle
ψ	Angular displacement about axis of symmetry between two adjacent blade span axes
ϕ	Local flow angle along the blade
Θ	Local blade twist angle between the chord line and a plane through the Y axis
Δ	Adjustment vector for a node in the vortex wake structure for the (n+1th) iteration
Ω	Rotational speed of the wind turbine

INTRODUCTION

A major constraint in conventional wind turbine design is the reduction in rotational speed as the size of the rotor is increased. This means expensive gearboxes are unavoidable for electrical generation. The rotor also becomes considerably more complicated in design and heavier as the size increases, to mitigate working stresses.

Flow concentrators have been investigated in an attempt to alleviate these problems, but these usually incur the expense of high structural weight and size. (Dick (1986)). The Helical Vortex Wind Concentrator is a recent addition to the list of flow concentrator types. Its full potential is as yet unknown.

The CWT consists of a Helical Vortex Wind Concentrator and a wind turbine. The wind concentrator is an annular disc of stationary, radial, aerofoil sectioned blades which entrain the wind, through the orifice formed by the surrounding blades, onto the wind turbine downstream, whose diameter is no larger than that of the orifice. The vortex shedding from the inboard tips of the stationary blades causes the entrainment effect to take place. (See Figure 1a). The main aim of the research reported here is to predict the performance of the CWT by wake analysis only. With this method of analysis the CWT can be designed from a specified blade circulation distribution, number of blades, R/h ratio and blade span.

2. CONCENTRATOR THEORY

2.1 Energy and Momentum

The balance of energy of a Helical Vortex Wind Concentrator is considered most conveniently by assuming the concentrator to be stationary in a stream of air of velocity V directed along its axis. Considering only the blade elements at distance r from the axis, the power put into the concentrator is zero. The drag thrust dT operates on air moving with the axial velocity u and does the work $-u\,dT/dr$ in unit time. Similarly the torque dT_Q operates on air moving with the angular velocity $\frac{1}{2}\omega$ and does the work $\frac{1}{2}\omega$

dT_Q/dr in unit time. Hence if dE/dr is the rate of loss of energy of the system. the energy equation becomes

$$\frac{dQ}{dt} - \frac{dW}{dt} = -u\frac{dT}{dr} + \tfrac{1}{2}\omega\frac{dT_Q}{dr} + \frac{dE}{dr} = 0 \qquad (1)$$

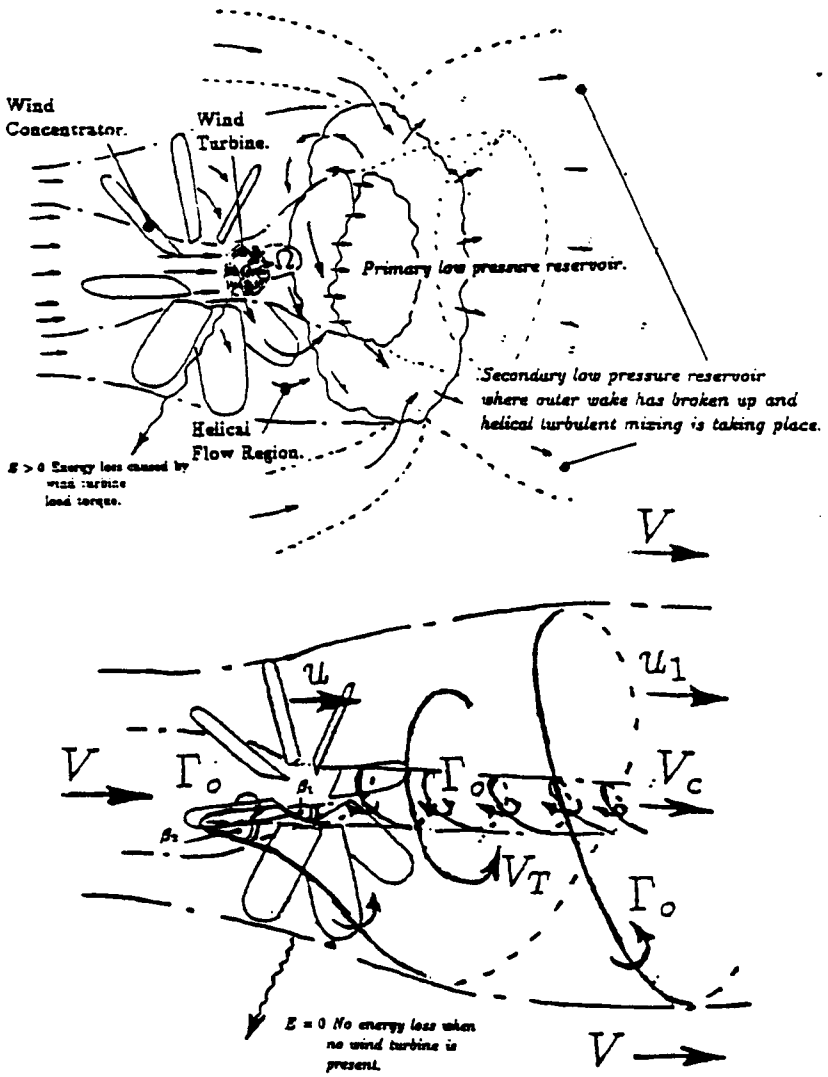

Figure 1. Ideal aerodynamics of the CWT.

since there has been no heat transfer Q or work transfer W. Now the rate of energy loss due to the profile drag of N blade elements. each experiencing the resultant velocity V_r due to the induced velocity from the local blade circulation and free stream velocity V. is as follows

$$\frac{dE}{dr} = \tfrac{1}{2}N\,c\rho V_r^3 C_D \qquad (2)$$

where C_D and c are the local drag coefficient and chord respectively.

The energy of the air is represented by its total pressure head which is constant across the concentrator if C_D is small. As the air passes through the concentator disc it reduces in pressure by p' by virtue of an increase in angular velocity ω without any

change in axial and radial components of velocity, and hence the increase of total pressure head is

$$H_1 - H_0 = -p' + \tfrac{1}{2}\rho\omega^2 r^2 = 0 \tag{3}$$

$$\therefore \quad p' = \tfrac{1}{2}\rho\omega^2 r^2 \tag{4}$$

This effect on the air is due to an energy exchange process between the drag thrust and the torque $(-udT + \tfrac{1}{2}\omega dT_Q)$ on a volume of air $2\pi r u dr$. Hence

$$-u\frac{dT}{dr} + \tfrac{1}{2}\omega\frac{dT_Q}{dr} = 2\pi r u(-p' + \tfrac{1}{2}\rho\omega^2 r^2) = 0 \tag{5}$$

But the element of drag thrust is clearly equal to the decrease of pressure over the annulus, or

$$\frac{dT}{dr} = 2\pi r p' \tag{6}$$

and the element of torque is equal to the angular momentum imparted to the air in unit time, or

$$\frac{dT_Q}{dr} = 2\pi\rho u\omega r^2 \tag{7}$$

These two expressions are consistent with the previous equation for energy, since the constant total pressure head is due to the exchange between drag thrust and torque of blade elements respectively.

2.2 Blade Element Theory

Applying Blade Element Theory at first sight seems the obvious approach but in fact this proved to be an inadequate method for determining vortex wake geometry. The Blade Element Theory was developed on the assumption of negligible wake swirl and trailing vortex effects, this is clearly not the case with the concentrator. (Note that $u>(V+u_1)/2$, see Figure 1b). The trailing vortices coming off each blade element would constitute a roll up into two discrete vortices of equal and opposite strength. The accuracy of the helical vortex angles of the two discrete vortices, (shown as β_1 and β_2), and their position in space is of great importance for determining the increase in flow velocity through the core. (See Figure 1b).

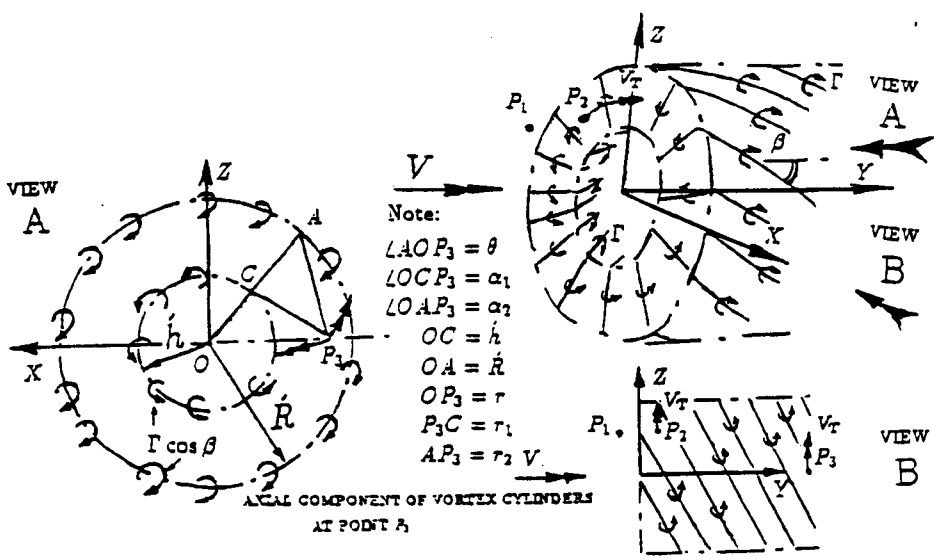

Figure 2. Concentrator with semi-prescribed cylindrical wake.

2.3 Biot Savart Theory

The problems described in subsection 2.2 indicated a need for a method which took into account the inter-dependent nature of the wake. Biot Savart Theory if applied to a free wake scheme would solve this problem. In section 3 this approach is investigated numerically.

In this section, an analytical approach will be adopted, involving a semi-prescribed cylindrical wake, the initial problem being the determination of angles β_1 and β_2. Figures 2 and 3 show the method of analysis. The flow is assumed to be inviscid and incompressible throughout. Each blade with its wake is represented as a horseshoe vortex of rectangular blade circulation loading, equivalent to the prescribed elliptic loading. (The span of each blade being (R-h) long).

Figure 2 represents the fixed concentrator blades as an annular bound vortex sheet, while the rolled up discrete trailing vortices are shown as cylindrical vortex sheets of radii h′ and R′ respectively. By considering points P_2 and P_1 at radial distance r just ahead of and just behind the disc, the symmetry of the bound vortex sheet will induce no axial velocity at these points. Therefore the axial velocity u through the disc remains the same. Now if the bound vortex sheet induces an angular velocity V_t at P_1, by symmetry it must induce an angular velocity $-V_t$ at P_2. Therefore the total induced angular velocity can be written as $\frac{1}{2}V_T + V_t$ at P_1 and $\frac{1}{2}V_T - V_t$ at P_2. But P_2 is in the irrotational flow field and therefore $\frac{1}{2}V_T - V_t = 0$. This means that the total angular velocity induced at P_1 by both bound and free vortices is $V_T = 2V_t$. This value of V_T will remain constant downstream for a constant radial distance r.

Now from Figure 3 it is assumed that $\beta_1 = \beta_2$. The annular vortex sheet can be simplified into two parallel vortex strips of infinite length reflected about the z, y plane. For the trailing vortices, only the cylindrical component is considered. This is finally simplified into two semi-infinite sheets reflected about the z, y plane. The strength of each of the three vortex sheets is derived from the following

$$\tan\beta = \frac{V_T}{u} \tag{8}$$

Now
$$\gamma = d(\Gamma\sin\beta)/dl \simeq \Gamma\sin\beta/(2\pi h'\cos\beta/N)$$

$$\therefore \quad \gamma = N\Gamma/(2\pi h')\tan\beta \tag{9}$$

Also
$$\gamma' = d\Gamma/dl' \simeq N\Gamma/(2\pi((R'+h')/2))$$

$$\therefore \quad \gamma' = N\Gamma/(\pi(R'+h')) \tag{10}$$

And
$$\gamma'' = N\Gamma\cos\beta/(2\pi h') \tag{11}$$

The outer vortex sheet strength is of $\gamma h'/R'$ since a constant helical vortex angle β is assumed for both the cylindrical vortex sheets down the wake.

From previous reasoning, the tangential velocity distribution across the annular area of the wake would be the same at any axial position downstream of the blades. For far wake conditions at P_3 (see Figure 2), we get the following from the Biot Savart Law for the tangential induced velocity (it can also be shown from the Biot Savart Law that the radial induced velocity is zero)

$$V_T = \int_0^{2\pi} \left\{ \frac{\gamma'' h'\cos(\theta+\alpha_1)}{2\pi r_1} - \frac{(\gamma'' h'/R')R'\cos(\theta+\alpha_2)}{2\pi r_2} \right\} d\theta \tag{12}$$

Now from Figure 2 we see that

$$r_1 = \sqrt{h'^2 + r^2 - 2h'r\cos\theta}$$

$$r_2 = \sqrt{R'^2 + r^2 - 2R'r\cos\theta}$$

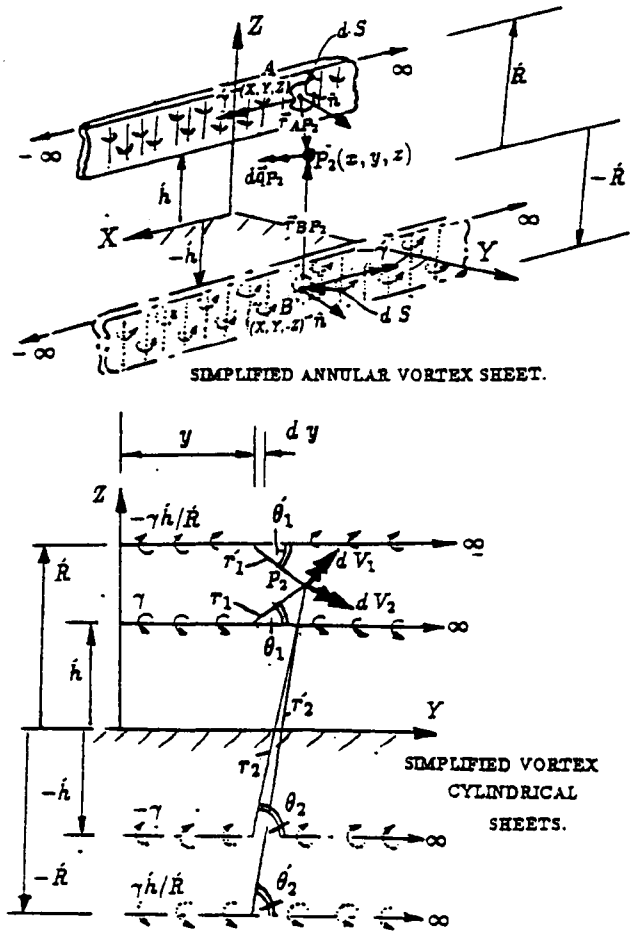

Figure 3. Simplified concentrator wake.

Using the above equations to solve equation 12 we get the following results

$$V_T = \frac{\gamma' h'}{r} \quad \text{for} \quad h' < r < R'$$

$$V_T = 0 \quad \text{for and} \quad 0 < r < h',\ r > R' \qquad (13)$$

From equation 13 it can be seen that the equation is that for free vortex flow between $h' < r < R'$ if γ' is constant downstream for both vortex cylindrical sheets. We also notice that the core flow is irrotational. This would seem a reasonabe result, since the flow through the core does not experience any angular momentum from blades or any other device. (The experimental results in section 4, based on the test work done at Queen Mary College by the author, confirm this conclusion).

Now Figure 3 is a simplification of Figure 2. If we first consider the induced velocity at P_2 from both infinitely long strips, which are of equal and opposite strength γ', the total induced velocity will be $\vec{q}_{p_2}$. Points A and B are at separate points on each strip. The position vector connecting points A to P_2 is expressed as $\vec{r}_{AP_2}$. Similarly for points B to P_2 we have $\vec{r}_{BP_2}$. Also at each point A and B, the unit normals are the same and equal to $\hat{n}$ over an elemental surface area of dS. Considering the situation at P_2 in Figure 3 and applying the Biot Savart Law we get the following

$$\overrightarrow{q_{P_2}} = \frac{1}{4\pi}\int \frac{(\hat{n}\wedge\vec{\gamma})\wedge\overrightarrow{r_{AP2}}}{|\overrightarrow{r_{AP2}}|^3}\,dS$$

$$+ \frac{1}{4\pi}\int \frac{(\hat{n}\wedge(-\vec{\gamma}))\wedge\overrightarrow{r_{BP2}}}{|\overrightarrow{r_{BP2}}|^3}dS$$

$$= \frac{\gamma'}{4\pi}\int_{-\infty}^{\infty}\int_{h'}^{R'} \frac{[iy - j(x - X)]dX\,dZ}{[(z - Z)^2 + (x - X)^2 + y^2]^{3/2}}$$

$$- \frac{\gamma'}{4\pi}\int_{-\infty}^{\infty}\int_{-h'}^{-R'} \frac{[iy - j(x - X)]dX\,dZ}{[(z - Z)^2 + (x - X)^2 + y^2]^{3/2}}.$$

If we solve the above integral we find that the Y component is zero, while the X component will equal Vx so that

$$Vx = \frac{\gamma'}{2\pi}\left\{-\tan^{-1}\left(\frac{z - R'}{y}\right) + \tan^{-1}\left(\frac{z - h'}{y}\right)\right\}$$

$$- \frac{\gamma'}{2\pi}\left\{-\tan^{-1}\left(\frac{z + R'}{y}\right) + \tan^{-1}\left(\frac{z + h'}{y}\right)\right\} \qquad (14)$$

Now the induced velocity also at P_2 (x,y,z) from the semi-infinite sheets shown in Figure 3 is again derived from the Biot Savart Law. The total elemental induced velocity at P_2 shown in Figure 3 will be

$$dVa = dV_1 + dV_2 = \left(\frac{\gamma dy}{2\pi r_1} - \frac{(\gamma h'/R')dy}{2\pi r'_1}\right) - \left(\frac{\gamma dy}{2\pi r_2} - \frac{(\gamma h'/R')dy}{2\pi r'_2}\right)$$

Now consider only the Y component of induced velocity dVa and integrating we get

$$Vy = \int_0^{\infty}\left(\frac{\gamma\sin\theta_1}{2\pi r_1} - \frac{\gamma h'/R'\sin\theta'_1}{2\pi r'_1}\right)dy$$

$$- \int_0^{\infty}\left(\frac{\gamma\sin\theta_2}{2\pi r_2} - \frac{\gamma h'/R'\sin\theta'_2}{2\pi r'_2}\right)dy$$

$$= \frac{\gamma}{2\pi}\left\{\pi - \tan^{-1}\left(\frac{y}{z - h'}\right) + \tan^{-1}\left(\frac{y}{z + h'}\right)\right\}$$

$$- \frac{\gamma h'}{2\pi R'}\left\{\pi - \tan^{-1}\left(\frac{y}{z - R'}\right) + \tan^{-1}\left(\frac{y}{z + R'}\right)\right\}$$

$$\text{for } |z| < h' \qquad (15)$$

$$= \frac{\gamma}{2\pi}\left\{\pi - \tan^{-1}\left(\frac{y}{z - h'}\right) + \tan^{-1}\left(\frac{y}{z + h'}\right)\right\}$$

$$- \frac{\gamma h'}{2\pi R'}\left\{\pi - \tan^{-1}\left(\frac{y}{z - R'}\right) + \tan^{-1}\left(\frac{y}{z + R'}\right)\right\}$$

$$\text{for } h' < |z| < R' \qquad (16)$$

The reason for not including in the above the influence of the axial component of the helical trailing vortices is to simplify the analysis by use of the previous reasoning, involving the significant relationship between V_T and V_t. The induced velocity from the bound vortices will be equal to the contribution from the axial component of the helical trailing vortices at the concentrator disc face. (This contribution would steadily increase to twice this value at far wake conditions, hence maintaining the constancy of V_T downstream of the concentrator at a constant radial distance r for cylindrical wake conditions). Therefore from previous reasoning it would be reasonable to assume for values of R/h near unity that

$$V_t \simeq Vx \tag{17}$$

Also

$$u = V + Vy \tag{18}$$

Equations 17 and 18 now enable a relatively simple analysis to be conducted. By applying the results of equations 8 to 10, 14 and 16 for $y = \varepsilon$ and $z = h'$, where ε is a very small positive value, we get the following

$$\tan\beta = \frac{N\Gamma/V}{2\pi(R'+h')\left(1 - \frac{N\Gamma/V \tan\beta}{4\pi R'}\right)} \tag{19}$$

which can be solved quadratically to give

$$\beta = \tan^{-1}\left(1 - \frac{\sqrt{(N\Gamma/V)^2/(2\pi^2 R'(R'+h'))}}{N(\Gamma/V)/(2\pi R')}\right) \tag{20}$$

This is valid for inviscid theory with assumed infinite wake as

$$(N\Gamma/V)^2/(2\pi^2 R'(R'+h')) < 1$$

Now from equation 15 we have the expression for the axial increase in velocity through the core for $|z| < h'$ and $y \longrightarrow \infty$ of the form

$$Vy = \gamma - \gamma h'/R' \tag{21}$$

Therefore the velocity through the core becomes

$$V_c = V + \gamma - \gamma h'/R' \tag{22}$$

By substituting equations 9 and 20 in to equation 22 and dividing by V we get

$$\frac{V_c}{V} = 1 + \left(R'/h' - 1\right)\left(1 - \sqrt{1 - \frac{(N\Gamma/V)^2}{2\pi^2 R'(R'+h')}}\right) \tag{23}$$

If we define the concentration ratio C_R as the kinetic ratio of the energy of flow at the core to the kinetic energy of flow at far upstream conditions through a stream tube of radius h we get

$$C_R = \frac{1/2\pi\rho h'^2 V_c^3}{1/2\rho\pi h^2 V^3} \tag{24}$$

Therefore the potential power that could be extracted from the core can be interpreted as

$$P = C_R C_p 1/2\rho\pi h^2 V^3 \quad (25)$$

When a wind turbine is placed in the way of the flow, there will obviously be a wake interaction between the wind turbine wake and concentrator wakes. The effect of this on V_c will possibly lead to a reduction in power P. Unfortunately this cannot be assessed analytically because of the interactive nature of both concentrator and wind turbine wakes. Using a numerical model should solve this problem. Now from Rosenbrock (1983) the upper limit of the Concentration Ratio $C_R = (R/h)^2$. This is in line with Betz Theory since a concentrator and wind turbine would ideally be equivalent to a larger wind turbine of radius R.

There is also another performance parameter that has been used by Hunter *et al* (1988) called 'Velocity Concentration Factor' or V_{CF}. This is defined mathematically

$$V_{CF} = \frac{V_c}{V}$$

3. NUMERICAL WAKE MODELLING

The method by which wake modelling can be achieved is called 'Wake Relaxation'.

Figure 4 highlights the approach involved. An elliptic loading is specified for each blade which is simplified into an equivalent rectangular loading. (The core radius of each vortex filament is one percent of the concentrator span). The wake of one blade is considered with the effect of other blade wakes. The other blade wakes are represented by transfering the current blade wake geometry of one blade about the Y axis, by a particular angle equivalent to the angular position of each blade, relative to the one blade and wake considered. (This is indicated as ψ in Figure 4). The procedure for wake relaxation is shown in Figure 4 and is as follows:

1. Induced velocities are calculated at mid-points B1 and B2 from all the elements in the wake.
2. The wake is then adjusted at each node C1 and C2 with the adjustable vectors $\Delta(1)$ and $\Delta(2)$. (Note that the number in brackets refers to column number and not iteration number).
3. This is repeated across each row of nodes from E to I say, using the same adjustment vectors.
4. Now new induced velocities are calculated for the next row of mid points D1 and D2 and steps 2 to 3 are repeated except that new wake adjustment vectors will ripple down from nodes E1 and E2 to I1 and I2.
5. Step 4 will be repeated for new starting mid points F1 and F2 up to H1 and H2 say.
6. Repeat steps 1 to 5 until convergence has occurred.
7. Increase the number of elements which can be relaxed beyond nodes I1 and I2 each by one element length with the semi-infinite filaments attached now at nodes K1 and K2, and repeat steps 1 to 6 until the required length of relaxed wake has been met.

The above procedure is based on that given in Hunt (1981). Step 6 usually involves no special process for a convergence test if the wake converges quadratically. For the kind of wake relaxation work involved with a heavily loaded wake structure a much better method must be employed, since near the solution convergence is very slow. In reference 6 a method called 'Aitken Acceleration' offers a way of accelerating the iterative scheme since even if it does converge, the convergence is in general only linear. This means that close to a root say ε_1, we have

$$|\delta x_{n+1}| \simeq |g'(\varepsilon)||\delta x_n|$$

therefore convergence will be very slow if $|g'(\varepsilon)|$ is only just less than one. To accelerate to the root the following method is used:

If x_0 is the starting value of the iterative scheme for only one node then

(a) Calculate $x_1 = g(x_0)$, (i.e. do steps 1 to 5), and set n=2.

(b) Calculate $x_n = g(x_{n-1})$.

(c) Calculate the X component of the adjustment vector for the node and divide this by the previous value which will give you some value λ.

(d) Increase n by 1 and repeat steps (b) and (c) until successive values of λ seem to be settling down to some approximately constant value.

(e) Calculate the new X component for the node

$$x_{new} = x_n + \frac{\lambda}{1-\lambda} |\vec{\Delta}_{n-1} \cdot \hat{i}|$$

where

$$\vec{\Delta}_{n-1} = \vec{r}_n - \vec{r}_{n-1}$$

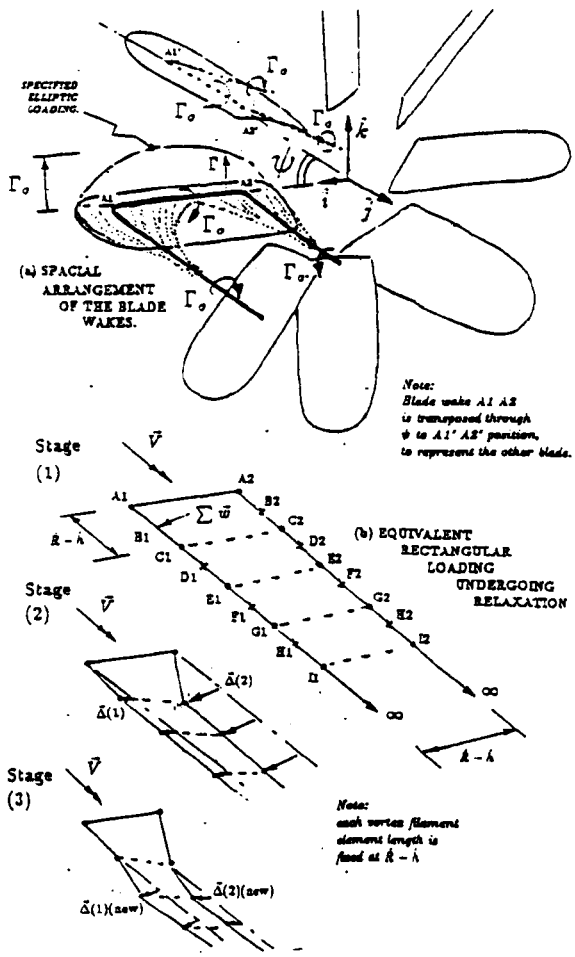

Figure 4. Wake relaxation method.

(f) Replace x_n by x_{new} and repeat from step (b) until the req.. ed accuracy is reached.

The above procedure is also applied to the other components Y and Z for the individual node. This process is simultaneously applied to every X,Y,Z coordinate of all the nodes throughout the wake to ensure proper convergence is met. The final result of this method is a three dimensional wake developed from the influence of the axial free stream velocity and the interdependent nature of each trailing vortex ele-

ment in the wake.

To design the concentrator blades involves previous knowledge of the characteris tics of the chosen aerofoil for single blade 2D flow and what maximum value of C_L should be tolerated along the span to avoid stall. By using the approximate fluid model shown in Figure 5 the following relationships are used to determine the value of chord c for the rectangular blade plan form and the local blade twist:

$$\vec{W} = \vec{\Sigma}\,\omega(y_p, z_p) = \vec{V}_y + \vec{V}_z \tag{26}$$

$$\phi = \tan^{-1}\left(\frac{|\vec{V}_z|}{|\vec{V} + \vec{V}_y|}\right) \tag{27}$$

$$C_L = \frac{2\Gamma\cos\phi}{|(\vec{V} + \vec{V}_y)|c} \tag{28}$$

$$\Theta = \phi + \alpha \tag{29}$$

The procedure to find Θ and c is as follows

(A) Calculate $\vec{V}_y$, $\vec{V}_z$ and ϕ.
(B) Assumes a value for c.
(C) Calculate C_L and if its value is too small return to (B) and consider a larger value of c. If not continue.
(D) Find the value of α from aerofoil characteristic.
(E) Calculate Θ.

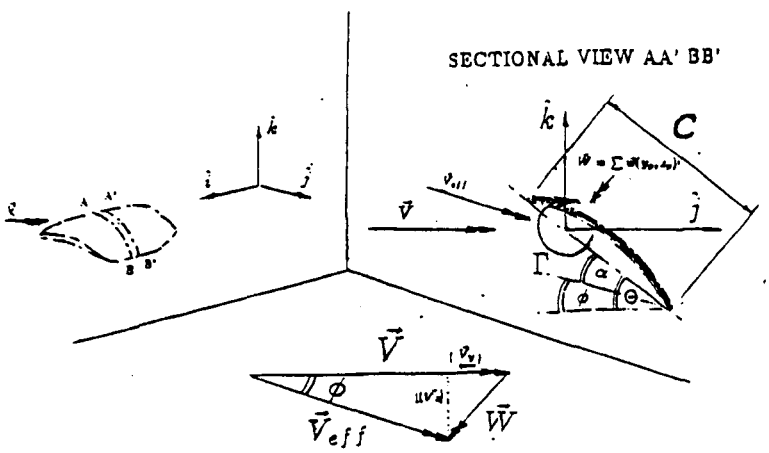

Figure 5. Concentrator blade design method on a blade element.

4. RESULTS

Experimental results on the concentrator performance are unfortunately sparse at this point in time. The experimental data that is available is based on work done by the author at Queen Mary College. London and the earlier work by Rechenberg (1984)). In both cases open jet wind tunnels were used. In Table 1, the test data for V_{CF} from two different experiments are compared with various theoretical approaches to predicting V_{CF}. Each experiment involved a test model of different design. indicatd by $N\Gamma/(V(R-h))$ and R/h parameters. $(\Gamma/(V(R-h))$ is a non-dimensional scaling factor which represents the required mid-blade circulation. divided by the free stream velocity and blade span). The position in the wake where the maximum V_{CF} was found is indicated non-dimensionally by y/h and z/h.

Table 1. Comparison of performance predictions from different theories with experimental data

THEORIES & EXPERIMENT	V_{CF}	
	1	2
Blade Element (Axial Momentum)	1.31	*
Biot.Savart (Analytical)	1.013	1.54
Rechenberg (Analytical)	1.05	2.64
Wake Relaxation (Numerical)	1.054	1.92
Experimental	1.058	1.94

Note:
Column 1: y/h = 0.5, z/h = 0, R/h = 5, N = 20, Γ/V(R−h)) = 0.0469 (Olivieri)
Column 2: y/h = 2.0, z/h = 0, R/h = 5.545, N = 8, Γ/(V(R−h)) = 0.4775 (Rechenberg)

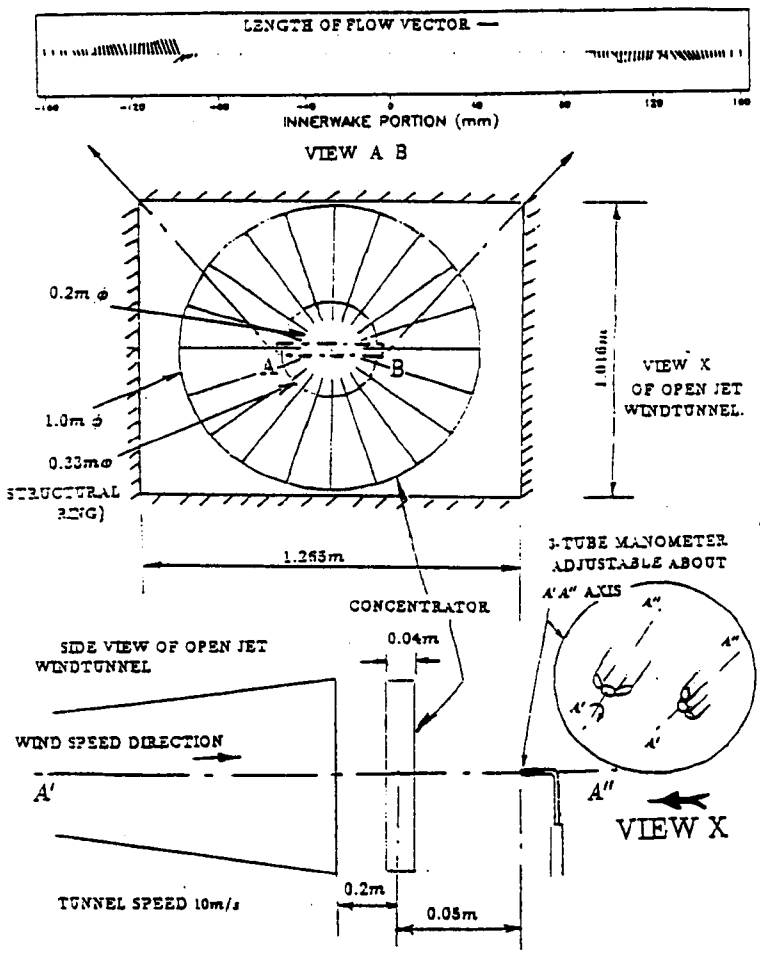

Figure 6. Wake traverse of concentrator (Flow direction only).

* Solution was not possible due to momentum theory breakdown.

Figure 6 gives a diametrical plot of swirl and radial flow vectors across the core flow area, calculated from the results derived from the tests done at Queen Mary College. The unusual swirl at the boundary of the orifice is due to the inboard tip vortices.

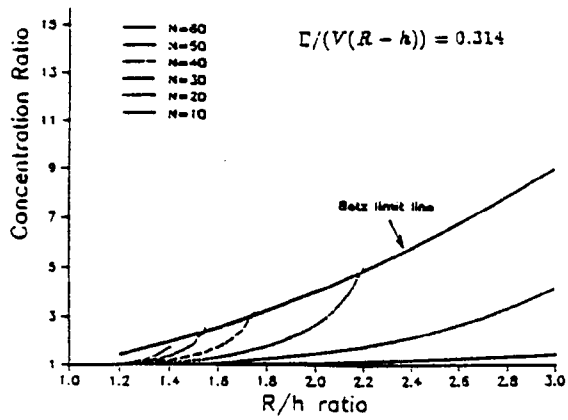

Figure 7. Parametric study of the wind concentrator (Analytical model).

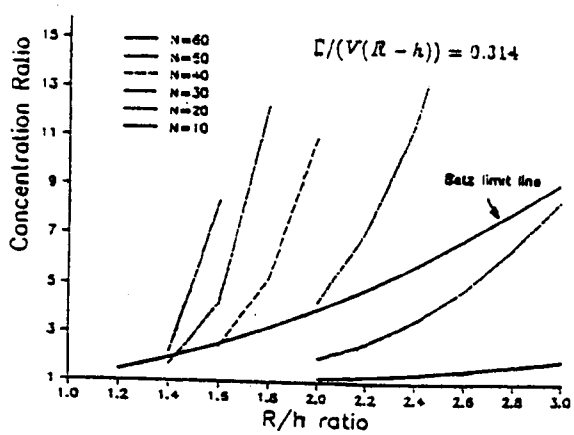

Figure 8. Parametric study of the wind concentrator (Wake relaxation).

Figure 7 is derived from equations 20 to 24. Figure 8 as stated was generated from the numerical model described in section 3. The Betz limit line is derived from what was earlier stated in relation to the limit of C_R from Rosenbrock (1983) which is

$$C_R < (R/h)^2$$

for an infinite wake. This coincides with the limiting condition of equation 20.

Figure 8 show the results from the inviscid numerical model for infinite and truncated wakes. Significant wake truncation is required above the Betz limit line. In this region solutions become progressively more difficult, causing less wake to be available. It should be remembered that these graphs show only the potential concentration of kinetic energy at the core without a wind turbine in place.

Recent test work was conducted on a CWT with the following design characteristics: N = 54, R/h = 1.6, Γ/(V(R−h)) = 0.314 and with a Marlec WG910 wind turbine. The test work was conducted at Marlec Engineering's test site at Gretton, Northamptonshire. The VCF should have been 2 but only 1.26 was noticed. Later flow visualization was conducted at Gretton as well to investigate the problem using smoke (see Figure 10). Wake truncation was noticed at a much shorter wake length of y/h ≈ 0.75 rather than the expected value of y/h ≈ 5. Later at Goldstein Laboratory of the Manchester University other flow visualization techniques were conducted in their Avro tunnel with just the concentrator. Figure 11 shows the result of the observations

in a sketch form. Vortex inference caused the truncation and could have been avoided if higher aspect ratio blades with higher camber were to be used instead. This would allow the tip vortices to roll up sooner therefore avoiding wake interference. Figure 12 shows the effect of premature wake truncation on VCF.

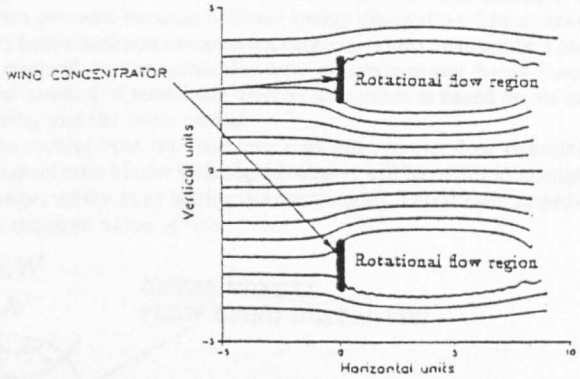

Figure 9. Theoretical streamline plot across a wind concentrator.

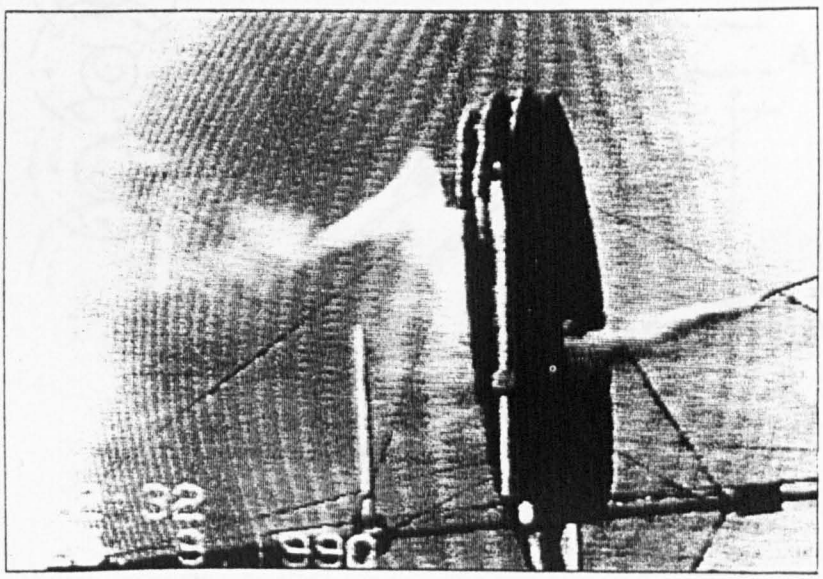

Figure 10. Smoke equipment working at the field test site indicating inboard vortex tip development.

5 CONCLUSIONS

The results given in Table 1 show encouraging agreement between the experimental values and those obtained by use of the numerical model. The Biot Savart analytical model significantly underestimates the performance. This indicates the importance of free wake modelling. Rechenberg's model appearrs to have little agreement with the experimental results especially at higher blade loading conditions.

The streamlines shown in Figure 9 show evidence of strong cross flow forces on the core flow stream tube. (This was derived from the numerical model for N = 54, R/h = 1.66 and $\Gamma/(V(R-h)) = 0.314$). The flow conditions near the core would be equivalent to that indicated in van Holten (1981) as a 'Diffuser-Type Augmentation' process under no-load conditions. (The length of wake possible was limited to y/h = 4.75 for this particular design).

The high C_Rs shown in Figure 8 will definitely need experimental verification. To exceed the Betz Limit an 'Ejector-Type Augmentation' process would need to be evi-

dent downstream of the concentrator and wind turbine. (See van Holten (1981) and Figure 1b). This effect has been noticed by van Holten using 'Tipvane' blades and a screen to represent a working turbine, under open jet wind tunnel conditions. (See van Holten (1982)). The theory of ejectors given by Bevilaqua (1978), shows that better energy transfer between two streams is achieved when mixing is done at lower than ambient pressure because of lower energy dissipation. The concentrator core flow is clearly below ambient pressure making conditions favourable. This effect has yet to be fully realized on the particular type of concentrator being investigated here. The current method of modelling used by the author is based on an inviscid assumption involving just the concentrator.

The results from the field tests and wind tunnel flow visualization indicate that high aspect ratio blades with higher camber will be required to improve the likelihood of a longer vortex wake behind the concentator. This should improve the value of VCF to the required value of two.

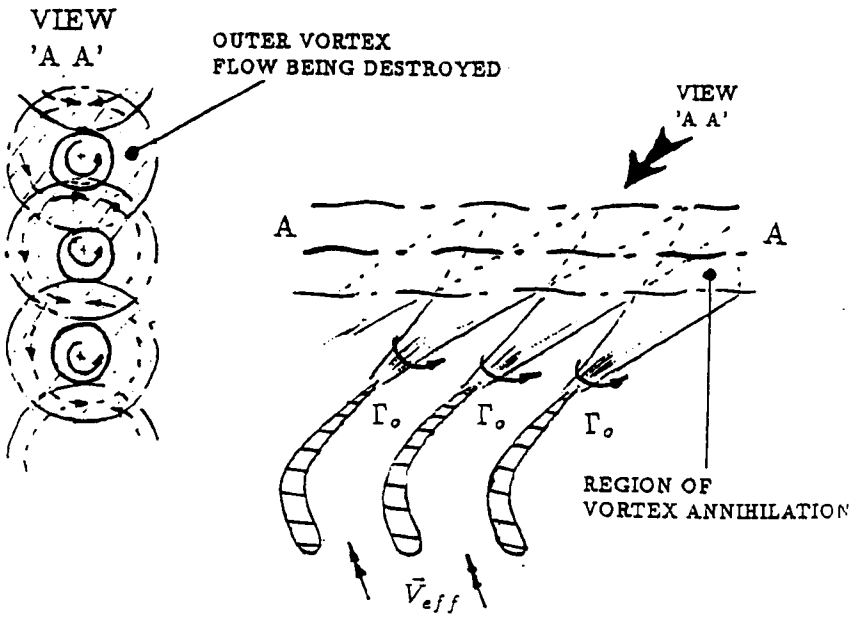

Figure 11. The effect of tip vortex interference on the wake.

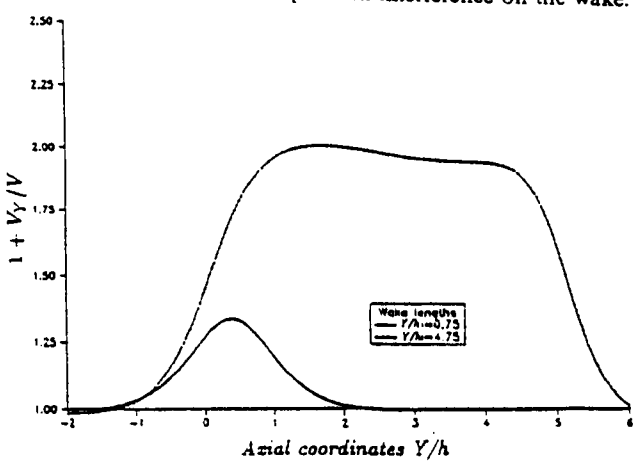

Figure 12. The effect of tip vortex interference on VCF.

ACKNOWLEDGEMENTS

This work is currently funded by Marlec Engineering Ltd and the Science and Engineering Research Council. Wind tunnel test facilities were provided by Queen

Mary and Westfield College, London and Goldstein Laboratory, Manchester.

I would like to thank the following people for their help during this research: David Sharpe and Godfrey Boyle for their encouragement and supervision, and Dr. David Smith, manager of Goldstein Laboratory for use of their wind tunnel test facilities.

REFERENCES

1. **Rosenbrock, H.H. (1983):** *Proposal for a New Design of Wind Power Generator. Wind Engineering, Vol. 7, No. 1.*

2. **Hunter, R. and Derrick, A. (1988):** *Progress in Theoretical Investigation of a Stator Flow Concentrator. Wind Energy Conversion 1988. (Proceedings of BWEA). Mechanical Engineering Publications.*

3. **Rechenberg, I. (1984):** *Berwian Concentrates the Wind: a report on a development at the Technical University of Berlin. Sonnenergie. pp 6-10 (in German).*

4. **Dick, E. (1986):** *Power Limits for Wind Energy Concentrator Systems. Wind Engineering, Vol. 10, No. 1, pp 29-45.*

5. **Hunt, B. (1981):** *The Role of Computational Fluid Dynamics in High Angle-of-Attack Aerodynamics. AGARD Conference Proceeding No. 335. pp 6-1, 6-28.*

6. *The Course Team. (1988): Introduction to Numerical Methods. M371 Unit 1.1 The Open University Press. pp 39, 41.*

7. **van Holten, Th. (1981):** *Concentrator Systems for Wind Energy, with Emphasis on Tip-vanes. Wind Engineering, vol. 5, No. 1, pp 29, 45.*

8. **van Holten, Th. (1982):** *An Analytical theory for Rotor-Tipvane Performance and Comparison with Experimental Results. 8th European Rotorcraft Forum, Aix-en-Provence.*

9. **Bevilaqua, P.M. (1978):** *Lifting Surface Theory for Thrust-Augmenting Ejectors. AIAA Journal Vol. 16, no. 5, pp 475, 481.*